Department of Electronic and Electrical Engineering.

DOCTOR OF PHILOSOPHY

Framework for Calculating Root-Mean-Squares of State Variables in Power Electronic Converter Models

by

Yuqing Wang

Supervised by Prof Martin Paul Foster and Dr Jonathan Neil Davidson

November 2023

Abstract

This thesis introduces a new framework to enhance the simulation performance of switch converters, motivated by the pursuit of more efficient energy conversion. This thesis offers improvements in the cyclic-mode model simulation of converters. Initially, a comprehensive review from the classification and operating principles of switch converters to their modelling methods sets the stage for subsequent analysis. Additionally, the thesis analyses and introduces the design methodologies for different types of switch converters. Subsequently, a cyclic-mode model for a class EF_2 inverter is constructed, and the accuracy of this simulation method is verified. A new application of Newton's method to accurately determine the multimode steady-state operating conditions of a switching converter by combining it with cyclic-mode model is then demonstrated, thus extending the applicability of the cyclic-mode model. Furthermore, a novel technique based on cyclic-mode modelling is proposed, which allows obtaining the root-means-square values of switch converter signals without generating waveforms, this greatly reduces the difficulty of finding the exact RMS value of a switching power supply. Finally, this technique, combined with the Newton method, forms a complete simulation method for power supplies. This method accurately and swiftly analyses DC-input power supplies in multiple operating modes, precisely obtaining their signal waveforms, periodic averages, and root-mean-square values.

Acknowledgements

As my PhD journey comes to an end, I would like to take this opportunity to express my sincere gratitude to those who have supported and helped me along the way. Without their encouragement, I would not have reached this point, and I extend my heartfelt thanks to them.

First and foremost, I would like to express my deep appreciation to my supervisors, Jonathan Davidson and Martin Foster. They provided invaluable assistance when my research encountered challenges and offered warm encouragement during difficult times.

I also extend my heartfelt thanks to my parents, Hongmei You and Xindong Wang, for their unwavering material and emotional support, which was instrumental in completing this journey. Additionally, I am deeply grateful to my girlfriend Huayi Pan for the love and joy she has brought into my life.

Lastly, but certainly not least, I want to thank my colleagues who have assisted me: Zijiang Yang, Jack Forrester, Alexander Parillo, Sajad Ansari and Zeyuan Wang.

Contents

Nomenclature

$\boldsymbol{A}_i$, $\overline{\boldsymbol{A}}_i$: System dynamics matrix for operation mode i

$\boldsymbol{B}_i$, $\overline{\boldsymbol{B}}_i$: System input vector for operation mode i

$\overline{\overline{\boldsymbol{A}}}_i$: System matrix for operation mode i, include dynamics and input.

$\boldsymbol{G}$: Newton's iteration method cost vector

$\boldsymbol{J}$: Jacobian matrix of partial derivatives of Newton iteration method

L: Inductance (H)

C: Capacitance (F)

C_p: Power coefficient

R: Resistance (Ω)

S: Switch

D: Diode

V_{in}: Input voltage (V)

V_{dc}: DC input voltage (V)

i, I: Current (A)

$\boldsymbol{K}, \overline{\boldsymbol{K}}$: Vector correcting the value of the state variable at the moment of switching

q: The amount of charge passing through a component (C)

Q_L: Load quality factor

t: Time interval (S)

Δ: The amount of change in a value over a period

$\bar{i}$: Cycle average current (A)

W: Energy stored in a component at a point (J)

$\omega_{\text{sw}}, f_{\text{sw}}$: Switching frequency (rad/s, Hz)

ω_0, f_0: Resonant frequency (rad/s, Hz)

$\boldsymbol{X}$: Newton iteration method variables

$\boldsymbol{x}(t_i^+)$: Discontinuity in the state-vector at $t = t_i$

x_i: The i^{th} element in the state vector $\boldsymbol{x}$

N: Equivalent number of turns ratio for an ideal transformer.

Z: Impedance (Ω)

f_n: Normalised frequency

P_{out}: Output power (W)

T_{sw}: The time required for a steady-state system to operate for one cycle. (s)

δ_i: Duty ratio of a mode of operation in a system in steady state operation

$\boldsymbol{\Phi}_i$, $\bar{\boldsymbol{\Phi}}_i$: Matrix exponential operations product on system dynamic matrices $\boldsymbol{A}_i$

$\bar{\bar{\boldsymbol{\Phi}}}_i$**:** Matrix exponential operations product on system dynamic matrices $\bar{\bar{\boldsymbol{A}}}_i$

$\boldsymbol{\Gamma}_i$, $\bar{\boldsymbol{\Gamma}}_i$: Argument input vector for i^{th} mode of operation

List of Figures

List of Tables

Chapter 1. Introduction

This Chapter provides an overview of the contributions made in this thesis. It includes an introduction to the research background, the motivation for the study, and the main innovations of this thesis. Subsequently, it lists the papers that have been published and currently under review. Then introduces the structure of the thesis and briefly describes the main contributions of each Chapter.

1.1 Background

In today's world, electricity is not only a basic necessity for daily life but also the driving force behind modern industrial and technological innovations. With rapid developments in material science and breakthroughs in advanced software technologies, we are witnessing a fundamental transformation in the generation and use of electricity. At the heart of this transformation, power electronic devices play a crucial role, acting as the bridge between energy generation and consumption.

The development and application of power electronics are ubiquitous, influencing every industry and aspect of life. Household appliances such as refrigerators, washing machines, air conditioners, and microwaves rely on power electronics for power control and energy efficiency [1.1]. In more advanced applications such as industrial automation [1.2], robotics [1.3], medical imaging equipment [1.4], and aerospace engineering [1.5], power electronics ensure precise control and high reliability of devices.

The advancement of power electronics is fundamentally a continuous pursuit of efficiency improvements and increasing power density. Especially in the case of resonant converters, their efficiency advantages are transforming them into key components in various energy conversion applications [1.6]. This phenomenon has heightened academic interest in its study, with researchers dedicated to optimizing the design and control strategies of resonant

converters through improved models, aiming for higher energy efficiency and better performance. This thesis proposes further research in this area.

1.2 Motivation

In recent years, with the rise of resonant converters, the field of power technology has witnessed a new development surge. These converters, with their significant advantages in efficiency [1.7] and electromagnetic compatibility [1.8], are beginning to replace traditional switched-mode converters in many areas.

Resonant converters create resonant circuits by connecting inductors and capacitors in series, parallel, or a combination of both, achieving zero-voltage switching [1.9] or zero-current switching [1.10] (soft switching). This characteristic significantly reduces energy loss and electromagnetic interference during switching, not only enhancing the efficiency of resonant conversion but also laying the foundation for higher energy density and smaller sizes. The power density can reach up to $2.5\ \mathrm{kW/in^3}$ [1.11].

The superior performance of resonant converters in terms of low energy loss makes them increasingly popular in high-end applications requiring high efficiency and low electromagnetic interference, such as in medical devices [1.12], and high-end audio equipment [1.13]. Similarly, in the application of electric vehicles, the advantages of resonant converters are significant. In the electric vehicle industry, the development of fast-charging technology has raised higher demands for power technology. Resonant converters, with their high efficiency and low heat loss, provide strong support for fast-charging technology in electric vehicles. An example of the onboard charger application is shown in Fig. 1.1.

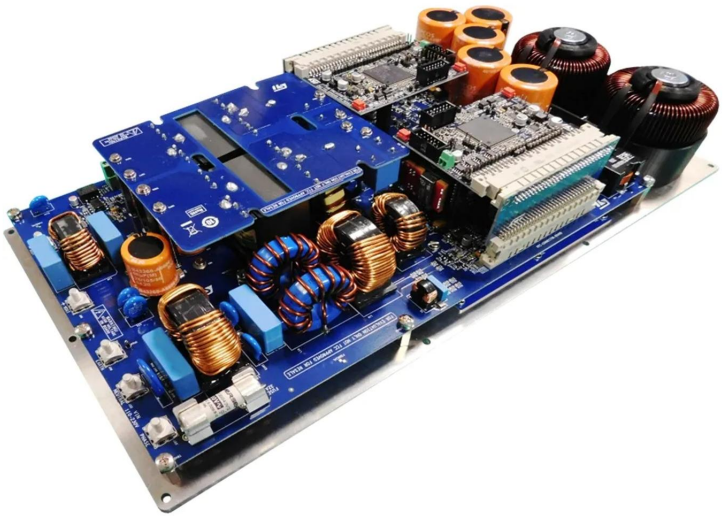

Fig. 1.1. A 7-kW electric vehicle onboard charger utilizing an LLC resonant topology [1.14]

However, with the increasing complexity of converter structures and diversifying application requirements, precisely predicting their performance behaviour has become a challenge. While simulation technologies for hard-switching converters are relatively mature, simulating resonant converters faces more challenges. Existing simulation methods often rely on specific assumptions about converter behaviours. For example, state-variable averaging assumes that the internal dynamic frequency of the system is much smaller than the switching frequency. This can be achieved for some hard switched converters such as buck converters, but for resonant converters, where the system dynamic frequency is close to the switching frequency, this assumption will no longer holds, resulting in an inability to fully capture their true performance and leading to discrepancies [1.15][1.16].

The cyclic-mode model, as an innovative modelling approach, has drawn extensive academic interest due to its advantages in precision and simulation speed [1.17] [1.18]. This thesis provides a detailed exploration of the cyclic-mode model's potential and limitations in accurately simulating switch converter performance. It further proposes innovative solutions to overcome current technological deficiencies, aiming to enhance the precision and speed of resonant converter simulations.

The significance of the root mean square (RMS) value in the modeling analysis of new converters, including resonant converters, is paramount. It is crucial for calculating converter losses, selecting essential components, and planning the spatial layout of the converter. Consequently, an accurate and rapid estimation of the RMS value can significantly streamline these processes. This thesis thoroughly examines existing techniques for calculating the RMS value, highlighting their benefits and drawbacks. Then, it proposes a modeling framework designed to quickly and accurately determine the RMS values of critical parameters in the converter model. This framework aims to provide easier access to RMS values, thereby enhancing the analysis and design process for users.

In the modelling analysis of new converters, including resonant converters, the importance of the root mean square (RMS) value cannot be overstated. It plays a key role not only in converter loss calculation but also in the selection of key components and spatial planning of the converter. Therefore, accurate and fast estimation of the RMS value is crucial for these processes. The thesis will discuss and study in detail the accurate and fast calculation of the RMS value of converters, providing insights and methodologies to greatly facilitate the aforementioned processes.

1.3 Novelty

The novelty of the work described in this thesis focuses on improvements to the cyclic-mode model. Cyclic-mode modelling is a technique used to estimate the values of state variables in dc-dc and dc-ac converters during steady state operation, which is based on an accurate determination of the converter's operating state. To precisely determine the converter's operating state of the cyclic-mode model, a combined approach with Newton's method has been proposed, allowing for accurate identification of the circuit's operating states. Subsequently, cyclic-mode modelling technique was improved so that the root mean square (RMS) values of the state variables (typically inductor currents and capacitor voltages) could be obtained without the need to generate waveforms, making it easier and quicker to obtain

these RMS values and extending the scope of the cyclic-modelling. Finally, the simplification of the modelling approach reduces the extensive time required for modelling across different converters. Finally, a comprehensive RMS modelling process based on the cyclic-mode model has been established, allowing more convenient modelling of different types of converters with multiple operating modes.

1. **Development of a cyclic-mode model for class EF_2 Inverters with a Piezoelectric Resonator as the auxiliary Network**

The class EF resonant inverters, formed by paralleling an LC series auxiliary network with the switch in class E inverters, can reduce voltage stress on the switch. Chapter 4 introduces a cyclic-mode model designed to predict the behaviour of the class EF inverters operating in 2-mode with a piezoelectric resonator replacing the auxiliary resonant circuit. The performance of the proposed model is demonstrated using a class EF_2 resonant inverter, wherein the piezoelectric resonator's resonant frequency is tuned to twice the resonant frequency of the main branch.

2. **Demonstrating the application of Newton's method to a particular converter cyclic-mode model**

Chapter 5 introduces a technique combining the Newton-Raphson method with the cyclic-mode model. It can precisely determine circuits operating states. This technique enables the cyclic-mode model to accurately simulate converters with multiple operating modes (circuit configurations). This technique has been applied to various switch converters in Chapter 5, Chapter 6, and Chapter 8, respectively.

3. **Evaluating state variables root mean square values in switching converters using cyclic-mode modelling**

Chapter 6 introduces a novel technique for evaluating Root Mean Square (RMS) values in switch converters, which is also the major contribution of this thesis. The technique employing cyclic-mode modelling and matrix operations represented by state variables. This approach leads to a generalized expression that is applicable to a variety of switch converters, facilitating the estimation of RMS current and voltage values without the need for generating waveforms prior to RMS calculation. The effectiveness of this technique is further validated across various types of converters in Chapters 7 and 8.

1.4 List of publications

Conference paper:

Wang, Yuqing, Jonathan N. Davidson, and Martin P. Foster. "Cyclic-mode modelling of class EF 2 inverters featuring a piezoelectric resonator as the auxiliary network." 11th International Conference on Power Electronics, Machines and Drives (PEMD 2022). Vol. 2022. IET, 2022.

1.5 Thesis structure

The thesis is divided into eight Chapters, each interconnected. The publications corresponding to each Chapter are listed in Section 1.4. A complete list of references can be found at the end of each Chapter. Below is a brief introduction to each Chapter:

Chapter 1 explains the crucial role of power electronics in modern society, the overall background of the study, and the research motivation. The thesis structure section offers a brief overview of each Chapter.

Chapter 2 reviews the work reported in the literature, divided into two main parts. The first part includes a background introduction to switch converters, their classification, and an

introduction and analysis of the operational principles of the converter topologies addressed in this thesis. The second part is a review of mainstream switch converter modelling methods. This includes basic concepts, as well as their advantages and disadvantages. It also explains why these modelling methods are ineffective for simulating resonant converters.

Chapter 3 introduces the design methodologies for various switch converter topologies, along with the associated modelling processes. In the boost converter section, a method decomposing the circuit based on the switch's conducting state is used to analyse typical current and voltage waveforms. The class EF_2 inverter section makes a series of assumptions to model class EF_2 inverters, employing descriptive functions. For LLC converters design section, fundamental mode analysis techniques are applied in their simulation and design.

Chapter 4 establishes a cyclic-mode model for class EF inverters and applies it to the optimal switching operations class EF_2 inverters which piezoelectric transformer (PT) as auxiliary resonant branch. The effectiveness of the cyclic-mode model through validation with SPICE simulation models. Additionally, the feasibility of replacing traditional LC series branch with PT is proven by comparing the results with practical models.

Chapter 5 introduces a technique using the Newton-Raphson method with the cyclic-mode model for determining the steady-state operating conditions of switch converters. This technique uses the Newton method, based on numerical Jacobian matrices, to correlate the cyclic-mode operating conditions with the mode switching conditions of the converter. Through iteration, it determines the converter's steady-state operating conditions. The method was tested under suboptimal operation in a class E inverter.

Chapter 6 describes the main contribution of the thesis which is a new technique to evaluate RMS values based on cyclic-mode modelling. As previous chapters have already described how the cyclic-mode can be used to integrate signals through the use of an augmented model, thereby providing the mean (average) section of the RMS calculation. The squared section of the RMS calculation is determined by linearising term that is somewhat similar to $\boldsymbol{x}^2$.

However, this is not straightforward, and it is necessary to use Hadamard and Kronecker products of matrices and vectors to obtain an algebraic solution. Although the derivation process is detailed and lengthy the final set of equations (termed the cyclic-RMS framework) can be used by just providing the framework with piecewise linear models for each mode, the mode duration times and the cyclic-mode initial condition thereby, resulting in a generalized expression applicable to various switch converters.

Chapter 7 applies the Newton method techniques described in Chapter 5 and the RMS cyclic-mode modelling techniques from Chapter 6, sequentially to a boost converter operating in discontinuous mode. Initially, it uses the Newton method and cyclic-mode modelling to determine the steady-state operating conditions of the converter under given parameter conditions. Subsequently, it constructs the RMS cyclic-mode model of the converter based on these steady-state operating conditions. The effectiveness of these two techniques is validated through SPICE simulations and practical models.

Chapter 8 introduces a simulation technique named 'cyclic RMS technique', which combines the Newton method from Chapter 5 with the RMS cyclic-mode modelling technique from Chapter 6. This technique accurately predicts the signal waveforms and precise RMS values of DC-input switch converters operating in multiple modes. This technique is sequentially applied to a class E inverter in suboptimal operation, a class EF_2 inverters in suboptimal operation, and an LLC converter in discontinuous operation condition. The effectiveness of this simulation technique is validated through both simulation models and practical experiments.

1.6 References

[1.1] Riffat, S. B., and Xiaoli Ma. “Thermoelectrics: A Review of Present and Potential Applications.” *Applied Thermal Engineering*, vol. 23, no. 8, June 2003, pp. 913–35, https://doi.org/10.1016/s1359-4311(03)00012-7.

[1.2] Tan, Kok Kiong, and Andi Sudjana Putra. “Drives and Control for Industrial Automation.” *Advances in industrial control*, 2011, https://doi.org/10.1007/978-1-84882-425-6.

[1.3] Moradewicz, Artur, and Marian P. Kaźmierkowski. “Resonant Converter Based Contactless Power Supply for Robots and Manipulators.” *Journal of Automation, Mobile Robotics & Intelligent Systems*, Jan. 2008, pp. 20–25。

[1.4] Patyuchenko, Anton. "High performance data converters for medical imaging systems." *Analog devices 53-02* (2019), Feb. 2019.

[1.5] Nasir, U, et al. “A SiC Based 2-Level Power Converter for Shape-And-Space-Restricted Aerospace Applications.” *Repository@Nottingham (University of Nottingham)*, 1 July 2019, https://doi.org/10.1109/peds44367.2019.8998907. Accessed 2 July 2024.

[1.6] Zeng, Junming, et al. "LLC resonant converter topologies and industrial applications—A review." *Chinese Journal of Electrical Engineering 6.3* (2020), pp.73-84.

[1.7] Fang, Xiang, et al. “Efficiency-Oriented Optimal Design of the LLC Resonant Converter Based on Peak Gain Placement.” *IEEE Transactions on Power Electronics*, vol. 28, no. 5, May 2013, pp. 2285–96. https://doi.org/10.1109/tpel.2012.2211895.

[1.8] Youssef, Mohamed, et al. “Electromagnetic Compatibility Results for an LCC Resonant Inverter for the Tranportation Systems.” *Twenty-Fifth Annual IEEE Applied Power Electronics Conference and Exposition (APEC)*. IEEE, 2010., 1 Feb. 2010, https://doi.org/10.1109/apec.2010.5433477. Accessed 2 July 2024.

[1.9] Lin, Bor-Ren, and Jia-Yu Dong. “ZVS Resonant Converter With Parallel–Series Transformer Connection.” *IEEE Transactions on Industrial Electronics*, vol. 58, no. 7, July 2011, pp. 2972–79. https://doi.org/10.1109/tie.2010.2077612.

[1.10] Lee, Jaeyeon, et al. “An Isolated Single-Switch ZCS Resonant Converter With High Step-Up Ratio.” *IEEE Transactions on Power Electronics*, vol. 36, no. 10, Oct. 2021, pp. 11555–64. https://doi.org/10.1109/tpel.2021.3072647.

[1.11] Ye, Zichao, et al. “The Cascaded Resonant Converter: A Hybrid Switched-Capacitor Topology With High Power Density and Efficiency.” *IEEE Transactions on Power Electronics*, vol. 35, no. 5, May 2020, pp. 4946–58. https://doi.org/10.1109/tpel.2019.2947218.

[1.12] Cavalcante, F. "High output voltage series-parallel resonant DC-DC converter for medical X-ray imaging applications." *These de la Swiss Federal Institute of technology Zurich* (2006), https://doi.org/10.3929/ethz-a-005212928..

[1.13] Enrico Orietti, et al. “Current Sharing in Three-Phase LLC Interleaved Resonant Converter.” *2009 IEEE Energy Conversion Congress and Exposition.* IEEE, Sept. 2009, https://doi.org/10.1109/ecce.2009.5316510. Accessed 10 May 2024.

[1.14] "STDES-7KWOBC - 7 kW On-Board Charger (OBC) Reference Design." STMicroelectronics, www.st.com/en/evaluation-tools/stdes-7kwobc.html. Accessed 22 Nov. 2023.

[1.15] Adragna, Claudio. “LLC Resonant Converters: An Overview of Modeling, Control and Design Methods and Challenges.” *Foundations and Trends in Electric Energy Systems*, vol. 5, no. 2–4, Jan. 2022, pp. 75–491. https://doi.org/10.1561/3100000029.

[1.16] Visser, H. R., and P. P. J. Van den Bosch. "Modelling of periodically switching networks." *PESC'91 Record 22nd Annual IEEE Power Electronics Specialists Conference*. IEEE, 1991, https://doi.org/10.1109/pesc.1991.162655.

[1.17] Foster, M. P., et al. “Cyclic-averaging for high-speed analysis of resonant converters.” *IEEE Transactions on Power Electronics*, vol. 18, no. 4, July 2003, pp. 985–93. https://doi.org/10.1109/tpel.2003.813763.

[1.18] Yang, Zijiang, et al. “Soft Switching Voltage Regulation for Inductorless Piezoelectric Transformers: A Cyclic-Mode Analysis.” *IEEE Transactions on Power Electronics*, vol. 38, no. 12, Dec. 2023, pp. 15645–58. https://doi.org/10.1109/tpel.2023.3305558.

Chapter 2. Review of switching converters, their modelling and applications

This Chapter reviews the classification of switching converters, various topologies, their operating principles, and applications. It also covers the latest techniques in converter modelling, including their fundamental principles and characteristics. This Chapter provides readers with the foundational knowledge needed to understand the current research in this field. Some of this content will be utilized in subsequent Chapters.

2.1 Introduction

Switching converters, fundamental to modern electronics, have experienced a significant increase in applications, extending from everyday consumer devices to advanced industrial machinery. Their versatility and efficiency are highlighted by the variety of available topologies, each meticulously tailored to specific operational needs and characteristics. Switching converters have a broad spectrum of applications, playing a pivotal role in powering electric vehicles [2.1], battery charging [2.2], and optimal power management [2.3]. Another growing area is the integration of renewable energy sources, like solar photovoltaic (PV) systems, into microgrids, which necessitates efficient power conversion and integration [2.4]. Additionally, the introduction of wide-bandgap materials such as silicon carbide (SiC) in power devices has significantly expanded the capabilities of switching converters. SiC-based devices are able to operate at higher switching speeds, voltages, and temperatures, thereby offering enhanced efficiency and power density across various applications, further broadening the range of switching converter applications [2.5].

As the technological landscape advances, so does the need for more sophisticated and efficient power conversion solutions. This demand has placed converter design at the forefront, where engineers contend with a complex array of parameters. The design of these

converters varies widely, influenced by numerous specific parameters such as output voltage and power [2.5]-[2.8], as well as optimization objectives like size [2.9] and cost [2.10], or a combination of those objectives [2.11][2.12]. These parameters, encompassing output voltage and power specifications to complex optimization goals, are fundamental to any converter design.

At the heart of converter design process is the accurate estimation of currents and voltages during operation. These estimations are crucial, impacting the converter's performance, reliability [2.13], and lifespan [2.14]. For example, the loss in an inductor is intricately linked to the frequency and shape of its current waveform. As the field of power electronics expands, traditional modelling techniques, while foundational, often fail to adequately capture the subtleties of contemporary converter topologies. This has led to the development of advanced modelling techniques, with cyclic-mode modelling standing out as a notable advancement [2.15].

This review explores the operational principles of selected hard-switching and resonant converters and outlines the current mainstream methods of switching converter modelling. The aim is to provide a comprehensive understanding of the existing approaches to switching converters modelling and their application, highlighting their benefits and limitations.

2.2 Hard switching converters

2.2.1 Introduction

Hard-switching converters, a cornerstone in modern power electronics [2.16], function by toggling switching devices between on and off states under conditions of non-zero voltage or current. This operational mode, generally simpler and more cost-effective than soft-switched alternatives, presents unique challenges. The simplicity of hard-switching converters, marked by fewer components, leads to straightforward design and implementation, making them well-suited for a wide range of applications.

In renewable energy, particularly in high-gain DC-DC converters like boost converters, hard-switching converters have established a significant presence. For example, in photovoltaic (PV) systems, assessments of hard-switching converters with Silicon and GaN switches have demonstrated that GaN-based options provide enhanced efficiency and power density [2.17].

However, it is important to note that the inherent simplicity of hard-switching converters often leads to increased switching losses [2.18], particularly at higher frequencies. This not only impacts system efficiency and complicates thermal management but also presents challenges like electromagnetic interference (EMI) in applications [2.19].

2.2.2 Classification of hard-switching converters

In contemporary power electronics, traditional hard-switching converters are key components, each designed for specific voltage transformations. Based on their input and output voltage characteristics, these converters can be broadly classified into four categories:

1. DC-DC Converters: These converters are designed to adjust DC voltage levels. The buck converter, a prime example, efficiently reduces a higher input voltage to a lower output level. Cui, *et al.,* [2.20] demonstrate their application in complex systems, including microprocessors and LiDAR.

2. DC-AC Converters: These converters transform DC voltage into an AC waveform. Single phase full-bridge inverter, as detailed by Zhu, *et al.,* [2.21], is a notable example, characterized by its four-switch configuration that facilitates DC to AC conversion.

3. AC-DC Converters: Tasked with converting AC voltage into a rectified DC output, the Full-Wave Rectifier is a prime example. Using four diodes, it is mainly used in power adapters and battery charging systems[2.22].

4. AC-AC Converters: These converters are designed to change one AC voltage frequency to another. The Cycloconverter, for instance, directly converts a high-frequency AC input to a lower frequency AC output, eliminating the need for an intermediary DC stage [2.23].

2.2.3 Buck converter

2.2.3.1 Introduction

The Buck Converter, commonly known as the step-down converter, is a fundamental example of the DC-to-DC converter family. Its primary role is to decrease voltage levels while simultaneously increasing current from input to output. As a key member of the switched-mode power supply (SMPS) systems, it is renowned for its exceptional power efficiency can exceeding 90% [2.24]. Buck converters, along with their counterparts, boost converters, are integral to power electronics. Their evolution, marked by significant technological advancements, has led to their widespread use in various sectors, notably telecommunications and automotive electronics [2.25].

2.2.3.2 Structural Overview

As depicted in Fig. 2.1, a buck converter typically comprises semiconductor components, such as a diode D and a transistor switch S. The converter also includes energy storage elements, namely a capacitor C and an inductor L. The inductor L is crucial in energy transfer, storing energy when the switch is on and releasing it when off. To reduce voltage ripple, capacitive filters are often integrated at the converter's output (load-side).

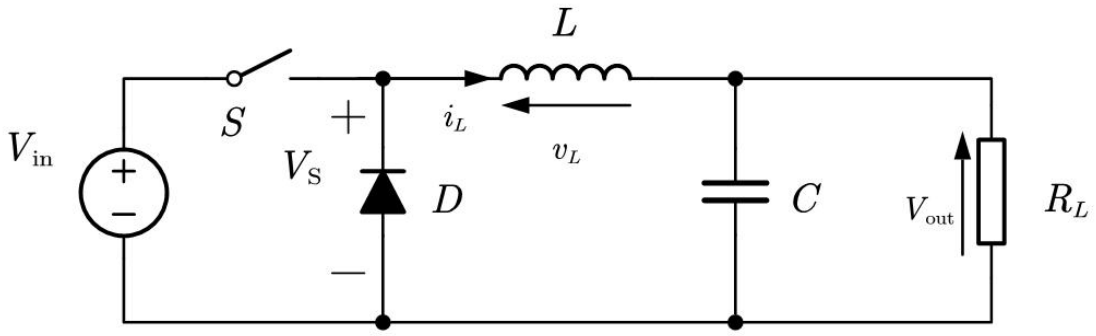

Fig. 2.1. Circuit diagram of a buck converter

2.2.3.3 Operational Dynamics

Buck converters operate predominantly in two operation condition: Continuous Conduction Mode (CCM) and Discontinuous Conduction Mode (DCM) [2.26] . In CCM, the inductor current does not drop to zero, maintaining a constant flow of current throughout the switching cycle and resulting in a stable output voltage and current. However, this mode may lead to increased switching losses. In contrast, in DCM, the inductor current reduces to zero during each cycle, resulting in intermittent current flow. While CCM provides stable output due to continuous current flow, it might incur higher switching losses. DCM, with its intermittent current, can lead to output instability but usually has lower switching losses. The efficiency of a buck converter depends on its conduction mode, with transitions between CCM and DCM largely dictated by the load conditions.

2.2.3.3.1 Continuous Conduction Mode Operation analysis

CCM is commonly chosen for applications with higher inductor currents, as it ensures that the inductor current remains non-zero throughout the switching cycle. The operational dynamics of this condition can be segmented into two phases: the 'switch turned on' state (also referred to as Mode 1) and the 'switch turned off' state (or Mode 2), as illustrated in Fig. 2.2,

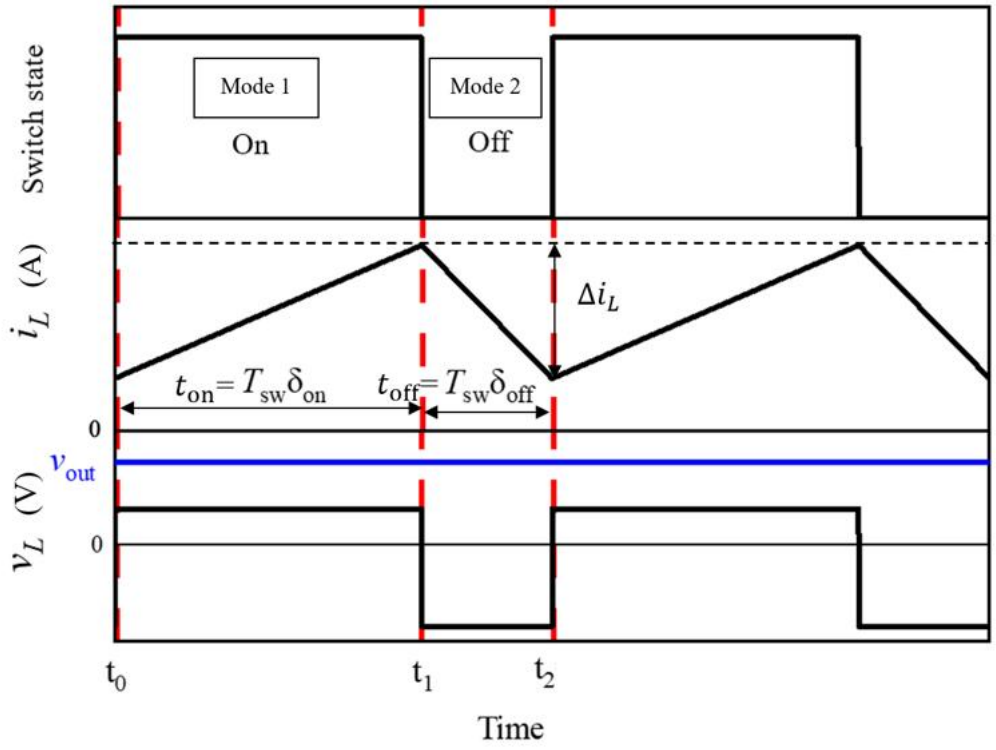

Fig. 2.2. Buck converter's switch state, inductor current i_L and inductor voltage v_L waveforms in CCM operation

The rate of change of i_L can be calculated by the following equation,

$$\frac{\mathrm{d}i_L}{\mathrm{dt}} = \frac{v_L}{L} \tag{2.1}$$

Mode 1 ($t_0 \leq t < t_1$): In this phase, the switch is on. The input voltage source supplies power to both the load and the inductor, causing the inductor to store energy and its current to increase linearly. Concurrently, the diode is reverse-biased. The increase in inductor current during the conduction state is given by:

$$\Delta i_{L\,\mathrm{on}} = \frac{v_L}{L} t_{\mathrm{on}} = \frac{V_{\mathrm{in}} - V_{\mathrm{out}}}{L} t_{\mathrm{on}} \tag{2.2}$$

where $t_{\mathrm{on}} = \delta_{\mathrm{on}} T_{\mathrm{sw}}$.

Mode 2 ($t_1 \leq t < t_2$): In this operational phase, the switch is turned off while the diode transitions to a forward-biased state. The energy previously stored within the inductor is channelled through the diode to supply the load. This results in a linear decrement in the inductor current. If the forward voltage drop of the diode is ignored, the change in inductor current is

$$\Delta i_{L\,\text{off}} = \frac{v_L}{L} t_{\text{off}} = -\frac{V_{\text{out}}}{L} t_{\text{off}} \tag{2.3}$$

where

$$t_{\text{off}} = \delta_{\text{off}} T_{\text{sw}} = (1 - \delta_{\text{on}}) T_{\text{sw}} \tag{2.4}$$

in this case.

Assuming that the converter operates in a cyclic steady state, then at the end of an operational cycle T_{sw}, the energy stored in each element is equal to the energy at the beginning of the cycle, which means,

$$i_L(t_0) = i_L(t_0 + T_{\text{sw}}) \tag{2.5}$$

Thus, the change in inductor current i_L should be consistent in both modes,

$$\Delta i_{L\,\text{on}} + \Delta i_{L\,\text{off}} = 0 \tag{2.6}$$

Substitute (2.2) and (2.3) into (2.6) ,

$$\frac{V_{\text{in}} - V_{\text{out}}}{L} t_{\text{on}} - \frac{V_{\text{out}}}{L} t_{\text{off}} = 0 \tag{2.7}$$

Substitute (2.4) into (2.7) gives ratio between voltage gain and duty cycle of buck converter under CCM ,

$$\frac{V_{\text{out}}}{V_{\text{in}}} = \delta_{\text{on}} \tag{2.8}$$

2.2.3.3.2 Discontinuous Conduction Mode operation analysis

In DCM operation, the inductor current intermittently drops to zero during the switching cycle. This mode often occurs in systems with lighter load current, causing the inductor's stored energy to be fully discharged before the cycle's end [2.27]. Despite these dynamics, the converter maintains a steady state, meaning the energy in the inductor is consistent at both the

beginning and the end of the cycle. DCM is typically initiated under low load currents, and its operation can be divided into three modes, as shown in Fig. 2.3.

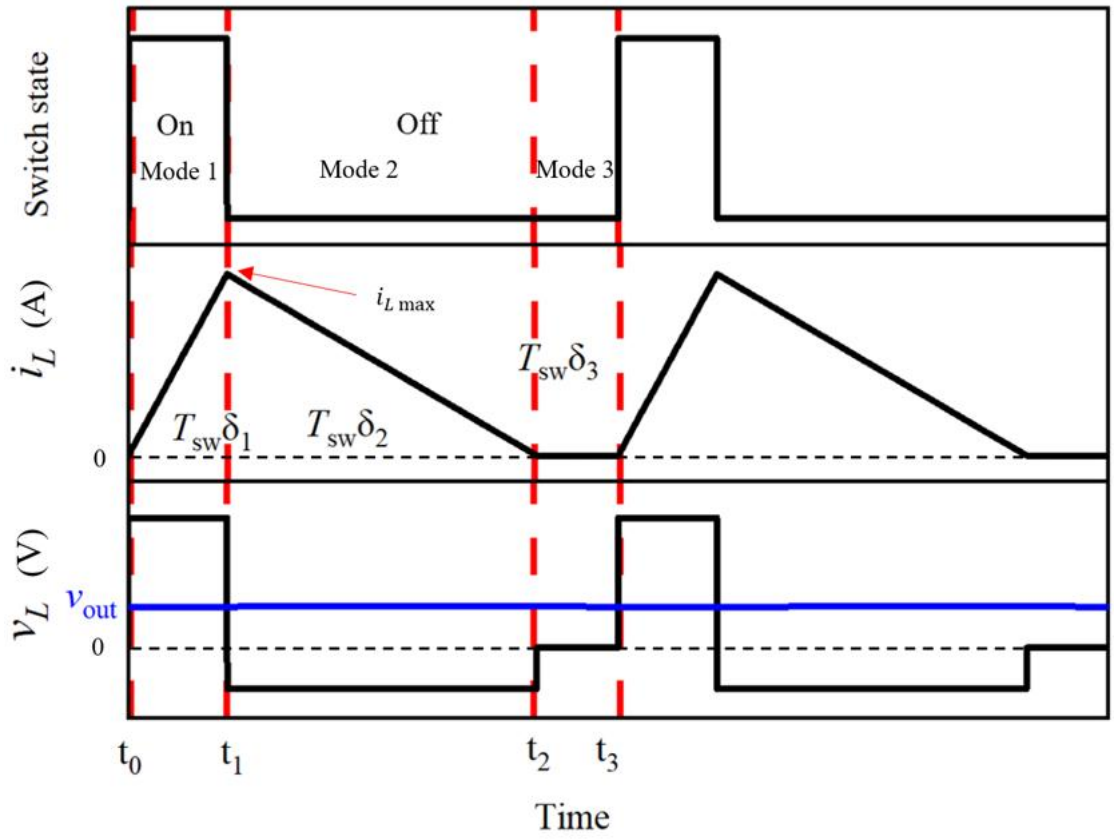

Fig. 2.3. Buck converter's switch state, inductor current i_L and inductor voltage v_L waveforms in DCM operation

Mode 1 ($t_0 \leq t < t_1$): The switch is turned on. Similar to CCM, the input source powers the load and charges the inductor. The operational state of the converter in this mode is similar with Mode 1 in CCM.

Mode 2 ($t_1 \leq t < t_2$): When the switch is off, the energy stored in the inductor drives a current through the diode to support the load. The inductor current reduces from its peak value until zero during this phase. The duty cycle relevant to this mode is characterized by:

$$\delta_2 = 1 - \delta_1 - \delta_3 \qquad (2.9)$$

δ_3 representing the duration of Mode 3 (zero inductor current mode). As i_L decreases to zero at the end of Mode 2, the inductor current i_L at the beginning of the cycle should be equal to that at the end of Mode 2.

$$i_L(t_0) = i_L(t_2) \tag{2.10}$$

Rearrangement of (2.7) gives relationship between two mode duty cycles and input and output voltages,

$$\delta_2 = \frac{V_{\text{in}} - V_{\text{out}}}{v_{\text{out}}}\delta_1 \tag{2.11}$$

Mode 3 ($t_2 \leq t < t_3$): In this phase, the switch remains off. Consequently, the energy in the inductor is completely used up, resulting in zero inductor current. The load is now powered solely by the energy previously stored in the capacitor, with the main circuitry in a quiescent state, ready for the next switching cycle.

The cycle average inductor current $\bar{i}_{\text{L}}$ is equal to the load current i_{out},

$$\bar{i}_{\text{L}} = i_{\text{out}} = \frac{\left(\frac{1}{2}i_{L\,\max}(t_1 - t_0) + \frac{1}{2}i_{L\,\max}(t_2 - t_1)\right)}{T_{\text{sw}}} \tag{2.12}$$

Simplifying (2.12) gives

$$i_{\text{out}} = \frac{1}{2}i_{L\,\max}(\delta_1 + \delta_2) \tag{2.13}$$

Substituting (2.2) into (2.13) gives

$$i_{\text{out}} = \frac{(V_{\text{in}} - V_{\text{out}})(\delta_1 T_{sw})\ (\delta_1 + \delta_2)}{2L} \tag{2.14}$$

Substituting (2.11) into (2.14) gives

$$i_{\text{out}} = \frac{(V_{\text{in}} - v_{\text{out}})(\delta_1 T_{sw})\left(1 + \frac{V_{\text{in}} - V_{\text{out}}}{V_{\text{out}}}\right)\delta_1}{2L} \tag{2.15}$$

Finally, the equation for the voltage gain of the buck converter under DCM can be formulated,

$$\frac{V_{\text{out}}}{V_{\text{in}}} = \frac{1}{1 + \frac{2L\, i_{\text{out}}}{\delta_1^2 V_{\text{in}} T_{\text{sw}}}} \tag{2.16}$$

Based on (2.8) and (2.16), it is evident that in both DCM and CCM, the output voltage modulation is primarily governed by the switch's duty cycle. Adjusting this duty cycle allows the buck converter to effectively regulate the output voltage.

The transition point between DCM and CCM operation occurs when the inductor current reaches zero precisely at the end of the switching cycle. The operating state of the converter now conforms to both CCM and DCM criteria. Hence, at the transition point, according to (2.13) and (2.4) the output current $i_{\text{out,lim}}$ is given by,

$$i_{\text{out,lim}} = \frac{1}{2} i_{L\,\max}(\delta_1 + \delta_2) = \frac{1}{2} i_{L\,\max} \tag{2.17}$$

Substituting (2.2) into (2.17), $i_{\text{out,lim}}$ become to,

$$i_{\text{out, lim}} = \frac{V_{\text{in}} - V_{\text{out}}}{2L} t_{\text{on}} \tag{2.18}$$

Therefore, by substituting (2.4) into (2.18), we can determine the load current at this transition point. This load current represents the threshold at which the converter transitions from DCM to CCM.

$$i_{\text{out, lim}} = \frac{V_{\text{in}} T_{\text{sw}} (1 - \delta_1)\delta_1}{2L} \tag{2.19}$$

where δ_1 in this formula represents the duty ratio when the switch turned on.

2.2.4 Boost converter

2.2.4.1 Introduction

A boost converter, a type of DC-DC power converter, is designed to step up voltage (while stepping down current) from its input (supply) to its output (load). It consists of several fundamental components that work in tandem to achieve the desired voltage increase. Each component plays an integral role in the converter's functioning [2.28].

2.2.4.2 Structural overview

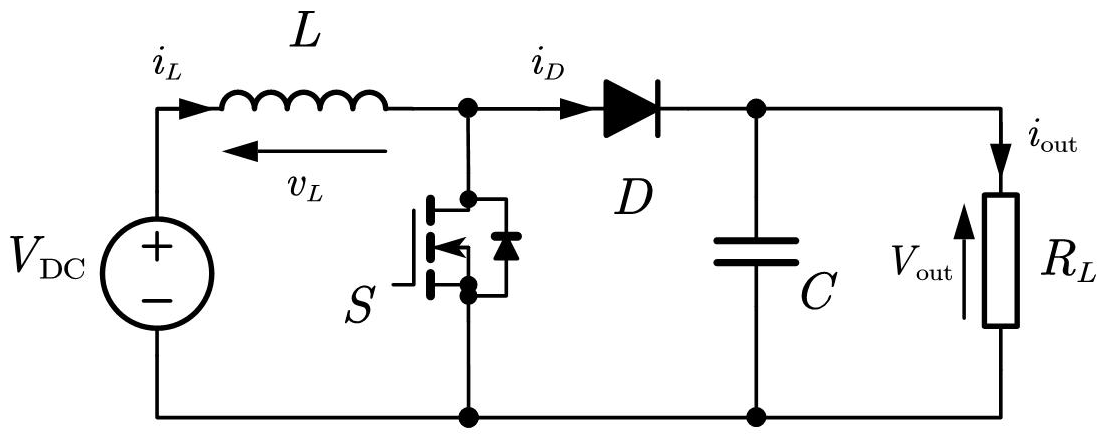

Fig. 2.4. Circuit diagram of a boost converter

The circuit diagram of a boost converter is illustrated in Fig. 2.4. The fundamental components of a boost converter and their respective functions are as follows:

Inductor L: An essential component, the inductor stores energy in a magnetic field when the switch is on. When the switch is off, the stored energy is released, resulting in a higher output voltage. The inductor's resistance to current variations is crucial in the voltage boosting process.

Capacitor C: The capacitor serves dual purposes: energy storage and voltage smoothing. It absorbs energy from the inductor, ensuring a stable output voltage. By filtering voltage

fluctuations, the capacitor maintains a nearly constant output regardless of input or load variations.

Diode D: In a boost converter, the diode prevents current backflow from the output to the input when the switch is on. When the switch is off, the diode conducts, allowing the inductor to release its stored energy to the output.

Switch S: Typically, a transistor, this switch is central to the boost converter's control mechanism. The operation of the converter is regulated by controlling the switch. When the switch is on, energy is stored in the inductor; when it is off, this stored energy, along with the input, is transferred to the output, leading to a voltage boost.

In a boost converter, the precise coordination and timing of these components are critical. The duration for which the switch turned on significantly influences the voltage boost achieved.

2.2.4.3 Operating Principle

The boost converter operates based on two primary states: the "switch turned on" state and the "switch turned off" state. The converter's behaviour in these states, combined with the roles of its primary components, determines its performance and the resulting output voltage. The converter's operation can be categorized into two operation conditions: Continuous Conduction Mode (CCM) and Discontinuous Conduction Mode (DCM).

2.2.4.3.1 Continuous Conduction Mode Operation analysis

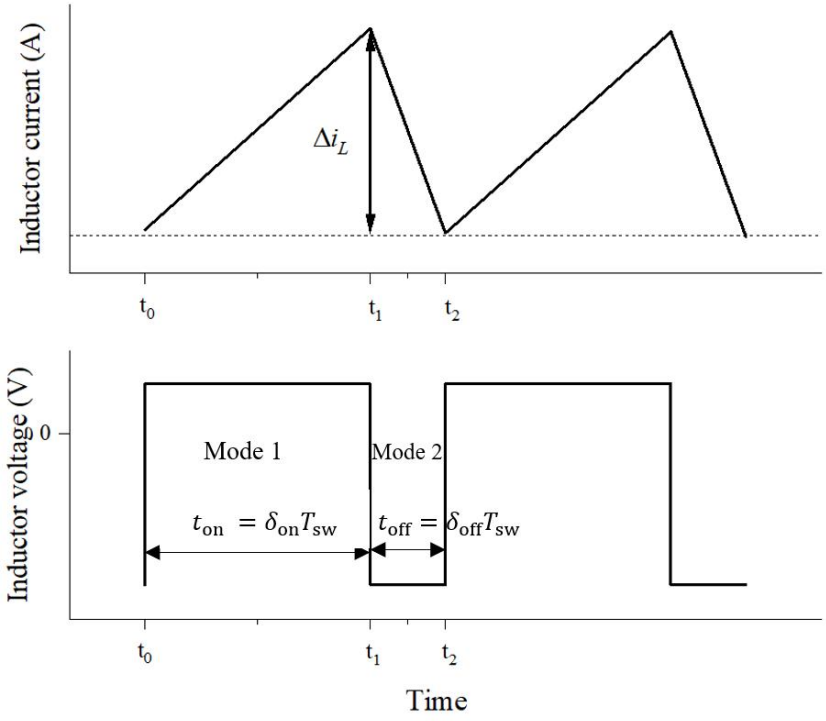

Fig. 2.5. Boost converter inductor current i_L and inductor voltage v_L waveforms in CCM operation

In CCM operation the operation waveform is shown in Fig. 2.5, similar with buck converter, the operation can be split into two modes:

Mode 1(Switch on state) $t_0 \leq t < t_1$: During this phase, the switch is turned on, allowing the input voltage to be applied across the inductor. The inductor current increases linearly as it stores energy. This change in inductor current can be mathematically represented as:

$$\Delta i_{\mathrm{L}} = \frac{V_{\mathrm{DC}} t_{\mathrm{on}}}{L} \tag{2.20}$$

The diode is reverse biased during this phase, preventing the inductor current from flowing to the output.

Mode 2 (Switch off state) $t_1 \leq t < t_2$: With the switch turned off, the inductor releases its stored energy to the load. The relationship between the output voltage, input voltage, and the change in inductor current is given by:

$$V_{\text{out}} = V_{\text{DC}} + L\,\frac{\Delta i_{\text{L}}}{t_{\text{off}}} = \frac{V_{\text{DC}}}{1-\delta_{\text{on}}} \tag{2.21}$$

The diode becomes forward biased, allowing the energy to be transferred to the output. The capacitor smoothens the output voltage by absorbing the excess energy and releasing it when required, ensuring a steady output.

2.2.4.3.2 Discontinuous Conduction Mode operation analysis

In DCM operation, calculating the converter's output gain becomes challenging due to the unknown duration of Mode 3, which is characterized by zero inductor current. The example inductor current waveform of in DCM operation is illustrated in Fig. 2.6. To derive the expression for voltage gain in DCM, an initial analysis of Mode 1 is required.

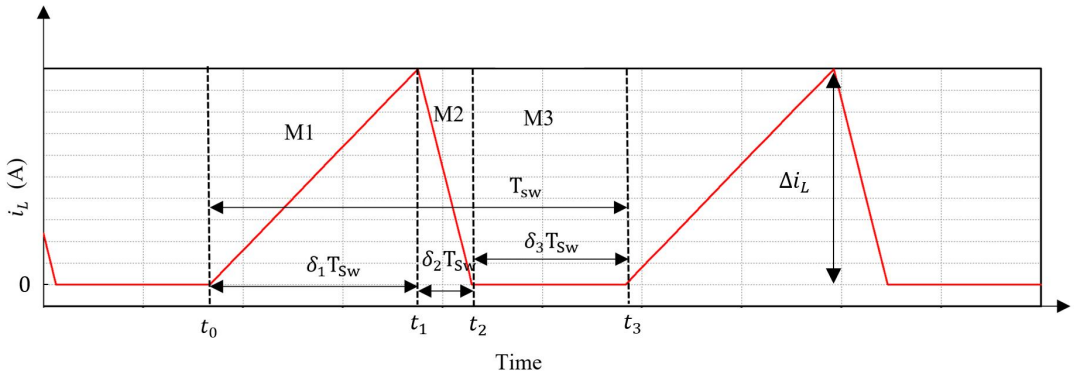

Fig. 2.6. Inductor current of a boost converter in DCM operation

When the switch turned on, similar to CCM operation, the inductor stores energy during this state. The increase in its current can be expressed as follows:

$$\Delta i_{\mathrm{L\,on}} = \frac{V_{\mathrm{DC}}\delta_1}{L} \tag{2.22}$$

After the switch is turned off, the inductor current drops to zero at the end of Mode 2 which is $t_2 = (\delta_1 + \delta_2)T_{\mathrm{sw}}$. So, the variation of inductor current i_{L} in Mode 2 can be obtained as

$$\Delta i_{\mathrm{L\,off}} = \frac{(V_{\mathrm{out}} - V_{\mathrm{DC}})\delta_2 T_{\mathrm{sw}}}{L} \tag{2.23}$$

The relationship between the duty cycles of the two modes and the input and output voltages can be expressed as follows:

$$\delta_2 = \frac{V_{\mathrm{DC}}\delta_1}{V_{\mathrm{out}} - V_{\mathrm{DC}}} \tag{2.24}$$

Consequently, the output current at the load is equal to the integral of the total current passing through the diode q_{D}, divided by the duration of the cycle.

$$V_{\mathrm{out}} = \frac{q_{\mathrm{D}}}{T_{\mathrm{sw}}} = \frac{i_{\mathrm{L\,max}}\delta_2}{2} \tag{2.25}$$

Substituting (2.23) and (2.24) into (2.25) gives,

$$V_{\mathrm{out}} = \frac{V_{\mathrm{DC}}^2\delta_1^2 T_{\mathrm{sw}}}{2L(V_{\mathrm{out}} - V_{\mathrm{in}})} \tag{2.26}$$

Thus, the voltage gain is given by rearrange (2.26),

$$\frac{V_{\mathrm{out}}}{V_{\mathrm{DC}}} = 1 + \frac{V_{\mathrm{DC}}\delta_1^2 T_{\mathrm{sw}}}{2Li_{\mathrm{out}}} \tag{2.27}$$

Then according to $i_{\mathrm{out}} = \frac{v_{\mathrm{out}}}{R_{\mathrm{L}}}$, could rewrite the output voltage gain in (2.27),

$$\frac{V_{\mathrm{out}}}{V_{\mathrm{DC}}} = \frac{1 + \sqrt{1 + \frac{4\delta_1^2 R_L T_{\mathrm{sw}}}{2L}}}{2} \tag{2.28}$$

In DCM operation, the output voltage tends to be more sensitive to variations in load and can be less predictable compared to CCM. This sensitivity often necessitates the implementation of control strategies to maintain operation in CCM, particularly in applications that demand precise voltage regulation.

In both DCM and CCM, the diode is crucial for ensuring unidirectional current flow. Meanwhile, the capacitor serves as an energy reservoir, storing and releasing energy as needed to maintain a stable and smooth output voltage. The Boost Converter's versatility in power electronics stems from its ability to achieve desired voltage amplification by adjusting the duty cycle. Feedback control, often employing a PID controller, is utilized to fine-tune the duty cycle, ensuring the output voltage remains consistent despite changes in input voltage or load [2.28].

For hard-switching converters, it is essential to pay close attention to the average inductor current and average output voltage. These parameters significantly affect the converter's behaviour, efficiency, and stability. Accurate estimation of these averages is vital for optimizing converter performance and extending its operational lifespan.

2.3 Resonant converters

2.3.1 Introduction

Hard switching is common in single-switch power supply circuits, which are widely used due to their simplicity, fewer components, and low manufacturing costs. Ideally, in hard-switching converters, the transition between switch states occurs instantaneously. Hard switching involves a switch turning off by moving from a high current state to zero under significant voltage, and turning on by transitioning from a high voltage state to zero while a significant current starts flowing. This transition time is practically instantaneous.

In practical applications, however, hard switching faces significant challenges. A major issue is the discharge of parallel capacitance (whether parasitically present on the switch or discretely present in the circuit), which reduces the converter's efficiency. When the switch turns on with non-zero voltage across it, energy stored in the capacitance is lost as discharge current. Additionally, turning on the switch at high voltage increases power dissipation. This dissipation grows with higher operating frequencies, exacerbated by the trend towards smaller, higher-frequency power electronics, where switching losses and parasitic components become increasingly significant [2.29].

To address the challenges of hard switching, engineers have developed alternatives like resonant converters. These inverters utilize resonant circuits to achieve Zero Voltage Switching (ZVS) and Zero Current Switching (ZCS) [2.30]-[2.32], activating the switch when both the voltage across it or the current through it are near zero. This approach enhances efficiency in both the switch and the inverter, a technique referred to as soft switching.

2.3.2 Characteristics and classification of resonant converters

Resonant converters, crucial in modern power electronics, come in various types, each with unique features and benefits for specific applications. Resonant converters are mainly categorized by the arrangement of their resonant tank elements: Series Resonant Converters (SRC) and Parallel Resonant Converters (PRC), known as two-element resonant converters; Series-Parallel Resonant Converters (LCC or LLC), known as three-element resonant converters; and CLLC converters, known as multi-element resonant converters [2.33].

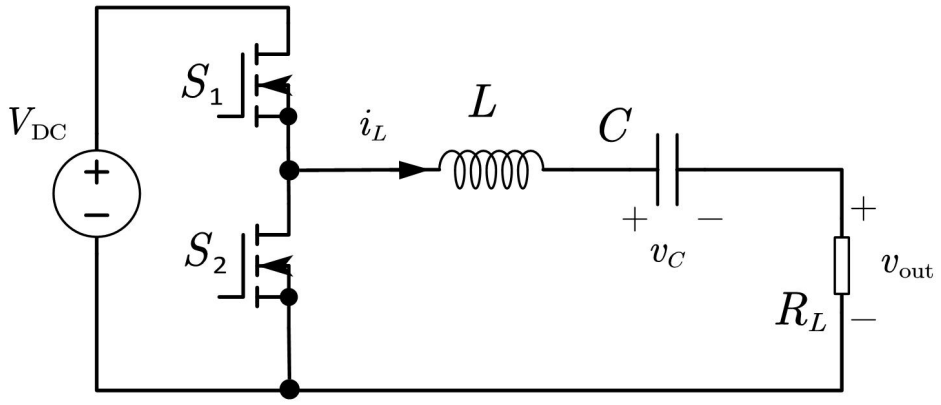

Fig. 2.7. Example circuit diagram of a series resonant converter

SRC is a key category in power converters, as outlined in [2.33]. An example of this circuit layout is illustrated in Fig. 2.7. Characterized by its series connected resonant components, the SRC configuration uses ZVS or ZCS, offering multiple operational advantages [2.34]. Notably, the SRC excels in significantly reducing the switching losses common in power converters. These attributes enhance the SRC's operational efficiency, making it ideal for energy conservation scenarios [2.35]. As a result, the SRC has a high-power density, as cited in [2.34]. However, the SRC is not without limitations. For example, output voltage modulation requires a wide frequency variation range, and adjusting the voltage under no-load or light-load conditions is challenging, as indicated in [2.33].

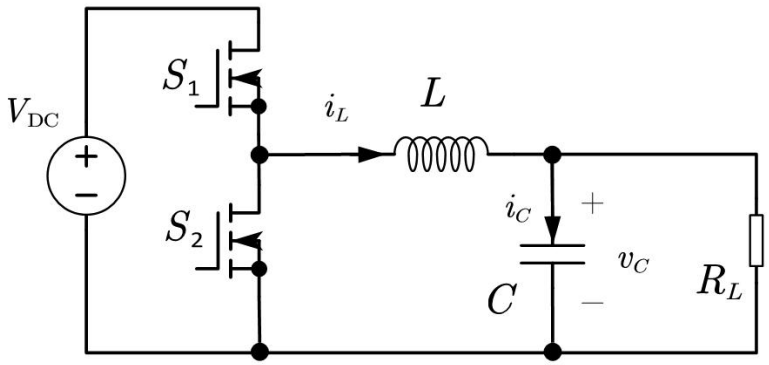

Fig. 2.8. Example circuit diagram of a parallel resonant converter

In PRCs, the resonant elements are configured in parallel. An example of this circuit diagram is illustrated in Fig. 2.8. Although PRCs and SRCs both facilitate ZVS, their operational characteristics differ significantly. A notable feature of PRCs is their inherently high current levels. While these high currents pose challenges, such as thermal management and increased component stress, they are advantageous for applications requiring high current delivery, as emphasized in [2.36]. Compared to SRCs, PRCs have some drawbacks. Under light load conditions, PRCs exhibit increased circulating currents, leading to reduced efficiency. The resonant circuitry can cause increased switching losses, resulting in overall reduced efficiency, as explained in [2.37].

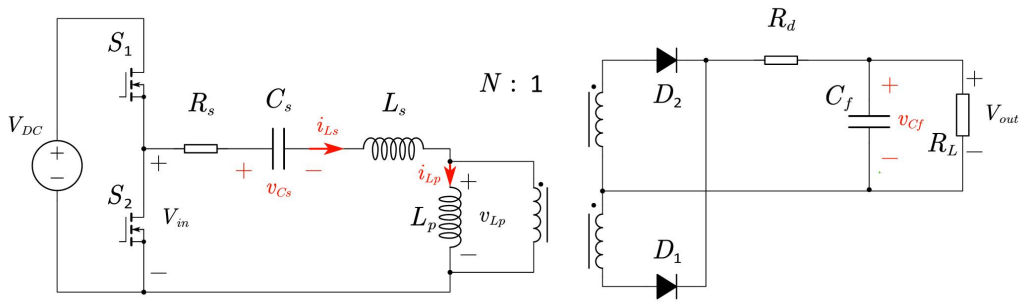

Fig. 2.9. Example circuit diagram of three-elements resonant converter-LLC converter

Series-parallel resonant converters, such as LCC or LLC converters, combine the attributes of both SRC and PRC, creating a hybrid configuration, An example of this circuit layout is illustrated in Fig. 2.9. This classification aims to take advantage of the merits of both converter types, providing a balanced approach in performance and applicability. LCC or LLC converters, which combine the high efficiency of SRCs with the strong current capability of PRCs, are well-suited for a broader range of applications requiring this synergistic combination of features.

In comparison with other resonant converters, LCC or LLC converters offer numerous advantages, including a wide voltage range, increased efficiency, and reduced Electromagnetic Interference (EMI), as mentioned in [2.38]. However, it is important to

consider the complexities of these converters. LLC resonant converters, for instance, have more complex designs due to the need to optimize resonant components for peak efficiency, as highlighted in [2.39]. Their voltage gain is also inherently limited, posing a challenge in applications requiring high voltage gains. LLC converters are notably sensitive to frequency variations [2.40], demanding precise simulation models.

The CLLC resonant converter combines the benefits of LLC converters in both power directions. It outperforms the traditional Dual Active Bridge (DAB) converter in efficiency and power density, offering high power density and a wide regulation range, among other benefits [2.41]. However, analysing the CLLC resonant converter is challenging due to its complex multi-resonant nature and multiple storage elements.

In conclusion, resonant converters have a broad classification, with each type suited to specific operating requirements and application environments. This classification is crucial for selecting and applying resonant converters in power electronic systems to ensure optimal system performance.

2.3.3 Class E inverter

2.3.3.1 Introduction

In modern times, where wireless infrastructure increasingly replaces wired systems, the demand for high-frequency, low-loss power amplifiers in wireless networks is growing [2.42]. Resonant inverters, especially class E, EF, and E/F types, are emerging as optimal for megahertz-switching power applications. Introduced by Gutmann in 1980 [2.43], class E inverters are known for their high efficiency in the MHz range, making their design at such frequencies and output powers less complex than expected [2.44].

The growing interest in class E inverters stems from their ability to perform ZVS or ZCS in each switching cycle, significantly reducing switching losses and enabling higher frequency operation and enhanced energy output compared to other inverters. The benefits of class E inverters include high efficiency leading to lower heat generation and reduced cooling needs [2.45]. Its design simplicity lowers manufacturing costs and improves reliability. They are versatile and suitable for a variety of applications from RF amplifiers to wireless power transfer systems [2.46].

However, class E inverters have limitations. While their design is simple in terms of components, optimizing peak performance is complex. Their performance is frequency-dependent, with deviations from the design frequency leading to efficiency losses. Harmonic generation necessitates filtering for clean power output, and their high switching voltage stress demands careful device selection [2.47].

2.3.3.2 Operation principle

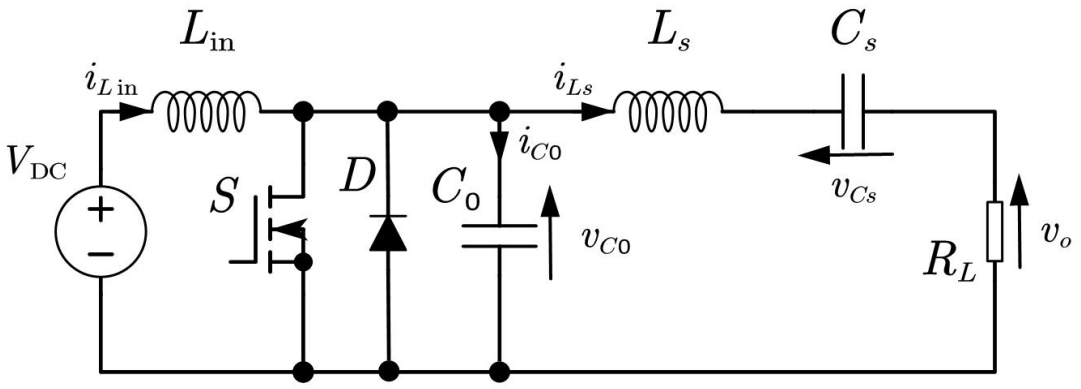

Fig. 2.10. Circuit diagram of a class E inverter

The class E inverter circuit, depicted in Fig. 2.10, comprises a power MOSFET functioning as switch S, a series-resonant circuit consisting of $L_s - C_s - R_L$, a shunt capacitor C_0, and a choke inductor L_{in}. The switch S operates on and off at the operation frequency f_{sw}.The operation frequency f_{sw} should exceed the resonant frequency of the L_sC_s series-resonant

circuit f_0, which at f_{sw} behaves like an inductive load, necessary for achieving ZVS operating condition [2.48].

Ideal ZVS conditions in the inverter are attainable under optimal operation, which requires precisely selected components. However, due to excessive costs, suboptimal operation is often chosen, allowing for a broader selection of circuit loads.

Let R_{opt} represent the load at optimal operation. If R_L is less than R_{opt}, the current amplitude through the resonant circuit increases, resulting in a higher maximum switch voltage $v_{s(\max)}$ than in optimal conditions. Consequently, the voltage drops across shunt capacitor C_0 rises, and the switch voltage is below zero at turn-on. To achieve ZVS in this scenario, an antiparallel diode is connected with the switch. This allows the duty ratio to vary within certain limits. Once the switch voltage reaches the antiparallel diode's conduction voltage $-v_d$, the diode activates. This conduction clamps the switch voltage to a lower level, typically the forward voltage drops of the antiparallel diode, reach a condition close to ZVS upon switch activation.

However, if the load is greater than the R_{opt} the amplitude of the current through resonant circuit is lower than in optimum operation, so the voltage drop across to the shunt capacitor C_0 will decrease and the maximum switch voltage v_{C0} is lower than it in optimum operation, voltage drop across the shunt capacitor C_0 will decrease and the switch voltage is higher than zero at turn-on. This case can be solved by impedance matching [2.48].

The operation of the inverter is divided into three modes during a single switching period, as illustrated in Fig. 2.11.

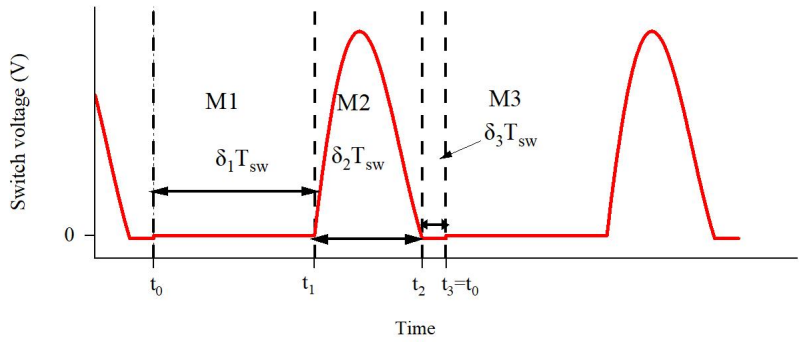

Fig. 2.11. Class E inverter example switch voltage waveform of suboptimal operation

Mode 1 (M1) $t_0 \leq t < t_1$: The switch S is on for a period δ_1/f_{sw}. During this mode, both the switch voltage and the capacitor C_0 voltage are zero, and the input voltage V_{DC} is applied to the choke inductor L_{in}.

Mode 2 (M2) $t_1 \leq t < t_2$: In this mode, the switch S is off. Current flows from L_{in} into C_0 and the main resonant branch. The current i_{Lin} equals the sum of i_{C0} and i_{Ls}. As current flows into the resonator, its voltage rises from zero to a maximum and then decreases.

Mode 3 (M3) $t_2 \leq t < t_3$: S remains off, and the voltage v_S drops below zero, activating S antiparallel diode D.

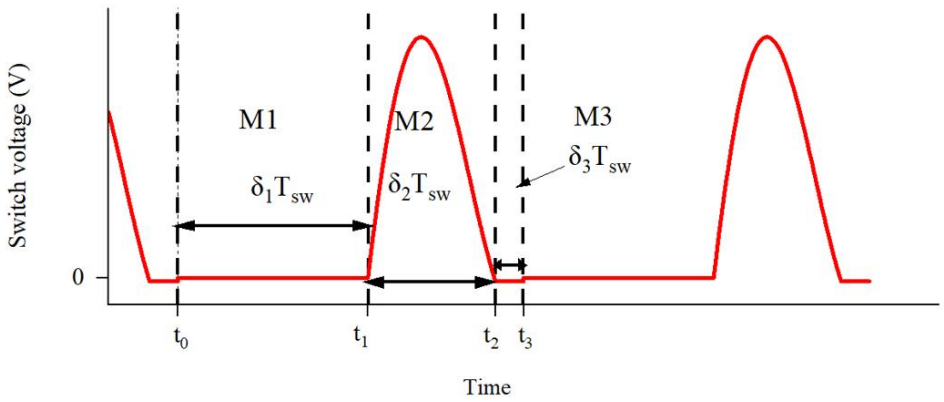

Fig. 2.12. Class E inverter example switch voltage waveform of optimal operation

If the switching frequency f_{sw} and the duty ratio δ_1 are chosen correctly, the inverter operates in only two modes, alternating between M1 and M2 (M1-M2-M1-M2-…), as shown in Fig. 2.12. ZVS is achieved when $v_{C0}(t_0 + T_{\mathrm{sw}}) = 0$. However, if v_{C0} drops below zero before $t = t_0 + T_{\mathrm{sw}}$, activating the antiparallel diode of the switch D, the circuit enters Mode 3. The operational sequence then becomes M1-M2-M3-M1…, as illustrated in Fig. 2.11. In this sequence, t_0 marks the cycle's beginning and the start of Mode 1. The transition point $t_1 = \delta_1 T_{sw}$ indicates the end of Mode 1 and the beginning of Mode 2. The end of Mode 2 is marked by t_2. The switch antiparallel diode starts conducting at t_2, and the cycle ends at t_3 when S is switched on again.

After examining the operational modes of class E inverters, it is essential to address the challenges and limitations inherent in this technology. While class E inverters are renowned for their efficiency and suitability for standard operations, they are not without their drawbacks. A notable concern is the potential for the maximum switch voltage to exceed the input voltage significantly. During typical operation, this voltage can surge to over 3.5 times the input voltage. In scenarios involving very high frequencies, the non-linear variation in switch capacitance can cause the voltage to rise even further, up to 4.4 times the input voltage, as noted in [2.49]. These high voltages impose considerable stress on the switch. Moreover, class E inverters may produce less power compared to other resonant inverters when subjected to the same voltage and current stress conditions. These issues highlight the critical need for strategies to mitigate voltage stress on the switch.

2.3.4 Class EF inverter

2.3.4.1 Introduction

Class E inverters, known for their ZVS capability particularly in the MHz range, are highly efficient [2.44]. This feature ensures minimal energy losses during operation. However, these inverters face a significant challenge: the high voltage stress on switches [2.50]. Elevated voltage levels require switches and shunt capacitors with higher voltage ratings, resulting in increased manufacturing costs.

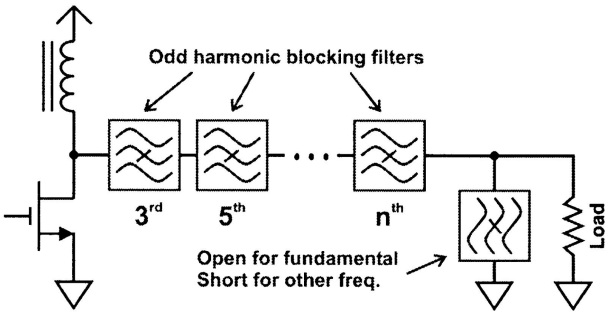

Fig. 2.13. Example of class F amplifier [2.51]

The class F amplifier architecture, shown in Fig. 2.13, were primarily developed to enhance the efficiency of class-A/B and class-B designs. Class F amplifiers incorporate resonant networks to shape output waveforms, enhancing efficiency by reducing voltage and current overlap. Additional resonators in series with the load create open circuits at certain low-order odd harmonics. As more harmonic blocking filters are added, the waveform shifts from sinusoidal to square. In contrast, class 1/F topology open-circuits even harmonics while short-circuiting odd ones. The novel integration of class F or 1/F amplifiers with a class E inverter was first proposed by Kee in 2002 [2.51]. Kee's work suggested reducing voltage stress by adding a resonant network parallel or series with the load but lacked detailed design equations.

To address voltage stress in class E inverters, hybrid class EF inverters were developed. These combine a series LC branch in parallel with the switch of a class E inverter. Tuning the auxiliary LC circuit's resonant frequency helps control peak switching voltages.

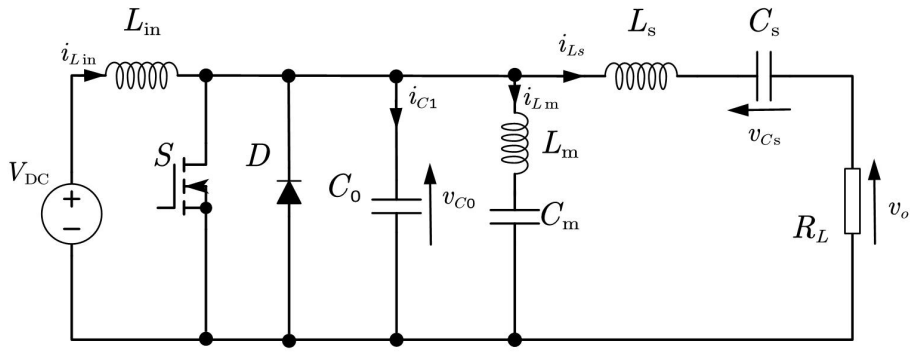

Fig. 2.14. Example circuit diagram of a class EF_2 inverter

Kaczmarczyk's research [2.52] confirmed the superior performance of class EF_2 inverters, the circuit diagram is shown in Fig. 2.14. Adjusting the shunt auxiliary branch's resonant frequency to double the operating frequency enhanced power output compared to class E/F_3 (the shunt auxiliary branch resonates at three times the inverter operating frequency) and class E inverters. The class EF_2 inverter stands out for its reduced harmonic content, improving efficiency and EMI profile compared to class E and E/F_3 inverters. Aldhaher*, et al.,* [2.53] further explored the voltage reduction mechanism in class EF inverters, showing that peak switching voltage in class EF_2 inverters could be reduced to about twice the input voltage.

The class EF_2 inverter represents a significant advancement in inverter technology, effectively addressing both voltage stress and harmonic content issues prevalent in traditional designs.

2.3.4.2 Operation principle

Fig. 2.14 illustrates the circuit of a class EF_2 inverter. In this design, L_{s} and C_{s} form the main resonant branch, ensuring a sinusoidal current through the load R_{L}. The MOSFET switch S operates at a frequency f_{sw}, close to the $L_{\text{s}}C_{\text{s}}$ resonant frequency of $f_0 =$

$1/2\pi\sqrt{L_s C_s}$ and with a duty cycle δ_1. The input inductor L_{in} acts as a filter, allowing only DC current i_{Lin} from the input voltage V_{DC}. L_m and C_m create an auxiliary resonant branch. This auxiliary branch aims to reduce the MOSFET voltage v_{C0} by injecting a current into C_0 at a frequency of $2f_{sw}$.

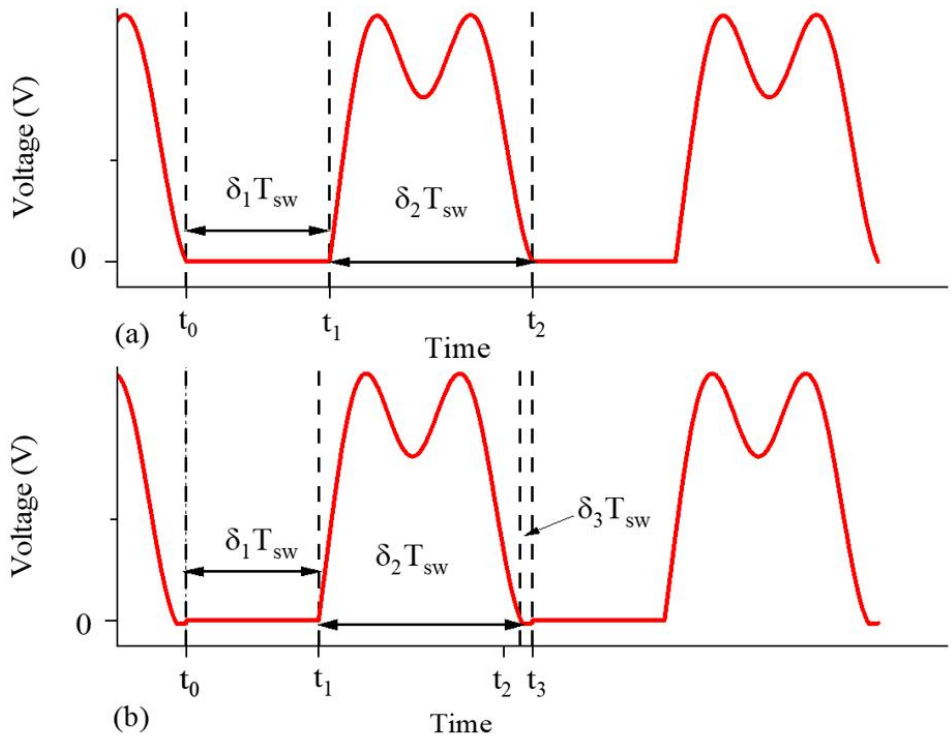

Fig. 2.15. The class EF_2 inverter shunt capacitor voltage v_{C0} waveform at optimal operation (a) and suboptimal operation (b)

The operation of the class EF_2 inverter is similar to that of the class E inverter and can be broken down into three modes during a single switching period, as shown in Fig. 2.15. Define t_0 as the cycle's start and the start of Mode 1, t_1 as the end of Mode 1 and start of Mode 2, t_2 as the end of Mode 2 and start of Mode 3, and t_3 as the end of Mode 3 and the cycle.

Mode 1 (M1): At $t = t_0$ MOSFET S1 is switched on for a duration $t_1 - t_0 = \delta_1 T_{sw}$. Since S is on, $v_{C0} = 0$ and so $V_{Lin} = V_{DC}$. Although $v_{C0} = 0$ the current i_{Lm} continues to flow as L_m and C_m are in resonance at a frequency $2f_{sw}$.

Mode 2 (M2): At $t = t_1$, S1 is switched off. A current $i_{C0} = i_{Lin} - i_{Ls} - i_{Lm}$ flows into C_0 and its voltage increases from zero to a maximum value and then decreases. Eventually the v_{C0} falls below 0 V (actually $-v_d$) turning on the MOSFET's anti-parallel diode.

$$v_{\mathrm{C0}}(t_2) = v_{C1}([\delta_1 + \delta_2]T_{\mathrm{sw}}) = -v_d \tag{2.29}$$

The duration of Mode 2 is $t_2 - t_1 = \delta_2 T_{\mathrm{sw}}$.

Mode 3 (M3): Switch S's anti-parallel diode is forward biased, and this clamps the shunt capacitor voltage to the on-state voltage drop of the body diode, $v_{\mathrm{C0}} = -v_{\mathrm{d}}$. At the end of Mode 3, the switch voltage rises to zero to maintain steady state operation.

Similar to the operation of a class E inverter, when optimized parameter values are selected for the class EF_2 inverter, it operates in a cycle of Modes M1 and M2, alternating in a pattern of M1-M2-M1-M2.

ZVS is achieved if v_{C0} equals zero at the point of T_{sw}, shown in Fig. 2.15a. However, if v_{C0} falls below zero before T_{sw}, it activates the antiparallel diode of switch S, transitioning the circuit into Mode 3. This alteration changes the operating sequence to M1-M2-M3-M1, as illustrated in Fig. 2.15b.

2.4 Modelling methods of converters

This section introduces three primary modelling approaches for power electronic converters: Fundamental Mode Analysis (FMA), State-Space Method (SSM), and State-Space-Averaging Method (SSAM). It outlines the modelling processes, principles, and distinct characteristics of each method.

2.4.1 Introduction

In power electronics, the significance of accurate modelling techniques cannot be overstated. As power electronics emerges as a foundational technology for contemporary power systems, the role of modelling in predicting and optimizing system performance becomes paramount [2.54]. Power converters are increasingly employed across diverse applications, each with varying levels of importance in power systems. Optimal decision-making for the system manufacturing, control, operation, and maintenance necessitates a comprehensive understanding of their operation within these systems.

Accurate modelling is essential in the converter design process. Neutral-point-clamped (NPC)-based converters highlight the significance of capacitor voltage balancing for the reliability of the converters [2.55]. Additionally, the design of high-gain three-phase current-fed push–pull DC–DC converters underscore the reliance on the quality of waveform characteristics for optimal performance [2.56].

Importance of modelling in power converters are given below:

1. Predictive performance: Modelling allows for the prediction of how power electronic systems will perform under different conditions. This foresight is crucial for optimizing systems before they are physically produced.
2. System design: A comprehensive modelling framework assists engineers in identifying crucial parameters and making informed choices about components.
3. Control strategy development: Precise models are essential in developing and validating control strategies, especially for complex power electronic systems [2.57].
4. Fault diagnosis: Comparing models with actual systems helps in identifying and resolving potential problems or malfunctions [2.58] .

2.4.2 Fundamental Mode Analysis

2.4.2.1 Definition and Basic Concepts

Fundamental mode analysis (FMA), also known as first harmonic approximation (FHA), is an important technique in power electronics that converts nonlinear resonant circuits into sinusoidal AC circuits, and the use of sinusoidal steady-state circuit analysis simplifies the analysis and calculations. It is mainly used to analyse and simulate the steady-state behaviour of a system. The essence of FMA lies in its focus on the primary or 'fundamental' components of the signal in system, these typically include the dominant components of a system's response. By dissecting these components, engineers can acquire a deeper understanding of the system's dynamic behaviour, anticipate its performance under various conditions, and consequently devise more effective control strategies [2.59].

In power electronics modelling, FMA typically excludes the effects of higher-order harmonics or other non-fundamental frequency components. The primary objective of FMA is to simplify the analysis of complex systems by focusing only on the most critical frequency responses, capturing the system's essential behaviours and characteristics.

In the context of resonant converters or other power electronic systems, FMA equips engineers with the tools to comprehend and predict the performance of systems operating predominantly at their base frequency. This methodology is particularly pertinent for systems that primarily operate at their fundamental frequency, where the influences of higher-order harmonics can be disregarded. In essence, FMA offers a simplified avenue for understanding and dissecting the core behaviour of power electronic systems without delving into all potential complexities.

The FMA method only allowing the fundamental harmonic to transmit energy. In this process, the frequency response of the resonant circuit modifies the input voltage spectrum to generate the desired output spectrum. By aligning the input voltage frequency with the resonant circuit's centre frequency, the fundamental harmonic is closely matched. This attenuation of

higher-order harmonics results in the current through the resonant circuit become a sinusoidal wave.

The basic assumptions of FMA are:

1. The inductors, transformers, capacitors, and switches of a resonant circuit are ideal components.

2. Neglect the high harmonics in the circuit, only the fundamental wave transmits energy.

3. The output filter capacitance value is large enough, and the output voltage has no ripple.

Under the principles of Fourier analysis, a periodic function $f(t)$ can be expressed as an infinite summation of sines and cosines:

$$f(t) = a_0 + \sum_{n=1}^{\infty} (a_n \cos(n\omega_{\mathrm{sw}} t) + b_n \sin(n\omega_{\mathrm{sw}} t)) \tag{2.30}$$

where n is harmonic order and ω_{sw} is angular switching frequency. So, the Fourier coefficients are given by [2.60],

$$a_0 = \frac{1}{T_{\mathrm{sw}}} \int_{-\frac{T_{\mathrm{sw}}}{2}}^{\frac{T_{\mathrm{sw}}}{2}} f(t)\,\mathrm{dt} \tag{2.31}$$

$$a_{\mathrm{n}} = \frac{2}{T_{\mathrm{sw}}} \int_{-\frac{T_{\mathrm{sw}}}{2}}^{\frac{T_{\mathrm{sw}}}{2}} f(t) \cos(n\omega_{\mathrm{sw}} t)\,\mathrm{dt} \tag{2.32}$$

$$b_{\mathrm{n}} = \frac{2}{T_{\mathrm{sw}}} \int_{-\frac{T_{\mathrm{sw}}}{2}}^{\frac{T_{\mathrm{sw}}}{2}} f(t) \sin(n\omega_{\mathrm{sw}} t)\,\mathrm{dt} \tag{2.33}$$

FMA's effectiveness is based in the band-pass filter response of the resonant circuit, which ensures that only a specific band of frequencies contributes power to the output. Based on the waveform's symmetry properties, and assuming that only its fundamental frequency component flows through the circuit, the relevant coefficients are:

$$a_1 = f(t)\frac{2}{\pi}\cos(\omega_{sw}t) \tag{2.34}$$

and

$$b_1 = f(t)\frac{2}{\pi}\sin(\omega_{sw}t) \tag{2.35}$$

Take a DC-DC resonant converter as an example to introduce the basic concept of FMA, a classic DC-DC resonant converter can be divided into three main parts, switching circuit, resonant circuit and rectification and filtering circuit, as shown in the figure, the switching circuit The input DC signal is converted to a square wave signal, and the higher harmonics are filtered out due to the resonant circuit. The input voltage to the resonant circuit is a square wave, but only sinusoidal current flows through the resonant circuit. The input voltage to the rectifier is a square wave signal and the current is sinusoidal. It is assumed that only the fundamental component of the switching frequency f_{sw} is fed into the resonant tank.

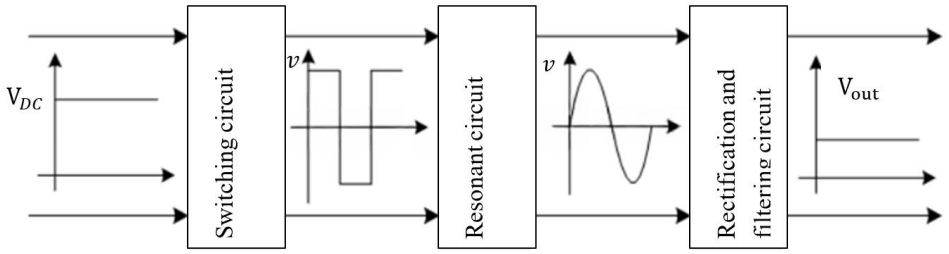

Fig. 2.16. Simplified circuit of a DC-DC resonant converter topology

The switching circuit converts the DC voltage to a high-frequency square wave, which can be achieved by using the Fourier series introduced earlier to expand the square wave voltage so as to obtain the fundamental component of the square wave voltage, thus realising the

switching circuit as an equivalent AC voltage source. Then the resonant circuit filters out the higher harmonics so that the current in the resonant cavity is a sinusoidal waveform, and the sinusoidal frequency is the switching frequency. Finally, the rectifier input voltage is square wave, current is sinusoidal. Assuming that the load is resistive, continue to use the Fourier series to expand the square wave voltage to obtain its fundamental component, thus realising the combination of the rectifier-filtered part and the DC load part is equivalent to an AC load.

This enables the equivalence and simplification of the entire converter circuit. This enables the derivation and calculation of the converter gain. It should be noted that the FHA has almost no error when switching frequency equal to resonant frequency, but there is an error when the switching frequency deviates from (above or below) the resonant frequency, and the larger the frequency deviation, the larger the error.

2.4.2.2 Advantages and Limitations of FMA

FMA has emerged as a valuable tool in the analysis of power electronic systems. Like any analytical method, FMA presents both advantages and limitations that influence its applicability and effectiveness in various scenarios.

Advantages:

1. High efficiency: FMA concentrates on the fundamental mode analysis of the system, ignoring the effects of other harmonic components on the system. This reduces the computational complexity of the analysis.
2. Accurate prediction: FMA focuses on the main components of the system response and, subject to key assumptions (i.e., switching frequency equal to or sufficiently close to the resonant frequency of the system), accurately reflects the intrinsic behaviour and overall performance of the system.

3. Generality: Given the simplicity of the modelling, the model can be easily changed and extended, thus allowing this analysis method to be applied to a wide range of power electronic systems. From simple switching circuits to complex power systems, this method can be used..

Limitations [2.61]:

1. Oversimplification: While it is beneficial to focus on the main model, real-world power systems are subject to a variety of dynamics, such as load fluctuations and unstable power supply. These may be reflected in the higher harmonics. The fundamental approximation may not adequately capture these complex dynamic behaviours.
2. Limitations of assumptions: FMA usually operates on the basis of certain assumptions about the system (e.g., ignoring the effects of higher harmonics) that do not always hold in the real world, and when the system operates away from these assumptions this can lead to errors that reduce the validity of the analysis.
3. Limitations for complex topologies: In power electronics, complex topologies (e.g., multistage converters and composite control strategies) may lead to complex interactions between fundamental and other harmonics, and the fundamental approximation may not be able to handle these complex interactions effectively.

The Fundamental mode analysis method significantly streamlines circuit analysis by utilizing a set of assumptions, which offers a considerable speed advantage. When these assumptions are satisfied, FMA can achieve high levels of analytical accuracy. However, its application is limited in scenarios like resonant converters, where system regulation involves altering the switching frequency. This adjustment makes it challenging to maintain the assumption that the resonant and switching frequencies are equal, thus compromising FMA's accuracy. Moreover, the method's oversimplification can fail to capture complex real-world changes, further restricting its utility. Therefore, while FMA is a rapid and user-friendly approach for power electronics modelling and analysis, its reliance on strict assumptions poses significant limitations.

2.4.3 State Space Averaging Method

2.4.3.1 Definition and Basic Concepts

State Space Averaging Method (SSAM) is a tailored, powerful technique for studying and modelling power electronic systems. It is primarily utilized in the analysis and design of switching power converters. SSAM combines state space analysis with time-domain averaging, offering a distinct approach to capture the dynamic behaviour of systems with switching components.

SSAM is a variant of State Space Method (SSM), centred around state variables [2.63]. These variables define the system's state at any given moment and are organized into a state vector that represents the system's current condition. State equations detail the dynamic changes of these state variables in relation to time and system inputs [2.62]. All possible states of the system are mapped in a multidimensional state space, where each unique point corresponds to a specific state of the system.

Hard-switching converters' rapid on-off switching is aligned with SSAM's underlying assumptions. These converters switch consistently in a set pattern each cycle, which SSAM captures by averaging out the behaviour. SSAM's efficacy is most pronounced when the converter's main dynamics occur at a much slower rate than its switching speed. By simplifying the complexities of rapid switching, SSAM transforms rapid switching behaviour into a more computationally manageable average model, thus reducing the complexity of modelling. [2.64].

SSAM averages state-space equations over one switching cycle, offering a continuous-time system representation. This simplification aids in analysing the dynamic behaviour of the system. First are some key assumptions of SSAM:

Periodic steady state assumption: It is assumed that the system reaches a steady state, meaning the behaviour of the system is repetitive in each cycle. This assumption allows for the prediction of average behaviour by analysing just a single cycle.

Switching device idealization: Switching elements are assumed to have no losses during switching operations. This means there is no voltage drop when in the 'on' state and no leakage current when in the 'off' state, effectively eliminating the impact of switching losses on system performance.

Continuous conduction assumption: It is assumed that inductor currents and capacitor voltages vary continuously and smoothly throughout the switching cycle. This simplifies the analysis by avoiding the complexities associated with intermittent currents or abrupt voltage changes.

Operating frequency assumption: It is assumed that the switching frequency of the system is significantly higher than the system's dynamic frequency. This allows for the averaging out of system state changes, enabling a typically nonlinear switching electronic system to be described by a linear averaging model.

The method involves the following steps [2.65]:

1. Determine the state variables:

Firstly, similar to the SSM, SSAM employs state variables that represent the essential quantities required to define the entire state of a system at any given moment. In power electronics, these could encompass inductor currents and capacitor voltages.

$$\boldsymbol{x}(t) = \begin{bmatrix} x_1(t) \\ x_2(t) \\ \vdots \\ x_n(t) \end{bmatrix} \tag{2.36}$$

2. Derivation of switching state equations:

Then is needed to analyse the system for each of its switching states. For a fundamental two-state system, this involves deriving both the on and off state equations. These equations for each state should then be expressed in matrix form,

$$\begin{aligned}
\frac{\mathrm{d}\boldsymbol{x}(t)}{\mathrm{dt}} &= \boldsymbol{A}_1\boldsymbol{x}(t) + \boldsymbol{B}_1 u(t) \quad (\text{for state} 1) \\
\frac{\mathrm{d}\boldsymbol{x}(\mathrm{t})}{\mathrm{dt}} &= \boldsymbol{A}_2\boldsymbol{x}(t) + \boldsymbol{B}_2 u(t) \quad (\text{for state } 2) \\
&\ldots \\
\frac{\mathrm{d}\boldsymbol{x}(\mathrm{t})}{\mathrm{dt}} &= \boldsymbol{A}_{\mathrm{n}}\boldsymbol{x}(t) + \boldsymbol{B}_{\mathrm{n}} u(t) \quad (\text{for state } n)
\end{aligned} \tag{2.37}$$

3. Averaging over one switching cycle:

This step involves averaging system variables over the entire switching period. The method thereby transforms a switching system into an equivalent non-switching one, simplifying the analysis. The duty cycle, represented by δ_i, is the ratio of the duration of state i (Mode i) to the total switching period, T_{sw}.

$$\begin{aligned}
\frac{\mathrm{d}\boldsymbol{x}_{\mathrm{av}}(\mathrm{t})}{\mathrm{dt}} &= (\delta_1\boldsymbol{A}_1 + \delta_2\boldsymbol{A}_2 + \ldots + \delta_{\mathrm{n}}\boldsymbol{A}_{\mathrm{n}})\boldsymbol{x}(t) \\
+ (\delta_1\boldsymbol{B}_1 + \delta_2\boldsymbol{B}_2 + \ldots + \delta_{\mathrm{n}}\boldsymbol{B}_{\mathrm{n}})u(t) &= \boldsymbol{A}_{av}\boldsymbol{x}(t) + \boldsymbol{B}_{av}u(t)
\end{aligned} \tag{2.38}$$

4. Steady state analysis and solution

Equation (2.38) describes the evolution of the averaged state-vector from an arbitrary initial condition $\boldsymbol{x}(t_0)$ to its steady-state value. This equation captures the transient dynamics of the system. By applying the condition $\dot{\boldsymbol{x}}_{\mathrm{av}} = 0$, the steady-state value of the averaged state-vector $\boldsymbol{x}_{\mathrm{av}}$, denoted as $\boldsymbol{x}_{\mathrm{av,ss}}$, can be determined.

$$\boldsymbol{x}_{\mathrm{av,ss}} = -(\boldsymbol{A}_{\mathrm{av}})^{-1}\boldsymbol{B}_{\mathrm{av}}\boldsymbol{u}(t) \tag{2.39}$$

Through time-domain averaging, SSAM creates an equivalent continuous-time system, capturing the average behaviour of the original switching system over a cycle. A key assumption of SSAM is that the converter's main dynamics occur at frequencies much lower than the switching frequency.

In power electronics, SSAM is particularly useful for analysing converters with rapid switching system. It allows researchers and engineers to deeply understand system dynamics without the complexity of switching processes. This approach simplifies the complexities of switching activities and deepens insight into system dynamics. Like the SSM, SSAM's representation adapts well to modern control design techniques, invaluable for developing controllers for these systems.

2.4.3.2 Advantages and Limitations of the State Space Averaging Method

SSAM is an effective tool for analysing and modelling power switching converters. SSAM simplifies the analysis of switching systems by converting them into their non-switching equivalents, thus making them easier to study, as noted by Wang *et al.,* [2.66]. It focuses the average behaviour across a switching cycle, reducing complexities from switching events. Additionally, SSAM's adaptability allows its application across various power electronic systems with distinct switching characteristics. A key advantage is its ability to enhance simulation efficiency, especially in large systems, by concentrating on averaged behaviours.

However, SSAM faces certain challenges. A crucial aspect of SSAM is its foundational assumption that the primary dynamics' frequencies of the converter are much lower than the switching frequency. This assumption becomes problematic in resonant converters modelling, where the resonant frequency often close with the switching frequency, challenging SSAM's core assumption and potentially leading to inaccuracies. In such cases, alternative methodologies might be more effective in predicting resonant converters' operational states. At the same time, due to its assumption of continuous conduction for inductor current and

capacitor voltage, SSAM cannot be applied to systems operating in discontinuous mode. This limitation restricts the scope of SSAM's applicability.

Then, its reliance on averaging can introduce approximations, affecting accuracy. While adaptable, SSAM may not suit systems where instantaneous behaviours are crucial. Additionally, implementing SSAM necessitates a comprehensive understanding of system dynamics and the intricacies involved in the averaging process.

In conclusion, SSAM is well-suited for analysing the steady-state behaviour of switching converters where the switching frequency significantly exceeds the system's internal dynamic frequency. This method offers the benefits of simple analysis, speed, and accuracy. However, the averaging process inherent in SSAM introduces significant limitations in analysing both the transient behaviour and the internal dynamics of the system. Furthermore, the assumptions regarding switching frequency result in poor performance when analysing systems like resonant converters, where the switching frequency closely aligns with the system's dynamic frequency.

2.4.4 Cyclic-mode Modelling

2.4.4.1 Introduction

For hard switched converters operating in continuous current mode, the SSAM analysis method can be used. For resonant converters operating at the resonant frequency, the FMA analysis method can be chosen. However, for analysing the behaviour of a hard switched converter in intermittent mode versus a resonant converter operating away from the resonant frequency, both methods still have inherent shortcomings. Thus cyclic-mode modelling was found as a strong contender. Cyclic-mode modelling is considered to be a variant of the Floquet based technique [2.67]. In stable dynamic systems, if the inputs to the system are constant, the state vectors converge to specific steady state values. But in switching converter

systems, the situation changes. Since the system parameters are constantly changing, the state vector of the system will not converge to a specific steady-state value, but will reach a repeated, stable state after a certain period of time, with each cycle behaving in the same way as the previous one. The closest analogy to the concept of steady state in such systems is the concept of cyclic-mode. A system is said to be in cyclic-mode if its state vector varies periodically with the frequency of operation of the system.

2.4.4.2 Definition and Basic Concepts

The cyclic-mode modelling of converters begins with the derivation of the cyclic-mode modelling process, as first presented in [2.67]. A wide variety of periodically excited DC input power electronic converters can be assumed to be operating in a cyclic-mode once the start-up or disturbance transient has subsided. Typically, a single operating cycle is decomposed into several modes depending on the conduction states of the switches and diodes. For each mode, a circuit configuration is constructed from which a system of linear equations can be determined. Thus, the operation of the DC-DC converter in the cyclic-mode is described by a piecewise linear model.

The key assumptions of the cyclic-mode model are:

The switching power supply system operates in periodic steady state: The method is used to predict the behaviour of the system in long term operation and simplifies the analysis of the dynamic characteristics of the system. The equation is expressed in (2.40),

$$\boldsymbol{x}(t_0) = \boldsymbol{x}(t_0 + \mathrm{T_{sw}}) \tag{2.40}$$

where $\boldsymbol{x}$ is the state variable of the system and $\mathrm{T_{sw}}$ is the switching frequency of the system.

The switching duty cycle of the system is fixed: the ratio of on-time and off-time of the switches remains constant over a switching cycle, making it unnecessary to consider the effect of changes in duty cycle on the behaviour of the system.

The inputs to the system are DC inputs: this is to simplify the circuit analysis and thus enable fast output of the model.

The switching components are ideal switches: the switching components are assumed to be ideal, i.e. they have zero resistance when on and infinite resistance when off, with no voltage drop or leakage current. This is to analyse the performance of the circuit more directly.

This analytical method consists of the following steps [2.68]:

1. Determine the state variables of the system, which, similar to SSAM, are identified as combinations of inductive currents and capacitive voltages in the circuit.

2. Determine the number of modes, their order of occurrence and duration: In cyclic-mode operation (steady state operation) with a fixed switching duty cycle, the circuit is broken down into different circuit configurations based on the conduction states of the switching devices, such as switches and diodes, and the number of modes, as well as the order and duration of each mode, are determined by analysing the circuit operation.

3. Determine the system of segmented linear equations: Based on the circuit configuration of each mode, a system of state variable equations corresponding to that mode is written. This is then written in the form of a matrix to facilitate subsequent modelling work.

4. Determine the initial values of state variables: After determining the order of appearance of each mode, the duration and the set of state variable equations for each mode, the initial values of state variables can be obtained through matrix integration and the

assumption of the cyclic-model operation that the initial values of state variables are equal to the end values, i.e. (2.40).

5. Plotting the state variable waveforms: Based on the initial values, matrix integration can be used. The value of the state variable at each time can be calculated, so as to draw the waveform of the change of the state variable in one cycle, that is, the cycle waveform under the steady state operation of the converter.

2.4.4.3 Advantages and limitations of Cyclic-mode Model

The advantages of the cyclic-model modelling are clear. Firstly, in the scope of application. It is not only applicable to this kind of hard-switching converter whose switching frequency is much larger than the dynamic frequency of the system, but also in the analyses of systems similar to resonant converters whose switching frequency is close to the internal dynamic frequency of the system, which is due to the fact that there is no assumption on the switching frequency of the system. Also, in terms of analysis accuracy, it not only outputs the period waveforms of key variables, but also obtains their period averages. This facilitates the analysis of the dynamic behaviour of the system.

But its disadvantages are also obvious. Firstly, the assumption of DC input makes it very difficult to simulate a switching converter system with AC input using this method. At the same time the method requires a high degree of accuracy in the duty cycle for each mode, and if the duty cycle data is not accurate enough this can lead to an exponential expansion of the system error. This leads to analysis errors. Finally, there is the modelling difficulty. Due to the complex structure of the resonant circuit and the fact that this method does not make assumptions about the operational behaviour of the circuit, this leads to complex modelling and an increased probability of error.

2.4.5 Comparison of the Three Methods

1. Fundamental Mode Analysis (FMA):

FMA focuses on the primary or 'fundamental' components of a system, providing insights into its dynamic behaviour by concentrating on dominant components. This method excels in capturing core responses but may overlook the dynamic behaviour of internal components due to its focus on fundamental elements. Its reliance on foundational assumptions also limits its universal applicability. FMA is most effective in systems where behaviour is primarily dictated by fundamental frequency components. It is suited for analysing the overall performance of a system rather than conducting a detailed analysis of system dynamics [2.69][2.70].

2. State-space averaging method (SSAM):

SSAM combines state space analysis and time domain averaging. It is particularly effective for systems exhibiting high-speed switching behaviour compared to the internal behaviour of the system. It reduces complexity and offers insights into both transient and average behaviours. However, SSAM introduces approximations due to its averaging technique, making it less suitable for systems requiring detailed transient analysis. Its primary application is in systems like converters with rapid switching dynamics. A notable limitation of SSAM is that the method requires the system's dynamic frequency to be much lower than the switching frequency, which poses challenges for applied to like resonant converters, where these operating frequencies closely to its system dynamical frequency [2.71].

3. Cyclic-mode modelling method

Similar to SSAM, cyclic-mode modelling is also a variant of the space state variable method. In contrast to the other two analysis methods, it not only allows the analysis of hard-switched converter systems, but also enables the accurate analysis of resonant switched converter systems, regardless of their resonant and switching frequencies. The wide range of applications is its advantage over the previous two methods. Second, very high accuracy.

Unlike SSAM and FMA, cyclic-mode modelling does not make assumptions about the operational behaviour of the system, which makes it possible to ensure the accuracy of the analysis without approximate behaviour [2.72].

On the other hand, the absence of assumptions about the system operation also means that the complexity of the modelling and the difficulty of the calculations will be much greater than the previous two methods [2.73]. Also due to its high accuracy requirement for each mode duty cycle. It also means that additional methods are needed to obtain the accurate duty cycle, which further increases the difficulty of the analysis.

Overall, by comparing the three modelling methods. both FMA and SSAM have the advantage of simplicity in modelling, but errors become inevitable due to the presence of approximate behaviour in the analysis process. When analysing a very sensitive system like a resonant switching converter, a small frequency error can make the analysis very wrong. So, these two methods are not good. Although the cyclic-mode model has the requirement of modelling high modelling complexity as well as high accuracy in duty cycle. But because of its advantages in accurately predicting the system performance and its wide range of applicability, the cyclic-mode model is chosen as the main research basis and its main defects are used as the improvement direction of modelling.

2.5 Root Mean Square value calculation methods

In the analysis of a DC system, the cycle average value of key variables mainly reflects the average performance of the power supply during the cycle, which is an important reference for the system effectiveness and is the focus of the analysis. However, in the modelling and analysis of resonant switching converters, many key values, such as inductor currents, the cycle average does not represent the actual behaviour of the system, and the root mean square value becomes an important parameter for analysis. The RMS value is a measure of the effect

of an alternating current (AC) voltage or current in terms of power transfer, independent of the DC component of the signal. It is equivalent to the voltage or current value of a DC current capable of producing the same amount of thermal energy. In the design of power converters, especially when analysing circuits that contain AC components the RMS value are crucial for designing efficient, stable, and reliable power converter system in several important aspects [2.74] to [2.77]:

1. Calculation of resistance (ohmic) losses for power devices: In power devices such as MOSFETs that dissipate power, the RMS value of current is the key factor in determining power dissipation.

2. Evaluation of copper losses in winding components: In magnetic components like transformers and inductors, the RMS value of current, at a given resistance, primarily determines copper losses.

3. Specification of rated current for inductors and rated voltage for capacitors: The RMS values of voltage and current are crucial in determining the rated values of these components.

4. Design of switch devices: Switch devices such as MOSFETs and IGBTs operate with rapid switching transitions at high frequencies. The RMS values of voltage and current are vital for evaluating switch losses, particularly those associated with the charging and discharging of internal capacitors in these devices.

5. Selection and sizing of energy storage components: For energy storage components like capacitors and inductors, the RMS values of voltage and current are important considerations when choosing suitable energy storage components. It ensures that they can handle the expected RMS values without exceeding their rated voltage or current limits.

Many studies exist for estimating RMS values for specific converter representations. Firstly, based on the fundamental approximation method described earlier, the waveform of the fundamental component of each key current or voltage can be obtained by eliminating the high harmonic components, and the RMS value can be realised based on the waveform. However, the assumptions of this method are strict, which often leads to a lack of accuracy in practical applications due to the inability to fully satisfy the assumptions [2.78] .

A model is presented in [2.77] based on the steady-state analysis of a Dual Active Bridge (DAB) DC-DC converter. The device and inductor current modelling assume all components are lossless and that the inductor current waveform is piecewise linear. The authors by assuming segmental linearity of the voltage waveforms, the differential equation for the inductor current is written, which consists of multiple segmental linear rectangular voltage waveforms. Afterwards, the waveform integration is used to decompose a complex waveform into a combination of multiple bipolar triangular waves with no DC component, thus enabling the inductor current waveform to be derived.

In solving for the root mean square (RMS) value of the current, the integration of the expression for the inductor current is simplified using the nature of the triangular waveform to obtain the RMS value of the current. This method does not require the use of detailed waveforms of the current nor does it integrate the current in segments, which can significantly reduce the computational effort in the analysis process while still maintaining a higher accuracy than the fundamental wave approximation. However, the nature of using a large number of rectangular and triangular waves results in a significant limitation of its scope of application. Therefore, its applicability is limited to dual active bridge isolated bi-directional DC/DC converters. Also, for resonant converters, the inductor current is generally sinusoidal or sinusoidal-like, and the assumption that the inductor current is segmentally linear is not valid, so this method is not applicable to the RMS value of resonant converters.

In [2.79], Kostakis *et al.,* introduce a method to determine the RMS values of currents and voltages for hard-switched power converters described by a second-order state variable model. The authors outlining a framework to extract the cyclic-mode initial conditions (referred to as singular points in [2.79]) to determine cyclic-mode state trajectories.

In the process of calculating the RMS values, the authors utilised the properties of the matrix integral with the properties of the root mean square values. Using the nature of the differentiation of the original variables, the integration of the cycle averaging process in the RMS value solution process into the solution of the matrix integral is achieved by directional generalisation of the original state matrix. Next, the differential equation of the state variable is brought into the differential term of the square of the state variable, and the differential equation of the square term of the state variable can be obtained, and based on this equation, the directional generalisation of the matrix of the state variable which has been generalised can be realised, so that the integration process in the process of solving for the root-mean-square value can be integrated into the matrix integral of the solving matrix. This enables the simplification of solving for the root mean square value of the state variable.

This method is applicable to second-order state variable models, i.e., conventional boost and buck converters. For second-order models it is straightforward to obtain the exact root-mean-square formulas for the state variables without the need to generate the periodic waveforms of the variables, which greatly simplifies the analysis of second-order models. For multi-order state variable models, the disadvantages of the method become apparent, as the method requires a lot of algebra for differentiating products of state variables (e.g. Square of the signal) and cannot be easily extended to other converters without significant mathematical overheads. However, this method gives a very useful idea that it is possible to avoid a complex analytical process by changing the state matrix so that some of the steps of solving the RMS can be integrated into the matrix integration process.

The cyclic-mode model described earlier in this thesis also uses what is known as the waveform evaluation RMS method (waveform method) to determine the root mean square

(RMS) values. Once an accurate cyclic-mode model has been established, the model can be used to obtain the periodic waveforms for each state variable, and then the periodic state variable waveforms can be used to calculate the RMS values for each inductor current and capacitor voltage. While the simplicity of the waveform method is attractive, its accuracy depends heavily on the precision of the depicted waveforms, which is a significant limitation. Moreover, generating highly accurate waveforms is time-consuming, especially for complex systems with multiple modes of operation. Although this method is simple to use, its accuracy issues make it unsuitable for use in analyses where high accuracy is required.

2.6 Conclusion

This Chapter presents a literature review of the fundamental topics related to the proposed research. It includes an introduction to hard-switching and resonant converters. These elements provide the basics of switching power supplies and their classification for subsequent in-depth study. Subsequently, the operational states of buck converters, boost converters, class E inverters, and class EF_2 inverters are discussed. This lays the theoretical foundation for the design and analysis of these types of converters in subsequent studies.

Following this, the principles of three modelling methods – fundamental harmonic approximation method, state space variable averaging method and cyclic-mode modelling method are elaborated, with their definitions, basic characteristics, analysis process, and the advantages and drawbacks of each method, respectively. Through the analysis of the three modelling methods with the advantages and disadvantages of each method, the cyclic-mode modelling technique is identified as the main modelling method and the basis for the improvement of the modelling technique in the subsequent studies.

Finally, after analysing various methods for calculating RMS values, cyclic-mode modelling has been identified as the fundamental approach for determining the RMS values of

switching power supplies. And the methodologies suggested by Kostakis *et al*., [2.79] will guide future enhancements in this study.

2.7 References

[2.1] Chakraborty, Sajib, et al. “DC-DC Converter Topologies for Electric Vehicles, Plug-in Hybrid Electric Vehicles and Fast Charging Stations: State of the Art and Future Trends.” *Energies*, vol. 12, no. 8, Apr. 2019, p. 1569. https://doi.org/10.3390/en12081569..

[2.2] Turksoy, Arzu, et al. “A comprehensive overview of the dc-dc converter-based battery charge balancing methods in electric vehicles.” *Renewable & Sustainable Energy Reviews*, vol. 133, Nov. 2020, p. 110274. https://doi.org/10.1016/j.rser.2020.110274.

[2.3] Bifaretti, S., et al. “Advanced Power Electronic Conversion and Control System for Universal and Flexible Power Management.” *IEEE Transactions on Smart Grid*, vol. 2, no. 2, June 2011, pp. 231–43. https://doi.org/10.1109/tsg.2011.2115260.

[2.4] Jagadeesh, Ingilala, and Vairavasundaram Indragandhi. “Comparative Study of DC-DC Converters for Solar PV with Microgrid Applications.” *Energies*, vol. 15, no. 20, Oct. 2022, p. 7569. https://doi.org/10.3390/en15207569.

[2.5] Yuan, Xibo, et al. “Opportunities, Challenges, and Potential Solutions in the Application of Fast-Switching SiC Power Devices and Converters.” *IEEE Transactions on Power Electronics*, vol. 36, no. 4, Apr. 2021, pp. 3925–45. https://doi.org/10.1109/tpel.2020.3024862.

[2.6] Wang, Weikang, et al. “A Dynamic Control Method for Buck + LLC Cascaded Converter With a Wide Input Voltage Range.” *IEEE Transactions on Power Electronics*, vol. 38, no. 2, Feb. 2023, pp. 1522–34. https://doi.org/10.1109/tpel.2022.3208872.

[2.7] Wang, Yongqing, et al. “A Low-Voltage and Power-Efficient Capless LDO Based on the Biaxially Driven Power Transistor Technique for Respiration Monitoring System.” *IEEE Transactions on Biomedical Circuits and Systems*, vol. 16, no. 6, Dec. 2022, pp. 1153–65. https://doi.org/10.1109/tbcas.2022.3223037.

[2.8] Ma, Dajun, Wu Chen, and Xinbo Ruan. "A review of voltage/current sharing techniques for series–parallel-connected modular power conversion systems." *IEEE Transactions on Power Electronics 35.11,* (2020), pp. 12383-12400.

[2.9] X. Huang, X. Yang, J. Wu, P. Ren, and W. Chen, “Optimal Design of Coupled Inductors for Multiphase Buck Converter.” *2022 IEEE International Power Electronics and Application Conference and Exposition (PEAC)*, Nov. 2022, pp. 734–738.

[2.10] Mattsson, A., et al. “Design of customer-end converter systems for low voltage dc distribution from a life cycle cost perspective,” *2018 International Power Electronics Conference (IPEC-Niigata 2018 -ECCE Asia)*, 2018, pp. 2948–2955, https://doi.org/10.23919/ipec.2018.8507675.

[2.11] Ren, Pengyuan, et al. “AC Copper Loss Reduction in Planar Inductors With Magnetic Building Blocks-Based Gapless Parallel Symmetrical Magnetoresistance Structure.” *IEEE Journal of Emerging and Selected Topics in Power Electronics*, vol. 11, no. 4, Aug. 2023, pp. 4295–312. https://doi.org/10.1109/jestpe.2023.3278689.

[2.12] De León-Aldaco, Susana Estefany, Hugo Calleja, and Jesús Aguayo Alquicira. "Metaheuristic optimization methods applied to power converters: A review." IEEE Transactions on Power Electronics 30.12 (2015): pp. 6791-6803.

[2.13] Ma, Ke, et al. “Evaluation and Design Tools for the Reliability of Wind Power Converter System.” *Journal of Power Electronics/Journal of Power Electronics*, vol. 15, no. 5, Sept. 2015, pp. 1149–57. https://doi.org/10.6113/jpe.2015.15.5.1149.

[2.14] Tavčar, Rok, et al. “Enhancing Power Module Lifespan Through Power Distribution Approaches in a Three-Phase Interleaved DC/DC Converter.” IEEE Access, vol. 11, Jan. 2023, pp. 96784–96. https://doi.org/10.1109/access.2023.3311894.

[2.15] Foster, M. P., et al. “Cyclic-averaging for high-speed analysis of resonant converters.” *IEEE Transactions on Power Electronics*, vol. 18, no. 4, July 2003, pp. 985–93. https://doi.org/10.1109/tpel.2003.813763.

[2.16] Siwakoti, Yam P., Mojtaba Forouzesh, and Ngoc Ha Pham. "Power electronics converters—An overview." *Control of power electronic converters and systems* (2018): pp. 3-29, https://doi.org/10.1016/b978-0-12-805245-7.00001-9.

[2.17] Ansari, Sajad A., et al. “Evaluation of silicon MOSFETs and GaN HEMTs in soft-switched and hard-switched DC-DC boost converters for domestic PV applications.” *IET Power Electronics*, vol. 14, no. 5, Feb. 2021, pp. 1032–43. https://doi.org/10.1049/pel2.12085.

[2.18] Cavalcanti, Marcelo C., et al. "Comparative evaluation of losses in soft and hard-switched inverters." *38th IAS Annual Meeting on Conference Record of the Industry Applications Conference*, 2003. Vol. 3, https://doi.org/10.1109/ias.2003.1257829.

[2.19] Blackwell, Margaret E., et al. "Direct 48 V to 6 V Automotive Hybrid Switched-Capacitor Converter with Reduced Conducted EMI." *2022 IEEE 23rd Workshop on Control and Modeling for Power Electronics (COMPEL)*, 2022, https://doi.org/10.1109/compel53829.2022.9830026.

[2.20] Cui, Xiaofan, and Al-Thaddeus Avestruz. “Large-Signal Stability Guarantees for Cycle-by-Cycle Controlled DC–DC Converters.” *IEEE Control Systems Letters*, vol. 7, Jan. 2023, pp. 763–68. https://doi.org/10.1109/lcsys.2022.3225586.

[2.21] Zhu, Guo-Rong, et al. “Enhanced Single-Phase Full-Bridge Inverter With Minimal Low-Frequency Current Ripple.” *IEEE Transactions on Industrial Electronics*, vol. 63, no. 2, Feb. 2016, pp. 937–43. https://doi.org/10.1109/tie.2015.2491881. ↩

[2.22] Gift, Stephan J. G. “A high-performance full-wave rectifier circuit.” *International Journal of Electronics*, vol. 87, no. 8, Aug. 2000, pp. 925–30. https://doi.org/10.1080/002072100404587.

[2.23] Wu, Bin, et al. “Current-Source Converter and Cycloconverter Topologies for Industrial Medium-Voltage Drives.” *IEEE Transactions on Industrial Electronics*, vol. 55, no. 7, July 2008, pp. 2786–97. https://doi.org/10.1109/tie.2008.924175.

[2.24] Gasparri, Osvaldo, et al. “A Fast Switching Current Controlled DC/DC Converter for Automotive Applications.” *Journal Electrical and Electronic*

Engineering/Journal of Electrical and Electronic Engineering, vol. 9, no. 4, Jan. 2021, p. 123. https://doi.org/10.11648/j.jeee.20210904.14.

[2.25] Korte, Christian, et al. "On-Line Multistep Predictive Spectral Control of the Distortion in Switched-Mode Converters." *IEEE Access*, vol. 10, Jan. 2022, pp. 106556–67. https://doi.org/10.1109/access.2022.3202978.

[2.26] Salimi, Mahdi, et al. "Adaptive nonlinear control of the DC-DC buck converters operating in CCM and DCM." *International Transactions on Electrical Energy Systems*, vol. 23, no. 8, Aug. 2012, pp. 1536–47. https://doi.org/10.1002/etep.1679.

[2.27] Sun, Mengyuan, et al. "A Fast Transient Adaptive On-Time Controlled BUCK Converter with Dual Modulation." *Micromachines*, vol. 14, no. 10, Sept. 2023, p. 1868. https://doi.org/10.3390/mi14101868.

[2.28] Daraz, Amil, et al. "Performance analysis of PID controller and fuzzy logic controller for DC-DC boost converter." *PloS One*, vol. 18, no. 10, Oct. 2023, p. e0281122. https://doi.org/10.1371/journal.pone.0281122.

[2.29] Perera, Nirmana, et al. "Hard-Switching Losses in Power FETs: The Role of Output Capacitance." *IEEE Transactions on Power Electronics*, vol. 37, no. 7, July 2022, pp. 7604–16. https://doi.org/10.1109/tpel.2021.3130831.

[2.30] Steigerwald, R. L. "A comparison of half-bridge resonant converter topologies." *IEEE Transactions on Power Electronics*, vol. 3, no. 2, Apr. 1988, pp. 174–82. https://doi.org/10.1109/63.4347.

[2.31] Kundu, Utsab, et al. "Accurate ZVS Analysis for Magnetic Design and Efficiency Improvement of Full-Bridge LLC Resonant Converter." *IEEE Transactions on Power Electronics*, vol. 32, no. 3, Mar. 2017, pp. 1703–06. https://doi.org/10.1109/tpel.2016.2604118.

[2.32] Vakacharla, Venkata R., and Akshay Kumar Rathore. "Current-Fed Isolated LCC-T Resonant Converter With ZCS and Improved Transformer Utilization." *IEEE Transactions on Industrial Electronics*, vol. 66, no. 4, Apr. 2019, pp. 2735–45. https://doi.org/10.1109/tie.2018.2844855.

[2.33] Deshmukh, Sheetal, et al. “Review on classification of resonant converters for electric vehicle application.” *Energy Reports*, vol. 8, Nov. 2022, pp. 1091–113. https://doi.org/10.1016/j.egyr.2021.12.013.

[2.34] Tang, Xinxi, et al. “Three-Port Bidirectional Series-Resonant Converter With First-Harmonic-Synchronized PWM.” *IEEE Journal of Emerging and Selected Topics in Power Electronics*, vol. 9, no. 2, Apr. 2021, pp. 1410–19. https://doi.org/10.1109/jestpe.2020.2975164.

[2.35] Kim, Jong-Woo, and Peter Barbosa. “PWM-Controlled Series Resonant Converter for Universal Electric Vehicle Charger.” *IEEE Transactions on Power Electronics*, vol. 36, no. 12, Dec. 2021, pp. 13578–88. https://doi.org/10.1109/tpel.2021.3072991.

[2.36] Ribeiro, Kelly, et al. "A Bidirectional Three-port Current-fed LC Parallel Resonant Converter." *2019 IEEE 13th International Conference on Power Electronics and Drive Systems (PEDS)*, vol. 2019, Jan. 2019, pp. 1–6, jglobal.jst.go.jp/en/detail?JGLOBAL_ID=202002252044457863.

[2.37] Outeiro, Maria Teresa, et al. “Resonant Power Converters: An Overview with Multiple Elements in the Resonant Tank Network.” *IEEE Industrial Electronics Magazine*, vol. 10, no. 2, June 2016, pp. 21–45. https://doi.org/10.1109/mie.2016.2549981.

[2.38] Yang, Yuchen, et al. "Analysis and reduction of common mode EMI noise for resonant converters." *2014 IEEE Applied Power Electronics Conference and Exposition-APEC 2014*, https://doi.org/10.1109/apec.2014.6803365.

[2.39] Lin, Bor-Ren, and Chu-Xian Dai. “Wide Voltage Resonant Converter Using a Variable Winding Turns Ratio.” *Electronics*, vol. 9, no. 2, Feb. 2020, p. 370. https://doi.org/10.3390/electronics9020370.

[2.40] de Juan, Aurora, et al. “Analytical Modelling of Single-Phase and Three-Phase DC/DC LLC Converters.” *2022 IEEE Applied Power Electronics Conference and Exposition (APEC)*, Mar. 2022, https://doi.org/10.1109/apec43599.2022.9773467.

[2.41] He, Peiwen, et al. “Design of a 1-MHz High-Efficiency High-Power-Density Bidirectional GaN-Based CLLC Converter for Electric Vehicles.” *IEEE*

Transactions on Vehicular Technology, vol. 68, no. 1, Jan. 2019, pp. 213–23. https://doi.org/10.1109/tvt.2018.2881276.

[2.42] Jiang, Chaoqiang, et al. “An Overview of Resonant Circuits for Wireless Power Transfer.” *Energies*, vol. 10, no. 7, June 2017, p. 894. https://doi.org/10.3390/en10070894.

[2.43] Gutmann, Ronald J. “Application of RF Circuit Design Principles to Distributed Power Converters.” *IEEE Transactions on Industrial Electronics and Control Instrumentation*, vol. IECI-27, no. 3, Aug. 1980, pp. 156–64. https://doi.org/10.1109/tieci.1980.351669.

[2.44] Kaczmarczyk, Z., and B. Grzesik. “800 W, 16 MHz laboratory class E inverter.” *Zeszyty Naukowe. Elektryka / Politechnika Śląska*, Jan. 2003, pp. 71–78. yadda.icm.edu.pl/yadda/element/bwmeta1.element.baztech-article-BSL6-0010-0008 .

[2.45] Kaczmarczyk, Z. “A high-efficiency Class E inverter – computer model, laboratory measurements and SPICE simulation.” *Bulletin of the Polish Academy of Sciences. Technical Sciences*, vol. 55, Jan. 2007, pp. 411–17. yadda.icm.edu.pl/yadda/element/bwmeta1.element.baztech-article-BPG5-0028-0019 .

[2.46] Phinney, Joshua W., et al. “Radio-Frequency Inverters With Transmission-Line Input Networks.” *IEEE Transactions on Power Electronics*, vol. 22, no. 4, July 2007, pp. 1154–61. https://doi.org/10.1109/tpel.2007.900465.

[2.47] Reza, Ali, and Sobhan Roshani. “A Reduced Switch Voltage Stress Class E Power Amplifier Using Harmonic Control Network.” *International Journal of Advanced Computer Science and Applications/International Journal of Advanced Computer Science & Applications*, vol. 7, no. 5, Jan. 2016, https://doi.org/10.14569/ijacsa.2016.070507.

[2.48] Kazimierczuk, Marian K., and Dariusz Czarkowski. *Resonant power converters*. John Wiley & Sons, 2012, ci.nii.ac.jp/ncid/BA25126057.

[2.49] Rivas, Juan M., et al. “A High-Frequency Resonant Inverter Topology With Low-Voltage Stress.” *IEEE Transactions on Power Electronics*, vol. 23, no. 4, July 2008, pp. 1759–71. https://doi.org/10.1109/tpel.2008.924616.

[2.50] Ashique, Ratil H., et al. “A Comparative Performance Analysis of Zero Voltage Switching Class E and Selected Enhanced Class E Inverters.” *Electronics*, vol. 10, no. 18, Sept. 2021, p. 2226. https://doi.org/10.3390/electronics10182226.

[2.51] Kee, S. D., et al. “The class-E/F family of ZVS switching amplifiers.” *IEEE Transactions on Microwave Theory and Techniques*, vol. 51, no. 6, June 2003, pp. 1677–90. https://doi.org/10.1109/tmtt.2003.812564.

[2.52] Kaczmarczyk, Z. “High-Efficiency Class E,$hboxEF_2$, and$hboxE/F_3$Inverters.” *IEEE Transactions on Industrial Electronics*, vol. 53, no. 5, Oct. 2006, pp. 1584–93. https://doi.org/10.1109/tie.2006.882011.

[2.53] Aldhaher, Samer, et al. “Modeling and Analysis of Class EF and Class E/F Inverters With Series-Tuned Resonant Networks.” *IEEE Transactions on Power Electronics*, vol. 31, no. 5, May 2016, pp. 3415–30. https://doi.org/10.1109/tpel.2015.2460997.

[2.54] Peyghami, Saeed, et al. *Failure Mode, Effects and Criticality Analysis (FMECA) in Power Electronic based Power Systems*. Sept. 2019, https://doi.org/10.23919/epe.2019.8915061.

[2.55] Song, Chaochao, et al. “Capacitor Voltage Balancing for Multilevel Dual-Active-Bridge DC–DC Converters.” *IEEE Transactions on Industrial Electronics*, vol. 70, no. 3, Mar. 2023, pp. 2566–75. https://doi.org/10.1109/tie.2022.3174287.

[2.56] Costa , André Elias Lucena, and Romero Leandro Andersen. “High-gain three-phase current-fed push–pull DC–DC converter.” *IET Power Electronics*, vol. 13, no. 3, Feb. 2020, pp. 545–56. https://doi.org/10.1049/iet-pel.2019.0843.

[2.57] Diaz, Matías, et al. “An Overview of Modelling Techniques and Control Strategies for Modular Multilevel Matrix Converters.” *Energies*, vol. 13, no. 18, Sept. 2020, p. 4678. https://doi.org/10.3390/en13184678.

[2.58] Poon, Jason, et al. “Model-Based Fault Detection and Identification for Switching Power Converters.” *IEEE Transactions on Power Electronics*, vol. 32, no. 2, Feb. 2017, pp. 1419–30. https://doi.org/10.1109/tpel.2016.2541342.

[2.59] Rathore, Akshay Kumar, and Venkata R. Vakacharla. “A Simple Technique for Fundamental Harmonic Approximation Analysis in Parallel and Series–Parallel Resonant Converters.” *IEEE Transactions on Industrial Electronics*, vol. 67, no. 11, Nov. 2020, pp. 9963–68. https://doi.org/10.1109/tie.2019.2952820.

[2.60] Reis, Manuel JCS, et al. "Teaching of Fourier series expansions in undergraduate education." *2013 IEEE Global Engineering Education Conference (EDUCON)*. Mar. 2013, https://doi.org/10.1109/educon.2013.6530141.

[2.61] Chen, Yiming, et al. “An Improved Fundamental Harmonic Approximation to Describe Filter Inductor Influence on Steady-State Performance of Parallel-Type Resonant Converter.” *IEEE Transactions on Power Electronics*, vol. 34, no. 3, Mar. 2019, pp. 2467–78. https://doi.org/10.1109/tpel.2018.2847900.

[2.62] Tan, Rodney HG, and Landon YH Hoo. "DC-DC converter modeling and simulation using state space approach." *2015 IEEE Conference on Energy Conversion (CENCON)*. Oct. 2015, https://doi.org/10.1109/cencon.2015.7409511.

[2.63] Borowska, Agnieszka, and Ruth King. “Semi-Complete Data Augmentation for Efficient State Space Model Fitting.” *Journal of Computational and Graphical Statistics*, vol. 32, no. 1, July 2022, pp. 19–35. https://doi.org/10.1080/10618600.2022.2077350.

[2.64] Venkataramana, , S. “Small Signal Modeling of Non-Isolated High Gain DC-DC converter.” *2020 International Conference for Emerging Technology (INCET)*, June 2020, https://doi.org/10.1109/incet49848.2020.9154171.

[2.65] Sarif, M. Shahriman M., et al. *Modeling, design and control of bidirectional DC-DC converter using state-space average model*. Apr. 2018, https://doi.org/10.1109/iscaie.2018.8405509.

[2.66] Wang, Lei, et al. “Electromagnetic Transient Modeling and Simulation of Power Converters Based on a Piecewise Generalized State Space Averaging Method.”

IEEE Access, vol. 7, Jan. 2019, pp. 12241–51. https://doi.org/10.1109/access.2019.2891122.

[2.67] Visser, H. R., and P. P. J. Van den Bosch. "Modelling of periodically switching networks." *PESC'91 Record 22nd Annual IEEE Power Electronics Specialists Conference.*1991, https://doi.org/10.1109/pesc.1991.162655.

[2.68] Gould, C., et al. “CLL resonant converters with output short-circuit protection.” *IEE Proceedings. Electric Power Applications*, vol. 152, no. 5, Jan. 2005, p. 1296. https://doi.org/10.1049/ip-epa:20045157.

[2.69] Wei, Yuqi, et al. “Comprehensive comparisons between frequency-domain analysis and time-domain analysis for LLC resonant converter.” *IET Power Electronics*, vol. 13, no. 9, May 2020, pp. 1735–45. https://doi.org/10.1049/iet-pel.2019.0831.

[2.70] Wei, Yuqi, Quanming Luo, Si Chen, et al. “Comparison among different analysis methodologies for LLC resonant converter.” *IET Power Electronics*, vol. 12, no. 9, July 2019, pp. 2236–44. https://doi.org/10.1049/iet-pel.2019.0027.

[2.71] Sarif, M. Shahriman M., Tan Xin Pei, and A. Z. Annuar. "Modeling, design and control of bidirectional DC-DC converter using state-space average model." *2018 IEEE symposium on computer applications & industrial electronics (ISCAIE)*. Apr. 2018, https://doi.org/10.1109/iscaie.2018.8405509.

[2.72] Foster, M. P., et al. “Predicting the zero-voltage switching profiles of half-bridge driven inductor-less piezoelectric transformer-based inverters.” *IET Power Electronics*, vol. 5, no. 7, Aug. 2012, pp. 1068–73. https://doi.org/10.1049/iet-pel.2011.0344.

[2.73] Foster, M. P., H. I. Sewell, et al. “Cyclic-averaging for high-speed analysis of resonant converters.” *IEEE Transactions on Power Electronics*, vol. 18, no. 4, July 2003, pp. 985–93. https://doi.org/10.1109/tpel.2003.813763.

[2.74] Vandelac, J. p., and P. D. Ziogas. “A novel approach for minimizing high-frequency transformer copper losses.” *IEEE Transactions on Power Electronics*, vol. 3, no. 3, July 1988, pp. 266–77. https://doi.org/10.1109/63.17944.

[2.75] Zhou, Zongjie, et al. “A Constant Frequency ZVS Control System for the Four-Switch Buck–Boost DC–DC Converter With Reduced Inductor Current.”

IEEE Transactions on Power Electronics, vol. 34, no. 7, July 2019, pp. 5996–6003. https://doi.org/10.1109/tpel.2018.2884950.

[2.76] Safaee, Alireza, et al. "A ZVS Pulsewidth Modulation Full-Bridge Converter With a Low-RMS-Current Resonant Auxiliary Circuit." *IEEE Transactions on Power Electronics*, vol. 31, no. 6, June 2016, pp. 4031–47. https://doi.org/10.1109/tpel.2015.2473822.

[2.77] Tong, Anping, et al. "Modeling and Analysis of a Dual-Active-Bridge-Isolated Bidirectional DC/DC Converter to Minimize RMS Current With Whole Operating Range." *IEEE Transactions on Power Electronics*, vol. 33, no. 6, June 2018, pp. 5302–16. https://doi.org/10.1109/tpel.2017.2692276.

[2.78] Choi, Wooin, et al. "Fundamental Duty Modulation of Dual-Active-Bridge Converter for Wide-Range Operation." *IEEE Transactions on Power Electronics*, vol. 31, no. 6, June 2016, pp. 4048–64. https://doi.org/10.1109/tpel.2015.2474135.

[2.79] Kostakis, G. T., et al. "A generalized method for calculating the RMS values of switching power converters." *IEEE Transactions on Power Electronics*, vol. 15, no. 4, July 2000, pp. 616–25. https://doi.org/10.1109/63.849031.

Chapter 3. Design of power converters

Following the description of switch converter classifications in previous Chapters, boost converters, LLC converters, and class EF_2 inverters were selected for detailed study. This Chapter introduces the design methodologies for these three types of converters, employing different analytical approaches for each. Additionally, this Chapter provides the design method for converters that will be utilized in subsequent Chapters, laying the groundwork for constructing test models later in the thesis.

3.1 Methodology for designing boost converters

3.1.1 Operating principle of a boost converter

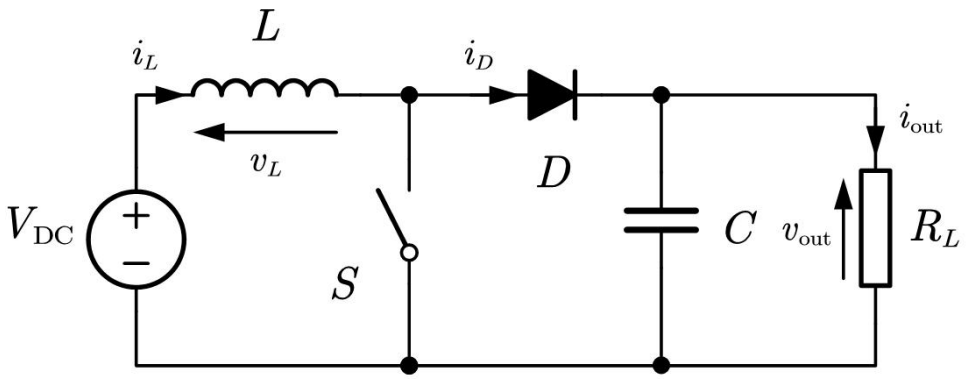

Fig. 3.1. Circuit diagram of a boost converter

Fig. 3.1 illustrates a Boost converter consisting of the following components: a DC input source V_{DC}, a switch S such as a MOSFET or IGBT, an inductor L to store energy, a diode D to ensure unidirectional current flow, a capacitor C to smooth out the output voltage, and a load resistor R_{L} representing the output device.

The working principle of a boost converter can be divided into two or three stages (modes):

Energy storage mode (Mode 1): During this stage, Switch S is turned on, and the inductor L charges from DC input V_{DC}, increasing current i_L. The inductor stores energy from the DC source.

Energy release mode (Mode 2): When switch S turned off, inductor L discharges through diode D, raising v_{out} as i_L decreases and energy flows to capacitor C and load R_L. If inductor current i_L reaches zero while switch S is still off, the circuit transitions to the zero current stage.

Zero current mode (Mode 3): Diode D acts as a blocker, preventing capacitor C from discharging into inductor L. During this stage, load R_L receives power only from capacitor C until the next cycle.

This initial step lays the foundation for all subsequent design phases, ensuring matching with expected applications and performance criteria. The analytical approach of this design is based on the methodology outlined in [3.1].

3.1.2 Operation topology selection

Selecting an appropriate topology is fundamental in boost converter design. This section explains the operation of the boost converter in both CCM and CCM operating condition including factors to consider when choosing between these modes.

3.1.2.1 Continuous Conduction Mode operation

In CCM operation, the inductor current does not drop to zero throughout the cycle. The boost converter continuously cycles between two modes in this operation. The operation in Mode 1, where the switch is on, and all the DC input voltage is applied to the inductor, this results in

an increase in the inductor current. In Mode 2, the switch is turning off, and the diode is forced into conduction due to the requirement for the inductor to maintain continuous current flow. This operating condition offers the advantages of reduced stress on components, lower output ripple, and improved transient response.

When deciding whether to operate a boost converter in CCM, it is essential to understand its key characteristics. Firstly, CCM operation is suited for high-current applications due to the continuity of the current flow. However, maintaining this continuous current significantly increases the complexity of control, necessitating the introduction of more sophisticated control strategies. Lastly, CCM operation generally requires larger magnetic components, resulting in increased converter size. This makes CCM less suitable for space-sensitive applications.

3.1.2.2 Discontinuous Conduction Mode operation

In DCM operation, the inductor current falls to zero during part of the switching cycle, resulting in three distinct modes within each period. DCM represents another operational approach for boost converters, each with its own set of unique advantages and considerations. It is particularly suitable for applications with low to medium load currents, improving efficiency under such conditions. DCM enables simpler control strategies, reducing design complexity and providing a more straightforward operational framework. However, DCM comes with drawbacks, including increased stress on components and higher output voltage and current ripples. The intermittent current flow in DCM can increase stress on converter components and result in higher output ripples.

3.1.2.3 Performance benchmarking

Efficiency: Under high-load conditions, the perpetual non-zero inductor current in CCM generally has higher efficiency. Conversely, DCM might engender superior efficiency under low to medium-load conditions due to the intermittent nature of the inductor current.

Output ripple: The continuous inductor current in CCM typically manifests lower output voltage and current ripple. In contrast, DCM may engender higher output ripple.

Control complexity: The mandate for a continuous current flow necessitates a more sophisticated control strategy, potentially increased design complexity. DCM allows for simpler and more straightforward control strategies, which improve design and implementation complexity.

Component size and cost: CCM requisites for larger magnetic components to accommodate the continuous current flow could impact the overall size and cost of the converter. Under low-to-medium-load conditions, DCM might permit the use of smaller components, thereby decreasing size and cost.

Table 3.1. Boost converter CCM and DCM operation performance comparison

Benchmark	CCM	DCM
Efficiency	Higher (high load)	Higher (low to medium load)
Output Ripple	Lower	Higher
Control Complexity	More Complex	Simpler
Component Size	Larger	Smaller
Cost	More Costly	Less Costly

Careful consideration of these trade-offs is necessary to ensure that the selected conduction mode matches the application's tolerance for ripple, component stress, efficiency, and control needs.

3.1.3 Inductor selection

In the operation of boost converters, CCM and DCM represent two distinct operational conditions, primarily differentiated by the waveform of the inductor current. Under CCM, the inductor current remains non-zero throughout the entire cycle, whereas in DCM, the inductor current descends to zero within each cycle. When discussing the boundary conditions of CCM and DCM, reference is made to a specific inductance value at which the converter transitions from CCM to DCM, or vice versa. At this boundary point, the inductor current precisely drops to zero as each cycle concludes. This particular inductance value serves as the minimum inductance required to sustain operation in CCM and, concurrently, the maximum inductance value to operate in DCM. This is attributed to the fact that, should the inductance value fall below this point, the converter would transition into DCM as it would be unable to maintain the continuity of the inductor current. Conversely, exceeding this inductance ensures continuous inductor current, keeping the converter in CCM operation.

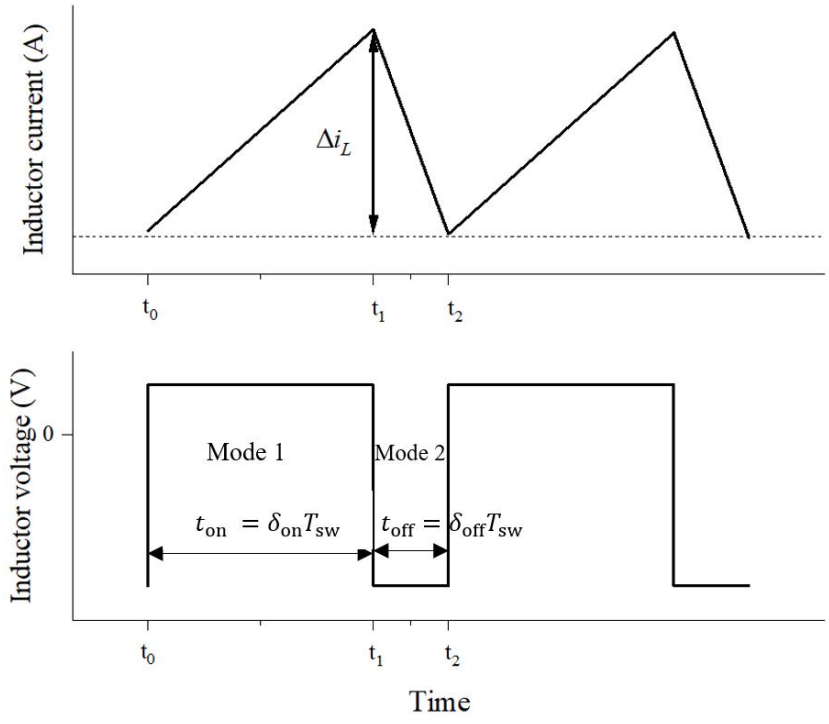

Fig. 3.2. Boost converter inductor current i_L and inductor voltage v_L waveform in CCM operation

The example inductor current waveform for a boost converter operate in CCM condition is shown in Fig. 3.2. Initially, assuming that the converter operates in CCM case. Since the inductor current never drops to zero during CCM, the minimum inductor current occurs at the beginning of the cycle, which corresponds to the end of the cycle,

$$i_{L\,(\min)} = i_L(t_0) = i_L(T_{\mathrm{sw}}) \tag{3.1}$$

Since diode D conducts only after the switch is turned off, the charge transferred through D during a cycle, is equal to the charge transferred through D when the switch is turned off, which is q_D, and is defined as,

$$q_D = \frac{1}{2}(T_{\mathrm{sw}} - t_{\mathrm{on}})\Delta i_L + i_{L\,(\min)}(T_{\mathrm{sw}} - t_{on}) \tag{3.2}$$

Additionally, the charge passing through the load during a single cycle is denoted as q_{RL}, is given by,

$$q_{RL} = i_{\mathrm{out}} T_{\mathrm{sw}} \tag{3.3}$$

The charge transferred through D in a cycle is equal to the charge passed through the load in a cycle, thus combining (3.2) and (3.3) can get,

$$i_{L\,(\min)} = i_{\mathrm{out}} \frac{T_{\mathrm{sw}}}{T_{\mathrm{sw}} - t_{\mathrm{on}}} - \frac{\Delta i_L}{2} \tag{3.4}$$

In the case of CCM, the inductor current never drops to zero, thereby always remaining above zero, so the inductor current change during a cycle is given by,

$$\Delta i_{\mathrm{L}} = \frac{V_{\mathrm{DC}} t_{\mathrm{on}}}{L} \tag{3.5}$$

and substituting (3.4) with the derived inequality which $i_{\mathrm{L}} > 0$, we have,

$$i_{L\,(\min)} = i_{\mathrm{out}} \frac{T_{\mathrm{sw}}}{T_{\mathrm{sw}} - t_{\mathrm{on}}} - \frac{V_{\mathrm{DC}} t_{on}}{2L} > 0 \tag{3.6}$$

The collation inequality (3.6) provides the condition for the minimum inductance value to satisfy the CCM based on the minimum output current,

$$L_{\min} > \frac{V_{\mathrm{DC}} t_{\mathrm{on}}}{2 i_{\mathrm{out\,(min)}}} (1 - \delta_{\mathrm{on}}) \tag{3.7}$$

Secondly, to choose an appropriate inductor, it's necessary to calculate both the peak inductor current $i_{L\,(\max)}$ and the average inductor current $\bar{i}_L$. Based on the operating waveform of the CCM in Fig. 3.2, the maximum inductor current $i_{L\,(\max)}$ is determined by adding the inductor current variation Δi_L to the minimum inductor current $i_{L\,(\min)}$,

$$i_{L\,(\max)} = i_{\mathrm{out}} \frac{T_{\mathrm{sw}}}{T_{\mathrm{sw}} - t_{\mathrm{on}}} + \frac{\Delta i_L}{2} = i_{\mathrm{out}} \frac{T_{\mathrm{sw}}}{T_{\mathrm{sw}} - t_{\mathrm{on}}} + \frac{V_{\mathrm{DC}} t_{\mathrm{on}}}{2L} \tag{3.8}$$

The total inductor current during a cycle can be calculated in two parts: A rectangle, with the minimum inductor current $i_{L\,(\min)}$ as the length and the cycle duration T_{sw} as the width, and a triangle, characterized by the change in inductor current Δi_L as the height and the time when the switch is turned off t_{off} as the base. Therefore, the average inductor current over a cycle $\bar{i}_L$ is the total inductor current during a cycle divided by the cycle time.

$$\bar{i}_L = \frac{1}{T_{\mathrm{sw}}} \left[\left(i_{\mathrm{out}} \frac{T_{\mathrm{sw}}}{T_{\mathrm{sw}} - t_{\mathrm{on}}} - \frac{\Delta i_L}{2} \right) T_{\mathrm{sw}} + \frac{1}{2} T_{\mathrm{sw}} \Delta i_L \right] \tag{3.9}$$

Simplifying (3.9) gives the average inductor current $\bar{i}_L$ based on the output current and duty cycle,

$$\bar{i}_L = \frac{i_{\mathrm{out}}}{1 - \delta_{\mathrm{on}}} \tag{3.10}$$

Similarly, it is also necessary to find the peak inductor current $i_{L\,(\max)}$ and cycle average inductor current $\bar{i}_L$ of the converter under DCM operation. The different operating states of the converter can be determined from the output current by rearranging (3.7),

$$\begin{cases} i_{\text{out}} \geq \dfrac{V_{\text{DC}} t_{\text{on}}}{2L}(1-\delta_{\text{on}}) & \text{CCM} \\ i_{\text{out}} \leq \dfrac{V_{\text{DC}} t_1}{2L}(1-\delta_1) & \text{DCM} \end{cases} \tag{3.11}$$

Next, we will conduct a detailed analysis of the DCM operation. An inductor current waveform at DCM operation is shown in Fig. 3.3,

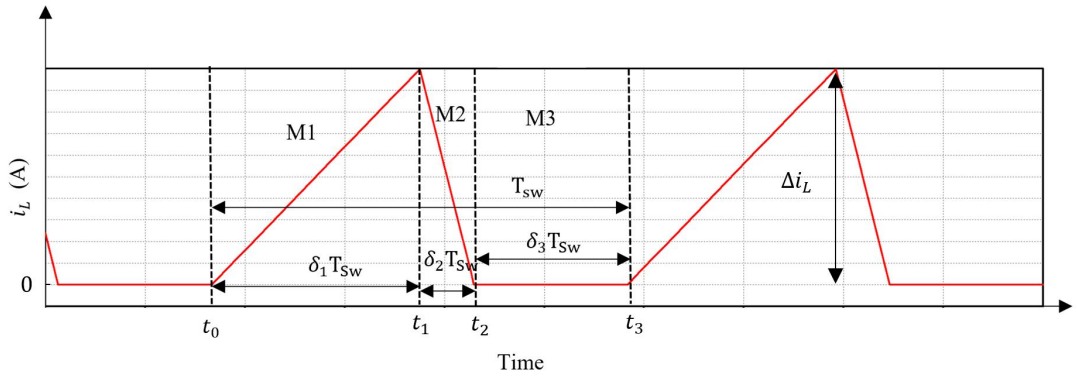

Fig. 3.3. Boost converter inductor current i_L waveform in DCM operation

When the converter operates in DCM state, the peak inductor current is the inductor current at the end of Mode 1,

$$i_{L(\max)} = \Delta i_L = \frac{V_{\text{DC}}(t_1 - t_0)}{L} \tag{3.12}$$

where $t_1 = \delta_1 T_{\text{sw}}$ is based on the value of the maximum switch turned on time required to regulate the output voltage when both the load and input voltages are varied by recalling (2.28) from Chapter 2,

$$\frac{v_{\text{out}}}{V_{\text{DC}}} = \frac{1 + \sqrt{1 + \frac{4\delta_1^2 R_L T_{\text{sw}}}{2L}}}{2} \tag{3.13}$$

The cycle-averaged inductor current $\bar{i}_L$ under DCM operation can be deduced analogously from the inductor current waveform inherent to DCM. In this scenario, the total charge flowing through the inductor within one cycle is encapsulated by a triangular area, with the apex representing the peak inductive current. The base of the triangle corresponds to the cumulative duration of Mode1 and Mode2. Therefore, the cycle-averaged inductive current is computed as the area of the triangle divided by the switch cycle time T_{sw},

$$\bar{i}_L = \frac{\Delta i_L (\delta_1 + \delta_2) T_{\text{sw}}}{2T_{\text{sw}}} \tag{3.14}$$

Then the Mode 2 duration is equal to,

$$\delta_2 T_{\text{sw}} = \frac{\Delta i_{\text{L}} L}{v_{out} - V_{DC}} \tag{3.15}$$

Substituting (3.15) and (3.12) into (3.14) gives the equation for the variation of the cycle-averaged inductor current with the converter operating parameters, switching duty cycle and inductor value,

$$\bar{i}_L = \frac{V_{DC} v_{\text{out}} \delta_1^2 T_{\text{sw}}}{2LT_{\text{sw}}(v_{\text{out}} - V_{DC})} \tag{3.16}$$

Finally, the total inductor current in a cycle is the sum of the current flowing through the switch i_S and the current flowing through the diode i_D within the cycle. The RMS values of these two currents can be determined using the formulas provided below,

$$i_{S\,(\text{RMS})} = \frac{V_{DC} t_1}{L}\sqrt{\frac{\delta_1 T_{sw}}{3T_{\text{sw}}}},\ i_{D\,(\text{RMS})} = \frac{V_{DC} t_1}{L}\sqrt{\frac{\delta_2 T_{sw}}{3T_{\text{sw}}}}, \tag{3.17}$$

The inductor current RMS value can be expressed as the sum of these two RMS values,

$$i_{\mathrm{L(RMS)}} = i_{S\,(\mathrm{RMS})} + i_{D\,(\mathrm{RMS})} = \frac{V_{DC} t_1}{L\sqrt{3T_{\mathrm{sw}}}} \sqrt{(\delta_1 + \delta_2) T_{\mathrm{sw}}} \tag{3.18}$$

In summary, the first step in selecting an inductor consists of determining the converter's operating parameters, which include input voltage, input current, output voltage, output current, and the converter's mode of operation, i.e., CCM or DCM. After specifying the mode of operation, the appropriate range of inductance values can be determined based on (3.7). The inductance value determined by this method will be the minimum inductance value in the CCM and also the maximum inductance value in the DCM.

$$\begin{aligned} L_{\min} &> \frac{V_{\mathrm{DC}} t_{\mathrm{on}}}{2 i_{\mathrm{out\ (min)}}} (1 - \delta_{\mathrm{on}}) \quad \mathrm{CCM} \\ L_{\max} &< \frac{V_{\mathrm{DC}} t_{\mathrm{on}}}{2 i_{\mathrm{out\ (min)}}} (1 - \delta_1) \quad \mathrm{DCM} \end{aligned} \tag{3.19}$$

Upon determining the inductance value range, several key parameters play a crucial role in the selection of the inductance. The maximum inductor current $i_{L(\max)}$ reveals the maximum current that the inductor may encounter, which is vital for preventing inductor saturation and designing overcurrent protection mechanisms. In CCM or DCM, $i_{L(\max)}$ can be ascertained respectively through (3.8) and (3.12). The cycle-averaged inductor current $\bar{i}_L$ provides information on the average current within a cycle, which is essential for evaluating the efficiency and stability of the converter. In CCM or DCM, $\bar{i}_L$ can be determined respectively through (3.10) and (3.16), respectively.

3.1.4 Capacitor selection

The primary role of capacitor C is to ensure that the measured output voltage ripple, $\Delta v_{\mathrm{out(measured)}}$, remains below the specified design output voltage ripple, $\Delta v_{\mathrm{out(specified)}}$.

Initially, analysing the CCM operating condition, it is noted that the amount of charge passing through diode D in a cycle is equivalent to the amount passing through the diode during the switch is turned off period. The current flowing through the diode diverges into two pathways: one channelling through the load, and the other through capacitor C. The current traversing through capacitor C is the primary source of the output voltage ripple. Therefore, the quantity of charge flowing through the load when the switch is turned off is given as,

$$q_{\mathrm{RL\,off}} = i_{\mathrm{out}}(T_{\mathrm{sw}} - t_{\mathrm{on}}) \tag{3.20}$$

Given the conduction condition of diode D and referring to (3.2), the charge flowing through the capacitor after the switch is turned off is determined by the difference between the charge flowing through D and the charge flowing through the load,

$$\begin{aligned} q_C &= q_D - q_{\mathrm{RL\,off}} \\ &= \frac{1}{2}(T_{\mathrm{sw}} - t_{\mathrm{on}})\Delta i_L + i_{L\,(\mathrm{min})}(T_{\mathrm{sw}} - t_{\mathrm{on}}) - i_{\mathrm{out}}(T_{\mathrm{sw}} - t_{\mathrm{on}}) = \mathrm{C}\Delta v_{\mathrm{out\,(measured)}} \end{aligned} \tag{3.21}$$

where $\Delta v_{\mathrm{out(measured)}}$ is the measured capacitor voltage ripple, which is the measured output voltage ripple. The measured output voltage ripple $\Delta v_{\mathrm{out(measured)}}$ should always be less than the rated output voltage ripple $\Delta v_{\mathrm{out(specified)}}$,

$$\Delta v_{\mathrm{out(specified)}} > \Delta v_{\mathrm{out\,(measured)}} \tag{3.22}$$

Substituting (3.21) into (3.22) and rearranging gives,

$$C > \frac{T_{\mathrm{sw}} - t_{\mathrm{on}}}{\Delta v_{\mathrm{out\,(specified)}}}\left(\frac{\Delta i_L}{2} + i_{L\,(\mathrm{min})} - i_{\mathrm{out}}\right) \tag{3.23}$$

By substituting (3.4) into (3.23), the relationship between the minimum capacitance and the switch turn on time can be derived, following the determination of the converter specifications,

$$C > \frac{1}{\Delta v_{\text{out(specified)}}} (T_{\text{sw}} - t_{\text{on}}) \left(\frac{\Delta i_L}{2} + i_{\text{out}} \frac{T_{\text{sw}}}{T_{\text{sw}} - t_{\text{on}}} - \frac{\Delta i_L}{2} - i_{\text{out}} \right) = \frac{i_{\text{out}} t_{\text{on}}}{\Delta v_{\text{out(specified)}}} \tag{3.24}$$

In the DCM case, the value of the capacitor is still determined by the rated output voltage ripple $\Delta v_{\text{out(specified)}}$, but unlike the calculation in the CCM case, the output voltage ripple can be calculated based on the conservation of energy principle in the DCM case.

As the converter operates in a steady-state condition, the energy input to the capacitor via the diode during Mode 2, which results in output voltage ripple, originates from the energy stored in the inductor during Mode 1. The energy stored in the inductor at the beginning of Mode 2 is given as,

$$W_L(t_1) = \frac{L i_L^2(t_1)}{2} = \frac{(V_{\text{DC}} t_1)^2}{2L} \tag{3.25}$$

In the steady-state operation of the converter, during Mode 2, the energy initially stored in the inductor is transferred to both the capacitor and the load. This occurs as the inductor current, i_L, linearly decreases to zero. Assuming a constant load current, the difference between the inductor current and the load current results in the output voltage ripple. The current charged the capacitor only during Mode 2, flowing from the inductor to the capacitor, leading to an increase in output voltage. As the operation shifts to Mode 3 and then to the next cycle's Mode 1, the load is only powered by the capacitor, causing a decrease in the output voltage.

At the end of Mode 2, the output voltage reaches its peak, $v_{\text{out(max)}}$, and at the conclusion of Mode 1, it drops to its lowest point, $v_{\text{out(min)}}$. The energy stored by the capacitor at these maximum and minimum output voltages is calculated as follows:

$$W_{\text{C(max)}} = \frac{Cv_{\text{out(max)}}^2}{2}, W_{\text{C(min)}} = \frac{Cv_{\text{out(min)}}^2}{2} \tag{3.26}$$

The difference between the energy stored at these two voltage levels is,

$$W_{\text{C(diff)}} = \frac{C}{2}(v_{\text{out(max)}}^2 - v_{\text{out(min)}}^2) \tag{3.27}$$

Meanwhile, the maximum and minimum values of the output voltage can be approximately defined as follows:

$$\begin{aligned} v_{\text{out(max)}} &\approx v_{\text{out}} + \frac{\Delta v_{\text{out}}}{2} \\ v_{\text{out(min)}} &\approx v_{\text{out}} - \frac{\Delta v_{\text{out}}}{2} \end{aligned} \tag{3.28}$$

where v_{out} is the DC (average) output voltage and Δv_{out} is the peak-to-peak ripple voltage superimposed on the output voltage.

So, substitute (3.28) into (3.27).

$$W_{\text{C(diff)}} = Cv_{\text{out}}\Delta v_{\text{out(measured)}} \tag{3.29}$$

Assuming a scenario with the maximum output voltage ripple, which corresponds to a condition of infinite load impedance, it is understood that all the energy accumulated in the inductor over a cycle is directed to the capacitor, contributing to the creation of the ripple voltage. Therefore, by combining (3.25) and (3.29),

$$W_L(t_1) = W_{\mathrm{C(diff)}} = \frac{(V_{\mathrm{DC}}\delta_1 T_{\mathrm{sw}})^2}{2L} = \frac{C v_{\mathrm{out}} \Delta v_{\mathrm{out(measured)}}}{2} \tag{3.30}$$

Finally, continue to use (3.22) to calculate the required capacitance value to ensure that the output ripple voltage meets the specification.

$$C > \frac{(V_{\mathrm{DC}}\delta_1 T_{\mathrm{sw}})^2}{2L v_{\mathrm{out}} \Delta v_{\mathrm{out(specified)}}} \tag{3.31}$$

In summary, after defining the operational state, the required minimum capacitance to achieve the specified output voltage ripple can be determined using relevant equations. In CCM operation, the minimum capacitance is calculated using (3.24), while in DCM operation, (3.31) is used to determine the minimum capacitance value.

3.2 Methodology for designing LLC converters

The LLC resonant converter is increasingly used in a variety of applications, establishing itself as a vital component in modern power supply design. Its rising popularity is due to its unique features and benefits. These advantages include low switching losses, high power density, and the ability to integrate three magnetic components into a single unit, making LLC resonant converters a popular choice in the current DC-DC power supply topology landscape [3.2].

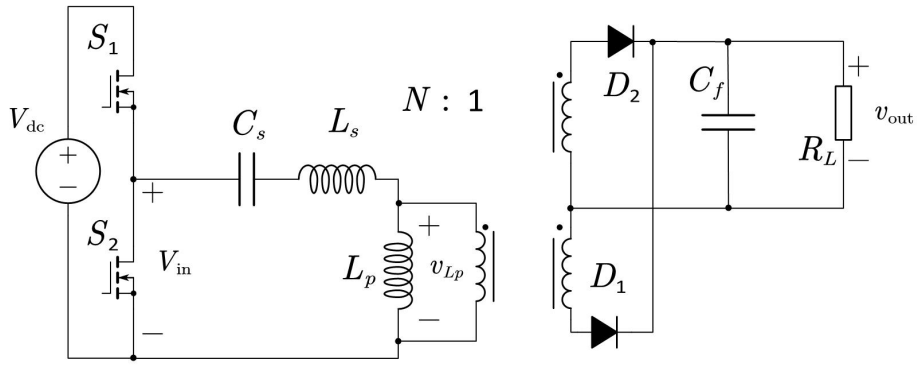

Fig. 3.4. Circuit diagram for the LLC resonant converter

Fig. 3.4 illustrates the circuit diagram of an LLC resonant converter. The converter employs a half-bridge structure comprising MOSFETs S_1 and S_2, which converts the DC voltage V_{dc} into a variable frequency square wave V_{in}. This square wave is then fed into the resonant tank circuit, composed of series inductor L_{s}, parallel inductor L_{p}, and series capacitor C_{s}. On the secondary side of the transformer, a current, flows through the rectifier composed of diodes D_1 and D_2. This current is subsequently smoothed by the filtering capacitor C_f, resulting in the output voltage v_{out}

3.2.1 Modelling method selection

As identified in Chapter 2, the Fundamental Mode Approximation (FMA), also referred to as the First Harmonic Approximation (FHA), is a widely acknowledged analytical method. The inherent band-pass filter characteristic of the resonant circuit diminishes high-order harmonic content in the input voltage while enhancing the fundamental content. This behaviour aligns with the fundamental assumption of FMA, which suggests that only the fundamental harmonic transmits energy, rendering FMA especially appropriate for the analysis of LLC converters [3.4].

The FMA method attenuates high-frequency components of the square wave, allowing only the fundamental harmonic to transmit energy. Since higher-order harmonics are attenuated, the current through resonant circuit closely resembles a sinusoidal wave. Based on the concept of Fourier analysis, a periodic function $f(t)$ can be constructed from an infinite summation of sines and cosines, as described in Chapter 2 on FMA techniques analysis,

3.2.2 AC equivalent circuit modelling

The circuit diagram of the LLC converter is shown in Fig. 3.4. It consists of a half bridge input and a full bridge rectifier part.

Assuming a half-bridge input, the input voltage of the resonant circuit is defined as

$$V_{\text{in}}(t) = \begin{cases} 0 & -T_{\text{sw}}/2 < t < 0 \\ V_{\text{dc}} & 0 < t < T_{\text{sw}}/2 \end{cases} \tag{3.32}$$

Given that the input waveform is an odd function, based on the properties of odd functions, the even harmonics in its Fourier series are zero. Additionally, the cosine part is also zero. Therefore, by substituting (3.33) and (3.35) into (3.32) , the Fourier series of $V_{\text{in}}(t)$ can be obtained,

$$V_{\text{in}}(t) = V_{\text{dc}}\left(\frac{1}{2} + \frac{2}{\pi}\sum_{n=1,3,5}^{\infty}\frac{1}{n}\sin(n\omega_{\text{sw}}t)\right) \tag{3.33}$$

Next, FMA technique is used to approximate $V_{\text{in}}(t)$ as its fundamental component V_{e},

$$V_{\text{in}}(t) \approx V_{\text{e}} = \frac{2}{\pi}V_{\text{dc}}\sin(\omega_{\text{sw}}t) \tag{3.34}$$

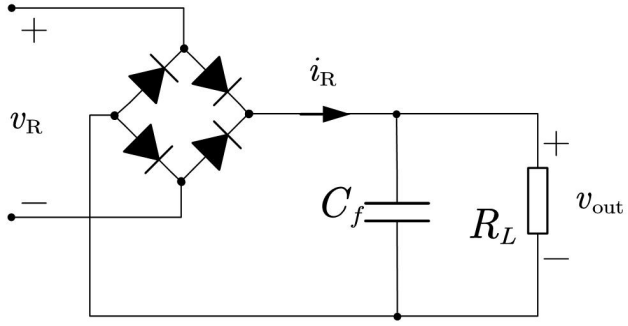

Fig. 3.5. Circuit diagram for the LLC converter rectifier and output part

Based on Fig. 3.5, assuming the full-bridge rectifier operates in continuous current mode which means the current will flow continuously between the resonant circuit and the output. Consequently, the average current through the rectifier will be equivalent to the output current. Due to the rectifier's constant conduction state, the voltage at its input will display a bipolar square wave characteristic, with an amplitude represented by v_{out}.

$$v_R = \begin{cases} v_{\mathrm{out}} & 0 < t < T_{\mathrm{sw}} \\ -v_{\mathrm{out}} & T_{\mathrm{sw}}/2 < t < T_{\mathrm{sw}} \end{cases} \tag{3.35}$$

FMA technique continues to be used to approximate v_{R} as its fundamental component.

$$v_{\mathrm{R}}(t) \approx \frac{4}{\pi} v_{\mathrm{out}} \sin(\omega_{sw} t) \tag{3.36}$$

The DC output current i_{out} is the cycle average of the inverter input current i_{R}.,

$$i_{\mathrm{out}} = \frac{1}{T_{\mathrm{sw}}} \int_0^{T_{\mathrm{sw}}} |i_R| \, \mathrm{dt} = \frac{2}{\pi} i_{R(\max)} \tag{3.37}$$

Considering C_{f} and R_{L} as an equivalent load impedance, denoted as R_{e}, where the input voltage at R_{e} corresponds to the rectifier input voltage (v_R) and the input current to the rectifier output current (i_R), the value of R_{e} can be calculated as:

$$R_{\mathrm{e}} = \frac{v_{\mathrm{R}}}{i_{\mathrm{R}}} = \frac{\frac{4}{\pi} v_{\mathrm{out}} \sin(\omega_{sw} t)}{\frac{\pi}{2} i_{\mathrm{out}} \sin(\omega_{sw} t)} = \frac{8}{\pi^2} R_L \tag{3.38}$$

Afterwards the AC equivalent circuit of the LLC converter can be drawn based on the approximation of the input by the FMA technique and the equivalence of the load branches.

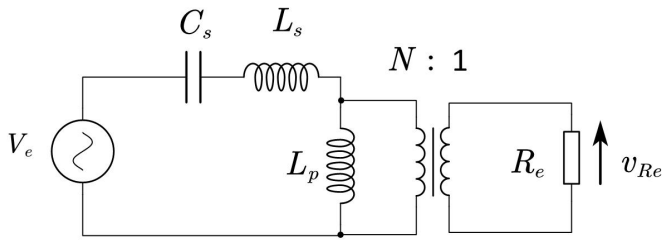

Fig. 3.6. AC equivalent circuit for the LLC resonant converter

The circuit can be further simplified by equating the equivalent load impedance R_e from the secondary side of the transformer to the primary side. The output voltage on the primary side of the transformer is Nv_R, and the output current is $\frac{1}{N} i_{\mathrm{R}}$, so the equivalent impedance of R_e on the primary side is,

$$R_{e(\mathrm{primary})} = \frac{N v_{\mathrm{R}}}{\frac{1}{N} i_{\mathrm{R}}} = N^2 R_e = \frac{8}{\pi^2} N^2 R_L \tag{3.39}$$

The transformer in Fig. 3.6 can be simplified based on (3.43) shown in Fig. 3.7

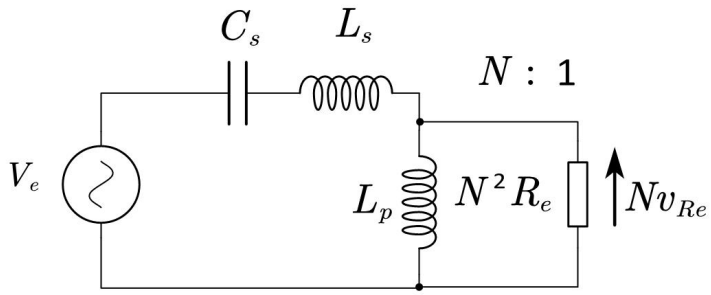

Fig. 3.7. Simplified AC equivalent circuit for the LLC converter

3.2.3 Voltage and current gain

Based on Fig. 3.7, the equivalent input voltage for the FMA technique is V_e. Therefore, the equivalent circuit is a series combination of L_p and N^2R_e in parallel with C_s and L_s, with the total circuit impedance denoted as,

$$Z_\mathrm{tot} = sL_s + 1/sC_s + sL_p||N^2R_e \tag{3.40}$$

Therefore, the voltage ratio across the equivalent load voltage Nv_{Re} to the equivalent input voltage V corresponds to the impedance ratio of the L_p and N^2R_e parallel branch to the total circuit impedance,

$$\begin{aligned}\frac{Nv_{Re}}{V_e} &= \frac{sL_p||N^2R_e}{sL_s + 1/sC_s + sL_p||N^2R_e} \\ &= \frac{s^2C_sL_pN^2R_e}{s^3C_sL_sL_p + s^2C_sN^2R_e\left(L_s + L_p\right) + sL_p + N^2R_e}\end{aligned} \tag{3.41}$$

where $s = j\omega_{sw}$.

Afterwards, defining A as the ratio between the series inductance and the parallel inductance $A = L_p/L_s$; $\omega_0 = 2\pi f_0$ as the series resonant angular frequency, Q_L as the quality factor of the series resonant circuit $Q_L = \frac{\omega_0 L_s}{N^2 R_e} = \frac{1}{\omega_0 C_s N^2 R_e}$ thus allowing for the simplification of the (3.43),

$$\frac{v_{out}}{V_{dc}} = \frac{1}{2N} \left| \frac{\frac{s^2}{\omega_0^2} A}{\frac{s^3}{\omega_0^3} A Q_L + \frac{S^2}{\omega_0^2}(A+1) + \frac{s}{\omega_0} A Q_L + 1} \right| \tag{3.42}$$

The resonant circuit current i_{Ls}, which is another key parameter of the converter, can also be obtained from the circuit diagram Fig. 3.7,

$$i_{\mathrm{Ls}} = \frac{V_e}{z_{\mathrm{tot}}} = \frac{2V_{\mathrm{dc}}}{\pi} \frac{1}{sL_s + 1/sC_s + sL_p || N^2 R_e} \tag{3.43}$$

After that, according to Fig. 3.7, the current through the equivalent load $n^2 R_e$ is equal to $\frac{1}{n} i_{\mathrm{out}}$, so the ratio between the resonant circuit current with the current through $N^2 R_e$ can be obtained from combine (3.47) and (3.41),

$$\frac{i_{\mathrm{out}}}{N i_{\mathrm{Ls}}} = \frac{2}{\pi} \left| \frac{sL_s}{sL_s + N^2 R_e} \right| = \left| \frac{\frac{s}{\omega_0} Q_L}{\frac{s}{\omega_0} Q_L + 1} \right| \tag{3.44}$$

Varying the switching frequency f_{sw}, (3.46) provides the steady-state output voltage response. And (3.48) provides the steady-state output current response. Define $M_{\mathrm{out}} = N v_{\mathrm{out}}/V_{\mathrm{dc}}$ as the output voltage gain normalised by the DC input voltage, and $J_{\mathrm{out}} = i_{\mathrm{out}}/N i_{\mathrm{Ls}}$ as the output current gain normalised by the resonant current. The waveforms of M_{out} and J_{out} can be plotted for different ranges of values of A and Q_L, which are shown in Fig. 3.8 and Fig. 3.9.

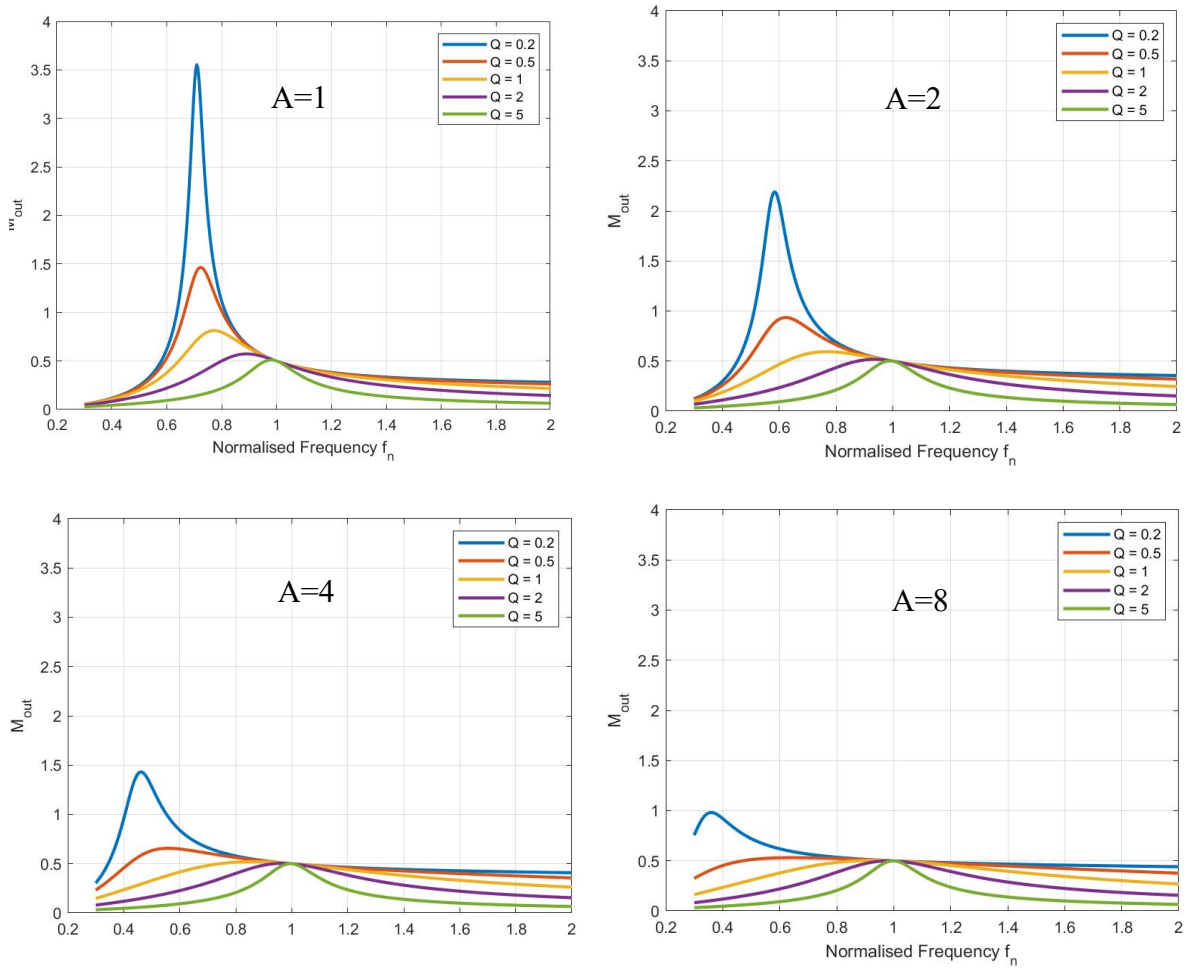

Fig. 3.8. Normalised voltage gain M_{out} control response waveform for different design points

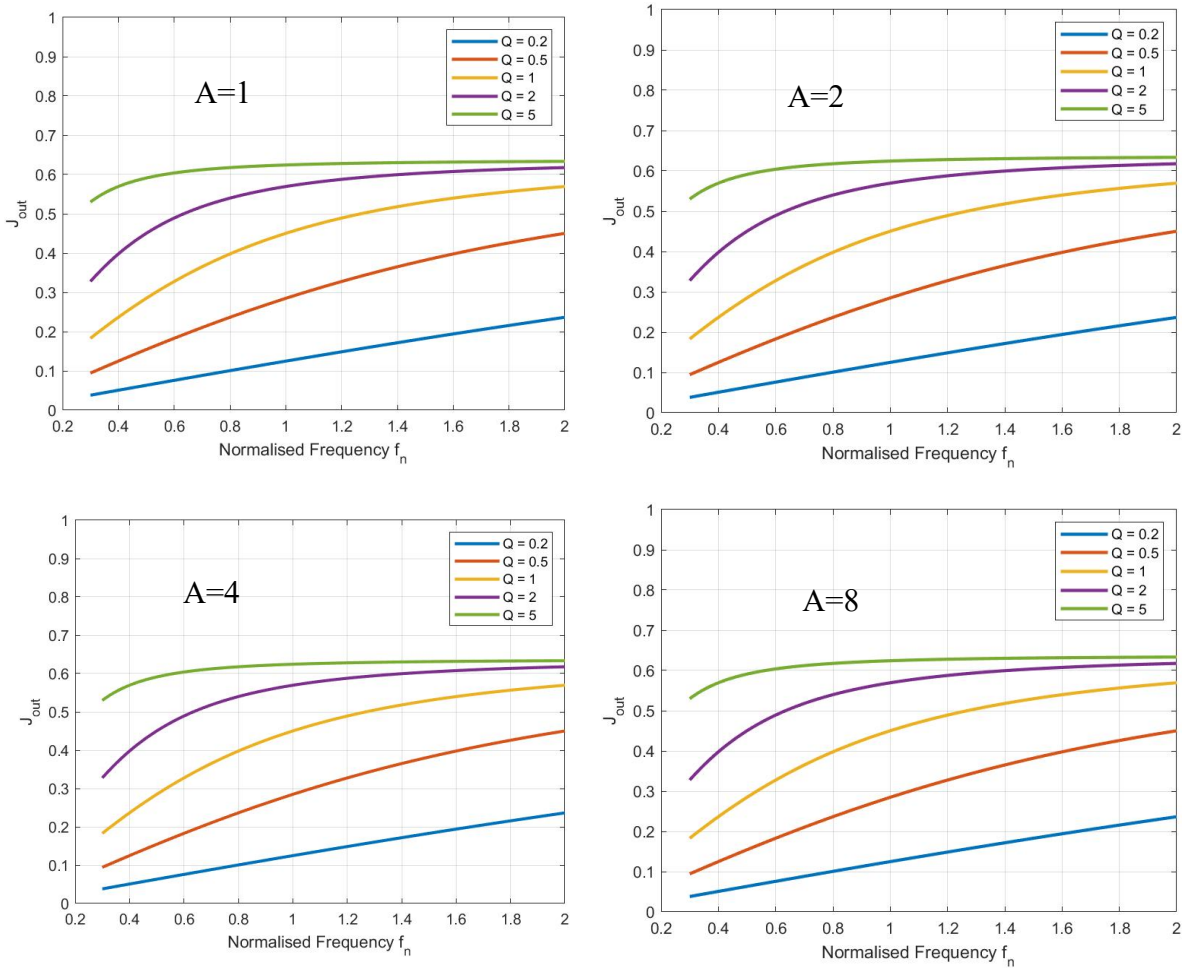

Fig. 3.9. Normalised current gain J_{out} control response waveform for different design points

The first step in the design process focuses on the load-independent point. Given the input and output voltages, the voltage gain at this point can be determined using the formula $\frac{v_{\text{out}}}{V_{\text{dc}}} = \frac{1}{2N}$. This equation is instrumental in establishing the transformer's turns ratio.

In the selection of converter components, utilizing an integrated magnetic component can reduce the number of individual components. In this setup, series and parallel inductors are realized through the transformer's leakage inductance and magnetizing inductance, respectively. However, this approach constrains the achievable ratio of series to parallel inductance, which typically ranges $A = 3$ to 5.

Subsequently, based on (3.46) and (3.48), a suitable combination of A and Q_L is determined to maximize J_{out} for minimal circulating current while also achieving M_{out}. Finally, the switching frequency f_{sw}, along with A and Q_L, dictates the values of the converter's components.

3.3 Methodology for designing class EF_2 inverters

3.3.1 Operation analysis

The design process is based on several assumptions:

1. The switch is an ideal switch, which means the switch time for the switch between turning on and turning off is zero. This also means that the resistance of the switch is infinite when the switch is off, and the resistance is zero when the switch is on.
2. Other components in the circuit are ideal, which means the average input power is equal to the output power.
3. The load quality factor of the LCR series branch is large enough to ensure the current through the load is sinusoidal ($Q_L = \frac{\omega_{\text{sw}} L_{\text{s}}}{R_L} > 5$)
4. The input inductor is an infinite inductor, which means the fluctuation of the input current is extremely low and the input current can be seen as a DC.
5. The resonant frequency f_{o2} of the auxiliary resonant branch, given by $f_{\text{o2}} = \frac{1}{2\pi\sqrt{L_{\text{m}} C_{\text{m}}}}$, is twice the operational frequency f_{sw}.

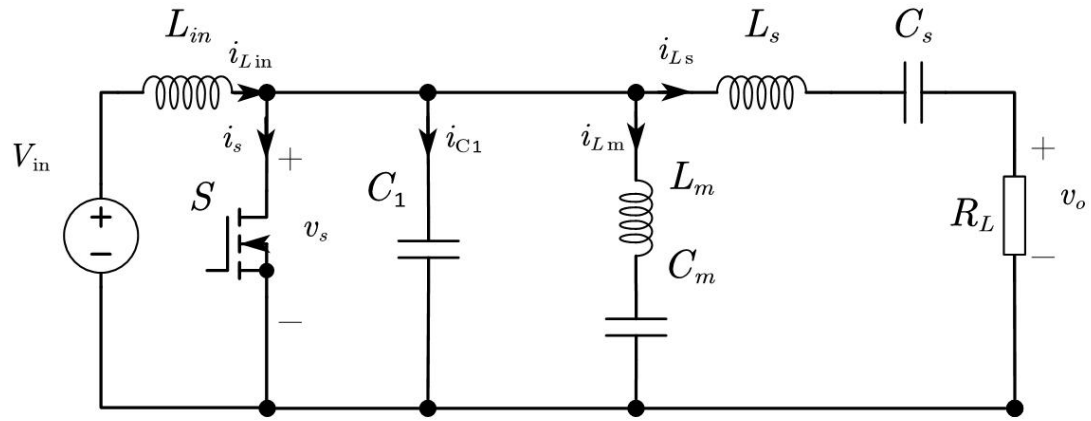

Fig. 3.10. Circuit diagram of the class EF_2 inverter

The circuit diagram of the class EF_2 inverter is shown in Fig. 3.10. In the operation of class EF_2 inverters, defined δ is the duty ratio when the switch is turned on. The analysis method for this part is similar to the one conducted by Aldhaher *et al.*,, as referenced in [3.5]. According to the circuit configurations, when the switch is turned on, the current flow through the switch is,

$$i_{\mathrm{s}}(\omega_{\mathrm{sw}}t) = i_{\mathrm{Lin}} - i_{\mathrm{Lm}}(\omega_{\mathrm{sw}}t) - i_{\mathrm{Ls}}(\omega_{\mathrm{sw}}t) \quad 0 < \omega_{\mathrm{sw}}t < 2\pi\delta \tag{3.45}$$

Defined the current through the series resonant circuit is,

$$i_{\mathrm{Ls}}(\omega_{\mathrm{sw}}t) = i_{\mathrm{m}} \sin(\omega_{\mathrm{sw}}t + \phi) \tag{3.46}$$

Where i_{m} is defined as the magnitude of series resonant current and ϕ represents its phase, which will be determined later based on the boundary condition equations.

q_1 is defined as the ratio between the resonant frequency of $L_{\mathrm{m}}C_{\mathrm{m}}$ combination and the operation frequency of the inverter; in this inverter, the ratio is 2.

$$q_1 = \frac{1}{\omega_{\mathrm{sw}}\sqrt{L_{\mathrm{m}}C_{\mathrm{m}}}} = 2 \tag{3.47}$$

The ratio between the input current and the current flowing through the auxiliary resonant branch $L_{\mathrm{m}}C_{\mathrm{m}}$ is defined as,

$$\frac{i_{\mathrm{Lm}}}{i_{\mathrm{Lin}}}(\omega_{\mathrm{sw}}t) = A_1\cos(q_1\omega_{\mathrm{sw}}t) + B_1\sin(q_1\omega_{\mathrm{sw}}t) \qquad 0 < \omega_{\mathrm{sw}}t < 2\pi\delta \qquad (3.48)$$

where the coefficients A_1 and B_1 will also be determined later based on the boundary condition equations.

Then during $2\pi\delta \le \omega_{\mathrm{sw}}t < 2\pi$ the switch is turned off and hence i_S become zero. The auxiliary resonant branch current become to,

$$\begin{aligned} & i_{\mathrm{Lm}}(\omega_{\mathrm{sw}}t) = i_{\mathrm{Lin}} - i_{\mathrm{Ls}}(\omega_{\mathrm{sw}}t) - i_{\mathrm{C1}}(\omega_{\mathrm{sw}}t) \\ & = i_{\mathrm{Lin}} - i_{\mathrm{m}}\sin(\omega_{\mathrm{sw}}t + \phi) - \omega_{\mathrm{sw}}C_1\frac{\mathrm{d}v_{C1}}{\mathrm{d}\omega_{\mathrm{sw}}t} \end{aligned} \qquad (3.49)$$

The voltage across auxiliary resonant branch is equal to the voltage across shunt capacitor v_{C1} can be represented by,

$$\begin{aligned} & v_{C1}(\omega_{\mathrm{sw}}t) \\ & = \omega_{\mathrm{sw}}L_m\frac{\mathrm{d}i_{Lm}(\omega_{\mathrm{sw}}t)}{\mathrm{d}\omega_{\mathrm{sw}}t} + \frac{1}{\omega_{\mathrm{sw}}C_2}\int_{2\pi\delta}^{\omega_{\mathrm{sw}}t} i_{\mathrm{Lm}}(\omega_{\mathrm{sw}}t)\,\mathrm{d}\omega_{\mathrm{sw}}t + v_{C1}(2\pi\delta) \end{aligned} \qquad (3.50)$$

So, the derivative of $v_{C1}(\omega_{\mathrm{sw}}t)$ can be written as,

$$\frac{dv_{C1}(\omega_{\mathrm{sw}}t)}{\mathrm{d}\omega_{\mathrm{sw}}t} = \omega_{\mathrm{sw}}L_{\mathrm{m}}\frac{\mathrm{d}^2i_{\mathrm{Lm}}(\omega_{\mathrm{sw}}t)}{\mathrm{d}^2\omega_{\mathrm{sw}}t} - \frac{1}{\omega_{\mathrm{sw}}C_2}i_{\mathrm{Lm}}(\omega_{\mathrm{sw}}t) \qquad (3.51)$$

Combining (3.53) and (3.55) gives the ratio of the input current to the current through the $L_{\mathrm{m}}C_{\mathrm{m}}$ branch,

$$\begin{aligned} \frac{i_{\mathrm{Lm}}}{i_{\mathrm{Lin}}}(\omega_{\mathrm{sw}}t) = 1 - \frac{i_{\mathrm{m}}}{i_{\mathrm{Lin}}}\sin(\omega_{\mathrm{sw}}t + \phi) - \omega_{\mathrm{sw}}^2L_{\mathrm{m}}C_1\frac{\frac{\mathrm{d}^2i_{\mathrm{Lm}}}{i_{\mathrm{Lin}}}(\omega_{\mathrm{sw}}t)}{\mathrm{d}^2\omega_{\mathrm{sw}}t} \\ - \frac{C_1}{C_2}\frac{i_{\mathrm{Lm}}}{i_{\mathrm{Lin}}}(\omega_{\mathrm{sw}}t); \end{aligned} \qquad (3.52)$$

In order to normalise the equations, define,

$$k = \frac{C_1}{C_{\mathrm{m}}} \qquad (3.53)$$

$$q_2 = \frac{1}{\omega_{\mathrm{sw}}}\sqrt{\frac{C_1 + C_{\mathrm{m}}}{L_{\mathrm{m}} C_1 C_{\mathrm{m}}}} = q_1\sqrt{\frac{k+1}{k}} = 2\sqrt{\frac{k+1}{k}}; \tag{3.54}$$

$$p = \frac{1}{k+1}\frac{i_m}{i_{\mathrm{Lin}}}; \tag{3.55}$$

So, the general solution of (3.56) is,

$$\frac{i_{Lm}}{i_{Lin}}(\omega_{\mathrm{sw}}t) = A_2\cos(q_2\omega_{\mathrm{sw}}t) + B_2\sin(q_2\omega_{\mathrm{sw}}t) - \frac{q_2^2 p}{q_2^2 - 1}\sin(\omega_{\mathrm{sw}}t + \phi) + \frac{1}{k+1} \tag{3.56}$$

$$2\pi\delta \le \omega_{\mathrm{sw}}t < 2\pi$$

where the coefficients A_2 and B_2 will be determined later based on the boundary condition equations.

Assuming that the converter operates under optimum operating conditions, i.e., zero voltage switching (ZVS) and zero voltage derivative switching (ZVDS) conditions, and because the inductor current is zero under ZVS conditions; the derivative of the inductor current is zero under ZVDS conditions, and because of the property of the inductor current that does not transiently change, the following six equations can be written,

$$v_{C1}(2\pi) = 0 \tag{3.57}$$

$$i_{C1}(2\pi) = 0 \tag{3.58}$$

$$i_{\mathrm{Lm}}(2\pi\delta^-) = i_{\mathrm{Lm}}(2\pi\delta^+) \tag{3.59}$$

$$i_{\mathrm{Lm}}(0) = i_{\mathrm{Lm}}(2\pi); \tag{3.60}$$

$$\frac{\mathrm{d}i_{\mathrm{Lm}}(\omega_{\mathrm{sw}}t)}{\mathrm{d}\omega_{\mathrm{sw}}t}\Big|_{\omega_{\mathrm{sw}}t=2\pi\delta^-} = \frac{\mathrm{d}i_{\mathrm{Lm}}(\omega_{\mathrm{sw}}t)}{\mathrm{d}\omega_{\mathrm{sw}}t}\Big|_{\omega_{\mathrm{sw}}t=2\pi\delta^+}; \tag{3.61}$$

$$\frac{\mathrm{d}i_{\mathrm{Lm}}(\omega_{\mathrm{sw}}t)}{\mathrm{d}\omega_{\mathrm{sw}}t}\Big|_{\omega_{\mathrm{sw}}t=0} = \frac{\mathrm{d}i_{\mathrm{Lm}}(\omega_{\mathrm{sw}}t)}{\mathrm{d}\omega_{\mathrm{sw}}t}\Big|_{\omega_{\mathrm{sw}}t=2\pi} \tag{3.62}$$

Afterwards, it can be find from (3.52) and (3.60) that there are eight coefficients in the system of equations, namely $A_1, A_2, B_1, B_2, p, k, \delta$ and ϕ. According to (3.61)-(3.66), once the values of k and δ are established, the values of the other six unknowns can be determined.

Since the voltage across the switch $v_S(\omega_{\mathrm{sw}}t)$ does not begin to be generated until the switch turns off. the voltage across the switch v_{S} is equal to the voltage across the capacitor C_1 during the period when the switch is turned off is,

$$v_{\mathrm{S}}(\omega_{\mathrm{sw}}t) = v_{\mathrm{C1}}(\omega_{\mathrm{sw}}t) = \frac{1}{\omega_{\mathrm{sw}}C_1}\int_{2\pi\delta}^{\omega_{\mathrm{sw}}t} i_{C1}(\tau)d\tau \quad 2\pi\delta \le \omega_{\mathrm{sw}}t < 2\pi \tag{3.63}$$

The current through capacitor C_1 for the period $2\pi\delta \le \omega_{\mathrm{sw}}t < 2\pi$ is,

$$i_{\mathrm{C1}}(\omega_{\mathrm{sw}}t) = i_{\mathrm{Lin}} - i_{\mathrm{Ls}}(\omega_{\mathrm{sw}}t) - i_{\mathrm{Lm}}(\omega_{\mathrm{sw}}t) \tag{3.64}$$

The normalizing current through C_1 with respect to the input current is can be obtained by combing (3.53), (3.57) and (3.59),

$$\frac{i_{\mathrm{C1}}}{i_{\mathrm{Lin}}}(\omega_{\mathrm{sw}}t) = 1 - p(k+1)\sin(\omega_{\mathrm{sw}}t + \phi) - \frac{i_{Lm}}{i_{\mathrm{Lin}}}(\omega_{\mathrm{sw}}t) \tag{3.65}$$

To normalise the parameters, define,

$$\beta(\omega_{\mathrm{sw}}t) = \int_{2\pi\delta}^{\omega_{\mathrm{sw}}t} \frac{i_{C1}}{i_{\mathrm{Lin}}}(\tau)d\tau \tag{3.66}$$

Then substituted (3.70) into (3.67) could get,

$$\begin{aligned} v_S(\omega_{\mathrm{sw}}t) = v_{C1}(\omega_{\mathrm{sw}}t) &= \frac{i_{\mathrm{Lin}}}{\omega_{\mathrm{sw}}C_1}\int_{2\pi\delta}^{\omega_{\mathrm{sw}}t} \frac{i_{C1}}{i_{\mathrm{Lin}}}(\tau)d\tau \\ &= \frac{i_{\mathrm{Lin}}}{\omega_{\mathrm{sw}}C_1}\beta(\omega_{\mathrm{sw}}t) \quad 2\pi\delta \le \omega_{\mathrm{sw}}t < 2\pi \end{aligned} \tag{3.67}$$

The cyclic average value of switch voltage v_s is equal to the input voltage V_{in},

$$V_{\text{in}} = \frac{i_{\text{Lin}}}{2\pi\omega_{\text{sw}}C_1}\int_{2\pi\delta}^{2\pi}\beta(\omega_{\text{sw}}t)d\omega_{\text{sw}}t \tag{3.68}$$

So the ratio between switch voltage with input voltage at $2\pi\delta \leq \omega_{\text{sw}}t < 2\pi$ can be obtained by combing (3.71) and (3.72),

$$\frac{v_S(\omega_{\text{sw}}t)}{V_{\text{in}}} = \frac{2\pi\beta(\omega_{\text{sw}}t)}{\int_{2\pi\delta}^{2\pi}\beta(\omega_{\text{sw}}t)\text{d}\omega_{\text{sw}}t} \tag{3.69}$$

By using (3.49), (3.50) and (3.52) and simplifying parameters p and k, the switching current i_s can be normalized to the input current i_{Lin} during $0 < \omega_{\text{sw}}t < 2\pi\delta$,

$$\begin{aligned}\frac{i_s(\omega_{\text{sw}}t)}{i_{\text{Lin}}} &= 1 - p(k+1)\sin(\omega_{\text{sw}}t + \phi) \\ &\quad - (A_1\cos(q_1\omega_{\text{sw}}t) + B_1\sin(q_1\omega_{\text{sw}}t))\end{aligned} \tag{3.70}$$

The periodic average value of the switch current i_s equals the DC input current i_{Lin}, thus

$$\frac{1}{2\pi}\int_0^{2\pi\delta}\frac{i_s(\omega_{\text{sw}}t)}{i_{\text{Lin}}}\text{d}\omega_{\text{sw}}t = 1 \tag{3.71}$$

Then combine (3.74) and (3.75) gives,

$$\begin{aligned}&\frac{p}{2\pi}(\cos(2\pi\delta + \phi) - cos\phi)(k+1) + \delta \\ &\qquad = \frac{1}{2\pi q_1}(A_1\sin(2\pi\delta q_1) + 2B_1\sin^2(\pi\delta q_1))\end{aligned} \tag{3.72}$$

Rearrange (3.76) gives,

$$p = \frac{2\pi(1-\delta) + \frac{A_1}{q_1}\sin(2\pi\delta q_1) + \frac{2B_1}{q_1}\sin^2(\pi\delta q_1)}{(k+1)(\cos(2\pi\delta + \phi) - cos\phi)} \tag{3.73}$$

Substituting (3.59) for (3.77) gives

$$\frac{i_{\text{m}}}{i_{\text{Lin}}} = \frac{2\pi(1-\delta) + \frac{A_1}{q_1}\sin(2\pi\delta q_1) + \frac{2B_1}{q_1}\sin^2(\pi\delta q_1)}{(\cos(2\pi\delta + \phi) - cos\phi)} \tag{3.74}$$

For the output power, based on the assumption of an ideal component, the output power is equal to the input power, i.e.,

$$V_{\text{in}} i_{\text{Lin}} = \frac{1}{2} i_{\text{m}}^2 R_{\text{L}} \tag{3.75}$$

Rearrange (3.79),

$$\frac{V_{\text{in}}}{i_{\text{Lin}}} = R_{\text{DC}} = \frac{1}{2}\left(\frac{i_{\text{m}}}{i_{\text{Lin}}}\right)^2 R_{\text{L}} \tag{3.76}$$

So, the load resistance value is given by substitute (3.78) into (3.80),

$$R_L = 2\left(\frac{i_{\text{Lin}}}{i_{\text{m}}}\right)^2 \frac{V_{\text{in}}^2}{P_{\text{out}}} \tag{3.77}$$

3.3.2 Operation condition determination

Given the converter's requirements, it is typically necessary to achieve maximum power output while minimizing switching current stress and switching voltage stress. This goal corresponds to the maximum output power capability point. As k and δ are adjustable variables, this optimal power capability point can be identified by varying these two parameters. Assuming ideal converter components, the output power equates to the input power, $P_{\text{out}} = V_{\text{in}} i_{\text{Lin}}$. The output power capability, denoted as C_p, is defined as follows:

$$C_p = \frac{V_{\text{in}} i_{\text{Lin}}}{v_{C1(\max)} i_{s,(\max)}} \tag{3.78}$$

Upon the determination of the operational parameters of the converter, the values of k and δ are ascertained as two distinct variables, subsequently enabling the calculation of the converter component values. Therefore, the process of identifying the point of maximum output power capability equates to finding the combination of k and δ values under which the power coefficient C_p reaches its maximum value.

The process to determine the corresponding values of the power coefficient C_p for various combinations of k and δ can be outlined as follows: Initially, the values of k and δ are established. Subsequently, these values are substituted into (3.61) to (3.66), facilitating the derivation of the values of the remaining unknown variables $A_1, A_2, B_1, B_2, p,$ and φ. Thereafter, by employing (3.73) and (3.74), the time-domain representations of the normalized switch voltage and switch current are determined, thereby ascertaining their respective maximal values. Upon substituting these maximal values into (3.82), the value of C_p under a specific combination of k and δ can be calculated. Ultimately, by setting the range of values for δ and k, and utilizing computational software, the graphical representation of C_p across different values of k and δ can be generated.

In this analysis, due to the difficulty of the calculations, a calculation software named Maple was used to calculate the results. Maple as a complex calculation software proved to be highly efficient in the calculation task. Variation of C_p within the duty cycle range 0.35 < δ < 0.6 and k value range 0.6 < k < 1.5 as illustrated in Fig. 3.11,

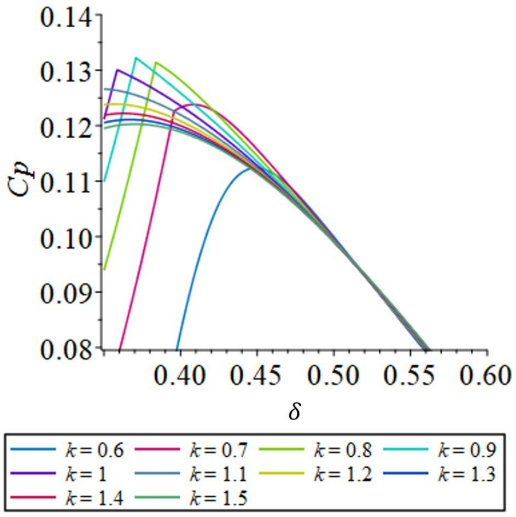

Fig. 3.11. Variation of c_p within the duty ratio δ range of 0.35 to 0.6, and k value

range of 0.6 to 1.5.

Consequently, the maximum value of C_p occurs within the range of 0.8 to 0.9 for k and 0.37 to 0.39 for δ. By refining the range of values within this interval and repeating the graphing process, a more detailed investigation into the maximal value of C_p can be conducted in Fig. 3.12,

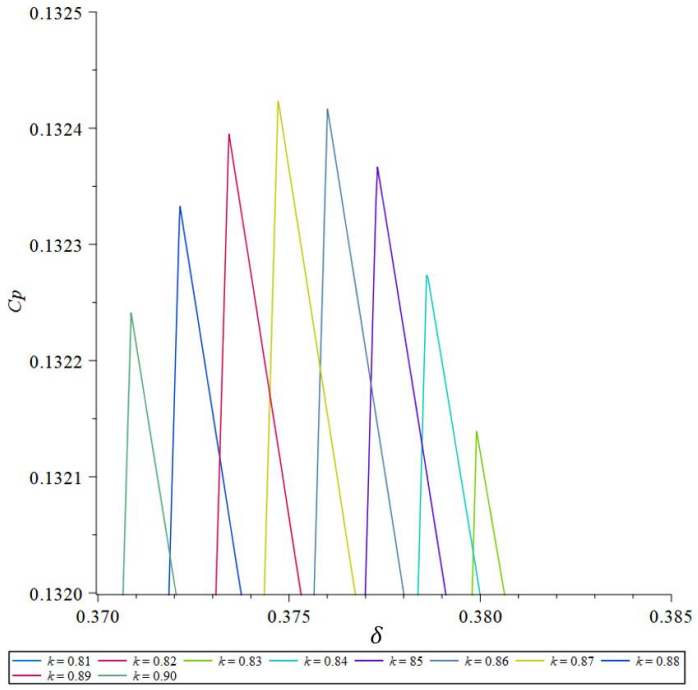

Fig. 3.12. Variation of C_p within the duty ratio δ range of 0.37 to 0.385, and k value range of 0.81 to 0.9

3.3.3 Components values determination

Through this plotting procedure, it can be deduced that at $k = 0.867$ and $\delta = 0.375$, C_p reaches its maximal value of 0.1324. Based on these values, by utilizing (3.61) to (3.66), the

specific values of the six variables A_1, A_2, B_1, B_2, p, and φ can be obtained. Subsequently, the normalized values of v_{C1} and i_s as functions of $\omega_{sw}t$ can be derived.

$$A_1 = -0.9393951308, A_2 = -0.8589433256, B_1 = -1.240479342, \\ B_2 = -1.227583813, \phi = 2.570055984, p = 1.920369596 \quad (3.79)$$

The value of $\int_{2\pi\delta}^{2\pi} \beta(\omega_{sw}t)d\omega_{sw}t$ can be obtained from combine (3.60) (3.69) (3.70) and (3.83)

$$\int_{2\pi\delta}^{2\pi} \beta(\omega_{sw}t)d\omega_{sw}t = 5.3241 \quad (3.80)$$

The normalised time-domain waveform of converter's switch currents based on input currents $\frac{i_s(\omega_{sw}t)}{i_{Lin}}$ can be derived by substituting (3.83) into (3.74). Similarly, the normalized time-domain waveform of the converter's switch voltages, based on input voltages $\frac{v_s(\omega_{sw}t)}{V_{in}}$ can be obtained by substituting (3.69), (3.70) and (3.83) into (3.73). The waveform of these is shown in Fig. 3.13.

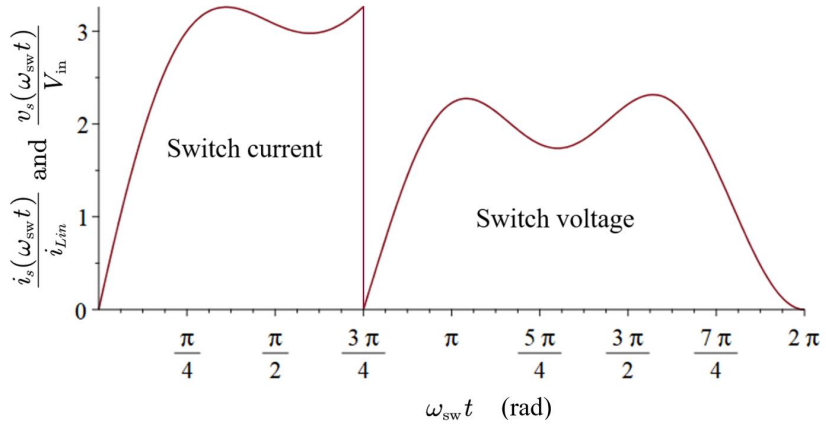

Fig. 3.13. Normalised time-domain switch current and switch voltage waveform at maximum c_p

Afterwards, substituting (3.84) into (3.72) yields,

$$V_{\text{in}} = 5.3241 \frac{i_{\text{Lin}}}{2\pi\omega_{\text{sw}} C_1} \tag{3.81}$$

Substituting (3.83) into (3.59) gives the ratio of the series resonant current amplitude i_{m} to the input current i_{Lin},

$$\frac{i_{\text{m}}}{i_{\text{Lin}}} = 3.58533 \tag{3.82}$$

Thus, combining (3.81) and (3.86) gives,

$$\frac{V_{\text{in}}}{i_{\text{Lin}}} = R_{\text{DC}} = 6.4273 R_L = \frac{5.3241}{2\pi\omega C_1} \tag{3.83}$$

Given that the converter operates under an inductive load condition, to determine the values of the components in the series resonant part, it is defined that L_R is the value of the residual impedance, is as follows:

$$\omega L_R = \frac{v_R}{i_{\text{m}}} \tag{3.84}$$

where v_R is the amplitude of the voltage across the residual impedance is equal to,

$$v_R = \frac{1}{\pi} \int_{2\pi\delta}^{2\pi} v_S \cos(\omega_{\text{sw}} t + \phi)\, d\omega_{\text{sw}} t \tag{3.85}$$

To obtain the normalised voltage across the residual impedance substituting (3.70), (3.84) and (3.89) into (3.73) gives,

$$\frac{v_R}{V_{\text{in}}} = \frac{2 \int_{0.75\pi}^{2\pi} \beta(\omega_{\text{sw}} t) \cos(\omega_{\text{sw}} t + \phi)\, d\omega_{\text{sw}} t}{\int_{0.75\pi}^{2\pi} \beta(\omega_{\text{sw}} t)\, d\omega_{\text{sw}} t} \tag{3.86}$$

Substituting (3.83) and (3.84) into (3.90) yields,

$$\frac{v_R}{V_{\text{in}}} = 1.1346 \tag{3.87}$$

Sub

stituting (3.91) , (3.80) and (3.86) into (3.88) gives,

$$\frac{\omega L_R}{R_L} = 2.0339 \tag{3.88}$$

So, the value of $\omega_{sw} R_L C_s$ is,

$$\omega_{sw} R_L C_s = \frac{1}{Q_L - 2.0339} \tag{3.89}$$

The value of L_s is based on the load quality factor of the $L_s C_s R_L$ branch, which is,

$$L_s = \frac{Q_L R_L}{\omega_{sw}} \tag{3.90}$$

Substituting (3.86) into (3.81) gives the relationship between load and input voltage and output power [3.5],

$$R_L = 0.156 \frac{V_{\text{in}}^2}{P_{\text{out}}} \tag{3.91}$$

In the design process of a class EF_2 inverter, the first step is to obtain the inverter's working parameters. With these parameters, the input inductor L_{in} can be calculated. Subsequently, the load resistance value can be ascertained using these working parameters and (3.95). Once the load resistance value is known, (3.85) can be used to calculate the value of shunt capacitor C_1. The parameter k is then used to deduce the value of C_m. Following this, the value of L_m can be calculated based on the q_1. Finally, the values of C_s and L_s can be determined using (3.93) and (3.94), respectively. This sequence of calculations and parameter assessments enables the effective design of the class EF_2 inverter.

3.4 Conclusion

This Chapter provides a detailed discussion of the design rationale and processes for the boost converter, LLC converter, and class EF_2 inverter. The design approach for the boost

converter is analysed using steady-state analysis. This is followed by an examination of the LLC converter with Fundamental Mode Analysis, Finally, an evaluation of the class EF_2 inverter using the transfer function method.

The analysis provided methods for determining the values of components in the three types of converters, serving as a reference for the design in subsequent Chapters. Meanwhile, the assumptions these methods make about the converter's operating behaviours during analysis highlight their limitations. This justifies the use of cyclic-mode modelling techniques for further analysis.

3.5 References

[3.1] Kazimierczuk, Marian K. Pulse-width modulated DC-DC power converters. John Wiley & Sons, 2015, https://doi.org/10.1002/9780470694640.

[3.2] Beiranvand, Reza, et al. “Using LLC Resonant Converter for Designing Wide-Range Voltage Source.” *IEEE Transactions on Industrial Electronics*, vol. 58, no. 5, May 2011, pp. 1746–56. https://doi.org/10.1109/tie.2010.2052537.

[3.3] M. J. C. S. Reis, S. Soares, S. Cardeal, R. Morais, E. Peres and P. J. S. G. Ferreira, "Teaching of Fourier series expansions in undergraduate education," *2013 IEEE Global Engineering Education Conference (EDUCON)*, Berlin, Germany, 2013, pp. 431-435, https://doi.org/10.1109/educon.2013.6530141.

[3.4] Martin P., et al. “Analysis of CLL Voltage-Output ResonantConverters Using Describing Functions.” *IEEE Transactions on Power Electronics*, vol. 23, no. 4, July 2008, pp. 1772–81. https://doi.org/10.1109/tpel.2008.924835.

[3.5] S. Aldhaher, D. C. Yates and P. D. Mitcheson, "Modeling and Analysis of Class EF and Class E/F Inverters With Series-Tuned Resonant Networks," *IEEE Transactions on Power Electronics*, vol. 31, no. 5, pp. 3415-3430, May 2016, https://doi.org/10.1109/tpel.2015.2460997.

Chapter 4. Cyclic-mode modelling of class EF_2 inverters featuring a piezoelectric resonator as the auxiliary network

This Chapter begins by introducing the process of cyclic-mode modelling. By integrating the Mason equivalent model of the piezoelectric resonator (PR) with cyclic-mode modelling, we have constructed a cyclic-mode model for a class EF_2 inverter operating under optimal conditions, with PR as its auxiliary resonant branch. The model's accuracy and the feasibility of replacing traditional auxiliary branches with a PR are validated through comparisons with SPICE simulations and experimental tests.

4.1 Introduction

In class EF inverters, an auxiliary series LC branch is connected in parallel with the switch. Through precise design, the resonant frequency of the auxiliary LC circuit is tuned to reduce the peak switch voltage compared to the traditional class E inverter. Aldhaher *et al.,* in [4.2], discerned optimal performance in the class EF_2 inverter, wherein the resonant frequency of the auxiliary branch is doubled in comparison to the inverter operating frequency. This design adaptation results in a reduction of the switch voltage from 3.5 times the power supply voltage, as seen in class E inverters, to 2.1 times the power supply voltage in the class EF_2 inverter. However, it is important to acknowledge that the improved performance comes at the cost of greater volume and complexity.

Piezoelectric resonating devices offer an alternative to traditional discrete component LC resonant networks. Piezoelectric transformers (PTs) have garnered popularity over the years, particularly in ionizing and cold-cathode fluorescent backlighting applications, as described in [4.3]. When compared with magnetic materials, PTs exhibit several advantages including improved power density, approximately $40\ \mathrm{W}/cm^3$ as indicated in [4.4], which, under similar power transmission conditions, usually translates to a reduction in volume owing to the absence of copper windings. The usage of PTs not only markedly decreases copper usage

in manufacturing but also allows for a higher voltage transformation ratio than that of magnetic transformers. Recent innovations include DC-DC power supply circuits that integrate a piezoelectric resonator (a one-port PT) within the resonant circuit, improving energy transfer efficiency as highlighted in [4.5]. The class EF_2 inverter, which utilizes a piezoelectric resonator in its auxiliary circuit, is detailed in [4.6].

The cyclic-mode model is a time-domain model used in state-space systems to determine the steady-state values of state variables [4.7]. This gives a theoretical framework for analysing and explaining periodic phenomena and can be used to simulate converters with DC inputs under steady-state operation. Although this representation may appear similar to the sampled-data model by Kassikian [4.8], it differs significantly. The cyclic-mode model method employs matrix augmentation to incorporate the necessary integration for input response evaluation directly into the matrix exponential, as shown in equation (4.2), resulting in a more succinct representation. This approach ensures precise determination of the initial cyclic-mode condition $\boldsymbol{x}(t_0)$, without any approximation. Foster *et al*., in references[4.9] and [4.10], applied cyclic-modelling to LCC and LLC resonant converters, illustrating its use in non-hard-switched converters.

4.2 Cyclic-mode modelling process

The cyclic-mode modelling of converters begins with the derivation of the cyclic-mode modelling process, as first presented in [4.7]. A wide variety of periodically excited DC input power electronic converters can be assumed to be operating in a cyclic-mode once the start-up or disturbance transient has disappeared. Typically, a single operating cycle is decomposed into several modes depending on the conduction states of the switches and diodes. For each mode, a circuit configuration is constructed from which a system of linear equations can be determined. Thus, the operation of the DC-DC converter in the cyclic-mode is described by a piecewise linear model.

The system of linear equations during any mode can be represented in state-variable form using,

$$\dot{\boldsymbol{x}} = \boldsymbol{A}_i \boldsymbol{x} + \boldsymbol{B}_i \tag{4.1}$$

where $\boldsymbol{x} = \boldsymbol{x}(t)$ is the state vector, $\dot{\boldsymbol{x}}$ is its time derivative, $\boldsymbol{A}_i$ is a square matrix of order h representing the system dynamics and $\boldsymbol{B}_i$ is the input vector for the i^{th} mode. Equation (4.1) can be solved to provide the state vector at time t during mode i:

$$\boldsymbol{x} = \exp\left(\boldsymbol{A}_i \cdot (t - t_0)\right) \boldsymbol{x}(t_0) + \int_{t_0}^{t} \exp\left(\boldsymbol{A_i} \cdot (t - \tau)\right) \boldsymbol{B}_i d\tau \tag{4.2}$$

where $\exp(\cdots)$ is the matrix exponential and $\boldsymbol{x}(t_{i-1})$ represents the state vector at the end of mode $i-1$ therefore $\boldsymbol{x}(t_{i-1}^{+})$ is the initial condition vector for the mode i. The + superscript used for the mode start time is used where state-variables exhibit discontinuous values between modes such as instantaneous capacitor voltage jumps due to switch commutations.

Since the input to the converter is constant (DC), $\boldsymbol{B}_i$ is constant and, therefore, (4.2) can be evaluated at the end of any mode i as,

$$\boldsymbol{x}(t_i) = \boldsymbol{\Phi}_i \boldsymbol{x}(t_{i-1}) + \boldsymbol{\Gamma}_i \tag{4.3}$$

$$\boldsymbol{\Phi}_i = \exp\left(\boldsymbol{A}_i(\boldsymbol{t}_i - \boldsymbol{t}_{i-1})\right) = \exp\left(\boldsymbol{A}_i \delta_i T_{\text{sw}}\right) \tag{4.4}$$

$$\boldsymbol{\Gamma}_i = \boldsymbol{A}_i^{-1}[\boldsymbol{\Phi}_i - \boldsymbol{I}]\boldsymbol{B}_i \tag{4.5}$$

where t_i is the time at the end of the i^{th} mode. For simplicity, $t_i - t_{i-1}$ may be formulated as $\delta_i T_{\text{sw}}$ where δ_i is the duty of mode i and T_{sw} is the switching period. $\boldsymbol{I}$ is $h \times h$ identity matrix.

According to (4.3) to (4.5) and assuming a cycle consists of m modes, then the state vector at the end of the cycle ($t = T_{\text{sw}}$) can be determined by cascading solutions for each mode as follows,

$$\boldsymbol{x}(T_{sw}) = \boldsymbol{\Phi}_{\text{tot}} \boldsymbol{x}(t_0) + \boldsymbol{\Gamma}_{\text{tot}} \tag{4.6}$$

where

$$\boldsymbol{\Phi}_{\text{tot}} = \prod_{j=0}^{m-1} \boldsymbol{\Phi}_{m-j}, \boldsymbol{\Gamma}_{\text{tot}} = \sum_{i=1}^{m-1} \left(\left(\prod_{j=0}^{m-i-1} \boldsymbol{\Phi}_{m-j} \right) \boldsymbol{\Gamma}_i \right) + \boldsymbol{\Gamma}_m \tag{4.7}$$

Since, by the definition of a cyclic-mode, the final condition must be equal to the initial state,

$$\boldsymbol{x}(t_0) = \boldsymbol{x}(t_0 + \mathrm{T_{sw}}) \tag{4.8}$$

Thus, if the mode sequence and mode durations are known a priori, then the cyclic-mode initial conditions can be found by applying (4.8) to (4.6) and solving , giving

$$\boldsymbol{x}(t_0) = [\boldsymbol{I} - \boldsymbol{\Phi}_{\text{tot}}]^{-1} \boldsymbol{\Gamma}_{\text{tot}} \tag{4.9}$$

To simplify the analysis process, explicit integration evaluation can be avoided by constructing the augmented system matrix $\widehat{\boldsymbol{A}}_i$ as described in the introduction.

$$\frac{\mathrm{d}}{\mathrm{dt}} \hat{\boldsymbol{x}} = \hat{\boldsymbol{A}}_i \hat{\boldsymbol{x}} \qquad t_{i-1} \leq t \leq t_i \tag{4.10}$$

where

$$\hat{\boldsymbol{x}} = \left[\frac{\boldsymbol{x}(t)}{1} \right], \hat{\boldsymbol{A}}_i = \left[\begin{array}{c|c} \boldsymbol{A}_i & \boldsymbol{B}_i \\ \hline \boldsymbol{0} & 0 \end{array} \right] \tag{4.11}$$

where $\boldsymbol{0}$ is the $1 \times h$ zero matrix.

Equation (4.10) and the corresponding mode duty cycle can be solved for $\widehat{\boldsymbol{x}}(t_i)$, given by,

$$\hat{\boldsymbol{x}}(t_i) = \hat{\boldsymbol{\Phi}}_i \hat{\boldsymbol{x}}(t_{i-1}) \tag{4.12}$$

$$\hat{\boldsymbol{\Phi}}_i = \left[\begin{array}{c|c} \boldsymbol{\Phi}_i & \boldsymbol{\Gamma}_i \\ \hline \boldsymbol{0} & 1 \end{array} \right] = \exp\left(\hat{\boldsymbol{A}}_i \delta_i T_{sw} \right) \tag{4.13}$$

This approach combines the calculation of $\boldsymbol{\Phi}$ and $\boldsymbol{\Gamma}$ into a single matrix integral, thus simplifying the modelling and analysis process. Similarly, the calculation of $\boldsymbol{\Phi}_{\text{tot}}$ and $\boldsymbol{\Gamma}_{\text{tot}}$ becomes simplified, given by,

$$\widehat{\boldsymbol{x}}(T_{\text{sw}}) = \widehat{\boldsymbol{\Phi}}_{\text{tot}} \widehat{\boldsymbol{x}}(t_0) \tag{4.14}$$

$$\hat{\boldsymbol{\Phi}}_{\text{tot}} = \left[\begin{array}{c|c} \boldsymbol{\Phi}_{\text{tot}} & \boldsymbol{\Gamma}_{\text{tot}} \\ \hline \boldsymbol{0} & 1 \end{array} \right] = \prod_{j=0}^{m-1} \hat{\boldsymbol{\Phi}}_{m-j} \tag{4.15}$$

At to this point, $\boldsymbol{\Phi}_{\text{tot}}$ and $\boldsymbol{\Gamma}_{\text{tot}}$ can be solved by (4.7) or (4.15). Their matrices can then be substituted into (4.9) to obtain the initial values of the periods of the state variables $\boldsymbol{x}(t_0)$.

Once the cyclic-mode initial condition, $\boldsymbol{x}(t_0)$, has been found, then the values for state-vector at the end of any mode $\boldsymbol{x}(t_i)$ can get based on (4.3) and each mode duration, The state vector at any given time point, t, can then be calculated. Firstly, the duty cycle of each mode and the value of t can be employed to determine the mode in which t is located. Secondly, the value of the state vector at the end of the previous mode, combine with (4.2), enables the calculation of $\boldsymbol{x}(t)$,

$$\boldsymbol{x}(t) = \exp\left(\boldsymbol{A}_i(t - t_{i-1})\right)\boldsymbol{x}(t_{i-1}) + \int_{t_{i-1}}^{t} \exp\left(\boldsymbol{A}_i(t - \tau)\right)\boldsymbol{B}_i d\tau \qquad (4.16)$$

where t exists within mode i, (i.e., $t_{i-1} \leq t \leq t_i$) and $\boldsymbol{x}(t_{i-1})$ is the initial condition of mode i.

It is important to note that if the input to the system is not a DC input which means the value of the input matrix $\boldsymbol{B}$ is not fixed, so (4.5) will no longer hold. Consequently, the value of Γ will become difficult to compute, rendering the analysis impossible. Therefore, a key assumption for cyclic-mode modelling is that the system inputs are DC inputs.

Once the cyclic-mode model is established, determining the values of state variables at any time within a cycle requires only the knowledge of the system's mode sequence and the exact duration of each mode. Unlike SSA, this method provides exact time values instead of relying on approximations.

4.3 Operation of the class EF_2 inverter

Fig. 4.1 shows the circuit diagram of the class EF_2 inverter. Components L_s and C_s constitute the principal resonant branch, inducing a sinusoidal current flow through the load R_L. Q1, a MOSFET switch, operates at a frequency, f_{sw}, close to the resonant frequency, $f_0 = 1/(2\pi\sqrt{L_s C_s})$, of the principal resonant circuit and with duty δ_1. Input inductor L_{in}

is a filter inductor .X1 is the piezoelectric resonator with the equivalent circuit shown in Fig. 4.2. Defined v_{C0} is the shunt capacitor voltage which is equal to the switch voltage.

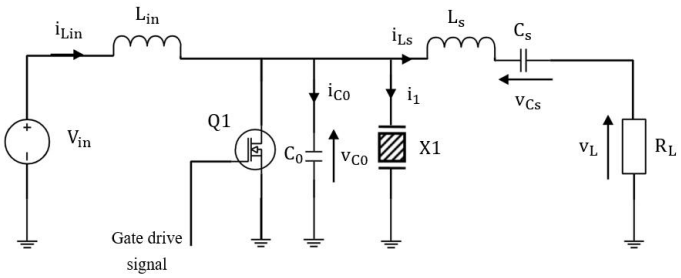

Fig. 4.1. Circuit diagram of the class EF_2 inverter which PT as auxiliary resonant branch

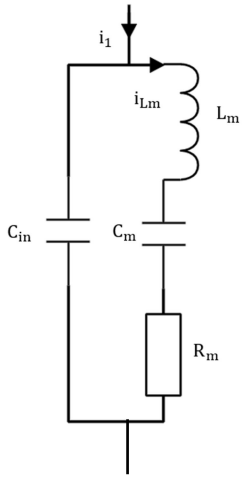

Fig. 4.2. Mason equivalent diagram of a piezoelectric transformer[4.11]

The main assumptions for the design of the EF_2 class inverter have been specified in the converter design section of Chapter 3 and will not be repeated here. With a suitable selection of switching frequency (f_{sw}) and duty cycle (δ), the inverter operates in a two-mode sequence: M1-M2-M1-M2…, as depicted in Fig. 4.3.

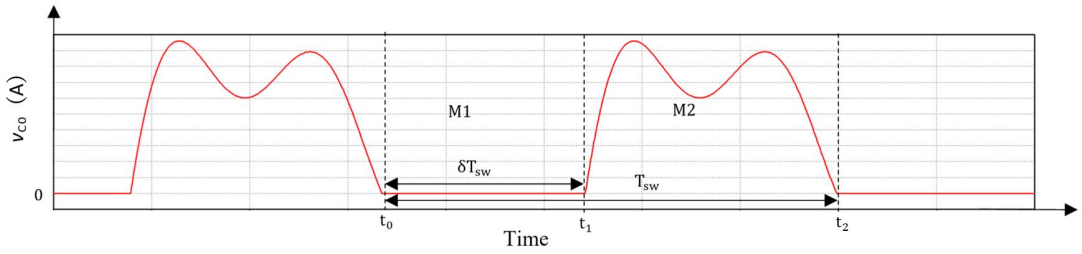

Fig. 4.3. Example of the switch voltage waveform for a class EF_2 inverter operating in 2-modes operation

We assume the switching frequency and duty cycle are selected to ensure the class EF_2 inverter operates with the two-mode operating sequence M1-M2-M1… Given that there are only two piecewise linear state-variable models per cycle, cyclic-mode analysis enables determination of the inverter's initial conditions using the control input δ. Subsequently, the value of the state variable at any point during the cycle can be accurately calculated [4.7].

4.4 Derivation of cyclic-mode model for class EF_2 inverter

In constructing the cyclic-model of the inverter, one needs to formulate first-order differential equations to describing the derivatives of the capacitor voltages and the inductor currents. Given that C_0 and C_{in} are connected in parallel, they are combined into a single equivalent capacitor C to streamline the ensuing analysis.

$$C = C_0 + C_{\text{in}} \tag{4.17}$$

Equation (4.18) to (4.23) shows a non-linear state-variable model for the class EF_2 inverter, where $h(t)$ is used to represent the switch controller,

$$\dot{i_{L\text{in}}} = \frac{V_{\text{in}}}{L_s} + (h(t) - 1)\frac{v_{\text{C}}}{L_s} \tag{4.18}$$

$$\dot{i_{Ls}} = (1 - h(t))\frac{v_{\mathrm{C}}}{L_s} - \frac{v_{\mathrm{Cs}}}{L_s} - \frac{R_{\mathrm{L}} i_{\mathrm{Ls}}}{L_s} \tag{4.19}$$

$$\dot{i_{L\mathrm{m}}} = (1 - h(t))\frac{v_{\mathrm{C}}}{L_m} - \frac{v_{C\mathrm{m}}}{L_m} - \frac{i_{L\mathrm{m}} R_{\mathrm{m}}}{L_m} \tag{4.20}$$

$$\dot{v_{\mathrm{C}}} = (1 - h(t))\frac{i_{L\mathrm{in}} - i_{L\mathrm{s}} - i_{L\mathrm{m}}}{C} \tag{4.21}$$

$$\dot{v_{\mathrm{Cs}}} = \frac{i_{Ls}}{C_s} \tag{4.22}$$

$$\dot{v_{\mathrm{Cm}}} = \frac{i_{L\mathrm{m}}}{C_{\mathrm{m}}} \tag{4.23}$$

$$h_1(t) = \begin{cases} 1 & t_0 \le t < \delta T_{sw} \\ 0 & \delta T_{\mathrm{sw}} \le t < T_{sw} \end{cases} \tag{4.24}$$

For Mode 1 (M1) $t_0 \le t < t_1$: Mode 1 (M1): $Q1$ is switched on, thus V_{in} is only applied to L_{in}. The commutation function is $h = 1$

Mode 2 (M2): $Q1$ is switched off. Current flows out of L_{in} and into C_0, the piezoelectric resonator $X1$ and the main resonant branch. The commutation functions are $h = 0$

Below is a piecewise linear model for the previously described operating sequence. This model, akin to those in references [4.9] and [4.10], was developed from the non-linear state-variable model (4.18)-(4.24), with the switch state sequence S={(1),(0)} substituted in.

$$\begin{bmatrix} \dot{i}_{Lin} \\ \dot{i}_{Ls} \\ \dot{i}_{Lm} \\ \dot{v}_C \\ \dot{v}_{Cs} \\ \dot{v}_{Cm} \end{bmatrix} = \begin{bmatrix} 0 & 0 & 0 & 0 & 0 & 0 \\ 0 & -\frac{R_L}{L_s} & 0 & 0 & -\frac{1}{L_s} & 0 \\ 0 & 0 & -\frac{R_m}{L_m} & 0 & 0 & -\frac{1}{L_m} \\ 0 & 0 & 0 & 0 & 0 & 0 \\ 0 & \frac{1}{C_s} & 0 & 0 & 0 & 0 \\ 0 & 0 & \frac{1}{C_m} & 0 & 0 & 0 \end{bmatrix} \begin{bmatrix} i_{Lin} \\ i_{Ls} \\ i_{Lm} \\ v_C \\ v_{Cs} \\ v_{Cm} \end{bmatrix} + \begin{bmatrix} \frac{V_{in}}{L_{in}} \\ 0 \\ 0 \\ 0 \\ 0 \\ 0 \end{bmatrix} \tag{4.25}$$

Equation (4.25) can be rewritten as

$$\dot{\boldsymbol{x}} = \boldsymbol{A}_1 \boldsymbol{x} + \boldsymbol{B}_1 \tag{4.26}$$

where the state-vector

$$\boldsymbol{x} = [i_{Lin}\ i_{Ls}\ i_{Lm}\ v_C\ v_{Cs}\ v_{Cm}]^T \tag{4.27}$$

M2 is like M1, except Q1 is off, $S_2 = 0$. The state-variable model for Mode 2 is,

$$\begin{bmatrix} \dot{i}_{Lin} \\ \dot{i}_{Ls} \\ \dot{i}_{Lm} \\ \dot{v}_C \\ \dot{v}_{Cs} \\ \dot{v}_{Cm} \end{bmatrix} = \begin{bmatrix} 0 & 0 & 0 & -\frac{1}{L_{in}} & 0 & 0 \\ 0 & -\frac{R_L}{L_s} & 0 & \frac{1}{L_s} & -\frac{1}{L_s} & 0 \\ 0 & 0 & -\frac{R_m}{L_m} & \frac{1}{L_m} & 0 & -\frac{1}{L_m} \\ \frac{1}{C} & -\frac{1}{C} & -\frac{1}{C} & 0 & 0 & 0 \\ 0 & \frac{1}{C_s} & 0 & 0 & 0 & 0 \\ 0 & 0 & \frac{1}{C_m} & 0 & 0 & 0 \end{bmatrix} \begin{bmatrix} i_{Lin} \\ i_{Ls} \\ i_{Lm} \\ v_C \\ v_{Cs} \\ v_{Cm} \end{bmatrix} + \begin{bmatrix} \frac{V_{in}}{L_{in}} \\ 0 \\ 0 \\ 0 \\ 0 \\ 0 \end{bmatrix} = \boldsymbol{A}_2 \boldsymbol{x} + \boldsymbol{B}_2 \tag{4.28}$$

Thus, (4.25) and (4.28) can be combined in a piecewise linear equation dependent on the mode duration times.

$$\dot{\boldsymbol{x}}(t) = \begin{cases} \boldsymbol{A}_1 \boldsymbol{x} + \boldsymbol{B}_1 & t_0 \le t < t_1 \\ \boldsymbol{A}_2 \boldsymbol{x} + \boldsymbol{B}_2 & t_1 \le t < t_2 \end{cases} \tag{4.29}$$

In the cyclic-mode of the class EF_2 inverter, the state variables' final conditions at the end of a cycle, $\boldsymbol{x}(t_2)$, must match their initial conditions, $\boldsymbol{x}(t_0)$. Thus,

$$\boldsymbol{x}(t_0) = \boldsymbol{x}(t_2) = \boldsymbol{x}(t_0 + T_{sw}) \tag{4.30}$$

Given that t_2 equals $t_0 + T_{sw}$ and beginning with $t = t_0$, the state vector at the end of Mode 1 is described as follows:

$$\boldsymbol{x}(t_1) = \boldsymbol{\Phi}_1 \boldsymbol{x}(t_0) + \boldsymbol{\Gamma}_1 \tag{4.31}$$

here $\boldsymbol{\Phi}_1 = \exp(\boldsymbol{A}_1(t_1 - t_0)) = \exp(\boldsymbol{A}_1 \delta T_{\text{sw}})$ and $\boldsymbol{\Gamma}_1 = \boldsymbol{A}_1^{-1}[\boldsymbol{\Phi}_1 - \boldsymbol{I}]\boldsymbol{B}_1$

Similarly, the state-vector at the end of Mode 2 is given by,

$$\boldsymbol{x}(t_2^-) = \boldsymbol{\Phi}_2 \boldsymbol{x}(t_1) + \boldsymbol{\Gamma}_2 \tag{4.32}$$

where $\boldsymbol{\Phi}_2 = \exp(\boldsymbol{A}_2(t_2 - t_1)) = \exp(\boldsymbol{A}_1(1 - \delta)T_{sw})$and $\boldsymbol{\Gamma}_2 = \boldsymbol{A}_2^{-1}[\boldsymbol{\Phi}_2 - \boldsymbol{I}]\boldsymbol{B}_2$.

To address a potential discontinuity at the end of Mode 2, it is ensured that $v_C(t_2)$ is set to zero if it is not already.

$$\boldsymbol{x}(t_0) = \boldsymbol{x}(t_2) = \boldsymbol{K}\boldsymbol{x}(t_2^-) \tag{4.33}$$

where,

$$\boldsymbol{K} = \begin{bmatrix} 1 & 0 & 0 & 0 & 0 & 0 \\ 0 & 1 & 0 & 0 & 0 & 0 \\ 0 & 0 & 1 & 0 & 0 & 0 \\ 0 & 0 & 0 & 0 & 0 & 0 \\ 0 & 0 & 0 & 0 & 1 & 0 \\ 0 & 0 & 0 & 0 & 0 & 1 \end{bmatrix} \tag{4.34}$$

The initial condition $\boldsymbol{x}(t_0)$ for the cyclic-mode is determined by assessing the final conditions of each mode [4.12]. Substituting (4.31) into (4.32) yields:

$$\boldsymbol{x}(t_2^-) = \boldsymbol{\Phi}_2 \boldsymbol{x}(t_1) + \boldsymbol{\Gamma}_2 = \boldsymbol{\Phi}_2 \boldsymbol{\Phi}_1 \boldsymbol{x}(t_0) + \boldsymbol{\Phi_2 \Gamma_1} + \boldsymbol{\Gamma_2} \tag{4.35}$$

Combining with (4.35) and (4.33), the result is:

$$\boldsymbol{x}(t_0) = \boldsymbol{K}[\boldsymbol{\Phi}_2 \boldsymbol{\Phi}_1 \boldsymbol{x}(t_0) + \boldsymbol{\Phi}_2 \boldsymbol{\Gamma}_1 + \boldsymbol{\Gamma_2}] \tag{4.36}$$

So,

$$\boldsymbol{x}(t_0) = [\boldsymbol{I} - \boldsymbol{K}\boldsymbol{\Phi}_2 \boldsymbol{\Phi}_1]^{-1} \boldsymbol{K}[\boldsymbol{\Phi}_2 \boldsymbol{\Gamma}_1 + \boldsymbol{\Gamma}_2] \tag{4.37}$$

Once the $\boldsymbol{x}(t_0)$ values are obtained, $\boldsymbol{x}(t_1)$ can be calculated using (4.31).

Finally, the state variable value at every time can be determined based on [4.12] ,

$$\boldsymbol{x}(t) = \begin{cases} \boldsymbol{\Phi}_1(t)\boldsymbol{x}(t_0) + \boldsymbol{\Gamma}_1(t) & t_0 \le t < t_1 \\ \boldsymbol{\Phi}_2(t)\boldsymbol{x}(t_1) + \boldsymbol{\Gamma}_2(t) & t_1 \le t < t_2 \end{cases} \tag{4.38}$$

where 1 and 2 is the mode index, $\boldsymbol{\Phi}_i(t) = \exp(\boldsymbol{A}_i(t - t_{i-1}))$ and $\boldsymbol{\Gamma}_i(t) = \boldsymbol{A}_i^{-1}[\boldsymbol{\Phi}_i(t) - \boldsymbol{I}]\boldsymbol{B}_i$.

4.5 Model validation

To validate the model presented in this Chapter, a prototype class EF_2 inverter design featuring a STEMiNC SMD25T85F234S piezoelectric resonator (PR) was developed [4.13]. The PR was characterised using an Omicron Bode 100 vector network analyser, which enabled the precise determination of the resonant frequency, identified as f_0 = 86.291 kHz. Using PR Mason equivalent circuit, a systematic approach to determined components was adopted, based on the design methodology propounded by Aldhaher, *et al*., in reference [4.2]. The switch is Infineon IRF530NPbF MOSFET and the values for the PR equivalent circuit and the class EF_2 are shown in Table 4.1.

Table 4.1. The class EF_2 inverter components values

Component's name	Component's value
R_m	4.27 Ω
L_m	8.25 mH
C_m	0.412 nF
C_{in}	1.04 nF
C_0	20 nF
L_{in}	10 mH
L_s	0.9 mH
C_s	22.8 nF
R_L	40 Ω
V_{in}	15 V

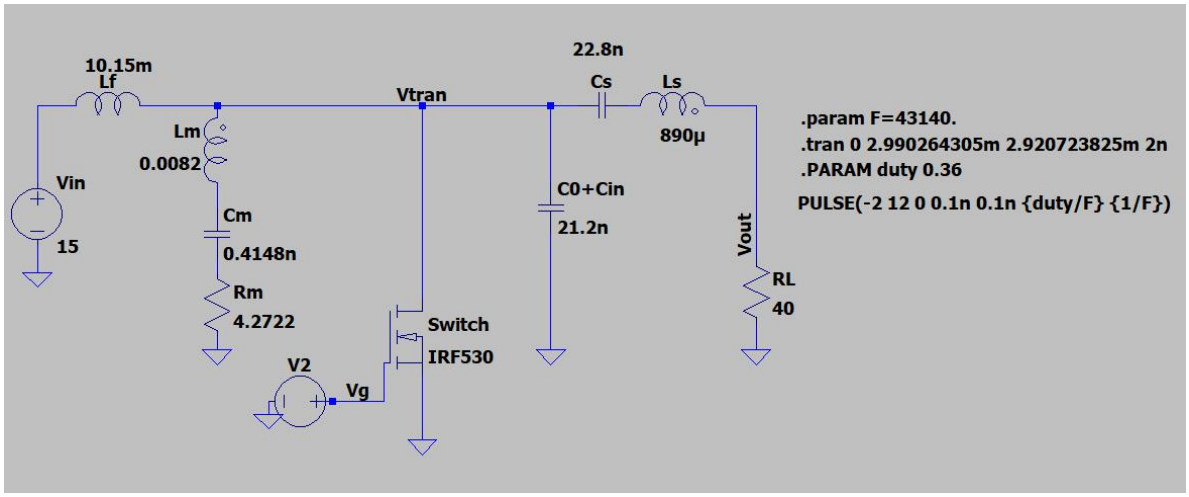

Fig. 4.4. SPICE model schematic of the class EF_2 inverter

The duty cycle and switching frequency parameters were set at $\delta = 0.36$ and f_{sw}= 43.14 kHz, respectively. The maximum time step of the SPICE model is two nanoseconds. Fig. 4.5 shows a comparative analysis of the experimental switch voltage waveform and those predicted by the SPICE and cyclic-mode models. In the figure, the experimental findings are illustrated by the solid black line, cyclic-model results by the blue dotted line, and SPICE model results by the green dotted line. The graphical representation reveals a notable similarity between the SPICE and cyclic-model waveforms, indicating a high degree of concordance between the model predictions and the SPICE simulations.

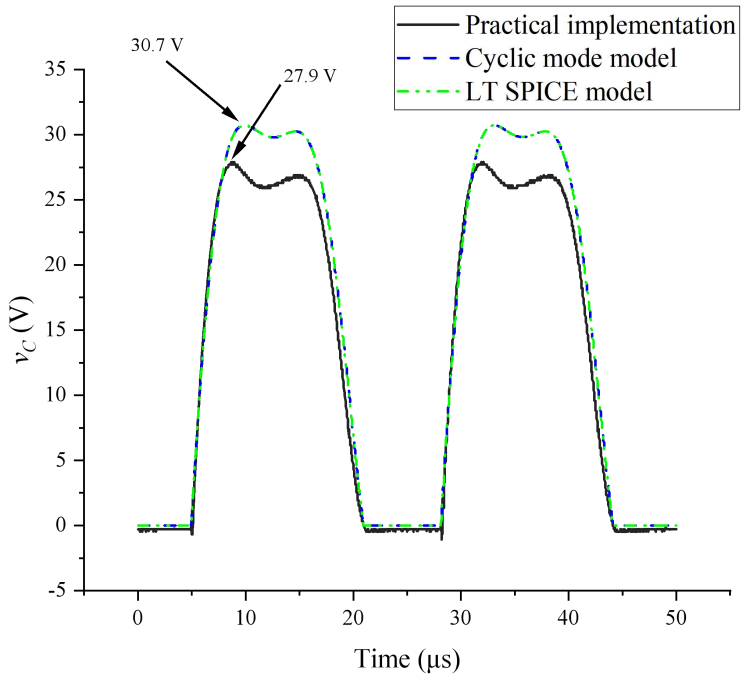

Fig. 4.5. Comparison of the switch voltage v_C waveform between the LT SPICE model, the cyclic-model, and the experimental circuit

However, there is a difference in the maximum switch voltage, the cyclic-mode model and SPICE model suggest the value of 30.7 V, while the experimental data shows a lower value of 27.9 V. This discrepancy could be due to various factors.

1. Differences Between Ideal and Actual Components: In the comparative experiment, both the SPICE model and the recurrent mode model initially used ideal components to simulate the circuit, including switches, inductors, capacitors, and wires. However, the components in the actual experimental prototype were not ideal, which could introduce discrepancies.

2. Errors from Selecting Equivalent Circuits for Piezoelectric Resonators: Piezoelectric resonators differ from traditional circuit structures and therefore do not have a unique equivalent circuit model. Common models include the Krimholtz, Leedom, and Matthaei (KLM) model, the Butterworth-van Dyke Model, and the Mason model [4.14]. For our experiments, the Mason model was chosen due to its widespread use. Nonetheless, this

model simplifies certain aspects, such as assuming material homogeneity and neglecting the frequency dependence of piezoelectric material nonlinearity. These assumptions can lead to inaccuracies in reflecting the resonator's electronic properties.

3. Measurement Errors Due to Piezoelectric Resonator Geometry: Fig. 4.6 illustrates the geometry of the piezoelectric resonator used in the experiment. Ideally, the connection point between the piezoelectric resonator and the circuit should be at the centre of the two circular bottom surfaces to closely match the equivalent circuit's performance. However, in practice, the performance is significantly affected by how the wires are welded to the resonator. An off-centre connection point during measurements also contributes to errors.

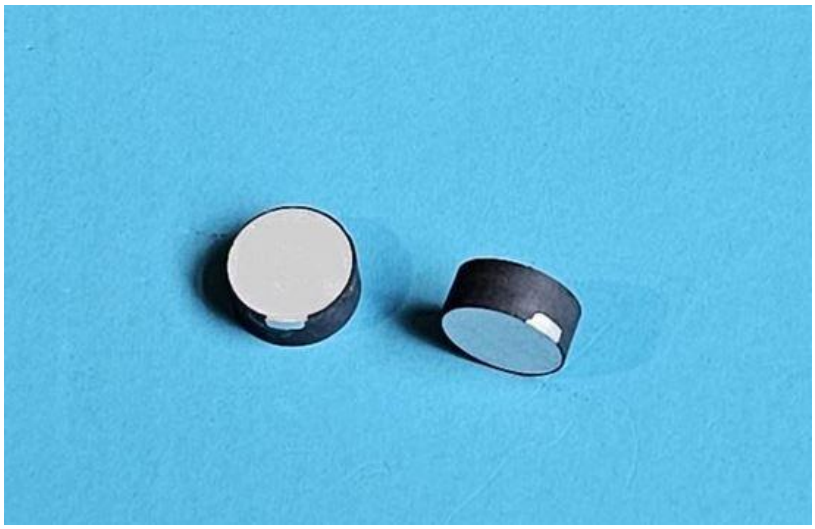

Fig. 4.6. Pictures of the piezoelectric resonator used in the experiments

Although the physical experiment results show approximately a ten percent error in the maximum switching voltage, the waveform trend of the inverter protype closely resembles that of the cyclic-mode model. Additionally, the waveform of the cyclic-mode model aligns well with that of the SPICE model. This consistency underscores the accuracy of the circular mode model in simulating the resonant converter.

To demonstrate the advantage of the class EF_2 topology, the circuit was modified to operate as a class E inverter by disconnecting the auxiliary network. Fig. 4.7 shows that, in this configuration, the switch voltage peaked at 44V. In contrast, the cyclic-model of the class EF_2 inverter, depicted in Fig. 4.5, indicates a much lower maximum switch voltage of 30.4V. These two figures show the maximum voltage of the class E inverter to be 46% higher than that of the class EF_2 inverter in this case. The significant difference in these voltages highlights the class EF_2 topology's effectiveness in reducing peak switch voltage stress.

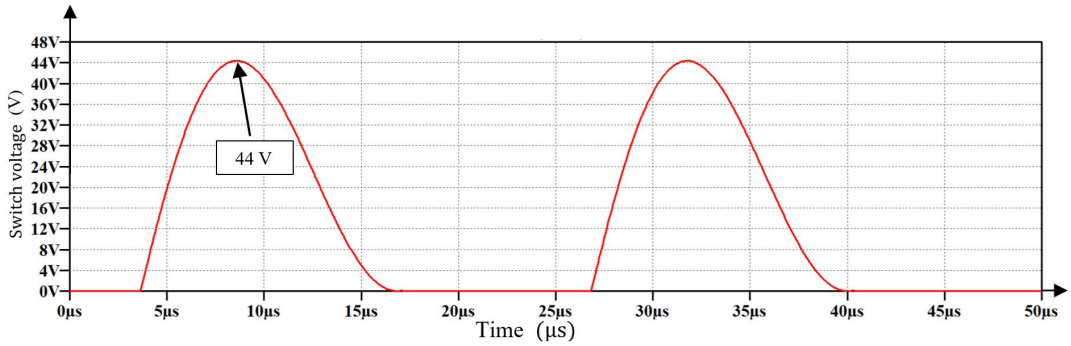

Fig. 4.7. The switch voltage of the class E inverter circuit

Fig. 4.8 presents a comparative analysis of the load voltage for the class EF_2 inverter, from cyclic-mode model, SPICE simulation and experimental model perspectives. The experimental load voltage waveform is denoted by a black solid line, the SPICE simulation load voltage by a green dotted line, and the cyclic-mode model load voltage by a blue dotted line. Both the cyclic-model and the SPICE simulation predict a peak-to-peak load voltage of 17.28 V, equating to an output power of 0.93 W. Conversely, the experimental results show a slightly lower peak-to-peak load voltage of 16.78 V, corresponding to an output power of 0.88 W. The close agreement between these values substantiates the accuracy of the cyclic-mode model in predicting the behaviour of load voltage.

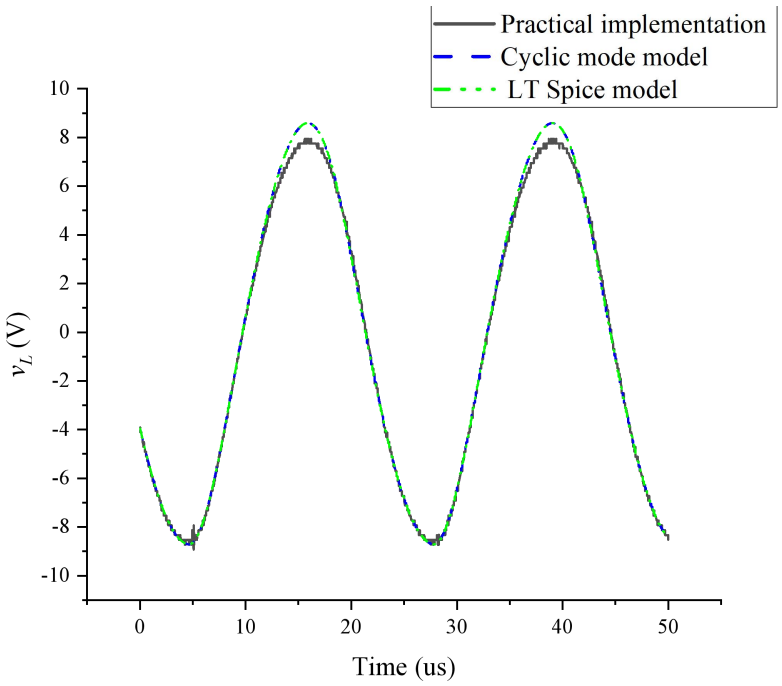

Fig. 4.8. A comparative analysis of the load voltage waveforms v_L from the LT SPICE model, cyclic-mode model, and experimental model

To evaluate the functionality of the piezoelectric resonator (PR), it was replaced with a combination of a traditional capacitor, an inductor, and a resistor, which were valued to match the PR's equivalent circuit parameters: C_{m}, L_{m}, and R_{m}. Fig. 4.9 and Fig. 4.10 delineate the SPICE model switch voltage v_{C} and load voltage v_{L} for the class EF_2 inverter with a standard capacitor and inductor. A peak switch voltage of 30.4 V is observed, with the peak-to-peak load voltage registering at 16.2 V, and the output power amounting to 0.82 W.

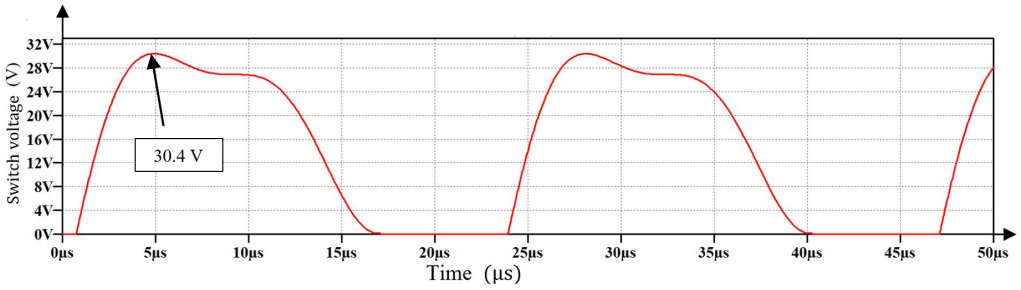

Fig. 4.9. The switch voltage v_C waveform of the class EF_2 inverter SPICE model, which uses standard inductor and capacitor as auxiliary network

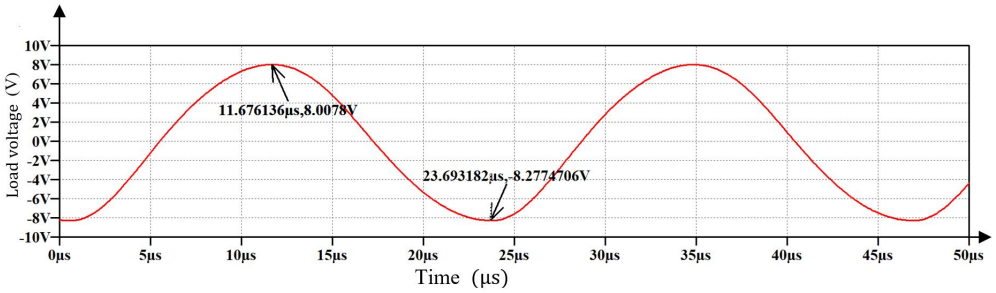

Fig. 4.10. The load voltage v_L waveform of the class EF_2 inverter SPICE model, which uses standard inductor and capacitor as auxiliary network

Comparing Fig. 4.5, Fig. 4.9, Fig. 4.8 and Fig. 4.10, it is evident that substituting standard inductors and capacitors in the auxiliary network of the class EF_2 inverter with a piezoelectric resonator results in similar switching and load voltage waveforms.

4.6 Conclusion

This chapter analyses and models the class EF_2 inverter under optimal operation by applying the cyclic-mode modelling technique. The results of the modelling analysis are compared with the results of the corresponding SPICE simulation model and the results measured on a physical prototype.

Firstly, and most importantly, the agreement between the cyclic-mode model results and the SPICE simulation results proves the accuracy of the cyclic-mode modelling technique in analysing the resonant converter, this confirms that the cyclic-mode modelling technique is a better choice for analysing resonant switching power supplies and also provides a basis for the subsequent use of cyclic-mode modelling as the main analytical approach. Then the use of PR on an experimental prototype confirms the potential of PR for resonant converter applications.

However, the precise requirement of a fixed duty cycle and the assumption that the components in the circuit are ideal limit the usage of cyclic-mode modelling. The main direction of improvement is to investigate new analytical methods to obtain the duty cycle of the modes to meet the precise duty cycle requirement of the technique. Attempts are also made to incorporate parasitic components in the modelling process to bring the model closer to reality.

4.7 References

[4.1] Wang, Yuqing, Jonathan N. Davidson, and Martin P. Foster. "Cyclic-mode modelling of class EF 2 inverters featuring a piezoelectric resonator as the auxiliary network." *11th International Conference on Power Electronics, Machines and Drives* (PEMD 2022). Vol. 2022, pp. 131-135, https://doi.org/10.1049/icp.2022.1120.

[4.2] S. Aldhaher, et al. “Modeling and Analysis of Class EF and Class E/F Inverters With Series-Tuned Resonant Networks.” IEEE Transactions on Power Electronics, vol. 31, no. 5, May 2016, pp. 3415–30. https://doi.org/10.1109/tpel.2015.2460997.

[4.3] Huang, Yao Tien, et al. “High-powered Backlight Inverter for LCD-TVs using Piezoelectric Transformers.” *Journal of Intelligent Material Systems and Structures*, vol. 18, no. 6, Feb. 2007, pp. 601–09. https://doi.org/10.1177/1045389x06067929.

[4.4] Carazo, Alfredo Vázquez. “50 Years Of Piezoelectric Transformers. Trends In The Technology.” *MRS Proceedings/Materials Research Society Symposia Proceedings*, vol. 785, Jan. 2003, https://doi.org/10.1557/proc-785-d1.7.

[4.5] Touhami, Mustapha, Ghislain Despesse, and François Costa. "A new inductorless DC-DC piezoelectric flyback converter." *IEEE Transactions on Power Electronics 37.6* , 2022, pp.6986-7000, https://doi.org/10.1109/ICIT.2018.8352243.

[4.6] Vincent, Massavie, et al. “A New Topology of Resonant Inverter Including a Piezoelectric Component.” HAL (Le Centre Pour La Communication Scientifique Directe), 6 Sept. 2021, https://doi.org/10.23919/epe21ecceeurope50061.2021.9570192. Accessed 2 July 2024.

[4.7] Visser, H. R., and P. P. J. Van den Bosch. "Modelling of periodically switching networks." *PESC'91 Record 22nd Annual IEEE Power Electronics Specialists Conference*. 1991, https://doi.org/10.1109/pesc.1991.162655.

[4.8] Kassakian, John G., et al. Principles of power electronics. Cambridge University Press, 2023, https://doi.org/10.1017/9781009023894.

[4.9] Gould, C., et al. "CLL resonant converters with output short-circuit protection." *IEE Proceedings. Electric Power Applications*, vol. 152, no. 5, Jan. 2005, p. 1296. https://doi.org/10.1049/ip-epa:20045157.

[4.10] Foster, M. P., H. I. Sewell, et al. "Cyclic-averaging for high-speed analysis of resonant converters." *IEEE Transactions on Power Electronics*, vol. 18, no. 4, July 2003, pp. 985–93. https://doi.org/10.1109/tpel.2003.813763.

[4.11] Forrester, Jack, et al. "Equivalent circuit parameter extraction methods for piezoelectric transformers." *21st European Conference on Power Electronics and Applications (EPE'19 ECCE Europe)*. 2019, https://doi.org/10.23919/epe.2019.8915189.

[4.12] Foste, M. P., et al. "Predicting the zero-voltage switching profiles of half-bridge driven inductor-less piezoelectric transformer-based inverters." *IET Power Electronics*, vol. 5, no. 7, Aug. 2012, pp. 1068–73. https://doi.org/10.1049/iet-pel.2011.0344.

[4.13] 'STEMiNC Steiner & Martins. Piezoelectric disc information'. https://www.steminc.com/PZT/en/piezoelectric-disc-25x85mm-s-235-khz Accessed 05 November 2023

[4.14] Shih, Wei-Che, et al. "Simulation of Solidly Mounted Resonator Using Mason Model and Its Implementation." *Sensors and Materials*, Jan. 2017, pp. 405-410. https://doi.org/10.18494/sam.2017.1522.

Chapter 5. Application of Newton's method for estimating the mode durations and initial condition of cyclic-mode models with specific application to the class E inverter

The previous Chapters have utilized the cyclic-mode modelling framework, as described in [5.1], to estimate the behaviours of DC input power converters. This Chapter details the technique of integrating the Newton method with the cyclic-mode model to ascertain the steady-state operating conditions of converters. It then applies this technique to a class E inverter operating under suboptimal conditions. In subsequent Chapters, the cyclic-mode modelling framework is further extended to facilitate the determination of RMS values of signals.

5.1 Introduction

To ensure the optimal working condition of a class E inverter, precise selection of resonant circuit component values, operating frequency, and duty cycle is essential. However, any change in component value can disrupt this optimal condition. Due to implementation challenges and sensitivity to component variations, this mode is not commonly chosen in practical applications.

On the other hand, in the suboptimal working condition, despite not fully achieving ideal ZVS, the operational state can still significantly reduce switching losses. This condition offers more flexibility in switch frequency and duty cycle selection and is more tolerant to component value changes, making it a more pragmatic choice in real-world scenarios.

For modelling a class E inverter under suboptimal operation, given the accuracy of the cyclic-mode model described in Chapter 4, this model is chosen. The cyclic-mode model

requires determining the periodic initial values, the sequence of different modes (circuit configurations), and each mode's duration. In optimal conditions, i.e., under a two-mode operation, the sequence and duration of modes are controlled. Thus, the periodic initial values of the model can be acquired through expression,

$$\boldsymbol{x}(t_0) = \boldsymbol{x}(t_0 + \mathrm{T_{sw}}) \tag{5.1}$$

However, under suboptimal operating conditions, i.e., in a three-mode operation, the sequence of modes is known, but only the duration of Mode 1 is known, hence a method is needed to ascertain the durations of Mode 2 and Mode 3, thereby achieving an accurate cyclic-mode model.

If suboptimal operating conditions are chosen for the inverter's operation, then the accuracy of the cyclic-model as demonstrated in Chapter 6 continues to be a reliable tool for predicting the circuit behaviour. The core requisites of the cyclic-model in this case are as follows:

Firstly, an in-depth understanding of the circuit behaviour is pivotal. This can be achieved by thoroughly comprehending circuit dynamics and employing fundamental principles like Kirchhoff's Current Law (KCL) and Kirchhoff's Voltage Law (KVL) to formulate the correct set of differential equations.

Secondly, identifying the order of modes within a cycle is also important. This process involves estimating the circuit behaviour using techniques.

Lastly, and most importantly, determining the duration of each mode is critical. Ensuring the correct duration for each mode is key to the model's accuracy. The Newton-Raphson method can be employed to obtain precise durations of each mode and the initial values for the model, thus ensuring a precise prediction of the circuit's performance under the given operational conditions.

5.2 Methodology of the Newton-Raphson method

The Newton-Raphson method, often abbreviated as Newton's method, is an iterative numerical technique that is extensively used for finding increasingly accurate approximations of the roots (or zeros) of a real-valued function. Originating from the work of Sir Isaac Newton and later promoted by Joseph Raphson, this method has gained attention for its rapid convergence characteristics, particularly when approaching the true root. By employing the Taylor series expansion of the equation, the Newton-Raphson method aims to linearize the nonlinear algebraic equations, thereby striving to ascertain the roots of the equation, making it an effective solution for tackling nonlinear algebraic equations [5.2].

The method hinges on the fundamental idea of linear approximation and is based on a Taylor series expansion of the function under investigation. At each step, a function $f(x)$ is approximated by a tangent line, and the *x*-intercept of this line is taken as the next approximation to the root. The process is then iteratively repeated using the updated value of *x* until a sufficiently accurate value is achieved. The goal being to determine the value of *x* such that $\left|f\left(x^k\right) - f\left(x^{k-1}\right)\right| < \varepsilon$ (where ε is an error bound and k is the iteration index) and is sufficiently close to zero for $f(x(k))\sim 0$.

The formulation for Newton's method is as follows: let $\boldsymbol{G}(\boldsymbol{X})$ be a differentiable function with continuous derivatives. The Newton method's formula to update the approximation $\boldsymbol{X}$ of the root is given by [5.3],

$$\boldsymbol{X}^{k+1} = \boldsymbol{X}^k - \frac{\boldsymbol{G}\left(\boldsymbol{X}^k\right)}{\boldsymbol{G}'\left(\boldsymbol{X}^k\right)} \tag{5.2}$$

where k is the index of current iteration step; $\boldsymbol{X}^{k+1}$ is the next approximation. $\boldsymbol{X}^k$ is the current approximation. $\boldsymbol{G}(\boldsymbol{X}^k)$ is the value of the function at the present approximation $\boldsymbol{X}^k$. $\boldsymbol{G}'(\boldsymbol{X}^k)$ is the value of the first derivative of the function at the current approximation $\boldsymbol{X}^k$.

For the Newton's method utilizing the Jacobian matrix [5.3], (5.2) can be rewritten as

$$\boldsymbol{X}^{k+1} = \boldsymbol{X}^{k} - \alpha \frac{\boldsymbol{G}(\boldsymbol{X}^{k})}{[\boldsymbol{J}(\boldsymbol{X}^{k})]} \tag{5.3}$$

where $0 < \alpha \leq 1$ is a relaxation factor to improve convergence and $\boldsymbol{J}(\boldsymbol{X}^{k})$ is the Jacobian matrix of partial derivatives evaluated at k^{th} iteration, $\boldsymbol{J}(\boldsymbol{X})$ is given by,

$$\boldsymbol{J}(\boldsymbol{X}) = \frac{\partial \boldsymbol{G}}{\partial \boldsymbol{X}} = \begin{bmatrix} \frac{\partial g_1}{\partial X_1} & \cdots & \frac{\partial g_1}{\partial X_p} \\ \vdots & \ddots & \vdots \\ \frac{\partial g_p}{\partial X_1} & \cdots & \frac{\partial g_p}{\partial X_p} \end{bmatrix} \tag{5.4}$$

where p represents the number of elements contained in vector $\boldsymbol{X}$**.** Given that equation (5.4) could be a difficult to differentiate, employing the numerical form of the Jacobian proves to be more convenient, wherein the partial derivatives are assessed using,

$$\frac{\partial g_i(\boldsymbol{X})}{\partial X_j} \approx \frac{g_i(\boldsymbol{X} + \Delta \boldsymbol{X_j}) - g_i(\boldsymbol{X})}{\alpha_j} \tag{5.5}$$

where i denotes the function index, j represents the variable index, and $\Delta \boldsymbol{X}_j = [0 \ldots \alpha_j \ldots 0]^T$ is a $p \times 1$ single-element row vector with a sufficiently small increment α_j in the j^{th} variable. The stopping criterion for the iteration is achieved when the L^1-norm diminishes below an acceptable value λ,

$$\left| \boldsymbol{X}^{\text{final}} - \boldsymbol{X}^{\text{final}-1} \right| < \lambda \tag{5.6}$$

where $\boldsymbol{X}^{\text{final}}$ is a vector of true root of function $\boldsymbol{G}(\boldsymbol{X})$.

Proceeding with a three-mode operating class E inverter as an example, the Newton-Raphson method based on the numerical Jacobian matrix will be utilized to obtain the initial values and the duration of each mode under three-mode operation. Initially, a brief introduction to the operation of the class E inverter will be provided.

5.3 Operation of class E inverter

Mode 1 (M1), $t_0 \leq t < t_1$: During the interval δ_1/f_{sw}, switch S is turned on. Throughout this period, the switch voltage is zero, with V_{in} being applied to L_{in}. Consequently, the voltage across the switch remains at zero. Since S is on the resonant current i_{Ls} that circulates through L_{s}, C_{s}, and R_{L} also flows through S.

Mode 2 (M2), $t_1 \leq t < t_2$: S is turned off. Current flows out of L_{in} and into C_0 and the main resonant branch. $i_{\text{Lin}} = i_{\text{C0}} + i_{\text{Ls}}$. The switch voltage increases from zero to a maximum value and then reduces below zero until reach D's forward bias voltage.

Mode 3 (M3), $t_2 \leq t < t_3$: S remains turned off, D is conducting and the switch voltage v_{C0} has been clamped at D's forward bias voltage $-v_{\text{d}}$. At the end of M3, the switch voltage v_{C0} is forced to zero by the turn-on of S. It should be noted that $v_{C0} = -v_{\text{d}}$ is typically less than 1 V and so switching losses are significantly reduced compared to the non-optimal, non-ZVS operating condition.

5.4 Derivation of cyclic-mode model for the class E inverter

Fig. 5.1 shows circuit diagram of the class E inverter. L_{s} and C_{s} form the main resonant branch; these force a sinusoidal shaped current to follow through the load R_L. S is the MOSFET switch and is operated at a frequency f_{sw} and with a duty δ_1, and D is the antiparallel diode of the switch. Input inductor L_{in} is a filter inductor ensuring that only a DC current i_{Lin} from the input voltage V_{DC}.

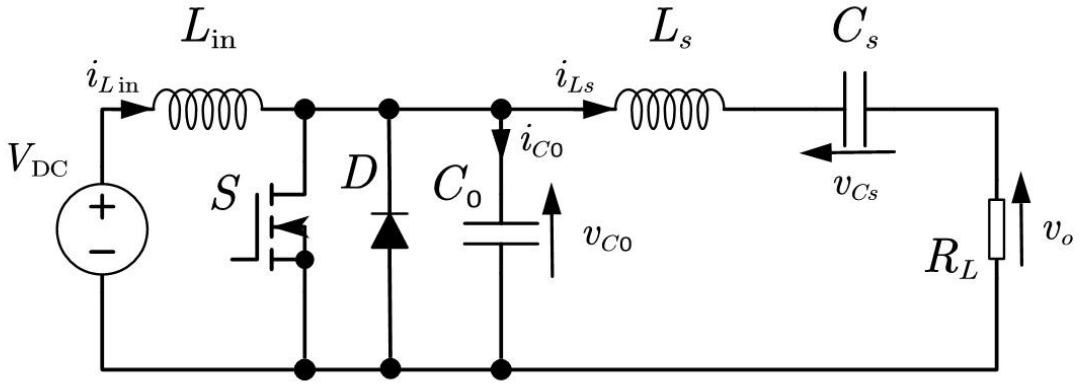

Fig. 5.1. Circuit diagram of the class E inverter

Under sub-optimal conditions, the operation of the class E inverter during a single switching cycle is divided into three modes. The detailed analysis of each mode has been thoroughly covered in Chapter 2 and will not be revisited here.

The following approach is used to derive the cyclic-model for the class E inverter:

1. For each mode, determine the differential equations for the inductor current and capacitor voltage and then form a piecewise linear state-variable model
2. Using describing functions to roughly estimate the duration of each mode. Based on these estimates, construct the cyclic-mode model to obtain an estimate of the state variable $\boldsymbol{x}(t)$ initial value, denoted as $\boldsymbol{x}(t_0)$.
3. Construct Newton's solving equations based on the mode-switching conditions.
4. Use Newton's method to determine the precise cyclic-mode initial conditions $\boldsymbol{x}(t_0)$ and each mode duration.

5.4.1 Differential equations and piecewise state-variable model for each mode

To construct the inverter's cyclic-model, the first-order differential equations are needed to describe the derivatives of the relevant capacitor voltages and the inductor currents.

For Mode 1 (M1) $t_0 \leq t < t_1$:

At $t=t_0$, S turns on and this signifies the start of a cycle. V_{DC} has been applied to L_{in}, the derivative of the input inductor current is given by,

$$\dot{i_{L\mathrm{in}}} = \frac{v_{L\mathrm{in}}}{L_{\mathrm{in}}} = \frac{V_{\mathrm{DC}}}{L_{\mathrm{in}}} \tag{5.7}$$

With the derivative being denoted by $\dot{z} \equiv \frac{dz}{dt}$. The series inductor current is found from,

$$\dot{i_{Ls}} = \frac{v_{Ls}}{L_{\mathrm{s}}} = \frac{-v_{Cs} - R_{\mathrm{L}} i_{Ls}}{L_{\mathrm{s}}} \tag{5.8}$$

For the derivative series capacitor voltage, it is noted that L_{s} and C_{s} are connected in series. Therefore,

$$\dot{v_{Cs}} = \frac{i_{Cs}}{C_{\mathrm{s}}} = \frac{i_{Ls}}{C_{\mathrm{s}}} \tag{5.9}$$

For the shunt capacitor C_0, since the switch is turned on and so $v_{C0} = 0$. Thus,

$$\dot{v_{C0}} = 0 \tag{5.10}$$

Combing (5.7)-(5.10) gives the state-variable model for M1,

$$\begin{bmatrix} \dot{i_{L\mathrm{in}}} \\ \dot{i_{Ls}} \\ \dot{v_{Cs}} \\ \dot{v_{C0}} \end{bmatrix} = \begin{bmatrix} 0 & 0 & 0 & 0 \\ 0 & -\frac{R_{\mathrm{L}}}{L_{\mathrm{s}}} & -\frac{1}{L_{\mathrm{s}}} & 0 \\ 0 & \frac{1}{C_{\mathrm{s}}} & 0 & 0 \\ 0 & 0 & 0 & 0 \end{bmatrix} \begin{bmatrix} i_{L\mathrm{in}} \\ i_{Ls} \\ v_{Cs} \\ v_{C0} \end{bmatrix} + \begin{bmatrix} \frac{V_{\mathrm{DC}}}{L_{\mathrm{in}}} \\ 0 \\ 0 \\ 0 \end{bmatrix} \tag{5.11}$$

(5.11) can be rewritten as,

$$\dot{\boldsymbol{x}} = \boldsymbol{A}_1 \boldsymbol{x} + \boldsymbol{B}_1 \tag{5.12}$$

where $\boldsymbol{A}_i$ is a square matrix of order h representing the system dynamics and $\boldsymbol{B}_i$ is the input vector for the i^{th} mode. The state-vector $\boldsymbol{x}$ is,

$$\boldsymbol{x} = [i_{L\mathrm{in}} \quad i_{Ls} \quad v_{Cs} \quad v_{C0}]^{\mathrm{T}} = [x_1 \quad x_2 \quad x_3 \quad x_4]^{\mathrm{T}} \tag{5.13}$$

During Mode 2 (M2) $t_1 \leq t < t_2$, At $t=t_1$, S is turned off, so the switch voltage starts to increase from zero, therefore the derivative of the input inductor current is given by,

$$\dot{i_{Lin}} = \frac{V_{DC} - v_{C0}}{L_{in}} \tag{5.14}$$

The derivative series inductor current is found from KVL rule,

$$\dot{i_{Ls}} = \frac{v_{C0} - v_{Cs} - R_L i_{Ls}}{L_s} \tag{5.15}$$

The derivative of shunt capacitor voltage $\dot{v_{C0}}$, which is also equal to the MOSFET drain-source voltage, is given by KCL rule,

$$\dot{v_{C0}} = \frac{i_{Lin} - i_{Ls}}{C_0} \tag{5.16}$$

Series connection of L_s and C_s means $\dot{v_{Cs}}$ is defined as for Mode 1,

$$\dot{v_{Cs}} = \frac{i_{Ls}}{C_s} \tag{5.17}$$

Combing (5.14)-(5.17) gives the state-variable model for M2,

$$\begin{bmatrix} \dot{i_{Lin}} \\ \dot{i_{Ls}} \\ \dot{v_{Cs}} \\ \dot{v_{C0}} \end{bmatrix} = \begin{bmatrix} 0 & 0 & 0 & -\frac{1}{L_{in}} \\ 0 & -\frac{R_L}{L_s} & -\frac{1}{L_s} & \frac{1}{L_s} \\ 0 & \frac{1}{C_s} & 0 & 0 \\ \frac{1}{C_0} & -\frac{1}{C_0} & 0 & 0 \end{bmatrix} \begin{bmatrix} i_{Lin} \\ i_{Ls} \\ v_{Cs} \\ v_{C0} \end{bmatrix} + \begin{bmatrix} \frac{V_{DC}}{L_{in}} \\ 0 \\ 0 \\ 0 \end{bmatrix} = \boldsymbol{A_2 x} + \boldsymbol{B_2} \tag{5.18}$$

For Mode 3 (M3) $t_2 \leq t < t_3$:

The current $i_{Lin} - i_{Ls}$ that flows through C_0 drives v_{C0} below zero. When $v_{C0}(t_2) = -v_d$ the switch's antiparallel diode conducts thereby clamping $v_{C0} = -v_d$ and this signifies the start of M3. The derivative of input inductor current is described by,

$$\dot{i_{Lin}} = \frac{V_{DC} - v_{C0}}{L_{in}} \tag{5.19}$$

The derivative of series inductor current is found from,

$$\dot{i_{Ls}} = \frac{v_{C0} - v_{Cs} - R_L i_{Ls}}{L_s} \tag{5.20}$$

Assuming the body diode voltage is constant during M3, the derivative of shunt capacitor voltage is,

$$\dot{v_{C0}} = 0 \tag{5.21}$$

As with the previous two modes,

$$\dot{v_{Cs}} = \frac{i_{Ls}}{C_s} \tag{5.22}$$

Combing (5.19)-(5.22) gives the state-variable model for M3.

$$\begin{bmatrix} \dot{i_{Lin}} \\ \dot{i_{Ls}} \\ \dot{v_{Cs}} \\ \dot{v_{C0}} \end{bmatrix} = \begin{bmatrix} 0 & 0 & 0 & -\frac{1}{L_{in}} \\ 0 & -\frac{R_L}{L_s} & -\frac{1}{L_s} & \frac{1}{L_s} \\ 0 & \frac{1}{C_s} & 0 & 0 \\ 0 & 0 & 0 & 0 \end{bmatrix} \begin{bmatrix} i_{Lin} \\ i_{Ls} \\ v_{Cs} \\ v_{C0} \end{bmatrix} + \begin{bmatrix} \frac{V_{DC}}{L_{in}} \\ 0 \\ 0 \\ 0 \end{bmatrix} = \boldsymbol{A_3 x} + \boldsymbol{B_3} \tag{5.23}$$

Hence, by referring to equations (5.11), (5.18) and (5.23), along with the mode sequences, a piecewise linear equation can be formulated, which is contingent on the duration times of the respective modes,

$$\dot{\boldsymbol{x}}(t) = \begin{cases} \boldsymbol{A_1 x}(t_0) + \boldsymbol{B_1} & t_0 \le t < t_1 \\ \boldsymbol{A_2 x}(t_1) + \boldsymbol{B_2} & t_1 \le t < t_2 \\ \boldsymbol{A_3 x}(t_2) + \boldsymbol{B_3} & t_2 \le t < t_3 \end{cases} \tag{5.24}$$

5.4.2 Cyclic-mode model of the class E inverter

The inverter is operating in a cyclic-mode, the final condition of state variables at the end of cyclic $\boldsymbol{x}(t_3)$ should equal the initial condition of that cyclic $\boldsymbol{x}(t_0)$,

$$\boldsymbol{x}(t_0) = \boldsymbol{x}(t_3) = \boldsymbol{x}(t_0 + T_{sw}) \tag{5.25}$$

Since the input is DC, starting from $t = t_0$, the state-vector at the end of Mode 1 is given by,

$$\boldsymbol{x}(t_1) = \boldsymbol{\Phi_1 x}(t_0) + \boldsymbol{\Gamma}_1 \tag{5.26}$$

where $\boldsymbol{\Phi}_1$ value can be obtained from $\boldsymbol{\Phi}_i = \exp\left(\boldsymbol{A}_i(\boldsymbol{t}_i - \boldsymbol{t}_{i-1})\right)$, so $\boldsymbol{\Phi}_1 = \exp\left(\boldsymbol{A}_1 \delta_1 T_{sw}\right)$ and $\boldsymbol{\Gamma}_1$ value can get from $\boldsymbol{\Gamma}_i = \boldsymbol{A}_i^{-1}[\boldsymbol{\Phi}_i - \boldsymbol{I}]\boldsymbol{B}_i$, $\boldsymbol{\Gamma}_1 = \boldsymbol{A}_1^{-1}[\boldsymbol{\Phi}_1 - \boldsymbol{I}]\boldsymbol{B}_1$. Similarly, the state-vector at the end of Mode 2 is given by,

$$\boldsymbol{x}(t_2) = \boldsymbol{\Phi}_2 \boldsymbol{x}(t_1) + \boldsymbol{\Gamma}_2 \tag{5.27}$$

where $\boldsymbol{\Phi}_2 = \exp(\boldsymbol{A}_2 \delta_2 T_{\text{sw}})$ and $\boldsymbol{\Gamma}_2 = \boldsymbol{A}_2^{-1}[\boldsymbol{\Phi}_2 - \boldsymbol{I}]\boldsymbol{B}_2$.

During Mode 3, $t_2 \leq t < t_3$, refer to the switch voltage waveform in Fig. 5.2, the switch voltage will discontinue at the end of Mode 3. So, it needs to be forcing $v_{C0}(t_3) = 0$, defined t_3^- symbolised the instant before t_3. Thus, the state-vector at the end of Mode 3, prior to discontinuity, is ascertained through a similar approach,

$$\boldsymbol{x}(t_3^-) = \boldsymbol{\Phi}_3 \boldsymbol{x}(t_2) + \boldsymbol{\Gamma}_3 \tag{5.28}$$

where $\boldsymbol{\Phi}_3 = \exp(\boldsymbol{A}_3 \delta_3 T_{\text{sw}}) = \exp(\boldsymbol{A}_3(1 - \delta_1 - \delta_2) T_{\text{sw}})$ and $\boldsymbol{\Gamma}_3 = \boldsymbol{A}_3^{-1}[\boldsymbol{\Phi}_3 - \boldsymbol{I}]\boldsymbol{B}_3$.

To ensure that all state variables at time t_3, marking the end of the cycle, are equivalent to those at the start of the cycle, it is imperative to set $v_{C0}(t_3)$ to zero. Subsequently, $\boldsymbol{K}$ is delineated as a unit matrix with identical dimensions to $\boldsymbol{A}_i$, with the exception that the fourth row is zero,

$$\boldsymbol{K} = \begin{bmatrix} 1 & 0 & 0 & 0 \\ 0 & 1 & 0 & 0 \\ 0 & 0 & 1 & 0 \\ 0 & 0 & 0 & 0 \end{bmatrix} \tag{5.29}$$

Thus, at time t_3, the value of the state variable $\boldsymbol{x}(t)$ is equivalent to the value of $\boldsymbol{x}$ at time t_0, represented as,

$$\boldsymbol{x}(t_3) = \boldsymbol{K}\boldsymbol{x}(t_3^-) = \boldsymbol{x}(t_0) \tag{5.30}$$

The cyclic-mode initial condition $\boldsymbol{x}(t_0)$ can be found by evaluating the final conditions of each mode.

$$\boldsymbol{x}(t_3) = \boldsymbol{K}(\boldsymbol{\Phi}_3(\boldsymbol{\Phi}_2(\boldsymbol{\Phi}_1 \boldsymbol{x}(t_0) + \boldsymbol{\Gamma}_1) + \boldsymbol{\Gamma}_2) + \boldsymbol{\Gamma}_3) = \boldsymbol{K}\boldsymbol{\Phi}_{\text{tot}} \boldsymbol{x}(t_0) + \boldsymbol{K}\boldsymbol{\Gamma}_{\text{tot}} \tag{5.31}$$

$\boldsymbol{\Phi}_{\text{tot}}$ and $\boldsymbol{\Gamma}_{\text{tot}}$ value is obtained from

$$\boldsymbol{\Phi}_{\text{tot}} = \prod_{i=m,m-1}^{1} \boldsymbol{\Phi}_i \,, \boldsymbol{\Gamma}_{\text{tot}} = \sum_{i=1}^{m-1} \left(\left(\prod_{j=m,m-1}^{i+1} \boldsymbol{\Phi}_{\text{j}} \right) \boldsymbol{\Gamma}_i \right) + \boldsymbol{\Gamma}_m \tag{5.32}$$

In this case $m = 3$. Thus, the expression of $\boldsymbol{\Phi}_{\text{tot}}$ and $\boldsymbol{\Gamma}_{\text{tot}}$ are give by,

$$\boldsymbol{\Phi}_{\text{tot}} = \boldsymbol{\Phi}_3\boldsymbol{\Phi}_2\boldsymbol{\Phi}_1 \tag{5.33}$$

and

$$\boldsymbol{\Gamma}_{\text{tot}} = (\boldsymbol{\Phi}_3(\boldsymbol{\Phi}_2(\boldsymbol{\Gamma}_1) + \boldsymbol{\Gamma}_2) + \boldsymbol{\Gamma}_3) \tag{5.34}$$

If δ_1 and δ_2 values are known, then δ_3 be determined using $\delta_3 = 1 - \delta_1 - \delta_2$ from which the final condition $\boldsymbol{x}(t_3)$ can be found. Substituting (5.29) into (5.31) and rearranging gives the initial (final) condition,

$$\boldsymbol{x}(t_3) = (\boldsymbol{I} - \boldsymbol{K}\boldsymbol{\Phi}_{\text{tot}})^{-1}(\boldsymbol{K}\boldsymbol{\Gamma}_{\text{tot}}) = \boldsymbol{x}(t_0) \tag{5.35}$$

$$\boldsymbol{x}(t) = \begin{cases} \boldsymbol{\Phi_1}(t)\boldsymbol{x}(t_0) + \boldsymbol{\Gamma_1}(t) & t_0 \le t < t_1 \\ \boldsymbol{\Phi_2}(t)\boldsymbol{x}(t_1) + \boldsymbol{\Gamma_2}(t) & t_1 \le t < t_2 \\ \boldsymbol{\Phi_3}(t)\boldsymbol{x}(t_2) + \boldsymbol{\Gamma_3}(t) & t_2 \le t < t_3 \end{cases} \tag{5.36}$$

where $\boldsymbol{\Phi}_i(t) = \exp(\boldsymbol{A}_i(t_i - t_{i-1}))$ and $\boldsymbol{\Gamma}_i(t) = \boldsymbol{A}_i^{-1}[\boldsymbol{\Phi}_i(t) - \boldsymbol{I}]\boldsymbol{B}_i$.

5.4.3 Determining the cyclic-mode initial condition using Newton's method

To accurately simulate a class E inverter operating under suboptimal conditions, it is necessary to determine the initial conditions and the duration of each mode for the cyclic-mode model. For this purpose, the aforementioned Newton-Raphson method can be employed. Since the duty cycle of Mode 1 δ_1 is controllable, it is only necessary to determine the duty cycle of Mode 2 δ_2 to establish the duration of all modes in a cycle. Therefore, the Newton-Raphson method, based on the numerical Jacobian matrix, is utilized to define the initial conditions of the cyclic-mode model and the duty cycle of Mode 2. The vector $\boldsymbol{X}$ in this case comprises the combination of the initial conditions $\boldsymbol{x}(t_0)$ of the cyclic-mode model and the duty cycle of Mode 2 δ_2,

$$\boldsymbol{X} = [\boldsymbol{x}^{\mathrm{T}}(t_0) \quad \delta_2]^T \tag{5.37}$$

where defined X_i is the i^{th} element of $\boldsymbol{X}$. So, refer to (5.13) $X_1 = x_1(t_0)$, $X_2 = x_2(t_0)$, $X_3 = x_3(t_0)$, $X_4 = x_4(t_0)$ and $X_5 = \delta_2$.

The matrix formulation of Newton's method, when applied to this problem is,

$$\boldsymbol{X}^{k+1} = \boldsymbol{X}^k - \left[\boldsymbol{J}(\boldsymbol{X}^k)\right]^{-1}\boldsymbol{G}(\boldsymbol{X}^k) \tag{5.38}$$

where k is the iteration number and $\boldsymbol{X}^k$ are $\boldsymbol{X}$ values at k^{th} iteration. $\boldsymbol{G}(\boldsymbol{X})$ is a vector function that is used to determine the cyclic-mode initial conditions and δ_2,

$$\boldsymbol{G}(\boldsymbol{X}) = \begin{bmatrix} g_1(\boldsymbol{X}) \\ g_2(\boldsymbol{X}) \\ g_3(\boldsymbol{X}) \\ \underline{g_4(\boldsymbol{X})} \\ g_5(\boldsymbol{X}) \end{bmatrix} \tag{5.39}$$

$g_{1..4}(\boldsymbol{X})$ represent the error between the cyclic-mode initial condition and final condition,

$$\begin{bmatrix} g_1(\boldsymbol{X}) \\ g_2(\boldsymbol{X}) \\ g_3(\boldsymbol{X}) \\ g_4(\boldsymbol{X}) \end{bmatrix} = \boldsymbol{x}(T_{\mathrm{sw}} + t_0) - \boldsymbol{x}(t_0) = 0 = \boldsymbol{K}\boldsymbol{\Phi}_{\mathrm{tot}}\boldsymbol{x}(t_0) + \mathbf{K}\boldsymbol{\Gamma}_{\mathrm{tot}} - \boldsymbol{x}(t_0) \tag{5.40}$$

Duty cycles δ_2 is determined by the MOSFET body diode conduction as described in converter operation section. At the end of Mode 2, the shunt capacitor voltage should equal to the switch body diode conducting voltage,

$$v_{C0}(t_2^-) = -\,v_{\mathrm{d}} \tag{5.41}$$

where represent by cyclic-mode model is,

$$[0 \quad 0 \quad 0 \quad 1][\boldsymbol{\Phi}_2(\boldsymbol{\Phi}_1\boldsymbol{x}(t_0) + \boldsymbol{\Gamma}_1) + \boldsymbol{\Gamma}_2] = -\,v_{\mathrm{d}} \tag{5.42}$$

So $g_5(X)$ is based on (5.42),

$$g_5(\boldsymbol{X}) = [0 \quad 0 \quad 0 \quad 1][\boldsymbol{\Phi}_2(\boldsymbol{\Phi}_1\boldsymbol{x}(t_0) + \boldsymbol{\Gamma}_1) + \boldsymbol{\Gamma}_2] + v_{\mathrm{d}} \tag{5.43}$$

When all these conditions are fulfilled $\boldsymbol{G}(\boldsymbol{X}) = 0$,

$$\boldsymbol{G}(\boldsymbol{X}) = \begin{bmatrix} g_1(\boldsymbol{X}) \\ g_2(\boldsymbol{X}) \\ g_3(\boldsymbol{X}) \\ \underline{g_4(\boldsymbol{X})} \\ g_5(\boldsymbol{X}) \end{bmatrix} = \begin{bmatrix} (\boldsymbol{K}\boldsymbol{\Phi}_{\mathrm{tot}} - \boldsymbol{I})\boldsymbol{x}(t_0) + \boldsymbol{K}\boldsymbol{\Gamma}_{\mathrm{tot}} \\ \underline{\quad} \\ \begin{bmatrix} 0 \\ 0 \\ 0 \\ 1 \end{bmatrix}^T [\boldsymbol{\Phi}_2(\boldsymbol{\Phi}_1\boldsymbol{x}(t_0) + \boldsymbol{\Gamma}_1 + \boldsymbol{\Gamma}_2] + v_{\mathrm{d}} \end{bmatrix} \tag{5.44}$$

Taking the partial derivative of $\boldsymbol{G}(\boldsymbol{X})$ with respect to each variable provides the Jacobin matrix,

$$J(\boldsymbol{X}) = \begin{bmatrix} \frac{\partial g_1}{\partial X_1} & \frac{\partial g_1}{\partial X_2} & \frac{\partial g_1}{\partial X_3} & \frac{\partial g_1}{\partial X_4} & \frac{\partial g_1}{\partial X_5} \\ \frac{\partial g_2}{\partial X_1} & \frac{\partial g_2}{\partial X_2} & \frac{\partial g_2}{\partial X_3} & \frac{\partial g_2}{\partial X_4} & \frac{\partial g_2}{\partial X_5} \\ \frac{\partial g_3}{\partial X_1} & \frac{\partial g_3}{\partial X_2} & \frac{\partial g_3}{\partial X_3} & \frac{\partial g_3}{\partial X_4} & \frac{\partial g_3}{\partial X_5} \\ \frac{\partial g_4}{\partial X_1} & \frac{\partial g_4}{\partial X_2} & \frac{\partial g_4}{\partial X_3} & \frac{\partial g_4}{\partial X_4} & \frac{\partial g_4}{\partial X_5} \\ \frac{\partial g_5}{\partial X_1} & \frac{\partial g_5}{\partial X_2} & \frac{\partial g_5}{\partial X_3} & \frac{\partial g_5}{\partial X_4} & \frac{\partial g_5}{\partial X_5} \end{bmatrix}$$

$$= \begin{bmatrix} \frac{\partial g_1}{\partial i_{\mathrm{Lin}}} & \frac{\partial g_1}{\partial i_{\mathrm{Ls}}} & \frac{\partial g_1}{\partial v_{\mathrm{Cs}}} & \frac{\partial g_1}{\partial v_{\mathrm{C0}}} & \frac{\partial g_1}{\partial \delta_2} \\ \frac{\partial g_2}{\partial i_{\mathrm{Lin}}} & \frac{\partial g_2}{\partial i_{\mathrm{Ls}}} & \frac{\partial g_2}{\partial v_{\mathrm{Cs}}} & \frac{\partial g_2}{\partial v_{\mathrm{C0}}} & \frac{\partial g_2}{\partial \delta_2} \\ \frac{\partial g_3}{\partial i_{\mathrm{Lin}}} & \frac{\partial g_3}{\partial i_{\mathrm{Ls}}} & \frac{\partial g_3}{\partial v_{\mathrm{Cs}}} & \frac{\partial g_3}{\partial v_{\mathrm{C0}}} & \frac{\partial g_3}{\partial \delta_2} \\ \frac{\partial g_4}{\partial i_{\mathrm{Lin}}} & \frac{\partial g_4}{\partial i_{\mathrm{Ls}}} & \frac{\partial g_4}{\partial v_{\mathrm{Cs}}} & \frac{\partial g_4}{\partial v_{\mathrm{C0}}} & \frac{\partial g_4}{\partial \delta_2} \\ \frac{\partial g_5}{\partial i_{\mathrm{Lin}}} & \frac{\partial g_5}{\partial i_{\mathrm{Ls}}} & \frac{\partial g_5}{\partial v_{\mathrm{Cs}}} & \frac{\partial g_5}{\partial v_{\mathrm{C0}}} & \frac{\partial g_5}{\partial \delta_2} \end{bmatrix} \tag{5.45}$$

As mentioned earlier, owing to the complexities of the model the numerical form of the Jacobian is used. The procedure for determining each element of the numerical Jacobian matrix is described below. Initially, the expression for $\Delta \boldsymbol{X}_1$ is defined by (5.5).

$$\Delta \boldsymbol{X}_1 = \begin{bmatrix} \alpha_1 \\ 0 \\ 0 \\ 0 \\ 0 \end{bmatrix} \tag{5.46}$$

So, the vector composed of the partial derivatives $\frac{\partial g_1(\boldsymbol{X})}{\partial X_1}$ to $\frac{\partial g_5(\boldsymbol{X})}{\partial X_1}$ as elements is obtained by substituting equations (5.44) and (5.46) into equation (5.5), yielding,

$$\left[\frac{\partial g_1(\boldsymbol{X})}{\partial X_1} \quad \frac{\partial g_2(\boldsymbol{X})}{\partial X_1} \quad \frac{\partial g_3(\boldsymbol{X})}{\partial X_1} \quad \frac{\partial g_4(\boldsymbol{X})}{\partial X_1} \quad \frac{\partial g_5(\boldsymbol{X})}{\partial X_1}\right]^{\mathrm{T}} \approx \frac{\boldsymbol{G}(\boldsymbol{X}+\Delta\boldsymbol{X}_1)-\boldsymbol{G}(\boldsymbol{X})}{\alpha_1} \quad (5.47)$$

$$\left[\frac{\partial g_1(\boldsymbol{X})}{\partial X_1} \quad \frac{\partial g_2(\boldsymbol{X})}{\partial X_1} \quad \frac{\partial g_3(\boldsymbol{X})}{\partial X_1} \quad \frac{\partial g_4(\boldsymbol{X})}{\partial X_1} \quad \frac{\partial g_5(\boldsymbol{X})}{\partial X_1}\right]^{\mathrm{T}} \approx \frac{\left[\frac{(\boldsymbol{K}\boldsymbol{\Phi}_{\mathrm{tot}}-\boldsymbol{I})\begin{bmatrix}X_1+\alpha_1\\X_2\\X_3\\X_4\end{bmatrix}+\boldsymbol{K}\boldsymbol{\Gamma}_{\mathrm{tot}}}{\begin{bmatrix}0\\0\\0\\1\end{bmatrix}^T\left[\boldsymbol{\Phi}_2\left(\boldsymbol{\Phi}_1\begin{bmatrix}X_1+\alpha_1\\X_2\\X_3\\X_4\end{bmatrix}+\boldsymbol{\Gamma}_1\right)+\boldsymbol{\Gamma}_2\right]+v_{\mathrm{d}}}\right]-\left[\frac{(\boldsymbol{K}\boldsymbol{\Phi}_{\mathrm{tot}}-\boldsymbol{I})\begin{bmatrix}X_1\\X_2\\X_3\\X_4\end{bmatrix}+\boldsymbol{K}\boldsymbol{\Gamma}_{\mathrm{tot}}}{\begin{bmatrix}0\\0\\0\\1\end{bmatrix}^T\left[\boldsymbol{\Phi}_2\left(\boldsymbol{\Phi}_1\begin{bmatrix}X_1\\X_2\\X_3\\X_4\end{bmatrix}+\boldsymbol{\Gamma}_1\right)+\boldsymbol{\Gamma}_2\right]+v_{\mathrm{d}}}\right]}{\alpha_1} \quad (5.48)$$

The values of $\frac{\partial g_1}{\partial X_2}$ to $\frac{\partial g_5}{\partial X_2}$; $\frac{\partial g_1}{\partial X_3}$ to $\frac{\partial g_5}{\partial X_3}$ and $\frac{\partial g_1}{\partial X_4}$ to $\frac{\partial g_5}{\partial X_4}$ can be derived by a similar approach.

For the ∂X_5 part, given that X_5 represents δ_2, which is the duty ratio of Mode 2, and referring to (5.27), (5.33), and (5.34), the values of $\boldsymbol{\Phi}_2$, $\boldsymbol{\Gamma}_2$, $\boldsymbol{\Phi}_{\mathrm{tot}}$ and $\boldsymbol{\Gamma}_{\mathrm{tot}}$ change with X_5. So, similar to (5.47), the vector composed of the partial derivatives $\frac{\partial g_1(\boldsymbol{X})}{\partial X_5}$ to $\frac{\partial g_5(\boldsymbol{X})}{\partial X_5}$ as elements is,

$$\left[\frac{\partial g_1(\boldsymbol{X})}{\partial X_5} \quad \frac{\partial g_2(\boldsymbol{X})}{\partial X_5} \quad \frac{\partial g_3(\boldsymbol{X})}{\partial X_5} \quad \frac{\partial g_4(\boldsymbol{X})}{\partial X_5} \quad \frac{\partial g_5(\boldsymbol{X})}{\partial X_5}\right]^{\mathrm{T}} \approx \frac{\boldsymbol{G}(\boldsymbol{X}+\Delta\boldsymbol{X}_5)-\boldsymbol{G}(\boldsymbol{X})}{\alpha_5} \quad (5.49)$$

where $\Delta\boldsymbol{X}_5 = [0 \quad 0 \quad 0 \quad 0 \quad \alpha_5]^{\mathrm{T}}$

Define the new expression of $\boldsymbol{\Phi}_2$, $\boldsymbol{\Gamma}_2$, $\boldsymbol{\Phi}_{\mathrm{tot}}$ and $\boldsymbol{\Gamma}_{\mathrm{tot}}$ when X_5 change to $X_5+\alpha_5$ as $\boldsymbol{\Phi}_{2,\mathrm{new}}$, $\boldsymbol{\Gamma}_{2,\mathrm{new}}$, $\boldsymbol{\Phi}_{\mathrm{tot,new}}$ and $\boldsymbol{\Gamma}_{\mathrm{tot,new}}$. So, similar to (5.48), the expression of vector in (5.49) is,

$$\left[\frac{\partial g_1(\boldsymbol{X})}{\partial X_5} \quad \frac{\partial g_2(\boldsymbol{X})}{\partial X_5} \quad \frac{\partial g_3(\boldsymbol{X})}{\partial X_5} \quad \frac{\partial g_4(\boldsymbol{X})}{\partial X_5} \quad \frac{\partial g_5(\boldsymbol{X})}{\partial X_5}\right]^{\mathrm{T}} \approx$$

$$\frac{\left[\begin{array}{c}\left(\boldsymbol{K}\boldsymbol{\Phi}_{\mathrm{tot,new}}-\boldsymbol{I}\right)\begin{bmatrix}X_1\\X_2\\X_3\\X_4\end{bmatrix}+\boldsymbol{K}\boldsymbol{\Gamma}_{\mathrm{tot,new}}\\ \hline \begin{bmatrix}0\\0\\0\\1\end{bmatrix}^{T}\left[\boldsymbol{\Phi}_{2,\mathrm{new}}\left(\boldsymbol{\Phi}_1\begin{bmatrix}X_1\\X_2\\X_3\\X_4\end{bmatrix}+\boldsymbol{\Gamma}_1\right)+\boldsymbol{\Gamma}_{2,\mathrm{new}}\right]+v_{\mathrm{d}}\end{array}\right]-\left[\begin{array}{c}\left(\boldsymbol{K}\boldsymbol{\Phi}_{\mathrm{tot}}-\boldsymbol{I}\right)\begin{bmatrix}X_1\\X_2\\X_3\\X_4\end{bmatrix}+\boldsymbol{K}\boldsymbol{\Gamma}_{\mathrm{tot}}\\ \hline \begin{bmatrix}0\\0\\0\\1\end{bmatrix}^{T}\left[\boldsymbol{\Phi}_2\left(\boldsymbol{\Phi}_1\begin{bmatrix}X_1\\X_2\\X_3\\X_4\end{bmatrix}+\boldsymbol{\Gamma}_1\right)+\boldsymbol{\Gamma}_2\right]+v_{\mathrm{d}}\end{array}\right]}{\alpha_5} \tag{5.50}$$

After following these procedures, each value in the numerical Jacobian matrix for the Newton method can be determined. Finally, as per equation (5.6), the criterion for ending the cycle is when the difference between two successive iteration values of $\boldsymbol{X}$ is sufficiently small. The defined $error$ is as follows:

$$error^k = |X_1^k - X_1^{k-1}| + |X_2^k - X_2^{k-1}| + |X_3^k - X_3^{k-1}| + |X_4^k - X_4^{k-1}| + |X_5^k - X_5^{k-1}| \tag{5.51}$$

When $error^{\mathrm{final}} < \lambda$, the Newton method will end and output a vector of true initial conditions for cyclic operation, $\boldsymbol{x}(t_0)$ and δ_2.

5.5 Model validation

To validate the proposed model, a class E inverter simulation model was developed. Set the circuit series resonant frequency is 100 kHz. The components were determined using Kazimierczuk, *et al.,* [5.4] methodology., components values for the design are listed in Table 5.1.

Table 5.1. Components parameters of the class E inverter for the design

Parameter	Value
R_L (Ω)	0.611
V_{DC} (V)	2.3
C_0 (nF)	100
L_s (μH)	30
C_s (nF)	84.52
v_{d} (V)	0.7
L_f (mH)	3.3
f_{sw} (kHz)	108

The initial value of Mode 2's duty ratio, δ_2, in the Newton iteration method is given by $\delta_2^0 = \frac{1-\delta_1}{2}$, while the initial iteration value of $\boldsymbol{x}(t_0)$, denoted as $\boldsymbol{x}^0(t_0)$, is derived from (5.35) and δ_2^0's value.

$$\boldsymbol{X}^0 = \begin{bmatrix} \boldsymbol{x}^0(t_0) \\ \delta_2^0 \end{bmatrix} = \begin{bmatrix} -0.3389 \\ 1.0325 \\ 6.0161 \\ 0 \\ 0.25 \end{bmatrix} \tag{5.52}$$

The results from Newton's method represent the true initial conditions of the cyclic-mode model, and the duration of Mode 2 after 8 iterations, as presented in (5.53):

$$\boldsymbol{X}^{\mathrm{final}} = \begin{bmatrix} \boldsymbol{x}^{\mathrm{final}}(t_0) \\ \delta_2^{\mathrm{final}} \end{bmatrix} = \begin{bmatrix} 0.3372 \\ 0.9050 \\ 21.2836 \\ 0 \\ 0.3327 \end{bmatrix} = \begin{bmatrix} i_{L\mathrm{in}}(t_0) \\ i_{Ls}(t_0) \\ v_{Cs}(t_0) \\ v_{C0}(t_0) \\ \delta_2 \end{bmatrix} \tag{5.53}$$

So, the cyclic-mode model precise initial conditions and duty ratio of each mode are given by Table 5.2.

Table 5.2. The class E inverter cyclic-mode model initial conditions and duty ratio of each mode after using Nethod's method

Parameter	Value
$i_{\mathrm{Lin}}(t_0)$ (A)	0.3372 A
$i_{\mathrm{Ls}}(t_0)$ (A)	0.9050 A
$v_{\mathrm{Cs}}(t_0)$ (V)	21.2836 V
$v_{\mathrm{C0}}(t_0)$ (V)	0 V
δ_1	0.5
δ_2	0.3327
δ_3	0.1673

Following the determination of the model's initial values and the duration of each mode through the Newton method, these values are then inputted into the cyclic-mode model in (5.36). This results in the waveform of each state variable during operation. To demonstrate the effectiveness of the Newton method, Fig. 5.2 shows the cyclic-mode model result waveforms without using Newton's method, meaning the model uses (5.52) as the operation condition.

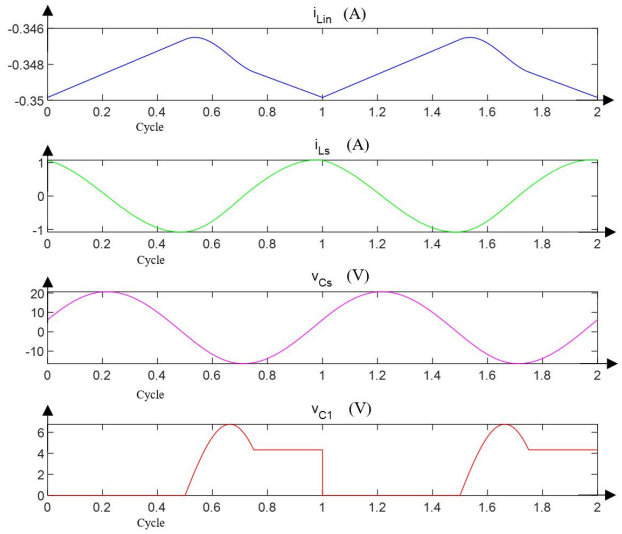

Fig. 5.2. The class E inverter three mode cyclic-mode model waveform with $\boldsymbol{X}^0$ as the operation condition

Subsequently, the corresponding LT SPICE simulation model of the converter is established according to the design parameters and the circuit diagram is shown in Fig. 5.3. The accuracy of the Newton method and the cyclic-mode model is evaluated by comparing their operational waveforms from the SPICE simulation,

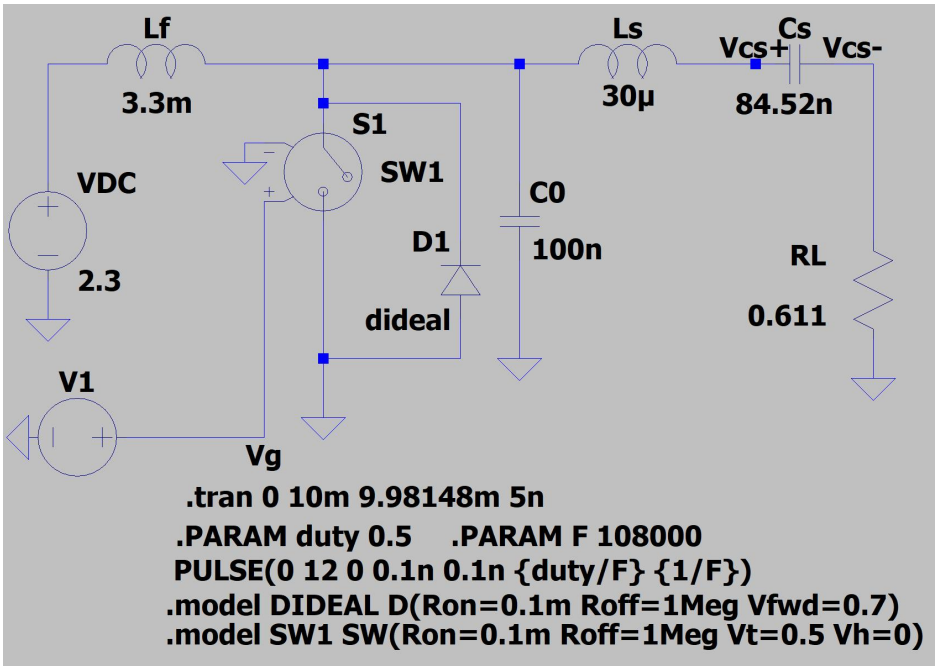

Fig. 5.3. SPICE model schematic of the class E inverter

As shown in Fig. 5.4. This comparison confirms that the combined use of the Newton method and the cyclic-mode model effectively determines the steady-state operating conditions of the class E inverter in three-mode operation.

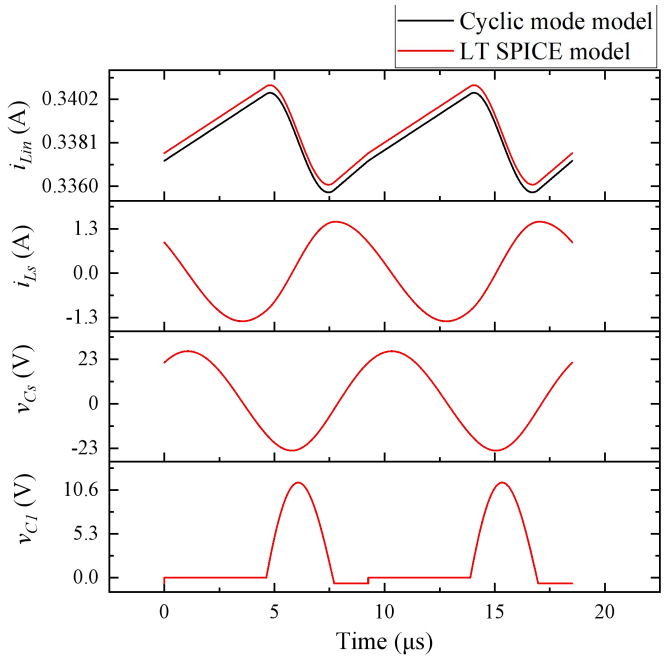

Fig. 5.4. The comparison between each inductor current and each capacitor voltage waveforms of the cyclic-mode model (black lines) and the SPICE model (red lines)

The Newton method's accuracy depends on the predicted modes' number and order matching those in the actual simulation, and the duty cycles of these modes being approximately accurate. If the predictions of the converter's operating state are incorrect, leading to improper conditions being fed into the Newton method, it will either produce erroneous results or fail to yield any output. For this case, the circuit operating under sub-optimal conditions with three modes (M1-M2-M3-M1). If the duty cycle of each mode is approximate estimate as 0.5, δ_2 =0.25, and δ_3 =0.25, Newton's method can iteratively generate an accurate initial model value. However, inaccurate predictions, such as duty cycles of δ_2 =0.5, and δ_3 =0, which wrongly assuming that the converter is running under optimal operation, will lead Newton's method output incorrect results as illustrated in Table 5.3.

Table 5.3. Output of Newton's method after using misestimation

Parameter	Value
$i_{\mathrm{Lin}}(t_0)$ (A)	2.0148 A
$i_{\mathrm{Ls}}(t_0)$ (A)	0.7260 A
$v_{\mathrm{Cs}}(t_0)$ (V)	67.5933 V
$v_{\mathrm{C0}}(t_0)$ (V)	0 V
δ_1	0.5
δ_2	0.5714
δ_3	−0.0714

The irrational values of δ_2 and δ_3 in the table indicate that if the initial iteration value in Newton's method deviates significantly from the correct result, the method becomes ineffective and outputs erroneous results. This highlights the need for alternative methods to estimate the initial values of the model and the duty cycles of each mode, thereby ensuring the effective application of Newton's method.

In order to further validate the accuracy of the cyclic-mode model and the Newton's method, a comparison of the Root Mean Square (RMS) values of each state variable obtained from both models is performed. The RMS values provide a measure of the magnitude of the varying quantities and are useful for comparing the overall energy handling capacity among different states of the models. By examining the RMS values from the cyclic-mode model and LT SPICE simulation, a more quantitative assessment of the model's accuracy can be achieved.

Using the waveforms generated by the cyclic-mode model while utilizing the definition of the root mean square value, the RMS values of each inductor current and capacitor voltage can be derived. The comparison between the cyclic-mode model result with SPICE model RMS values is shown in Table 5.3.

Table 5.4. Comparison of cyclic-mode model results and LT SPICE results RMS values

Measurement	**Cyclic-mode model results**	**LT SPICE results**	**Error (%)**
$i_{\mathrm{Lin(RMS)}}$ (A)	0.3382	0.3386	0.12
$i_{\mathrm{Ls(RMS)}}$ (A)	1.0376	1.0398	0.21
$v_{\mathrm{Cs(RMS)}}$ (V)	18.3093	18.238	0.39
$v_{\mathrm{C0(RMS)}}$ (V)	4.6464	4.6914	0.96

The maximum error rate of less than 1% demonstrates the accuracy of the RMS cyclic-mode model and the Newton's method. This low level of error showcases the reliability of the approaches employed, making the cyclic-mode model paired with Newton's method a trustworthy tool for analysing and understanding the dynamics of the inverter under study. The consistency between the modelled and simulated results affirms the validity of the cyclic-mode model, which is crucial for further analysis, optimization, and design modifications of the inverter system.

5.6 Conclusion

Due to the requirement of the cyclic mode model for accurate inputs, this limitation needs to be addressed through improvements in analysis methods. This chapter proposes a new application of Newton's method with cyclic-mode modelling to obtain the exact operating conditions of the cyclic mode model. As an example, a class E inverter under sub-optimal operation is used. The effectiveness of Newton's method is illustrated by comparing the results obtained using Newton's method with those of the cyclic mode model without Newton's method. The accuracy of Newton's method is further verified using the LT SPICE simulation model.

The proposed new application of Newton's method reduces the input requirements of the cyclic-mode modelling technique. This not only provides a methodology for finding the operating conditions for cyclic-mode models of different orders in subsequent chapters, also extends the scope of application of the cyclic-mode modelling technique but also makes its use more methodical, creating conditions for its wider application. While the need for iterative initial values highlights the limitations of its application, it also provides insights into potential improvements to the method.

5.7 References

[5.1] Visser, H. R., and P. P. J. Van den Bosch. "Modelling of periodically switching networks." *PESC'91 Record 22nd Annual IEEE Power Electronics Specialists Conference*. 1991， https://doi.org/10.1109/pesc.1991.162655.

[5.2] Farias Martins, Lais. Modelling and Analysis of DC-DC Converters for Bidirectional EV Charging Applications. Diss. University of Sheffield, 1 Nov. 2019， ethos.bl.uk/OrderDetails.do?uin=uk.bl.ethos.805401.

[5.3] Malyna, D. V., et al. “A comparison of methods for finding steady- state solution in power electronic circuits.” *International Power Electronics and Motion Control Conference*, vol. 3, Jan. 2004, pp. 1700–05. www.narcis.nl/publication/RecordID/oai%3Apure.tue.nl%3Apublications%2Fb41d8926-ee31-4229-bebb-237ffd33adaf.

[5.4] Kazimierczuk, Marian K., and Dariusz Czarkowski. Resonant power converters. John Wiley & Sons, 2012.

Chapter 6. A framework for determining the RMS value of signal using cyclic-mode modelling

The previous Chapters have used the cyclic-mode modelling framework described in [6.1] to estimate the behaviour of DC input power converters. In this Chapter, the cyclic-mode modelling framework is extended so that it can determine the RMS values of signals. Subsequent Chapters apply the developed RMS framework to a variety of DC input power converters.

6.1 Cyclic-mode average and RMS calculation framework

The significance of root mean square (RMS) values in the modelling and analysis of power electronic circuits was thoroughly addressed in Chapter 2. Progressing to a review of Chapter 2 on RMS value calculation methods, the cyclic-mode modelling technique was selected as the foundation for developing a methodology to calculate the RMS values of key variables in switching power supplies. Furthermore, the research approaches of Kostakis *et al.*, were incorporated to enhance cyclic-mode modelling [6.2]. The fundamental assumptions of this study are the same with the assumptions of cyclic-mode modelling, include:

1. The switching power supply system is in a cyclic steady state, which also means the duty cycle is fixed for each mode.
2. The system input is a DC input.
3. The switching elements are ideal switches.

These assumptions pave the way for establishing a modelling framework to derive the RMS values of the state variables.

The starting point for the cyclic-mode average that was first presented in [6.1].

6.1.1 Average values of states

The average of the state-variables, $\boldsymbol{x}_{\text{av}}$, are determined by evaluating

$$\boldsymbol{x}_{\text{av}} = \frac{1}{T_{sw}} \int_{t_0}^{t_0+T_{\text{sw}}} \boldsymbol{x} dt \tag{6.1}$$

The need for explicit integration is eliminated because differentiating (6.1) with respect to time yields,

$$\dot{\boldsymbol{x}}_{\text{acc}} = \frac{1}{T_{\text{sw}}} \boldsymbol{x} \tag{6.2}$$

where $\boldsymbol{x}_{\text{acc}}$ is the scaled and integrated (accumulated) state-variable vector from an arbitrary start time. Starting at $t = t_0$ and setting the initial condition $\boldsymbol{x}_{\text{acc}}(t_0) = \boldsymbol{0}$ and then integrating (6.2) until $t = t_0 + T_{\text{sw}}$ provides $\boldsymbol{x}_{\text{acc}}(t_0 + T_{\text{sw}})$ which is equal to $\boldsymbol{x}_{\text{av}}$ after a full cycle as shown in (6.3).

$$\boldsymbol{x}_{\text{av}} = \boldsymbol{x}_{\text{acc}}(t_0 + T_{\text{sw}}) - \boldsymbol{x}_{\text{acc}}(t_0) = \boldsymbol{x}_{\text{acc}}(t_0 + T_{\text{sw}}) \tag{6.3}$$

Having reformulated the averaging operation as a differential equation, (6.2) can be augmented with cyclic-mode state-variable model ($\dot{\boldsymbol{x}} = \boldsymbol{A}_i \boldsymbol{x} + \boldsymbol{B}_i$) to provide the new with-averaging piecewise model

$$\dot{\boldsymbol{z}}(t) = \widetilde{\boldsymbol{A}}_{\ i} \boldsymbol{z}(t) \tag{6.4}$$

$$\boldsymbol{z} = \begin{bmatrix} \boldsymbol{x} \\ \hline 1 \\ \hline \boldsymbol{x}_{\text{acc}} \end{bmatrix}, \quad \tilde{\boldsymbol{A}}_i = \left[\begin{array}{c|c|c} \boldsymbol{A}_i & \boldsymbol{B}_i & \boldsymbol{0} \\ \hline \boldsymbol{0} & 0 & \boldsymbol{0} \\ \hline \frac{1}{T_{sw}} \boldsymbol{I} & \boldsymbol{0} & \boldsymbol{0} \end{array}\right] \tag{6.5}$$

where $\widetilde{\boldsymbol{A}}_{\ i}$ is a square matrix of order $(2h + 1)$, $\boldsymbol{I}$ is a square identity matrix of order h and the $\boldsymbol{0}$ matrices are sized as required. The cyclic-mode initial condition for the with-averaging model (6.4) is

$$\boldsymbol{z}(t_0) = \left[\begin{array}{c} \boldsymbol{x}(t_0) \\ \hline 1 \\ \hline \mathbf{0} \end{array}\right] \tag{6.6}$$

Using $\widehat{\boldsymbol{x}}(T_{\text{sw}}) = \widehat{\boldsymbol{\Phi}}_{\text{tot}}\widehat{\boldsymbol{x}}(t_0)$ and (6.3), the average value state-vector, $\boldsymbol{x}_{\text{av}}$, is found by cascading mode solutions starting from the initial condition,

$$\boldsymbol{z}(t_0 + T_{sw}) = \left[\begin{array}{c} \boldsymbol{x}(t_0 + T_{\text{sw}}) \\ \hline 1 \\ \hline \boldsymbol{x}_{\text{av}} \end{array}\right] = \left(\prod_{i=m}^{1} \tilde{\boldsymbol{\Phi}}_i\right)\boldsymbol{z}(t_0) \tag{6.7}$$

where $\tilde{\boldsymbol{\Phi}}_i = \exp\left(\tilde{\boldsymbol{A}}\ {}_i\delta_i T_{\text{sw}}\right)$.

To summarise:

- The technique just described provides a method for determining the average values of the states in matrix form given the cyclic-mode initial condition
- Previous Chapters have demonstrated how to apply cyclic-mode modelling to different converters
- Combining provides a framework method for determining the Mean operation of the RMS calculation

6.1.2 Root-Mean Square of States

The RMS values of the state-variables can be determined by evaluating

$$\boldsymbol{x}_{rms} = \sqrt{\frac{1}{T_{sw}}\int_{t_0}^{t_0+T_{sw}} [\boldsymbol{x} \circ \boldsymbol{x}]\mathrm{d}t} \tag{6.8}$$

where $\boldsymbol{x} \circ \boldsymbol{x}$ represents the Hadamard product of $\boldsymbol{x}$, i.e., it is the vector $\boldsymbol{x} \circ \boldsymbol{x} = [x_1^2 \quad x_2^2 \quad \cdots \quad x_h^2]^T$. As with (6.1), the requirement for explicit integration is unnecessary since (6.8) can be differentiated with respect to time to give,

$$\frac{\mathrm{d}}{\mathrm{dt}}[\boldsymbol{x} \circ \boldsymbol{x}]_{\text{acc}} = \frac{1}{T_{sw}}[\boldsymbol{x} \circ \boldsymbol{x}] \tag{6.9}$$

where $[\boldsymbol{x} \circ \boldsymbol{x}]_{\text{acc}}$ is a scaled accumulated value of $\boldsymbol{x} \circ \boldsymbol{x}$, whose value is $\mathbf{0}$ at $t = t_0$. Note that $[\boldsymbol{x} \circ \boldsymbol{x}]_{\text{acc}}$ cannot be calculated from $\boldsymbol{x}_{\text{acc}}$ since $\left(\int x_n \mathrm{dt}\right)^2 \neq \int x_n^2 \mathrm{dt}$ for any $n \in [1, h]$. Referring to (6.3),

$$[\boldsymbol{x} \circ \boldsymbol{x}]_{\text{av}} = [\boldsymbol{x} \circ \boldsymbol{x}]_{\text{acc}}(t_0 + T_{\text{sw}}) - [\boldsymbol{x} \circ \boldsymbol{x}]_{\text{acc}}(t_0) = [\boldsymbol{x} \circ \boldsymbol{x}]_{\text{acc}}(t_0 + T_{\text{sw}}) \qquad (6.10)$$

From (6.8), the vector of the root mean squares of the states can be calculated as

$$\boldsymbol{x}_{rms} = \sqrt{[\boldsymbol{x} \circ \boldsymbol{x}]_{\text{acc}}(t_0 + T_{sw}) - [\boldsymbol{x} \circ \boldsymbol{x}]_{\text{acc}}(t_0)} = \sqrt{[\boldsymbol{x} \circ \boldsymbol{x}]_{\text{acc}}(t_0 + T_{sw})} \qquad (6.11)$$

6.1.3 Computationally efficient evaluation of the RMS

Equation (6.11) can be efficiently evaluated only if $[\boldsymbol{x} \circ \boldsymbol{x}]$ can be calculated directly from the piecewise state-variable matrices $\boldsymbol{A}_i$ and $\boldsymbol{B}_i$ and corresponding duties δ_i and T_{sw}.

In the derivation that follows, a sequence of operations are defined where the $[\boldsymbol{x} \circ \boldsymbol{x}]$ term is linearised allowing the cyclic averaging algorithm ((6.4)-(6.7)) to be applied to evaluate the mean-square values of the state-variables. The starting point for this process is to expand the derivative of the square of an individual state-variable (i.e. $x_n^2 = x_n x_n$ where $n \in [1, h]$ is an index for state-variable).

$$\frac{\mathrm{d}}{\mathrm{dt}}(x_n x_n) = \dot{x_n} x_n + x_n \dot{x_n} = 2 x_n \dot{x_n} \qquad (6.12)$$

It should be noted that the left-hand side of (6.12) is similar to the $\dot{w}(t)$ vector on the left hand side of (20) from [6.2]. Using $\dot{\boldsymbol{x}} = \boldsymbol{A}_i \boldsymbol{x} + \boldsymbol{B}_i$ allows some of the terms in (6.12) to be represented by the state-variable model,

$$\frac{\mathrm{d}}{\mathrm{dt}}(x_n x_n) = 2 x_n \langle \boldsymbol{A}_i \boldsymbol{x} + \boldsymbol{B}_i \rangle_n = 2 x_n \langle \boldsymbol{A}_i \boldsymbol{x} \rangle_n + 2 x_n \langle \boldsymbol{B}_i \rangle_n \qquad (6.13)$$

where $\langle \boldsymbol{P} \rangle_j$ represents an operator used to extract row j from $\boldsymbol{P}$. More formally, $\langle \boldsymbol{P} \rangle_j = \hat{e}_j{}^T \boldsymbol{P}$ where $\hat{e}_j \in \boldsymbol{R}^{h \times 1}$ is the j^{th} unit vector of $\boldsymbol{P}$ (i.e. $\hat{e}_j$ is a vector of order h, where all entries are zero except for j^{th} term which is 1). Using this notation, $x_n = \langle \boldsymbol{x} \rangle_n$. By extension, a single element of $\boldsymbol{P}$ at index (j, k) is defined as $p_{j,k} = \langle \boldsymbol{P} \rangle_{j,k} = \hat{e}_j{}^T \boldsymbol{P} \hat{e}_k$.

Equation (6.13) is for a single state-variable and it can be re-written for all $n \in [1, h]$ in a matrix form,

$$\frac{\mathrm{d}}{\mathrm{dt}}(\boldsymbol{x} \circ \boldsymbol{x}) = 2\boldsymbol{x} \circ (\boldsymbol{A}_i \boldsymbol{x}) + 2\boldsymbol{x} \circ (\boldsymbol{B}_i) \tag{6.14}$$

An individual row $n \in [1, h]$ of (6.14) can be written as,

$$\begin{aligned} \langle 2\boldsymbol{x} \circ (\boldsymbol{A}_i \boldsymbol{x}) + 2\boldsymbol{x} \circ (\boldsymbol{B}_i) \rangle_n &= 2x_n \left(\left(\sum_{s=1}^{h} \langle \boldsymbol{A}_i \rangle_{n,s} x_s \right) + \langle \boldsymbol{B}_i \rangle_n \right) \\ &= 2\langle \boldsymbol{A}_i \rangle_{n,1} x_n x_1 + \cdots + 2\langle \boldsymbol{A}_i \rangle_{n,h} x_n x_h + 2x_n \langle \boldsymbol{B}_i \rangle_n \end{aligned} \tag{6.15}$$

Applying simplifications and then recombing the rows gives,

$$\frac{\mathrm{d}}{\mathrm{dt}}(\boldsymbol{x} \circ \boldsymbol{x}) = 2\big(\boldsymbol{A}_i \circ (\boldsymbol{x}\boldsymbol{x}^{\mathrm{T}})\big)\mathbf{1}_h + 2\boldsymbol{x} \circ (\boldsymbol{B}_i) \tag{6.16}$$

where $\boldsymbol{x}\boldsymbol{x}^{\mathrm{T}}$ is the outer product of $\boldsymbol{x}$ and $\mathbf{1}_h$ is the column vector of h ones (and here represents column wise summation). The term $\boldsymbol{x}\boldsymbol{x}^{\mathrm{T}}$ as defined in (6.16) poses a problem since, as written, it cannot be expressed in form that lends itself to cyclic-mode analysis. However, $\boldsymbol{x}\boldsymbol{x}^{\mathrm{T}}$ can be vectorised giving,

$$\mathrm{vec}(\boldsymbol{x}\boldsymbol{x}^{\mathrm{T}}) = [x_1\boldsymbol{x} \quad x_2\boldsymbol{x} \quad \ldots \quad x_h\boldsymbol{x}]^T = \boldsymbol{x} \otimes \boldsymbol{x} \tag{6.17}$$

where $\otimes$ is the Kronecker product [6.3] and thereby provides all possible product combinations of the state-variables. Introducing a new vector $\overline{\boldsymbol{x}}$ which contains the original states, and their product combinations allows (6.16) to be expressed in a format compatible with cyclic-modelling. As shown by (6.18), the derivative of the squared state-variables is contained in the set $\boldsymbol{\Lambda}\overline{\boldsymbol{x}}$

$$\frac{\mathrm{d}}{\mathrm{dt}}(\boldsymbol{x} \circ \boldsymbol{x}) \equiv \boldsymbol{\Lambda}\overline{\boldsymbol{x}} \tag{6.18}$$

where all the terms in $\boldsymbol{x} \circ \boldsymbol{x}$ appear in $\boldsymbol{x} \otimes \boldsymbol{x}$, so

$$\overline{\boldsymbol{x}} = \left[\frac{\boldsymbol{x}}{\boldsymbol{x} \otimes \boldsymbol{x}}\right] \tag{6.19}$$

Although $\boldsymbol{\Lambda}$ applies a mapping to the elements of $\overline{\boldsymbol{x}}$, there is no straightforward solution to (6.18) as the left- and right-hand side vectors differ and $\boldsymbol{\Lambda}$ is not square. However, as all the terms in $\boldsymbol{x} \circ \boldsymbol{x}$ appear in $\overline{\boldsymbol{x}}$ by virtue of the Kronecker product, an equation in the solvable

form $\mathrm{d}\bar{\boldsymbol{x}}/\mathrm{d}t = \bar{\boldsymbol{A}}_i\bar{\boldsymbol{x}} + \bar{\boldsymbol{B}}_i$ can be formed and used to find the terms in $\boldsymbol{x} \circ \boldsymbol{x}$. The first step in forming this equation is to find the derivative of $\boldsymbol{x} \otimes \boldsymbol{x}$.

$$\frac{\mathrm{d}}{\mathrm{dt}}(\boldsymbol{x} \otimes \boldsymbol{x}) = \boldsymbol{x} \otimes \dot{\boldsymbol{x}} + \dot{\boldsymbol{x}} \otimes \boldsymbol{x} \tag{6.20}$$

and substituting $\dot{\boldsymbol{x}} = \boldsymbol{A}_i\boldsymbol{x} + \boldsymbol{B}_i$ into (6.20) gives

$$\frac{\mathrm{d}}{\mathrm{dt}}(\boldsymbol{x} \otimes \boldsymbol{x}) = \boldsymbol{x} \otimes (\boldsymbol{A}_i\boldsymbol{x} + \boldsymbol{B}_i) + (\boldsymbol{A}_i\boldsymbol{x} + \boldsymbol{B}_i) \otimes \boldsymbol{x} \tag{6.21}$$

It is important to note that $(\boldsymbol{x} \otimes \boldsymbol{x})$ contains all the elements of $(\boldsymbol{x} \circ \boldsymbol{x})$ and thus solving (6.21) implicitly solves (6.14). Equation (6.21) may be expanded as

$$\frac{\mathrm{d}}{\mathrm{dt}}(\boldsymbol{x} \otimes \boldsymbol{x}) = \boldsymbol{x} \otimes (\boldsymbol{A}_i\boldsymbol{x}) + \boldsymbol{x} \otimes \boldsymbol{B}_i + (\boldsymbol{A}_i\boldsymbol{x}) \otimes \boldsymbol{x} + \boldsymbol{B}_i \otimes \boldsymbol{x} \tag{6.22}$$

reordering and since $\boldsymbol{I}\boldsymbol{x} = \boldsymbol{x}$,

$$\frac{\mathrm{d}}{\mathrm{dt}}(\boldsymbol{x} \otimes \boldsymbol{x}) = (\boldsymbol{I}\boldsymbol{x}) \otimes (\boldsymbol{A}_i\boldsymbol{x}) + (\boldsymbol{A}_i\boldsymbol{x}) \otimes (\boldsymbol{I}\boldsymbol{x}) + \boldsymbol{x} \otimes \boldsymbol{B}_i + \boldsymbol{B}_i \otimes \boldsymbol{x} \tag{6.23}$$

Because Kronecker products have the mixed-product property$(\boldsymbol{A} \otimes \boldsymbol{B})(\boldsymbol{C} \otimes \boldsymbol{D}) = (\boldsymbol{A}\boldsymbol{C}) \otimes (\boldsymbol{B}\boldsymbol{D})$ [6.4],

$$\frac{\mathrm{d}}{\mathrm{dt}}(\boldsymbol{x} \otimes \boldsymbol{x}) = (\boldsymbol{I} \otimes \boldsymbol{A}_i)(\boldsymbol{x} \otimes \boldsymbol{x}) + (\boldsymbol{A}_i \otimes \boldsymbol{I})(\boldsymbol{x} \otimes \boldsymbol{x}) + \boldsymbol{x} \otimes \boldsymbol{B}_i + \boldsymbol{B}_i \otimes \boldsymbol{x} \tag{6.24}$$

again, using the mixed products property, $\boldsymbol{e} \otimes \boldsymbol{f} = (\boldsymbol{I} \otimes \boldsymbol{f})\boldsymbol{e} = (\boldsymbol{e} \otimes \boldsymbol{I})\boldsymbol{f}$ and $\boldsymbol{x}$ and $\boldsymbol{B}_i$ are vectors,

$$\frac{\mathrm{d}}{\mathrm{dt}}(\boldsymbol{x} \otimes \boldsymbol{x}) = [(\boldsymbol{I} \otimes \boldsymbol{A}_i) + (\boldsymbol{A}_i \otimes \boldsymbol{I})](\boldsymbol{x} \otimes \boldsymbol{x}) + [(\boldsymbol{I} \otimes \boldsymbol{B}_i) + (\boldsymbol{B}_i \otimes \boldsymbol{I})]\boldsymbol{x} \tag{6.25}$$

By the definition of the Kronecker sum $\oplus$ [6.3], the final form of (6.20) is given by,

$$\frac{\mathrm{d}}{\mathrm{dt}}(\boldsymbol{x} \otimes \boldsymbol{x}) = (\boldsymbol{A}_i \oplus \boldsymbol{A}_i)(\boldsymbol{x} \otimes \boldsymbol{x}) + (\boldsymbol{B}_i \oplus \boldsymbol{B}_i)\boldsymbol{x} \tag{6.26}$$

Combining with $\dot{\boldsymbol{x}} = \boldsymbol{A}_i\boldsymbol{x} + \boldsymbol{B}_i$ and (6.26) gives

$$\frac{\mathrm{d}}{\mathrm{dt}}\begin{bmatrix}\boldsymbol{x} \\ \hline \boldsymbol{x} \otimes \boldsymbol{x}\end{bmatrix} = \frac{\mathrm{d}}{\mathrm{d}t}\bar{\boldsymbol{x}} = \bar{\boldsymbol{A}}_i\bar{\boldsymbol{x}} + \bar{\boldsymbol{B}}_i \tag{6.27}$$

where

$$\begin{aligned}\bar{\boldsymbol{A}}_i &= \left[\begin{array}{c|c}\boldsymbol{A}_i & \boldsymbol{0} \\ \hline \boldsymbol{B}_i \oplus \boldsymbol{B}_i & \boldsymbol{A}_i \oplus \boldsymbol{A}_i\end{array}\right] \\ \bar{\boldsymbol{B}}_i &= \begin{bmatrix}\boldsymbol{B}_i \\ \hline 0\end{bmatrix}\end{aligned} \tag{6.28}$$

Equation (6.27) contains a linearised version of (6.14), augmented with the original state-variable model from $\dot{\boldsymbol{x}} = \boldsymbol{A}_i\boldsymbol{x} + \boldsymbol{B}_i$ and is somewhat similar to augmented system matrix $\widehat{\boldsymbol{A}}_i$ described in [6.1],

$$\frac{\mathrm{d}}{\mathrm{dt}}\widehat{\boldsymbol{x}} = \widehat{\boldsymbol{A}}_i\widehat{\boldsymbol{x}} \qquad t_{i-1} \le t \le t_i \tag{6.29}$$

where

$$\hat{\boldsymbol{x}} = \begin{bmatrix} \boldsymbol{x}(t) \\ \hline 1 \end{bmatrix}, \hat{\boldsymbol{A}}_i = \left[\begin{array}{c|c} \boldsymbol{A}_i & \boldsymbol{B}_i \\ \hline \boldsymbol{0} & 0 \end{array}\right] \tag{6.30}$$

Applying the cyclic-average process of (6.4)-(6.7) to (6.27) defines the Mean-Square system.

$$\frac{\mathrm{d}}{\mathrm{dt}}\begin{bmatrix} \bar{\boldsymbol{x}} \\ \hline 1 \\ \hline \bar{\boldsymbol{x}}_{\mathrm{acc}} \end{bmatrix} = \frac{d}{dt}\bar{\bar{\boldsymbol{z}}}(t) = \bar{\bar{\boldsymbol{A}}}_i\,\bar{\bar{\boldsymbol{z}}}\,(t) \tag{6.31}$$

where

$$\bar{\bar{\boldsymbol{A}}}_i = \left[\begin{array}{c|c|c} \bar{\boldsymbol{A}}_i & \bar{\boldsymbol{B}}_i & \boldsymbol{0} \\ \hline \boldsymbol{0} & 0 & \boldsymbol{0} \\ \hline \frac{1}{T_{\mathrm{sw}}}\boldsymbol{I} & \boldsymbol{0} & \boldsymbol{0} \end{array}\right] \tag{6.32}$$

Similar to (6.7), the average values of $\bar{\boldsymbol{x}}$, $\bar{\boldsymbol{x}}_{\mathrm{av}}$, are found by applying

$$\bar{\bar{\boldsymbol{z}}}\,(t_0 + T_{sw}) = \begin{bmatrix} \bar{\boldsymbol{x}}\,(t_0 + T_{sw}) \\ \hline 1 \\ \hline \bar{\boldsymbol{x}}_{\mathrm{av}} \end{bmatrix} = \left(\prod_{i=m}^{1} \bar{\bar{\boldsymbol{\Phi}}}_i\right)\bar{\bar{\boldsymbol{z}}}\,(t_0) \tag{6.33}$$

with

$$\bar{\bar{\boldsymbol{z}}}\,(t_0) = \begin{bmatrix} \bar{\boldsymbol{x}}\,(t_0) \\ \hline 1 \\ \hline \boldsymbol{0} \end{bmatrix} \tag{6.34}$$

$$\bar{\bar{\boldsymbol{\Phi}}}_i = \exp\left(\bar{\bar{\boldsymbol{A}}}_i\delta_i T_{sw}\right) \tag{6.35}$$

$\bar{\bar{\boldsymbol{z}}}(t_0 + T_{sw})$ contains $\bar{\boldsymbol{x}}_{\mathrm{av}}$ which is the average of all state variables and their products. To find the root-mean-squares of the state variables, the average values of x_1, x_2 etc must be extracted. $\boldsymbol{x}_{\mathrm{rms}}$ is the vector of the root mean squares of the states, and may be found from,

$$\langle \boldsymbol{x}_{\mathrm{rms}} \rangle_n = \sqrt{\langle \bar{\bar{\boldsymbol{z}}}(t_0 + T_{\mathrm{sw}}) \rangle_{h^2+(h+1)(n+1)}} = \sqrt{\langle \bar{\boldsymbol{x}}_{\mathrm{av}} \rangle_{(h+1)n}} \tag{6.36}$$

where n is the index of the state-variable.

6.2 Conclusion

This chapter outlines the development of a framework for efficient RMS computation in DC input converters, it integrates the squaring and averaging processes for calculating RMS values into matrix integrals through matrix transformations. Despite the intricate process involved in formulating this framework, a universal model applicable to all cyclic-mode models has been established. This allows the user to simply obtain the RMS values for each state variable by simply providing an accurate cyclic-mode model of a system, significantly simplifying the RMS calculation process in switching power supply systems.

This computational framework is a significant improvement to the cyclic-mode modelling technique. It not only extends the functionality of the cyclic mode modelling technique, but also makes the steady-state analysis of DC input switching power supplies much simpler and more efficient. This framework provides a methodology for the modelling and analysis of the switching power supply systems of different orders in later chapters.

6.3 References

[6.1] Visser, H. R., and P. P. J. Van den Bosch. "Modelling of periodically switching networks." *PESC'91 Record 22nd Annual IEEE Power Electronics Specialists Conference*. 1991， https://doi.org/10.1109/pesc.1991.162655.

[6.2] Kostakis, G. T., et al. “A generalized method for calculating the RMS values of switching power converters.” *IEEE Transactions on Power Electronics*, vol. 15, no. 4, July 2000, pp. 616–25. https://doi.org/10.1109/63.849031.

[6.3] Zhang, Huamin, and Feng Ding. “On the Kronecker Products and Their Applications.” *Journal of Applied Mathematics*, vol. 2013, Jan. 2013, pp. 1–8. https://doi.org/10.1155/2013/296185.

[6.4] Zhour, Zeyad Al, and Adem Kiliçman. “Some new connections between matrix products for partitioned and non-partitioned matrices.” *Computers & Mathematics With Applications*, vol. 54, no. 6, Sept. 2007, pp. 763–84. https://doi.org/10.1016/j.camwa.2006.12.045..

Chapter 7. The cyclic RMS framework applied to the boost converter

As Chapter 6 introduced the RMS cyclic-mode model framework, which is capable of determining the RMS values of signals for DC input converters. This Chapter focuses on integrating the Newton method, as discussed in Chapters 5, with the RMS cyclic-mode model framework. This integration enables the determination of RMS values for the inductor current and capacitor voltage under discontinuous operating conditions of a boost converter. Subsequent Chapters will apply this technique to a series of more complex resonant converters.

7.1 Operation of the boost converter

A boost converter consists of an inductor, a switch, a diode, and a capacitor. When the switch is turned on, the inductor charges and stores energy in the form of a magnetic field. When the switch is turned off, the energy stored in the inductor is transferred via the diode to the output capacitor and load, resulting in a higher output voltage. Assuming the circuit operated using PWM, the output voltage can be controlled by adjusting the duty cycle of the switch, which determines the time the switch turned off following being turned on at the start of a PWM cycle. The operation of a boost converter can be categorized into two operation conditions: discontinuous operation and continuous operation [7.1].

In continuous operation (CCM), the inductor current does not drop to zero during each switching cycle. In this mode, the inductor is always partially charged, and the peak-to-peak ripple current is relatively low compared to the output current.

In discontinuous operation (DCM), the inductor current drops to zero during each switching

cycle. In this mode, the inductor is allowed to discharge before the next switching cycle has fully started. As a result, the peak-peak ripple is high compared to the load current.

A boost converter circuit diagram is shown in Fig. 7.1. It consists of an inductor L to store the energy; a capacitor C to filter the output voltage and reduce ripple; a MOSFET switch S is operated with a duty cycle δ_1 and at switching frequency f_{sw}; a diode D to prevent reverse current flow.

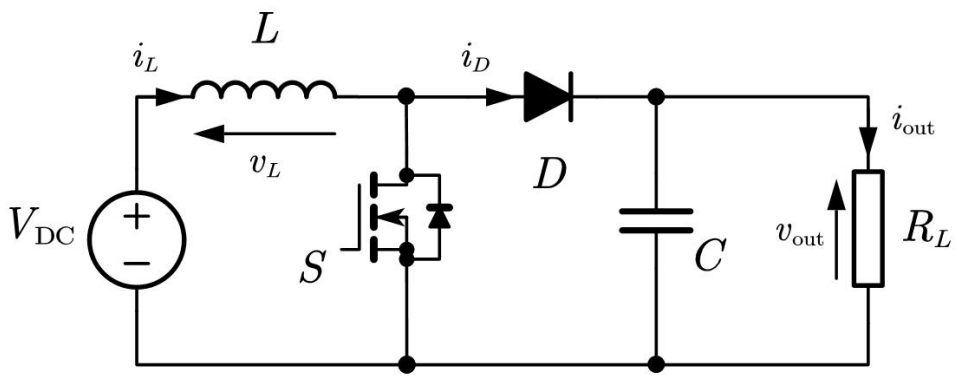

Fig. 7.1. Circuit diagram of a boost converter

Due to the computational framework's complexity outlined in Chapter 6 being directly proportional to the original system's complexity, this chapter simplifies the validation process by focusing on a second-order system with a less complex structure: a boost converter operating in DCM operation. Initially, the application of Newton's method with cyclic-mode modelling, introduced in Chapter 5, is employed to precisely calculate the duty cycle for each mode of this system model. Following this, the RMS calculation framework presented in Chapter 7 is utilised to generate waveform plots of key variables and calculate their RMS values. Because the behaviours of the boost converter in DCM have been comprehensively detailed in Chapter 2 and will not be repeated here.

7.2 Derivation of RMS cyclic-mode model for the boost converter

The following approach is used to derive the cyclic-model for the boost:

1. For each mode, determine the differential equations for the inductor current and capacitor voltage and then form a piecewise linear state-variable model
2. Use cyclic-mode analysis with Newton's method to determine the cyclic-mode model initial condition and each mode durations
3. Apply the RMS cyclic-mode modelling process described in Chapter 6 to determine the RMS values of the state-variables

7.2.1 Differential equations and piecewise state-variable model for each mode

In Mode 1 (M1) where $t_0 \leq t \leq t_1$, S1 turns on. The derivative of the inductor current is given by:

$$\dot{i}_L = \frac{v_L}{L} = \frac{V_{\mathrm{DC}}}{L} \tag{7.1}$$

The derivative of the capacitor voltage is,

$$\dot{v}_C = \frac{i_C}{C} = -\frac{v_C}{CR_L} \tag{7.2}$$

Combining equations (7.2) and (7.3) , combining provides the state-variable model for M1:

$$\begin{bmatrix} \dot{i}_L \\ \dot{v}_C \end{bmatrix} = \begin{bmatrix} 0 & 0 \\ 0 & -\frac{1}{CR_L} \end{bmatrix} \begin{bmatrix} i_L \\ v_C \end{bmatrix} + \begin{bmatrix} \frac{V_{\mathrm{DC}}}{L} \\ 0 \end{bmatrix} \tag{7.3}$$

(7.4) can be rewritten as,

$$\dot{\boldsymbol{x}} = \boldsymbol{A}_1 \boldsymbol{x} + \boldsymbol{B}_1 \tag{7.4}$$

where the state-vector is

$$\boldsymbol{x} = [i_L \; v_C \,]^{\mathrm{T}} = [x_1 \; x_2 \,]^{\mathrm{T}} \tag{7.5}$$

In Mode 2 (M2) for $t_1 \leq t \leq t_2$, the MOSFET is off, D is on, and so the inductor current decreases until it reaches zero. The derivative of the inductor current is described by:

$$\dot{i}_L = \frac{V_{\mathrm{DC}} - v_{\mathrm{d}}}{L} - \frac{v_C}{L} \tag{7.6}$$

The derivative of the capacitor voltage is determined as:

$$\dot{v}_C = \frac{i_C}{C} = \frac{i_L}{C} - \frac{v_C}{CR_L} \tag{7.7}$$

Combining (7.7) and (7.8) gives the state-variable model for M2,

$$\begin{bmatrix} \dot{i}_L \\ \dot{v}_C \end{bmatrix} = \begin{bmatrix} 0 & \frac{1}{L} \\ \frac{1}{C} & -\frac{1}{CR_L} \end{bmatrix} \begin{bmatrix} i_L \\ v_C \end{bmatrix} + \begin{bmatrix} \frac{V_{\mathrm{DC}} - v_d}{L} \\ 0 \end{bmatrix} = \boldsymbol{A}_2\boldsymbol{x} + \boldsymbol{B}_2 \tag{7.8}$$

In Mode 3 (M3), where $t_2 \le t \le t_3$, S remains off. D turns off at $t=t_2$ since the inductor current i_L has reached zero. The derivative of the inductor current is zero,

$$\dot{i}_L = 0 \tag{7.9}$$

For the derivative of the capacitor voltage is,

$$\dot{v}_C = \frac{i_C}{C} = -\frac{v_C}{CR_L} \tag{7.10}$$

Combining (7.10) and (7.11) provides a state-variable model for Mode 3,

$$\begin{bmatrix} \dot{i}_L \\ \dot{v}_C \end{bmatrix} = \begin{bmatrix} 0 & 0 \\ 0 & -\frac{1}{CR_L} \end{bmatrix} \begin{bmatrix} i_L \\ v_C \end{bmatrix} + \begin{bmatrix} 0 \\ 0 \end{bmatrix} = \boldsymbol{A}_3\boldsymbol{x} + \boldsymbol{B}_3 \tag{7.11}$$

Equations (7.4), (7.9) and (7.12) can be combined to form a piecewise linear equation based on the mode duration times.

$$\dot{\boldsymbol{x}}(t) = \begin{cases} \boldsymbol{A}_1\boldsymbol{x}(t_0) + \boldsymbol{B}_1 & t_0 \le t \le t_1 \\ \boldsymbol{A}_2\boldsymbol{x}(t_1) + \boldsymbol{B}_2 & t_1 \le t \le t_2 \\ \boldsymbol{A}_3\boldsymbol{x}(t_2) + \boldsymbol{B}_3 & t_2 \le t \le t_3 \end{cases} \tag{7.12}$$

7.2.2 Cyclic-mode model of the boost converter

Since the converter is operating in a cyclic-mode, the final state variables at the end of the cycle, $\boldsymbol{x}(t_3)$, should equal the cycle's initial condition $\boldsymbol{x}(t_0)$. Thus,

$$\boldsymbol{x}(t_0) = \boldsymbol{x}(t_3) = \boldsymbol{x}(t_0 + T_{sw}) \tag{7.13}$$

Since the input is DC, $\boldsymbol{B}_i$ is constant, allowing the integral to be evaluated to give the time solution,

$$\boldsymbol{x} = \boldsymbol{\Phi}_i\boldsymbol{x}(t_{i-1}) + \boldsymbol{\Gamma}_i \qquad t_{i-1} \le t < t_i \tag{7.14}$$

where $\boldsymbol{\Phi}_i = \exp\left(\boldsymbol{A}_i(t - t_{i-1})\right)$. Exp(…) represents the matrix exponential function. Additionally, $\boldsymbol{\Gamma}_i = \boldsymbol{A}_i^{-1}[\boldsymbol{\Phi}_i - \boldsymbol{I}]\boldsymbol{B}_i$ and $\boldsymbol{I}$ is an identity matrix having the same dimensions as $\boldsymbol{A}_i$.

Starting from $t = t_0$ and using (7.15), the state vector at the end of Mode 1 becomes:

$$\boldsymbol{x}(t_1) = \boldsymbol{\Phi}_1 \boldsymbol{x}(t_0) + \boldsymbol{\Gamma}_1 \tag{7.15}$$

Similarly, the state-vector at the end of Mode 2 is given by,

$$\boldsymbol{x}(t_2) = \boldsymbol{\Phi}_2 \boldsymbol{x}(t_1) + \boldsymbol{\Gamma}_2 \tag{7.16}$$

At the end of Mode 3, the state vector becomes:

$$\boldsymbol{x}(t_3) = \boldsymbol{\Phi}_3 \boldsymbol{x}(t_2) + \boldsymbol{\Gamma}_3 \tag{7.17}$$

The initial condition for the cyclic-mode, $\boldsymbol{x}(t_0)$, is derived from the final condition of each mode. Combining (7.16) to (7.18) gives,

$$\boldsymbol{x}(t_3) = (\boldsymbol{\Phi}_3(\boldsymbol{\Phi}_2(\boldsymbol{\Phi}_1 \boldsymbol{x}(t_0) + \boldsymbol{\Gamma}_1) + \boldsymbol{\Gamma}_2) + \boldsymbol{\Gamma}_3) = \boldsymbol{\Phi}_{\text{tot}} \boldsymbol{x}(t_0) + \boldsymbol{\Gamma}_{\text{tot}} \tag{7.18}$$

where,

$$\boldsymbol{\Phi}_{\text{tot}} = \boldsymbol{\Phi}_3 \boldsymbol{\Phi}_2 \boldsymbol{\Phi}_1 \text{ and } \boldsymbol{\Gamma}_{\text{tot}} = \boldsymbol{\Phi}_3(\boldsymbol{\Phi}_2(\boldsymbol{\Gamma}_1) + \boldsymbol{\Gamma}_2) + \boldsymbol{\Gamma}_3 \tag{7.19}$$

Substituting (7.19) into (7.14) yields:

$$\boldsymbol{x}(t_3) = (\boldsymbol{I} - \boldsymbol{\Phi}_{\text{tot}})^{-1}(\boldsymbol{\Gamma}_{\text{tot}}) = \boldsymbol{x}(t_0) \tag{7.20}$$

Thus, the expand expression of (7.21) is,

$$\boldsymbol{x}(t_0) = (\boldsymbol{I} - \boldsymbol{\Phi}_3 \boldsymbol{\Phi}_2 \boldsymbol{\Phi}_1)^{-1}(\boldsymbol{\Phi}_3 \boldsymbol{\Phi}_2 \boldsymbol{\Gamma}_1 + \boldsymbol{\Phi}_3 \boldsymbol{\Gamma}_2 + \boldsymbol{\Gamma}_3) \tag{7.21}$$

Having obtained $\boldsymbol{x}(t_0)$ and each mode duration, the state-variables throughout a cyclic can be determined using:

$$\boldsymbol{x}(t) = \begin{cases} \boldsymbol{\Phi}_1 \boldsymbol{x}(t_0) + \boldsymbol{\Gamma}_1 & t_0 \le t \le t_1 \\ \boldsymbol{\Phi}_2 \boldsymbol{x}(t_1) + \boldsymbol{\Gamma}_2 & t_1 \le t \le t_2 \\ \boldsymbol{\Phi}_3 \boldsymbol{x}(t_2) + \boldsymbol{\Gamma}_3 & t_2 \le t < t_3 \end{cases} \tag{7.22}$$

where 1,2 and 3 is the mode index; $\boldsymbol{\Phi}_i = \exp\left(\boldsymbol{A}_i(t - t_{i-1})\right)$ and $\boldsymbol{\Gamma}_i = \boldsymbol{A}_i^{-1}[\boldsymbol{\Phi}_i - \boldsymbol{I}]\boldsymbol{B}_i$.

7.2.3 Determining the cyclic-mode initial condition using Newton's method

The duration of mode M1 is the control input δ_1 and is assumed to be known. However, the durations of modes 2 & 3 (δ_2 & δ_3=1-δ_1-δ_2) depend on operating condition and, hence,

they must be determined alongside $\boldsymbol{x}(t_0)$. Below provides a detailed description of Newton's method used to determine unknown mode durations and model initial condition $\boldsymbol{x}(t_0)$.

For the specified mode sequence, the converter's operation in a single cycle depends on its initial conditions $\boldsymbol{x}(t_0)$ and the duty cycles of Mode 2 δ_2. Defining $\boldsymbol{X}$ as a vector representing these values:

$$\boldsymbol{X} = [\boldsymbol{x}^T(t_0) \quad \delta_2]^T \tag{7.23}$$

The initial condition model from (7.22) relates to both the initial condition and the duration of mode 2.

$$[g_1(\boldsymbol{X}) \quad g_2(\boldsymbol{X})]^T = (\boldsymbol{I} - \boldsymbol{\Phi}_{\text{tot}})^{-1}\boldsymbol{\Gamma}_{\text{tot}} - \boldsymbol{x}(t_0) \tag{7.24}$$

Duty cycles δ_2 is determined by the inductor current at end of Mode 2 is zero which is,

$$i_L(t_2^-) = 0 \tag{7.25}$$

where represent by cyclic-mode model is,

$$[1 \quad 0][\boldsymbol{\Phi}_2(\boldsymbol{\Phi}_1\boldsymbol{x}(t_0) + \boldsymbol{\Gamma}_1) + \boldsymbol{\Gamma}_2] = 0 \tag{7.26}$$

So $g_3(\boldsymbol{X})$ in this case is based on (7.27),

$$g_3(\boldsymbol{X}) = [1 \quad 0][\boldsymbol{\Phi}_2(\boldsymbol{\Phi}_1\boldsymbol{x}(t_0) + \boldsymbol{\Gamma}_1) + \boldsymbol{\Gamma}_2] \tag{7.27}$$

$\boldsymbol{G}(\boldsymbol{X})$ is derived from equations (7.25) and (7.28).

$$\boldsymbol{G}(\boldsymbol{X}) = \begin{bmatrix} g_1(\boldsymbol{X}) \\ g_2(\boldsymbol{X}) \\ \hline g_3(\boldsymbol{X}) \end{bmatrix} = \left[\begin{array}{c} (\boldsymbol{I} - \boldsymbol{\Phi}_{\text{tot}})^{-1}\boldsymbol{\Gamma}_{\text{tot}} - \boldsymbol{x}(t_0) \\ \hline [1 \quad 0][\boldsymbol{\Phi}_2(\boldsymbol{\Phi}_1\boldsymbol{x}(t_0) + \boldsymbol{\Gamma}_1 + \boldsymbol{\Gamma}_2] + v_{\text{d}} \end{array}\right] \tag{7.28}$$

Then using Newton's iterative method described in previous Chapters to estimate $\boldsymbol{X}$, beginning with an initial value of $\boldsymbol{X}^0$,

$$\boldsymbol{X}^{k+1} = \boldsymbol{X}^k - \left[\boldsymbol{J}\left(\boldsymbol{X}^k\right)\right]^{-1}\boldsymbol{G}(\boldsymbol{X}^k) \tag{7.29}$$

With k representing the current iteration step, and $\boldsymbol{J}\left(\boldsymbol{X}^k\right)$ denotes the numerical Jacobian matrix of partial derivatives for that step.

$$\boldsymbol{J}(\boldsymbol{X}) = \frac{\partial \boldsymbol{G}}{\partial X} = \begin{bmatrix} \frac{\partial g_1}{\partial X_1} & \frac{\partial g_1}{\partial X_2} & \frac{\partial g_1}{\partial X_3} \\ \frac{\partial g_2}{\partial X_1} & \frac{\partial g_2}{\partial X_2} & \frac{\partial g_2}{\partial X_3} \\ \frac{\partial g_3}{\partial X_1} & \frac{\partial g_3}{\partial X_2} & \frac{\partial g_3}{\partial X_3} \end{bmatrix} = \begin{bmatrix} \frac{\partial g_1}{\partial i_L} & \frac{\partial g_1}{\partial v_C} & \frac{\partial g_1}{\partial \delta_2} \\ \frac{\partial g_2}{\partial i_L} & \frac{\partial g_2}{\partial v_C} & \frac{\partial g_2}{\partial \delta_2} \\ \frac{\partial g_3}{\partial i_L} & \frac{\partial g_3}{\partial v_C} & \frac{\partial g_3}{\partial \delta_2} \end{bmatrix} \tag{7.30}$$

Each element of the Jacobian matrix at k^{th} iteration is given by,

$$\left[\frac{\partial g_1(\boldsymbol{X}^k)}{\partial X_i^k} \quad \frac{\partial g_2(\boldsymbol{X}^k)}{\partial X_i^k} \quad \frac{\partial g_3(\boldsymbol{X}^k)}{\partial X_i^k} \right]^{\mathrm{T}} \approx \frac{\boldsymbol{G}(\boldsymbol{X}^k + \Delta \boldsymbol{X}_i) - \boldsymbol{G}(\boldsymbol{X}^k)}{\alpha_i} \tag{7.31}$$

The stopping criterion for the iteration is achieved when the L^1-norm diminishes below an acceptable value λ,

$$\left| \boldsymbol{X}^{\text{final}} - \boldsymbol{X}^{\text{final}-1} \right| < \lambda \tag{7.32}$$

where $\boldsymbol{X}^{\text{final}}$ is a vector of true root of function $\boldsymbol{G}(\boldsymbol{X})$ which are the precise values of $\boldsymbol{x}(t_0)$ and δ_2.

7.2.4 RMS cyclic-mode modelling for the boost converter

The next step is to construct the Mean-Square system. As outlined in Chapter 6, the averaging piecewise model is initially derived. The formulas to construct averaging piecewise model is shown below,

$$\dot{\boldsymbol{z}}(t) = \widetilde{\boldsymbol{A}}_i \boldsymbol{z}(t) \tag{7.33}$$

$$\boldsymbol{z} = \begin{bmatrix} \boldsymbol{x} \\ \hline 1 \\ \hline \boldsymbol{x}_{\text{acc}} \end{bmatrix}, \quad \tilde{\boldsymbol{A}}_i = \left[\begin{array}{c|c|c} \boldsymbol{A}_i & \boldsymbol{B}_i & \boldsymbol{0} \\ \hline \boldsymbol{0} & 0 & \boldsymbol{0} \\ \hline \frac{1}{T_{sw}} \boldsymbol{I} & \boldsymbol{0} & \boldsymbol{0} \end{array}\right] \tag{7.34}$$

where $\boldsymbol{A}_i$ is $h \times h$ square matrix, $\widetilde{\boldsymbol{A}}_i$ is a square matrix of order $(2h+1)$, $\boldsymbol{I}$ is a square identity matrix of order h and the $\boldsymbol{0}$ matrices are sized as required. The cyclic-mode initial condition for the with-averaging models (6.4) is

$$\boldsymbol{z}(t_0) = \begin{bmatrix} \boldsymbol{x}(t_0) \\ \hline 1 \\ \hline \boldsymbol{0} \end{bmatrix} \tag{7.35}$$

The initial step is to derive the augmented matrix $\widetilde{\boldsymbol{A}}_1$ using (6.5) and (7.4).

$$\tilde{\boldsymbol{A}}_1 = \left[\begin{array}{cc|c|cc} 0 & 0 & \frac{V_{\mathrm{DC}}}{L} & 0 & 0 \\ 0 & -\frac{1}{CR_L} & 0 & 0 & 0 \\ \hline 0 & 0 & 0 & 0 & 0 \\ \hline \frac{1}{T_{\mathrm{sw}}} & 0 & 0 & 0 & 0 \\ 0 & \frac{1}{T_{\mathrm{sw}}} & 0 & 0 & 0 \end{array}\right] \tag{7.36}$$

Similarly, the formulas for $\widetilde{\boldsymbol{A}}_2$ and $\widetilde{\boldsymbol{A}}_3$ are derived using (7.9), (7.12) and (7.35). Next, using (7.36), we determine the initial value of $\boldsymbol{z}(t)$, denoted as $\boldsymbol{z}(t_0)$.

$$\boldsymbol{z}(t_0) = \begin{bmatrix} \boldsymbol{x}(t_0) \\ \hline 1 \\ \hline \boldsymbol{0} \end{bmatrix} = \begin{bmatrix} x_1(t_0) \\ x_2(t_0) \\ \hline 1 \\ \hline 0 \\ 0 \end{bmatrix} \tag{7.37}$$

where $\boldsymbol{x}(t_0) = \begin{bmatrix} x_1(t_0) \\ x_2(t_0) \end{bmatrix}$

The cyclic average value of state-vector, $\boldsymbol{x}_{\mathrm{av}}$, is found by cascading mode solutions starting from the initial condition,

$$\boldsymbol{z}(t_0 + T_{sw}) = \begin{bmatrix} \boldsymbol{x}(t_0 + T_{\mathrm{sw}}) \\ \hline 1 \\ \hline \boldsymbol{x}_{\mathrm{av}} \end{bmatrix} = \left(\prod_{i=m}^{1} \tilde{\boldsymbol{\Phi}}_i \right) \boldsymbol{z}(t_0) \tag{7.38}$$

where $\tilde{\boldsymbol{\Phi}}_i = \exp\left(\widetilde{\boldsymbol{A}}_i \delta_i T_{\mathrm{sw}}\right)$.

The periodic average value of the state variable $\boldsymbol{x}$ can be determined by recalling (6.7), which is

$$\boldsymbol{z}(t_0+T_{sw})=\tilde{\boldsymbol{\Phi}}_3\tilde{\boldsymbol{\Phi}}_2\tilde{\boldsymbol{\Phi}}_1\boldsymbol{z}(t_0)=\begin{bmatrix}\boldsymbol{x}(t_0+T_{\mathrm{sw}})\\ \hline 1\\ \hline \boldsymbol{x}_{\mathrm{av}}\end{bmatrix}=\begin{bmatrix}x_1(t_0+T_{\mathrm{sw}})\\ x_2(t_0+T_{\mathrm{sw}})\\ \hline 1\\ \hline x_{1(\mathrm{av})}\\ x_{2(\mathrm{av})}\end{bmatrix} \tag{7.39}$$

where $\tilde{\boldsymbol{\Phi}}_i=\exp\left(\tilde{\boldsymbol{A}}\ \ {}_i\delta_i T_{\mathrm{sw}}\right)$, and $\boldsymbol{x}_{\mathrm{av}}$ denotes the periodic average value of $\boldsymbol{x}$.

Having obtained the cyclic averaging model, the next step is to acquire the extended piecewise linear model which $\overline{\boldsymbol{x}}$ as the state variable, as outlined in equations below,

$$\frac{\mathrm{d}}{\mathrm{dt}}\begin{bmatrix}\boldsymbol{x}\\ \hline \boldsymbol{x}\otimes\boldsymbol{x}\end{bmatrix}=\frac{\mathrm{d}}{\mathrm{d}t}\overline{\boldsymbol{x}}=\overline{\boldsymbol{A}}_i\overline{\boldsymbol{x}}+\overline{\boldsymbol{B}}_i \tag{7.40}$$

where

$$\begin{aligned}\overline{\boldsymbol{A}}_i&=\left[\begin{array}{c|c}\boldsymbol{A}_i & \boldsymbol{0}\\ \hline \boldsymbol{B}_i\oplus\boldsymbol{B}_i & \boldsymbol{A}_i\oplus\boldsymbol{A}_i\end{array}\right]\\ \overline{\boldsymbol{B}}_i&=\begin{bmatrix}\boldsymbol{B}_i\\ \hline 0\end{bmatrix}\end{aligned} \tag{7.41}$$

Initially, it is essential to derive the matrices $\overline{\boldsymbol{A}}_i$ and $\overline{\boldsymbol{B}}_i$. Taking $\overline{\boldsymbol{A}}_1$ and $\overline{\boldsymbol{B}}_1$ as examples, the expressions for the Kronecker sums $\boldsymbol{A}_1\oplus\boldsymbol{A}_1$ and $\boldsymbol{B}_1\oplus\boldsymbol{B}_1$ are necessary, according to (7.42). Then based on reference [7.2] along with (7.4), the expression of $\boldsymbol{A}_1\oplus\boldsymbol{A}_1$ and $\boldsymbol{B}_1\oplus\boldsymbol{B}_1$ can be obtained,

$$\boldsymbol{A}_1\oplus\boldsymbol{A}_1=\begin{bmatrix}0 & 0 & 0 & 0\\ 0 & -\frac{1}{CR_L} & 0 & 0\\ 0 & 0 & -\frac{1}{CR_L} & 0\\ 0 & 0 & 0 & -\frac{2}{CR_L}\end{bmatrix}\ \text{and}\ \ \boldsymbol{B}_1\oplus\boldsymbol{B}_1=\begin{bmatrix}2\frac{V_{\mathrm{DC}}}{L} & 0\\ 0 & \frac{V_{\mathrm{DC}}}{L}\\ 0 & \frac{V_{\mathrm{DC}}}{L}\\ 0 & 0\end{bmatrix} \tag{7.42}$$

By substituting (7.43) and (7.4) into (7.42), the expressions of $\overline{\boldsymbol{A}}_1$ and $\overline{\boldsymbol{B}}_1$ can be obtained.

$$\bar{\boldsymbol{A}}_1=\left[\begin{array}{c|c}\boldsymbol{A}_1 & \boldsymbol{0} \\ \hline \boldsymbol{B}_1\oplus\boldsymbol{B}_1 & \boldsymbol{A}_1\oplus\boldsymbol{A}_1\end{array}\right]=\left[\begin{array}{cc|cccc} 0 & 0 & 0 & 0 & 0 & 0 \\ 0 & -\frac{1}{CR_L} & 0 & 0 & 0 & 0 \\ \hline 2\frac{V_{\mathrm{DC}}}{L} & 0 & 0 & 0 & 0 & 0 \\ 0 & \frac{V_{\mathrm{DC}}}{L} & 0 & -\frac{1}{CR_L} & 0 & 0 \\ 0 & \frac{V_{\mathrm{DC}}}{L} & 0 & 0 & -\frac{1}{CR_L} & 0 \\ 0 & 0 & 0 & 0 & 0 & -\frac{2}{CR_L}\end{array}\right] \tag{7.43}$$

$$\bar{\boldsymbol{B}}_1=\left[\begin{array}{c} \frac{V_{\mathrm{DC}}}{L} \\ \hline 0 \\ 0 \\ 0 \\ 0\end{array}\right] \tag{7.44}$$

Next, using (7.41), we can obtain an expression for the derivative of $\bar{\boldsymbol{x}}(t)$ in the interval $t_0 \le t \le t_1$,

$$\frac{\mathrm{d}}{\mathrm{d}t}\bar{\boldsymbol{x}}=\frac{\mathrm{d}}{\mathrm{d}t}\left[\begin{array}{c}\boldsymbol{x} \\ \hline \boldsymbol{x}\otimes\boldsymbol{x}\end{array}\right]=\left[\begin{array}{c} x_1 \\ x_2 \\ \hline x_1x_1 \\ x_1x_2 \\ x_2x_1 \\ x_2x_2\end{array}\right]=\bar{\boldsymbol{A}}_1\bar{\boldsymbol{x}}(t_0)+\bar{\boldsymbol{B}}_1 \quad t_0\le t\le t_1$$

$$=\left[\begin{array}{cc|cccc} 0 & 0 & 0 & 0 & 0 & 0 \\ 0 & -\frac{1}{CR_L} & 0 & 0 & 0 & 0 \\ \hline 2\frac{V_{\mathrm{DC}}}{L} & 0 & 0 & 0 & 0 & 0 \\ 0 & \frac{V_{\mathrm{DC}}}{L} & 0 & -\frac{1}{CR_L} & 0 & 0 \\ 0 & \frac{V_{\mathrm{DC}}}{L} & 0 & 0 & -\frac{1}{CR_L} & 0 \\ 0 & 0 & 0 & 0 & 0 & -\frac{2}{CR_L}\end{array}\right]\left[\begin{array}{c} x_1(t_0) \\ x_2(t_0) \\ \hline x_1(t_0)x_1(t_0) \\ x_1(t_0)x_2(t_0) \\ x_2(t_0)x_1(t_0) \\ x_2(t_0)x_2(t_0)\end{array}\right]+\left[\begin{array}{c} \frac{V_{\mathrm{DC}}}{L} \\ 0 \\ 0 \\ 0 \\ 0 \\ 0\end{array}\right] \tag{7.45}$$

Similarly, the expansion expressions for $\bar{\boldsymbol{A}}_2$, $\bar{\boldsymbol{B}}_2$, $\bar{\boldsymbol{A}}_3$ and $\bar{\boldsymbol{B}}_3$ can be derived based on equations (7.9) and (7.12) respectively.

The piecewise linear model for $\bar{\boldsymbol{x}}$ throughout the cycle is as follows:

$$\frac{\mathrm{d}}{\mathrm{d}t}\bar{\boldsymbol{x}}=\frac{\mathrm{d}}{\mathrm{d}t}\left[\begin{array}{c}\boldsymbol{x} \\ \hline \boldsymbol{x}\otimes\boldsymbol{x}\end{array}\right]=\begin{cases}\bar{\boldsymbol{A}}_1\bar{\boldsymbol{x}}(t_0)+\bar{\boldsymbol{B}}_1 & t_0\le t\le t_1 \\ \bar{\boldsymbol{A}}_2\bar{\boldsymbol{x}}(t_1)+\bar{\boldsymbol{B}}_2 & t_1\le t\le t_2 \\ \bar{\boldsymbol{A}}_3\bar{\boldsymbol{x}}(t_2)+\bar{\boldsymbol{B}}_3 & t_2\le t\le t_3\end{cases} \tag{7.46}$$

Next, by applying the cyclic averaging process in Chapter 6 (which are equations (6.4), (6.5), (6.6) and (6.7)) to state variable $\bar{\boldsymbol{x}}$, we can derive the mean-square system. Implementing this model allows for the determination of the periodic average values of x_1^2 and x_2^2 . Finally, the RMS values are obtained by calculating the square root of these average values.

The formulas for mean-square system are,

$$\frac{\mathrm{d}}{\mathrm{dt}}\begin{bmatrix}\bar{\boldsymbol{x}}\\ \hline 1\\ \hline \bar{\boldsymbol{x}}_{\mathrm{acc}}\end{bmatrix}=\frac{d}{dt}\bar{\bar{\boldsymbol{z}}}(t)=\bar{\bar{\boldsymbol{A}}}_i\,\bar{\bar{\boldsymbol{z}}}(t) \tag{7.47}$$

where

$$\bar{\bar{\boldsymbol{A}}}_i=\left[\begin{array}{c|c|c}\bar{\boldsymbol{A}}_i & \bar{\boldsymbol{B}}_i & \mathbf{0}\\ \hline \mathbf{0} & 0 & \mathbf{0}\\ \hline \dfrac{1}{T_{\mathrm{sw}}}\boldsymbol{I} & \mathbf{0} & \mathbf{0}\end{array}\right] \tag{7.48}$$

The average values of $\bar{\boldsymbol{x}}$, $\bar{\boldsymbol{x}}_{\mathrm{av}}$, are found by applying

$$\bar{\bar{\boldsymbol{z}}}(t_0+T_{sw})=\begin{bmatrix}\bar{\boldsymbol{x}}(t_0+T_{sw})\\ \hline 1\\ \hline \bar{\boldsymbol{x}}_{\mathrm{av}}\end{bmatrix}=\left(\prod_{i=m}^{1}\bar{\bar{\boldsymbol{\Phi}}}_i\right)\bar{\bar{\boldsymbol{z}}}(t_0) \tag{7.49}$$

where $\bar{\bar{\boldsymbol{\Phi}}}_i=\exp\left(\bar{\bar{\boldsymbol{A}}}_i\delta_i T_{sw}\right)$ with

$$\bar{\bar{\boldsymbol{z}}}(t_0)=\begin{bmatrix}\bar{\boldsymbol{x}}(t_0)\\ \hline 1\\ \hline \mathbf{0}\end{bmatrix} \tag{7.50}$$

To build the mean-square cyclic-mode model, first, using $\bar{\bar{\boldsymbol{A}}}_1$ as an example. The response matrix $\bar{\bar{\boldsymbol{A}}}_1$ of the mean square piecewise linear model's structure is given by (7.49). By substituting (7.44) and (7.45) into (7.49), we can derive the matrix expansion expression for $\bar{\bar{\boldsymbol{A}}}_1$,

$$\overline{\overline{\boldsymbol{A}}}_1 = \left[\begin{array}{c|c|c} \bar{\boldsymbol{A}}_1 & \bar{\boldsymbol{B}}_1 & \mathbf{0} \\ \hline \mathbf{0} & 0 & \mathbf{0} \\ \hline \frac{1}{T_{\mathrm{sw}}}\boldsymbol{I} & \mathbf{0} & \mathbf{0} \end{array}\right]$$

$$= \left[\begin{array}{cccccc|c|ccccccc} 0 & 0 & 0 & 0 & 0 & 0 & \frac{V_{\mathrm{DC}}}{L} & 0 & 0 & 0 & 0 & 0 & 0 \\ 0 & -\frac{1}{CR_L} & 0 & 0 & 0 & 0 & 0 & 0 & 0 & 0 & 0 & 0 & 0 \\ 2\frac{V_{\mathrm{DC}}}{L} & 0 & 0 & 0 & 0 & 0 & 0 & 0 & 0 & 0 & 0 & 0 & 0 \\ 0 & \frac{V_{\mathrm{DC}}}{L} & 0 & -\frac{1}{CR_L} & 0 & 0 & 0 & 0 & 0 & 0 & 0 & 0 & 0 \\ 0 & \frac{V_{\mathrm{DC}}}{L} & 0 & 0 & -\frac{1}{CR_L} & 0 & 0 & 0 & 0 & 0 & 0 & 0 & 0 \\ 0 & 0 & 0 & 0 & 0 & -\frac{2}{CR_L} & 0 & 0 & 0 & 0 & 0 & 0 & 0 \\ \hline 0 & 0 & 0 & 0 & 0 & 0 & 0 & 0 & 0 & 0 & 0 & 0 & 0 \\ \hline \frac{1}{T_{\mathrm{sw}}} & 0 & 0 & 0 & 0 & 0 & 0 & 0 & 0 & 0 & 0 & 0 & 0 \\ 0 & \frac{1}{T_{\mathrm{sw}}} & 0 & 0 & 0 & 0 & 0 & 0 & 0 & 0 & 0 & 0 & 0 \\ 0 & 0 & \frac{1}{T_{\mathrm{sw}}} & 0 & 0 & 0 & 0 & 0 & 0 & 0 & 0 & 0 & 0 \\ 0 & 0 & 0 & \frac{1}{T_{\mathrm{sw}}} & 0 & 0 & 0 & 0 & 0 & 0 & 0 & 0 & 0 \\ 0 & 0 & 0 & 0 & \frac{1}{T_{\mathrm{sw}}} & 0 & 0 & 0 & 0 & 0 & 0 & 0 & 0 \\ 0 & 0 & 0 & 0 & 0 & \frac{1}{T_{\mathrm{sw}}} & 0 & 0 & 0 & 0 & 0 & 0 & 0 \end{array}\right] \tag{7.51}$$

Similarly, $\overline{\overline{\boldsymbol{A}}}_2$, and $\overline{\overline{\boldsymbol{A}}}_3$ can be derived using similar process. Next, the piecewise linear state variable model of $\bar{\bar{\boldsymbol{z}}}(t)$ can be written down.

$$\frac{\mathrm{d}}{\mathrm{d}t}\bar{\bar{\boldsymbol{z}}}(t) = \frac{\mathrm{d}}{\mathrm{dt}}\left[\begin{array}{c} \bar{\boldsymbol{x}} \\ \hline 1 \\ \hline \bar{\boldsymbol{x}}_{\mathrm{acc}} \end{array}\right] = \begin{cases} \overline{\overline{\boldsymbol{A}}}_1 \bar{\bar{\boldsymbol{z}}}(t_0) & t_0 \le t \le t_1 \\ \overline{\overline{\boldsymbol{A}}}_2 \bar{\bar{\boldsymbol{z}}}(t_1) & t_1 \le t \le t_2 \\ \overline{\overline{\boldsymbol{A}}}_3 \bar{\bar{\boldsymbol{z}}}(t_2) & t_1 \le t \le t_2 \end{cases} \tag{7.52}$$

where $\bar{\bar{\boldsymbol{z}}}(t)$ initial value $\bar{\bar{\boldsymbol{z}}}(t_0)$ is based on (7.36) given by,

$$\bar{\bar{\boldsymbol{z}}}(t_0) = \left[\begin{array}{c} \bar{\boldsymbol{x}}(t_0) \\ \hline 1 \\ \hline \mathbf{0} \end{array}\right] = \left[\begin{array}{c} \bar{x}_1(t_0) \\ \bar{x}_2(t_0) \\ \bar{x}_3(t_0) \\ \bar{x}_4(t_0) \\ \bar{x}_5(t_0) \\ \bar{x}_6(t_0) \\ \hline 1 \\ \hline 0 \\ 0 \\ 0 \\ 0 \\ 0 \\ 0 \end{array}\right] = \left[\begin{array}{c} x_1(t_0) \\ x_2(t_0) \\ x_1(t_0)x_1(t_0) \\ x_1(t_0)x_2(t_0) \\ x_2(t_0)x_1(t_0) \\ x_2(t_0)x_2(t_0) \\ \hline 1 \\ \hline 0 \\ 0 \\ 0 \\ 0 \\ 0 \\ 0 \end{array}\right] \tag{7.53}$$

Finally, after determining the system's initial values, running this Mean-Square cyclic-mode model system yields the periodic average value of $\bar{\boldsymbol{x}}$, encompassing the periodic average values of x_1^2 and x_2^2.

$$\bar{\bar{z}}\,(t_0+T_{sw}) = \bar{\bar{\Phi}}_3\,\bar{\bar{\Phi}}_2\,\bar{\bar{\Phi}}_1\,\bar{\bar{z}}\,(t_0) = \begin{bmatrix} \bar{\boldsymbol{x}}\,(t_0+T_{\mathrm{sw}}) \\ \hline 1 \\ \hline \bar{\boldsymbol{x}}_{\mathrm{av}} \end{bmatrix} = \begin{bmatrix} x_1(t_0+T_{\mathrm{sw}}) \\ x_2(t_0+T_{\mathrm{sw}}) \\ x_1(t_0+T_{\mathrm{sw}})\,x_1(t_0+T_{\mathrm{sw}}) \\ x_1(t_0+T_{\mathrm{sw}})\,x_2(t_0+T_{\mathrm{sw}}) \\ x_2(t_0+T_{\mathrm{sw}})\,x_1(t_0+T_{\mathrm{sw}}) \\ x_2(t_0+T_{\mathrm{sw}})\,x_2(t_0+T_{\mathrm{sw}}) \\ \hline 1 \\ \hline x_{1(\mathrm{av})} \\ x_{2(\mathrm{av})} \\ x_1 x_{1(\mathrm{av})} \\ x_1 x_{2(\mathrm{av})} \\ x_2 x_{1(\mathrm{av})} \\ x_2 x_{2(\mathrm{av})} \end{bmatrix} \tag{7.54}$$

where $\bar{\bar{\boldsymbol{\Phi}}}_i = \exp\left(\bar{\bar{\boldsymbol{A}}}_i \delta_i T_{sw}\right)$

The RMS values of the original state variable $\boldsymbol{x}$ can be obtained from

$$\langle \boldsymbol{x}_{\mathrm{rms}} \rangle_n = \sqrt{\langle \bar{\bar{\boldsymbol{z}}}(t_0+T_{\mathrm{sw}}) \rangle_{h^2+(h+1)(n+1)}} = \sqrt{\langle \bar{\boldsymbol{x}}_{\mathrm{av}} \rangle_{(h+1)n}} \tag{7.55}$$

This represents the RMS values of the inductor current i_L and capacitor voltage v_C.

$$\begin{aligned} i_{L(\mathrm{RMS})} &= \sqrt{\langle \bar{\bar{\boldsymbol{z}}}(t_0+T_{\mathrm{sw}}) \rangle_{10}} = \sqrt{\langle \bar{\boldsymbol{x}}_{\mathrm{av}} \rangle_3} \\ v_{C(\mathrm{RMS})} &= \sqrt{\langle \bar{\bar{\boldsymbol{z}}}(t_0+T_{\mathrm{sw}}) \rangle_{13}} = \sqrt{\langle \bar{\boldsymbol{x}}_{\mathrm{av}} \rangle_6} \end{aligned} \tag{7.56}$$

7.3 Model validation

To verify the accuracy of the model, a boost converter was designed to operate from $V_{\mathrm{in}} = 12$ V and provide an output voltage at 48 V. Table 7.1 lists the component values for this design.

Table 7.1. The boost converter components values for the design

Component's name	Component's value
R_L	180 Ω − 500 Ω
L	100 uH
C	470 µF
f_{sw}	25 kHz
V_{DC}	12 V
v_{out}	48 V

The formula to determine the output voltage ratio is:

$$\frac{v_{\mathrm{out}}}{V_{\mathrm{DC}}} = \frac{LT_{\mathrm{sw}} + \sqrt{LT_{\mathrm{sw}}(LT_{\mathrm{sw}} + 2(\delta_1 T_{\mathrm{sw}})^2 R_L)}}{2LT_{\mathrm{sw}}} \tag{7.57}$$

The SPICE model schematics is shown in Fig. 7.3,

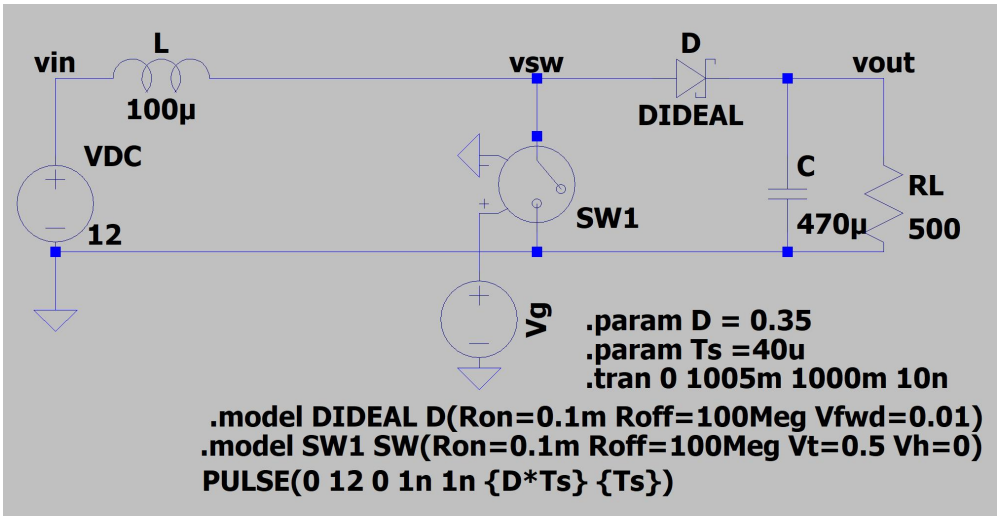

Fig. 7.2. SPICE model schematics of the boost converter at R_L=500 Ω

For the first experiment the load is to $R_L = 500\ \Omega$. The duty ratio of Mode 1 is determined usings (7.58) and the data from Table 7.1. Thus, define $\delta_1 = 0.35$. An initial estimate of δ_2, of δ_2=0.15 and so $\delta_3 = 0.5$. By employing Newton's method a refined value δ_2 as 0.1153 was obtained. Fig. 7.3 shows the comparison of SPICE model output voltage with cyclic-model output voltage, the red line represents the cyclic-mode model results, while the

grey line depicts the SPICE model results. The cyclic-model yields an average output voltage of 48.4207 V, nearly matching the SPICE model's 48.421 V.

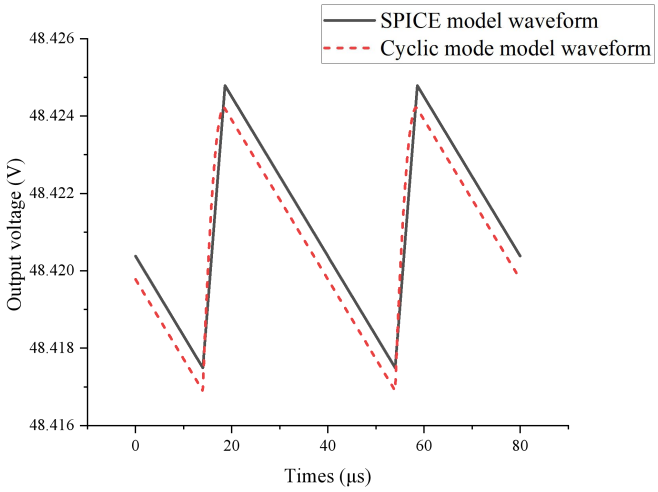

Fig. 7.3. The output voltage v_C waveforms of cyclic-mode model and SPICE simulation

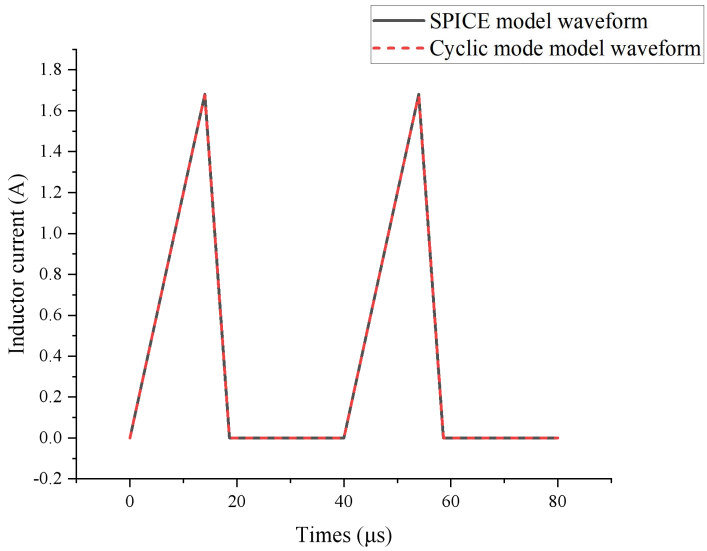

Fig. 7.4. The inductor current i_L waveforms of cyclic-mode model and SPICE simulation

Fig. 7.4 shows the inductor current waveform comparison of the SPICE model and the cyclic-mode model. The SPICE inductor current average value is 390.9 mA, the cyclic-mode

model inductor current average value is 390.06 mA. The accuracy of cyclic-mode model has been validated.

The RMS values of the cyclic-mode model, derived using the process described in (7.34)-(7.57), are compared with the LT SPICE model RMS values in Table 7.2.

Table 7.2. The RMS values comparison between RMS cyclic-mode model with SPICE model

	i_L	v_C
RMS Cyclic-mode model	661.62 mA	48.4207 V
SPICE model	661.32 mA	48.421 V
Error	0.045%	0.00062%

Since cyclic-mode modelling can output periodic waveforms of state variables, the accuracy of the waveforms depends on the time step set by the plotting, if a shorter time step is taken a more accurate waveform will be obtained, and the corresponding simulation time will increase. Afterwards, the definition of RMS value can be used to find the RMS value from the waveform. Similarly, the accuracy of the RMS value still depends on the time step of the plotting. This method of plotting the waveform with the corresponding time step and then calculating the RMS value from the waveform is known as the waveform evaluation RMS method, or simply the waveform method.

To compare the effectiveness of calculating RMS values using the RMS calculation framework (also known as the framework method) and the waveform method, a comparison of the two methods performance was conducted. Since the accuracy of the framework method has been proven through previous validations, the RMS values calculated by the framework method were used as a benchmark to determine the relative error between the waveform method and the framework method. Using i_L as an example the calculation formula of relative error is shown in (7.58),

$$\text{Relative error } i_L(t) = \frac{i_{\text{L (waveform method RMS)}}(t) - i_{\text{L (framework method RMS)}}}{i_{\text{L (framework method RMS)}}} \times 100\% \tag{7.58}$$

where $i_{\text{L (waveform method RMS)}}(t)$ means the RMS value of i_L calculated by the waveform method after consuming t milliseconds, and $i_{\text{L (framework method RMS)}}$ means the RMS value of i_L calculated by the framework method.

The accuracy of the waveform method at different time steps can be assessed by testing the relative error of the RMS values derived by the waveform method at various time steps against the results of the framework method. Simultaneously, the time required for the waveform method to find the RMS values of all state variables at different time steps is recorded. By varying the time step of the waveform method, relative error data can be obtained for different running times.

By continuously decreasing the time step of the waveform method, a graph can be plotted to show the relative error as a function of the run time of the waveform method. The horizontal axis of the graph represents the run time, while the vertical axis indicates the relative error in the waveform method results compared to the framework method results. The plot is shown in Fig. 7.5.

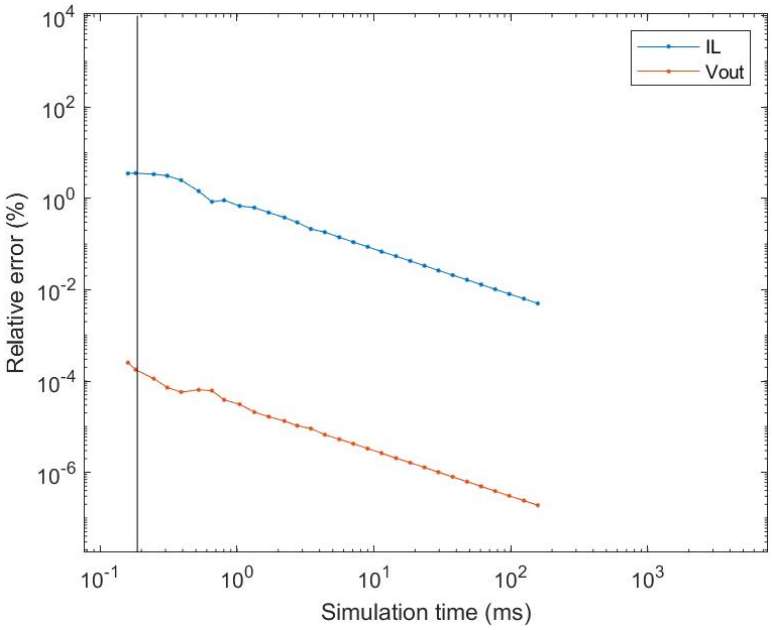

Fig. 7.5. The relative error figure as a function of the waveform method operation time.

Each point in the graph represents the value of the relative error between the RMS value obtained by the waveform method at that run time and the RMS value obtained by the framework method. The blue and red lines in the figure represent the relative error of the RMS values of i_L and v_C, respectively, as a function of the runtime of the waveform method.

In addition, since the running time required to calculate the RMS values of all state variables using the framework method can be measured and it is a fixed value. A grey vertical line with this value as the horizontal coordinate is plotted in the figure to facilitate subsequent comparative analyses.

The grey vertical line in the figure indicates the time taken to obtain the RMS value using the framework method, approximately 0.2 millisecond. The intersection of the blue and grey lines indicates that, at an equal time spent to the framework method, the inductor current's RMS value obtained by the waveform method has 5% error compared to the framework method result. The intersection of the orange and grey lines shows that, with a similar time investment as the framework method, the capacitor voltage's RMS value acquired by the waveform method exhibits negligible error relative to the framework method result.

Both curves display a similar trend: with each increase in runtime for the waveform method, which corresponds to enhanced waveform accuracy, the results of the waveform method progressively approximate those obtained by the framework method. This trend validates the accuracy of the framework method. The results are that the framework method showed a fast run time while maintaining accuracy. Conversely, the waveform method's accuracy directly correlates with runtime, needs longer durations to achieve superior precision.

The figure shows that both computational methods consume time on the order of milliseconds, which might suggest that constructing a complex modelling process for such a small efficiency gain is not worthwhile. But we believe that this approach is significant for several reasons.

1. The framework method minimises potential errors in the RMS calculation step, which is crucial in applications requiring high accuracy.

2. While both methods consume milliseconds when the circuit parameters are fixed, the time saved by the computational framework becomes significant when some parameters (e.g., inductance values) are variable within a range. In such cases, RMS values need to be derived for each parameter configuration.

3. The cyclic RMS framework is straightforward to program, whereas the waveform method is more complex. The waveform method requires determining the modes at each time point before generating the waveform, adding to the programming complexity.

Finally, we compare the cyclic-mode model results with the results from experimental measurements.

The circuit functions in a discontinuous mode, maintaining a load voltage of 48 V and a load resistance ranging from 178 to 366 ohms. Fig. 7.6, Fig. 7.7 and Fig. 7.8 display the inductor current waveform and capacitor voltage under various load conditions: $R_L = 178\ \Omega$ for condition 1, $R_L = 218\ \Omega$ for condition 2, and $R_L = 366\ \Omega$ for condition 3, with a consistent load voltage of 48 V.

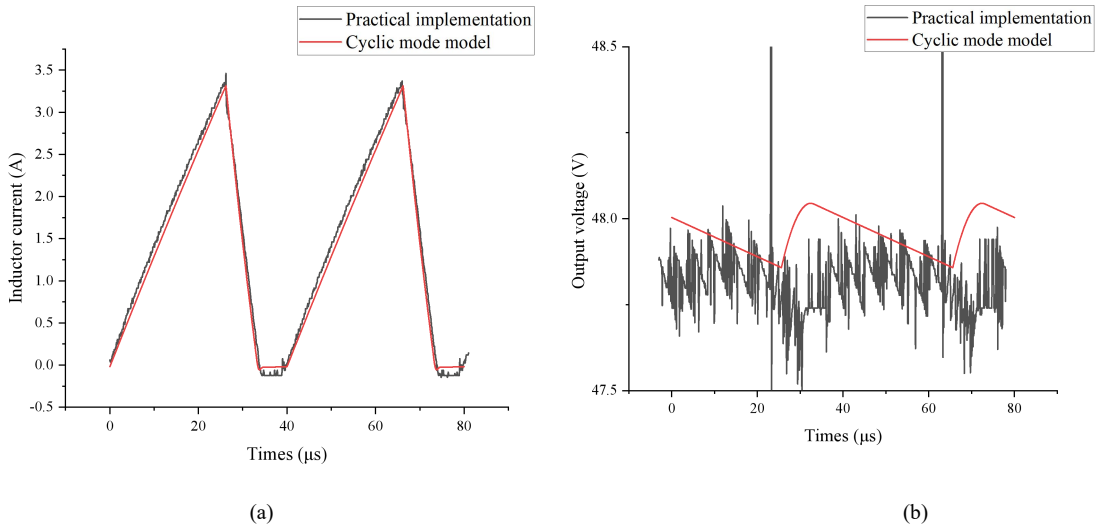

(a) (b)

Fig. 7.6. Comparison of inductor current (a) and capactor voltage (b) waveform between cyclic-mode model and practical implementation at $R_L = 178\ \Omega$

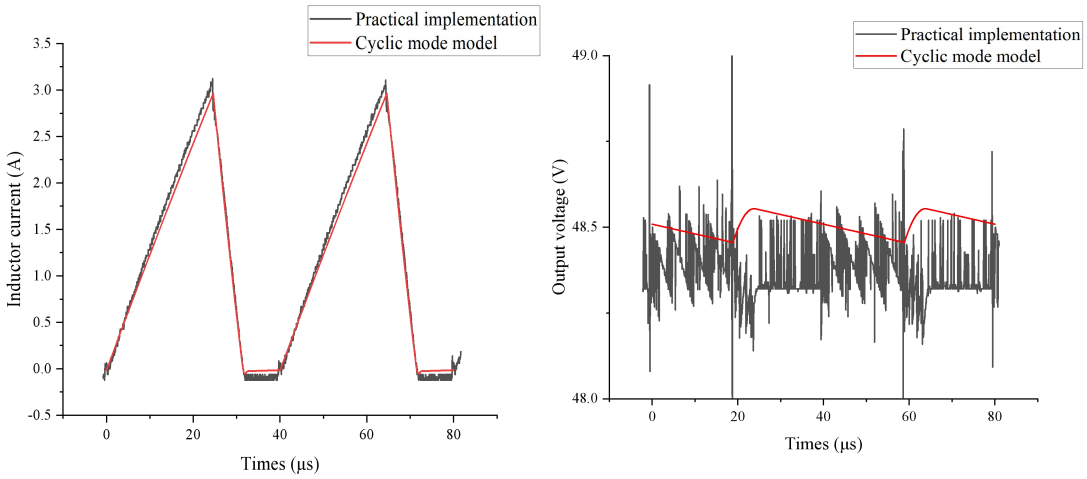

(a) (b)

Fig. 7.7. Comparison of inductor current (a) and capactor voltage (b) waveform between cyclic-mode model and practical implementation at $R_L = 218\ \Omega$

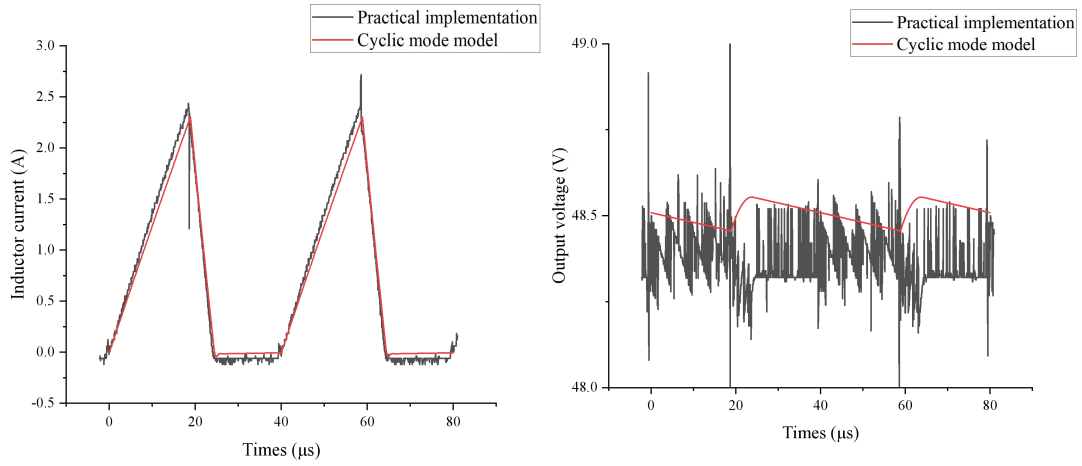

(a) (b)

Fig. 7.8. Comparison of inductor current (a) and capactor voltage (b) waveform between cyclic-mode model and practical implementation at at $R_L = 366\ \Omega$

7.4 Conclusion

This chapter describes the process of calculating the waveforms of key variables in a switching power supply using given parameters and finally derive their RMS values.

Focusing on the boost converter operating in DCM, Newton's method combined with the cycle model is first applied to obtain the converter's exact operating state. Then, the cyclic RMS framework for this converter is constructed. By incorporating the converter's operating states into the calculation framework, the periodic waveforms of key converter variables and their RMS values are obtained. The accuracy of this analysis is demonstrated through comparison with SPICE simulation results. Additionally, the comparison results show that the cyclic RMS framework is more effective than the waveform evaluation RMS method in RMS values calculation.

The results in this chapter demonstrate that, firstly, the cyclic RMS framework has excellent performance and is simple to use. It can be used as an effective method to RMS values of the key variables of the switching power supply, this effectively extends the use of cyclic-mode modelling and makes it more competitive. Also, through the use of Newton's method, the accuracy requirements of the framework on the inputs are reduced, making the analysis of DC input switching power supplies simpler. The next improvement goal is to build a complete analysis flow for switching power supplies using these two techniques as a starting point.

7.5 References

[7.1] Hasaneen, B. M., and Adel A. Elbaset Mohammed. "Design and simulation of DC/DC boost converter." 2008 12th International Middle-East Power System Conference. 2008, https://doi.org/10.1109/mepcon. MEPCON.2008.4562340.

[7.2] Al, Zeyad Al, and Adem Kiliçman. “Some new connections between matrix products for partitioned and non-partitioned matrices.” *Computers & Mathematics With Applications*, vol. 54, no. 6, Sept. 2007, pp. 763–84. https://doi.org/10.1016/j.camwa.2006.12.045.

Chapter 8. Evaluation of Root-Mean-Square state variables in class E, EF_2 inverters, and LLC converters using cyclic-mode modelling

As Chapter 7 have utilized the combination of the Newton method and the cyclic RMS framework on a boost converter operating under discontinuous conditions, resulting in the determination of its steady-state operating conditions and RMS values of signals. This Chapter first consolidates this combined technique into a universal framework for accurately computing the RMS values of the state vectors in any state-space system operating in cyclic steady-state. Subsequently, the method is applied to class E inverter and class EF_2 inverter operating under suboptimal conditions, as well as the LLC converter in a discontinuous operating state to provide further validation.

The process to build the cyclic RMS framework can be split into the following steps:

1. Fundamental understanding of the system: The foremost step of this method is based on a preliminary understanding of the system, which includes its switching states, circuit configuration, and operational waveforms.

2. Creation of a state-variable model: Develop a state variable model of the system by analysing and utilizing the circuit's structural configuration.

3. Decompose in piecewise linear model: The operation of the system over a single cycle is decomposed into different modes (circuit configurations), enabling the formulation of its piecewise linear equations.

4. Estimate mode duties: A rough prediction of the sequence and duration of different modes is made. Techniques such as Fundamental Mode Analysis or the Describing Function method can be employed for this purpose.

5. Estimate the cyclic-mode initial condition: Input the initial estimates of the modes' duty cycles into the cyclic-mode model, thereby obtaining an estimate of the state variable at the start of cyclic-mode model $\boldsymbol{x}(t_0)$

6. Using Newton's method to refine the estimated cyclic-mode initial condition and mode sequence: Using Newton's method and initial estimates of mode durations, combined with the cyclic-mode model, allows for precise estimation of each mode's duration and the initial values of the cyclic-mode model $\boldsymbol{x}(t_0)$.

7. Applying cyclic RMS calculation framework: After precisely defining the cyclic-mode, the RMS cyclic-mode modelling framework is employed to obtain the signal's waveform, periodic average values, and RMS values.

The flow chart of this process is shown in Fig. 8.1.

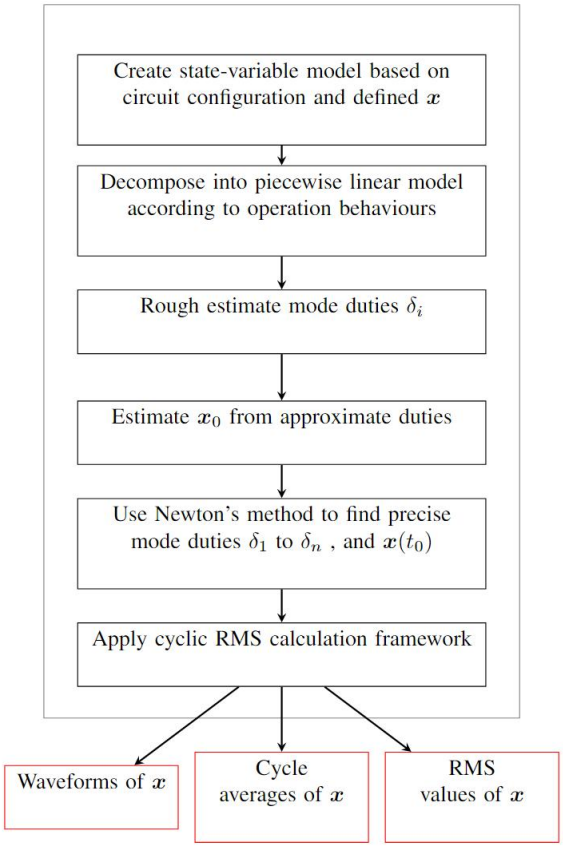

Fig. 8.1. Flow chart of the RMS cyclic-mode modelling process

8.1 RMS cyclic-mode modelling of the class E inverter

This section applies the RMS cyclic-mode framework to a suboptimal operating class E inverter, starting with the derivation of the state-variable model. Subsequently, the inverter's piecewise linear model is constructed. As Chapter 5 has already iterated the final values of $\boldsymbol{x}$ and δ using Newton's method, constructing the cyclic-mode model is not necessary. The following text describes the construction process of the RMS-cyclic-mode system. Finally, the RMS values of each state variable are obtained using the results from Newton's method.

8.1.1 Derivation of state-variable model for the class E inverter

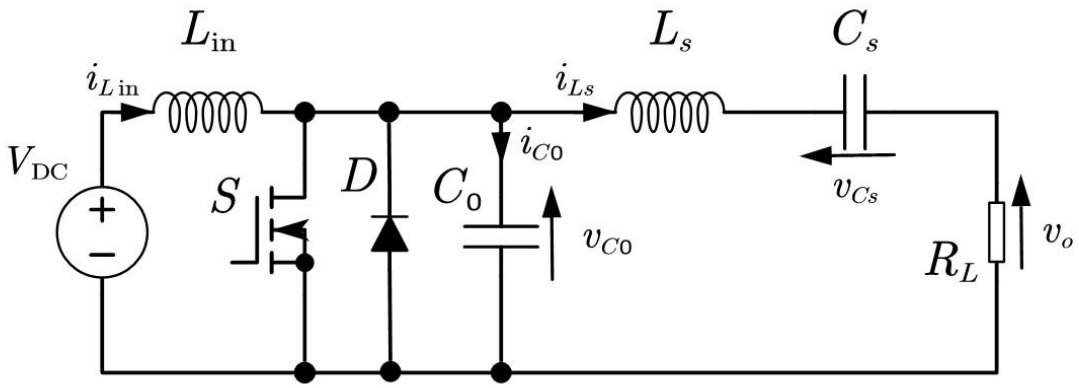

Fig. 8.2. Circuit diragram of the class E inverter

The inverter circuit diagram is shown in Fig. 8.2. Recalling Chapter 5 the piecewise linear state variables model of suboptimal class E inverter are shown below.

During Mode 1, $t_0 \le t < t_1$: the linear state variables model is

$$\begin{bmatrix} \dot{i}_{L\text{in}} \\ i_{Ls} \\ v_{Cs} \\ v_{C0} \end{bmatrix} = \begin{bmatrix} 0 & 0 & 0 & 0 \\ 0 & -\dfrac{R_{\text{L}}}{L_{\text{s}}} & -\dfrac{1}{L_{\text{s}}} & 0 \\ 0 & \dfrac{1}{C_{\text{s}}} & 0 & 0 \\ 0 & 0 & 0 & 0 \end{bmatrix} \begin{bmatrix} i_{L\text{in}} \\ i_{Ls} \\ v_{Cs} \\ v_{C0} \end{bmatrix} + \begin{bmatrix} \dfrac{V_{\text{DC}}}{L_{\text{in}}} \\ 0 \\ 0 \\ 0 \end{bmatrix} = \boldsymbol{A}_1\boldsymbol{x} + \boldsymbol{B}_1 \tag{8.1}$$

where

$$\boldsymbol{x} = [i_{L\text{in}} \quad i_{Ls} \quad v_{Cs} \quad v_{C0}]^{\text{T}} = [x_1 \quad x_2 \quad x_3 \quad x_4]^{\text{T}} \tag{8.2}$$

For Mode 2, $t_1 \le t < t_2$: the model is become,

$$\begin{bmatrix} \dot{i}_{L\text{in}} \\ i_{Ls} \\ v_{Cs} \\ v_{C0} \end{bmatrix} = \begin{bmatrix} 0 & 0 & 0 & -\dfrac{1}{L_{\text{in}}} \\ 0 & -\dfrac{R_{\text{L}}}{L_{\text{s}}} & -\dfrac{1}{L_{\text{s}}} & \dfrac{1}{L_{\text{s}}} \\ 0 & \dfrac{1}{C_{\text{s}}} & 0 & 0 \\ \dfrac{1}{C_0} & -\dfrac{1}{C_0} & 0 & 0 \end{bmatrix} \begin{bmatrix} i_{L\text{in}} \\ i_{Ls} \\ v_{Cs} \\ v_{C0} \end{bmatrix} + \begin{bmatrix} \dfrac{V_{\text{DC}}}{L_{\text{in}}} \\ 0 \\ 0 \\ 0 \end{bmatrix} = \boldsymbol{A}_2\boldsymbol{x} + \boldsymbol{B}_2 \tag{8.3}$$

During Mode 3, $t_2 \le t < t_3$: the model is,

$$\begin{bmatrix} \dot{i}_{Lin} \\ \dot{i}_{Ls} \\ \dot{v}_{Cs} \\ \dot{v}_{C0} \end{bmatrix} = \begin{bmatrix} 0 & 0 & 0 & -\frac{1}{L_{\text{in}}} \\ 0 & -\frac{R_{\text{L}}}{L_{\text{s}}} & -\frac{1}{L_{\text{s}}} & \frac{1}{L_{\text{s}}} \\ 0 & \frac{1}{C_{\text{s}}} & 0 & 0 \\ 0 & 0 & 0 & 0 \end{bmatrix} \begin{bmatrix} i_{Lin} \\ i_{Ls} \\ v_{Cs} \\ v_{C0} \end{bmatrix} + \begin{bmatrix} \frac{V_{\text{DC}}}{L_{\text{in}}} \\ 0 \\ 0 \\ 0 \end{bmatrix} = \boldsymbol{A}_3\boldsymbol{x} + \boldsymbol{B}_3 \qquad (8.4)$$

Hence, combining (8.1), (8.3) and (8.4), along with the mode sequences, a piecewise linear equation can be formulated, which is contingent on the duration times of the respective modes,

$$\dot{\boldsymbol{x}}(t) = \begin{cases} \boldsymbol{A_1}\boldsymbol{x}(t_0) + \boldsymbol{B_1} & t_0 \le t < t_1 \\ \boldsymbol{A_2}\boldsymbol{x}(t_1) + \boldsymbol{B_2} & t_1 \le t < t_2 \\ \boldsymbol{A_3}\boldsymbol{x}(t_2) + \boldsymbol{B_3} & t_2 \le t < t_3 \end{cases} \qquad (8.5)$$

Since the cyclic-mode model of the class E inverter was constructed in Chapter 5, and the operating conditions of the inverter were obtained using a Newton's method in Chapter 5, the next step is to perform RMS cyclic-mode modelling of the inverter.

8.1.2 RMS cyclic-mode modelling of the class E inverter

After deriving the piecewise linear state variables model for the class E inverter and combining it with the derivation process of the RMS cyclic-mode model for the boost converter, as detailed in Chapter 7, the derivation process for the class E inverter RMS cyclic-mode model can be outlined as follows:

1. Derive the cyclic-mode model for $\boldsymbol{x}$.
2. Using Newton's method to obtain the inverter steady state operating conditions.
3. Establish the piecewise linear model with $\bar{\boldsymbol{x}}$ as the state variable.
4. Derive the cyclic-mode model for $\bar{\boldsymbol{x}}$, then obtaining the initial value $\bar{\boldsymbol{x}}(t_0)$
5. Derive the expression of $\bar{\bar{\boldsymbol{A}}}_i$, and subsequently the cyclic-mode model for $\bar{\bar{\boldsymbol{z}}}(t)$.
6. Use $\bar{\boldsymbol{x}}(t_0)$ to obtain the initial value expression for $\bar{\bar{\boldsymbol{z}}}(t_0)$, and get the $\bar{\bar{\boldsymbol{z}}}(t_0 + T_{sw})$.

Since the initial conditions for the three-mode operation of the class E inverter have already been determined using the Newton method in Chapter 6, Steps 1 and 2 can be omitted. Therefore, the modelling process begins from step 3.

First to build the piecewise linear model for $\bar{\boldsymbol{x}}$. First is to obtain the Kronecker sum expressions for $\boldsymbol{A}_i \oplus \boldsymbol{A}_i$ and $\boldsymbol{B}_i \oplus \boldsymbol{B}_i$. According to the definition of the Kronecker product, if $\boldsymbol{E}$ is an $m \times n$ matrix and $\boldsymbol{F}$ as a $p \times q$ matrix, the Kronecker product, $\boldsymbol{E} \otimes \boldsymbol{F}$ is an $mp \times nq$ block matrix:

$$\boldsymbol{E} \otimes \boldsymbol{F} = \begin{bmatrix} E_{11}\boldsymbol{F} & \cdots & E_{1n}\boldsymbol{F} \\ \vdots & \ddots & \vdots \\ E_{m1}\boldsymbol{F} & \ldots & E_{mn}\boldsymbol{F} \end{bmatrix} \tag{8.6}$$

For $\boldsymbol{E}$ as a $m \times m$ matrix and $\boldsymbol{F}$ as a $n \times n$ matrix, the expression of Kronecker sum $\boldsymbol{E} \oplus \boldsymbol{F}$, is

$$\boldsymbol{E} \oplus \boldsymbol{F} = \boldsymbol{E} \otimes \boldsymbol{I}_n + \boldsymbol{I}_m \otimes \boldsymbol{F} \tag{8.7}$$

Here, the size of $\boldsymbol{I}$ (the identity matrix) changes to ensure that the dimensions of $\boldsymbol{E} \otimes \boldsymbol{I}$ and $\boldsymbol{I} \otimes \boldsymbol{F}$ are equal, allowing for their addition.

The expressions for $\boldsymbol{A}_i \oplus \boldsymbol{A}_i$ and $\boldsymbol{B}_i \oplus \boldsymbol{B}_i$ can be derived by combining (8.6) and (8.7) with (8.1), (8.3) and (8.4), respectively. $\boldsymbol{A}_i \oplus \boldsymbol{A}_i$ is $h^2 \times h^2$ square matrix, in this case the dimensions are 16×16. $\boldsymbol{B}_i \oplus \boldsymbol{B}_i$ is $h^2 \times h$ matrix, in this case the dimensions of them are 16×4. Due to size constraints, their expanded forms are not included here.

The derivation formulas for $\bar{\boldsymbol{A}}_i$ and $\bar{\boldsymbol{B}}_i$ are given by (8.8)

$$\bar{\boldsymbol{A}}_i = \left[\begin{array}{c|c} \boldsymbol{A}_i & \boldsymbol{0} \\ \hline \boldsymbol{B}_i \oplus \boldsymbol{B}_i & \boldsymbol{A}_i \oplus \boldsymbol{A}_i \end{array}\right], \quad \bar{\boldsymbol{B}}_i = \begin{bmatrix} \boldsymbol{B}_i \\ \hline 0 \end{bmatrix} \tag{8.8}$$

So, we get $\overline{\boldsymbol{A}}_i$ is $(h^2+h)\times(h^2+h)$ square matrix with dimensions 20×20 in this case, and $\overline{\boldsymbol{B}}_i$ are $(h^2+h)\times 1$ matrix of size 20×1. After obtaining the expressions for $\overline{\boldsymbol{A}}_i$ and $\overline{\boldsymbol{B}}_i$, the piecewise linear equations of $\overline{\boldsymbol{x}}$ can be written,

(8.9)

where

$$\overline{\boldsymbol{x}} = [x_1 \ \cdots \ x_4 \ \ x_1x_1 \ \cdots \ x_1x_4 \ \ x_2x_1 \ \cdots \ x_2x_4 \ \ x_3x_1 \ \cdots \ x_3x_4 \ \ x_4x_1 \ \cdots \ x_4x_4]^{\mathrm{T}} \tag{8.10}$$

To facilitate the computation within the RMS cyclic-mode model, initial values $\overline{\boldsymbol{x}}(t_0)$ are required. Equation (8.11) reveals that every element in the vector $\overline{\boldsymbol{x}}(t_0)$ results from combining one or two elements of $\boldsymbol{x}(t_0)$. If the vector $\boldsymbol{x}(t_0)$ is known, the values of $\overline{\boldsymbol{x}}(t_0)$'s elements are also determined, thereby establishing the values of $\overline{\boldsymbol{x}}(t_0)$.

$$\begin{aligned}\overline{\boldsymbol{x}}(t_0) &= \left[\frac{\boldsymbol{x}(t_0)}{\boldsymbol{x}(t_0)\otimes\boldsymbol{x}(t_0)}\right] \\ &= [x_1(t_0) \ \cdots \ x_4(t_0) \mid x_1(t_0)x_1(t_0) \ \ldots \ x_1(t_0)x_4(t_0) \ \cdots \ x_4(t_0)x_4(t_0)]^{\mathrm{T}}\end{aligned} \tag{8.11}$$

After acquiring the initial value $\boldsymbol{x}(t_0)$ from the original cyclic-mode model, the initial value $\overline{\boldsymbol{x}}(t)$ can be directly determined by (8.11). This approach eliminates the complex calculations involved in computing $\overline{\boldsymbol{x}}(t_0)$ based on steady-state operating conditions and using the extended cyclic-mode model.

After determining the initial value $\overline{\boldsymbol{x}}(t_0)$, the cyclic-mode model for $\overline{\boldsymbol{x}}(t)$ can be established,

$$\overline{\boldsymbol{x}}(t) = \begin{cases} \overline{\boldsymbol{\Phi}}_1(t)\overline{\boldsymbol{x}}(t_0) + \overline{\boldsymbol{\Gamma}}_1(t) & t_0 \le t < t_1 \\ \overline{\boldsymbol{\Phi}}_2(t)\overline{\boldsymbol{x}}(t_1) + \overline{\boldsymbol{\Gamma}}_2(t) & t_1 \le t < t_2 \\ \overline{\boldsymbol{\Phi}}_3(t)\overline{\boldsymbol{x}}(t_2) + \overline{\boldsymbol{\Gamma}}_3(t) & t_2 \le t < t_3 \end{cases} \tag{8.12}$$

where $\overline{\boldsymbol{\Phi}}_i(t) = \exp(\overline{\boldsymbol{A}}_i(t-t_{i-1}))$ and $\boldsymbol{\Gamma}_i(t) = \overline{\boldsymbol{A}}_i^{-1}[\overline{\boldsymbol{\Phi}}_i(t) - \boldsymbol{I}]\overline{\boldsymbol{B}}_i$.

The subsequent step involves applying the cyclic averaging method to the extended cyclic-mode model in (8.9) . Initially, determine the expression of $\overline{\overline{\boldsymbol{A}}}_i$ using (8.13)

$$\overline{\overline{\boldsymbol{A}}}_i = \left[\begin{array}{c|c|c} \bar{\boldsymbol{A}}_i & \bar{\boldsymbol{B}}_i & \mathbf{0} \\ \hline \mathbf{0} & 0 & \mathbf{0} \\ \hline \frac{1}{T_{\mathrm{sw}}}\boldsymbol{I} & \mathbf{0} & \mathbf{0} \end{array}\right] \tag{8.13}$$

$\overline{\overline{\boldsymbol{A}}}_i$ have dimensions $[2(h^2+h)+1] \times [2(h^2+h)+1]$, which in this case is 41×41. Upon deriving the expressions for $\overline{\overline{\boldsymbol{A}}}_1$, $\overline{\overline{\boldsymbol{A}}}_2$ and $\overline{\overline{\boldsymbol{A}}}_3$.

Define $\bar{\bar{\boldsymbol{z}}}(t)$ as the state variable vector that includes $\bar{\boldsymbol{x}}(t_0)$ and its cumulative proportional integral value, $\bar{\boldsymbol{x}}_{\mathrm{acc}}(t)$, from the start t_0 to end point t. The dimension of $\bar{\bar{\boldsymbol{z}}}(t)$ is $[2(h^2+h)+1] \times 1$, which is 41×1.

Thus, the piecewise-linear model for the state variable $\bar{\bar{\boldsymbol{z}}}(t)$ is formulated as follows,

$$\frac{\mathrm{d}}{\mathrm{d}t}\bar{\bar{\boldsymbol{z}}}(t) = \frac{\mathrm{d}}{\mathrm{dt}}\left[\begin{array}{c} \bar{\boldsymbol{x}} \\ \hline 1 \\ \hline \bar{\boldsymbol{x}}_{\mathrm{acc}} \end{array}\right] = \begin{cases} \overline{\overline{\boldsymbol{A}}}_1 \bar{\bar{\boldsymbol{z}}}(t_0) & t_0 \le t \le t_1 \\ \overline{\overline{\boldsymbol{A}}}_2 \bar{\bar{\boldsymbol{z}}}(t_1) & t_1 \le t \le t_2 \\ \overline{\overline{\boldsymbol{A}}}_3 \bar{\bar{\boldsymbol{z}}}(t_2) & t_1 \le t \le t_2 \end{cases} \tag{8.14}$$

The initial value of $\bar{\bar{\boldsymbol{z}}}(t)$, denoted by $\bar{\bar{\boldsymbol{z}}}(t_0)$, is expressed as follows:

$$\bar{\bar{\boldsymbol{z}}}(t_0) = \left[\begin{array}{c} \bar{\boldsymbol{x}}(t_0) \\ \hline 1 \\ \hline \mathbf{0} \end{array}\right] = \left[\begin{array}{c} x_1(t_0) \\ \vdots \\ x_4(t_0) \\ x_1(t_0)x_1(t_0) \\ \vdots \\ x_4(t_0)x_4(t_0) \\ \hline 1 \\ \hline 0 \\ \vdots \\ 0 \end{array}\right] \tag{8.15}$$

The value of $\bar{\boldsymbol{x}}(t_0)$ can be determined by using (8.11).

The final value of $\bar{\bar{\boldsymbol{z}}}(t)$, represented as $\bar{\bar{\boldsymbol{z}}}(t_0 + T_{\mathrm{sw}})$, can be derived from,

$$\bar{\bar{\boldsymbol{z}}}(t_0+T_{sw})=\begin{bmatrix}\bar{\boldsymbol{x}}(t_0+T_{sw})\\ \hline 1\\ \hline \bar{\boldsymbol{x}}_{\mathrm{av}}\end{bmatrix}=\left(\prod_{i=m}^{1}\bar{\bar{\boldsymbol{\Phi}}}_i\right)\bar{\bar{\boldsymbol{z}}}(t_0) \tag{8.16}$$

Utilizing equations (8.14) and (8.15), the Mean-Square cyclic-mode model for the three mode class E inverter can be established.

$$\bar{\bar{\boldsymbol{z}}}(t_0+T_{sw})=\bar{\bar{\boldsymbol{\Phi}}}_3\bar{\bar{\boldsymbol{\Phi}}}_2\bar{\bar{\boldsymbol{\Phi}}}_1\bar{\bar{\boldsymbol{z}}}(t_0)=\begin{bmatrix}\bar{\boldsymbol{x}}(t_0+T_{\mathrm{sw}})\\ \hline 1\\ \hline \bar{\boldsymbol{x}}_{\mathrm{av}}\end{bmatrix}=\begin{bmatrix}x_1(t_0+T_{\mathrm{sw}})\\ \vdots\\ x_4(t_0+T_{\mathrm{sw}})\\ x_1(t_0+T_{\mathrm{sw}})\,x_1(t_0+T_{\mathrm{sw}})\\ \vdots\\ x_4(t_0+T_{\mathrm{sw}})\,x_4(t_0+T_{\mathrm{sw}})\\ \hline 1\\ \hline (x_1)_{\mathrm{av}}\\ \vdots\\ (x_4)_{\mathrm{av}}\\ (x_1{}^2)_{\mathrm{av}}\\ \vdots\\ (x_2{}^2)_{\mathrm{av}}\\ \vdots\\ (x_3{}^2)_{\mathrm{av}}\\ \vdots\\ (x_4{}^2)_{\mathrm{av}}\end{bmatrix} \tag{8.17}$$

where

$$\bar{\bar{\boldsymbol{\Phi}}}_i=\exp\left(\bar{\bar{\boldsymbol{A}}}_i\delta_i T_{sw}\right) \tag{8.18}$$

Consequently, (8.17) reveals that the expanded form of $\bar{\bar{\boldsymbol{z}}}(t_0+T_{\mathrm{sw}})$ is a column vector that encompassing the periodic averages of the squares of each state variable in the initial cyclic-mode model which is $\left(x_1^2\right)_{\mathrm{av}}$, $\left(x_2^2\right)_{\mathrm{av}}$, $\left(x_3^2\right)_{\mathrm{av}}$ and $\left(x_4^2\right)_{\mathrm{av}}$.

The RMS values of the original state variable $\boldsymbol{x}$ are derived from

$$\langle \boldsymbol{x}_{\mathrm{rms}}\rangle_n=\sqrt{\langle \bar{\bar{\boldsymbol{z}}}(t_0+T_{\mathrm{sw}})\rangle_{h^2+(h+1)(n+1)}}=\sqrt{\langle \bar{\boldsymbol{x}}_{\mathrm{av}}\rangle_{(h+1)n}} \tag{8.19}$$

By substituting $h=4$ and $n=1,2,3,4$ into (8.19), the RMS values for each inductor current and capacitor voltage can be obtained.

$$x_{1(\mathrm{RMS})}=i_{\mathrm{Lin(RMS)}}=\sqrt{\langle \bar{\bar{\boldsymbol{z}}}(t_0+T_{\mathrm{sw}})\rangle_{26}}=\sqrt{\langle \bar{\boldsymbol{x}}_{\mathrm{av}}\rangle_5} \tag{8.20}$$

$$x_{2(\mathrm{RMS})} = i_{\mathrm{Ls(RMS)}} = \sqrt{\langle \bar{\bar{\boldsymbol{z}}}(t_0 + T_{\mathrm{sw}})\rangle_{31}} = \sqrt{\langle \bar{\boldsymbol{x}}_{\mathrm{av}}\rangle_{10}}$$

$$x_{3(\mathrm{RMS})} = v_{\mathrm{Cs(RMS)}} = \sqrt{\langle \bar{\bar{\boldsymbol{z}}}(t_0 + T_{\mathrm{sw}})\rangle_{36}} = \sqrt{\langle \bar{\boldsymbol{x}}_{\mathrm{av}}\rangle_{15}}$$

$$x_{4(\mathrm{RMS})} = v_{\mathrm{C0(RMS)}} = \sqrt{\langle \bar{\bar{\boldsymbol{z}}}(t_0 + T_{\mathrm{sw}})\rangle_{41}} = \sqrt{\langle \bar{\boldsymbol{x}}_{\mathrm{av}}\rangle_{20}}$$

After obtaining the cyclic-mode model for the three-mode operation class E inverter, we utilize the Newton's method combined with cyclic-mode model, as derived in earlier Chapters, to iterate the duration of each mode within the cyclic-mode model and the model state vector initial value $\boldsymbol{x}(t_0)$. Inputting $\boldsymbol{x}(t_0)$ into (8.15) determines $\bar{\bar{\boldsymbol{z}}}(t_0)$. Then, by incorporating these duty ratios and $\bar{\bar{\boldsymbol{z}}}(t_0)$ into (8.18) and using (8.17), we construct the precise RMS cyclic-mode model. The RMS values for each inductor current and capacitor voltage are then ascertained using (8.20). This method is referred to as the framework method.

8.1.3 Model validation

In order to validate the accuracy of the RMS cyclic-mode model and Newton's method, a comparison of the RMS values of each state variable obtained from both framework method and waveform method is performed.

The waveform method determines the RMS values from waveforms generated by the cyclic-mode model. To obtain the RMS values, square the waveform values for one cycle of the cyclic-mode model, sum them, divide by the number of points in the cycle, and finally take the square root of this total.

The key operational parameters for the class E inverter are listed in Table 8.1, which are the same as those in Chapter 5.

Table 8.1. The Components parameters of the class E inverter

Parameter	Value
R_L (Ω)	0.611
V_{DC} (V)	2.3
C_0 (nF)	100
L_s (μH)	30
C_s (nF)	84.52
v_{d} (V)	0.7
L_f (mH)	3.3
f_{sw} (kHz)	108

The SPICE model schematic diagram of this inverter is shown in Fig. 8.3,

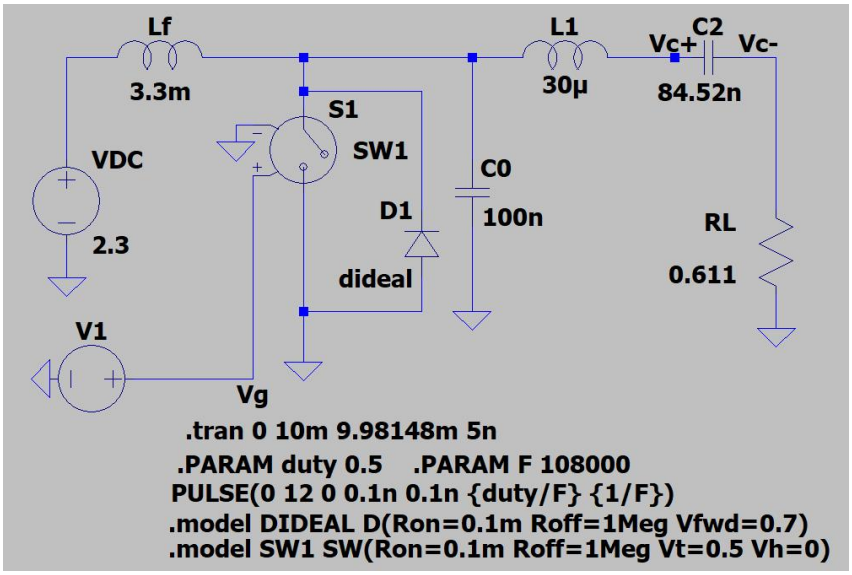

Fig. 8.3. SPICE model schematic diagram of the class E inverter

The initial values of the cyclic-mode model for the inverter and the duration of each mode are provided in Table 8.2. These values were obtained through Newton's method detailed in Chapter 5.

Table 8.2. The class E inverter cyclic-mode model initial conditions and duty ratio of each mode

Parameter	Value
$i_{\mathrm{Lin}}(t_0)$ (A)	0.3372 A
$i_{\mathrm{Ls}}(t_0)$ (A)	0.9050 A
$v_{\mathrm{Cs}}(t_0)$ (V)	21.2836 V
$v_{\mathrm{C0}}(t_0)$ (V)	0 V
δ_1	0.5
δ_2	0.3327
δ_3	0.1673

Inserting the initial value $\boldsymbol{x}(t_0)$ from Table 8.2 into (8.11) yields $\overline{\boldsymbol{x}}(t_0)$. Substituting $\overline{\boldsymbol{x}}(t_0)$ into (8.15) results in $\bar{\bar{\boldsymbol{z}}}(t_0)$. Then, inputting $\bar{\bar{\boldsymbol{z}}}(t_0)$ and each mode's duty cycle into (8.17) results in $\bar{\bar{\boldsymbol{z}}}(t_0 + T_{\mathrm{sw}})$. Finally, (8.20) calculates the RMS values for each original state variable, including all inductor currents and capacitor voltages. The framework method computes the RMS values in a runtime of 1.10 milliseconds.

The RMS values, determined by the waveform method, were derived from waveforms generated using the cyclic-mode model. Setting the waveform precision (which is the time step) to fifty points per cycle in this case, the waveform method takes time is the time from generate the waveforms until get the RMS values, which is 1.13 milliseconds at this level of accuracy. The following table displays a comparison of RMS values: those obtained by the waveform method and framework method, contrasted with the SPICE model RMS values.

Table 8.3. Comparison of the framework method RMS values and the waveform method RMS values with SPICE model RMS values in the class E inverter

Measurement	$i_{\mathrm{Lin(RMS)}}$ (A)	$i_{Ls(\mathrm{RMS})}$ (A)	$v_{Cs(\mathrm{RMS})}$ (V)	$v_{C0(\mathrm{RMS})}$ (V)
SPICE results	0.3386	1.0398	18.238	4.6914
Framework method results	0.3382	1.0402	18.2436	4.6928
Error (%)	0.13	0.038	0.031	0.029
Waveform method results	0.3382	1.0376	18.3093	4.6464
Error (%)	0.12	0.21	0.39	0.96

Table 8.3 illustrates that, for the same time spending, the framework method is more accurate than the waveform method. The framework method maximum error below 0.2% attests to the accuracy of the RMS cyclic-mode model combined with Newton's method. This emphasizes the methods' reliability, positioning the RMS cyclic-mode model and Newton's method as valuable tools for analysing the class E inverter's dynamics.

8.2 RMS cyclic-mode modelling of the class EF_2 inverter

8.2.1 Derivation of state-variable model of the class EF_2 inverter

The operating assumptions for the inverter are same with those outlined in Chapter 6, except for a slight reduction in the duty cycle of Mode 1 compared to the values in Chapter 6, which causes the inverter to shift from two-mode to three-mode operation. The circuit diagram is shown below,

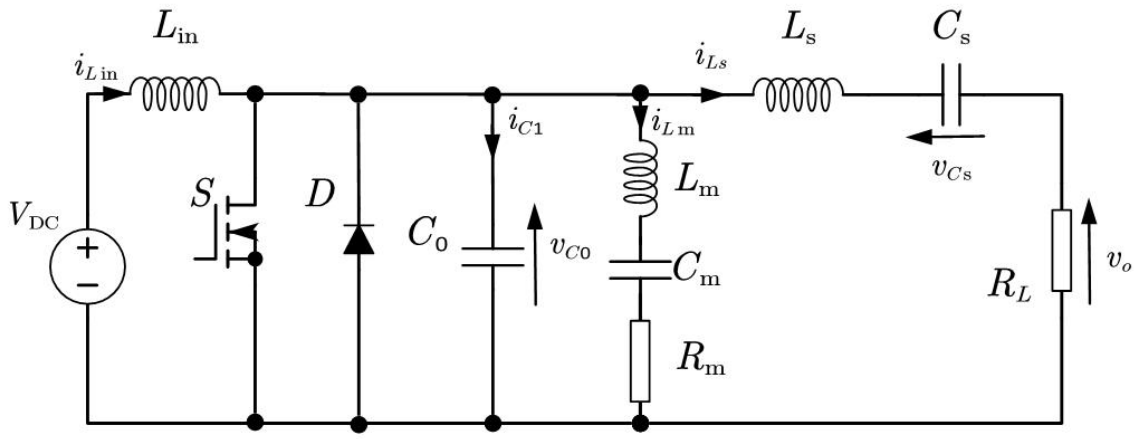

Fig. 8.4. Circuit diagram of the class EF_2 inverter

The inverter circuit diagram is illustrated in Fig. 8.4. An example of the switch voltage waveform for the inverter in three-mode operation is illustrated in the Fig. 8.5,

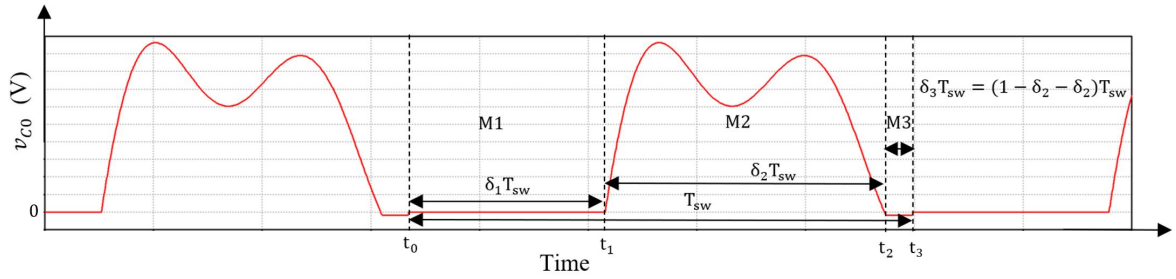

Fig. 8.5. Example shunt capacitor voltage waveform of three mode operation

Defining t_0 as the beginning of the cycle and the start of Mode 1, t_1 as the end of Mode 1 and the start of Mode 2, t_2 as the end of Mode 2 and the start of Mode 3 and finally, t_3, as the end of Mode 3 and the end of the cycle.

Mode 1 (M1) $t_0 \leq t < t_1$: At $t = t_0$ MOSFET S is switched on for a duration $t_1 - t_0 = \delta_1 T_{sw}$. Since S is on, $v_{C0} = 0$ and so $v_{Lin} = V_{DC}$. Although $v_{C0} = 0$, the current i_{Lm} continues to flow as L_m and C_m are in resonance at a frequency $2f_{sw}$.

Mode 2 (M2) $t_1 \leq t < t_2$: At $t = t_1$, S is switched off, and the MOSFET's anti-parallel diode is not conducting. Current $i_{C0} = i_{Lin} - i_{Ls} - i_{Lm}$ flows into C_0 and its voltage increases from zero to a maximum value and then decreases. Eventually, the v_{C0} falls below 0 V (actually $-v_d$) turning on the MOSFET's anti-parallel diode. The end time of mode two can be found by solving for the turn-on condition of D. The duration of Mode 2 is $t_2 - t_1 = \delta_2 T_{sw}$.

$$v_{C0}(t_2) = v_{C0}((\delta_1 + \delta_2)T_{sw}) = -v_d \tag{8.21}$$

Mode 3 (M3) $t_2 \leq t < t_3$: switch anti-parallel diode is forward biased and clamped the shunt capacitor voltage to the on-state voltage drop of the body diode, $v_{C0} = -v_d$.

To derive the inverter's cyclic-mode model, first-order differential equations are needed to describe the derivatives of the relevant capacitor voltages and the inductor currents.

Equations (8.22) to (8.29) show a non-linear state-variable model for the class EF_2 inverter, where $h_1(t)$ and $h_2(t)$ is used to represent different states,

$$\dot{i_{Lin}} = \frac{V_{\text{in}}}{L_{in}} + (h_1(t) - 1)\frac{v_{\text{C0}}}{L_{in}} \tag{8.22}$$

$$\dot{i_{Ls}} = \left(1 - h_1(t)\right)\frac{v_{\text{C0}}}{L_s} - \frac{v_{\text{Cs}}}{L_s} - \frac{R_{\text{L}} i_{\text{Ls}}}{L_s} \tag{8.23}$$

$$\dot{i_{Lm}} = (1 - h_1(t))\frac{v_{\text{C0}}}{L_m} - \frac{v_{\text{Cm}}}{L_m} - \frac{i_{\text{Lm}} R_{\text{m}}}{L_m} \tag{8.24}$$

$$\dot{v_{\text{C0}}} = (1 - h_1(t) - h_2(t))\frac{i_{\text{Lin}} - i_{Ls} - i_{\text{Lm}}}{C_0} \tag{8.25}$$

$$\dot{v_{\mathrm{Cs}}} = \frac{i_{Ls}}{C_s} \tag{8.26}$$

$$\dot{v_{\mathrm{Cm}}} = \frac{i_{Lm}}{C_{\mathrm{m}}} \tag{8.27}$$

$$h_1(t) = \begin{cases} 1 & t_0 \leq t < t_1 \\ 0 & t_1 \leq t < t_3 \end{cases} \tag{8.28}$$

$$h_2(t) = \begin{cases} 0 & t_0 \leq t < t_2 \\ 1 & t_2 \leq t < t_3 \end{cases} \tag{8.29}$$

For Mode 1 (M1): S is switched on, thus V_{DC} is only applied to L_{in}. The commutation function is $h_1 = 1,\ h_2 = 0$

Mode 2 (M2): S is switched off. Current flows out of L_{in} and into shunt capacitor C_0, the auxiliary resonant branch $L_{\mathrm{m}}C_{\mathrm{m}}R_{\mathrm{m}}$, and the main resonant branch. The commutation functions are $h_1 = 0,\ h_2 = 0$

Mode 3 (M3): S remains off, while the anti-parallel diode D is conducting. The voltage across the switch is clamped to -v_d. The commutation function is $h_1 = 0,\ h_2 = 1$. Using $SS_i = (h_1(t), h_2(t))$ to represent the switch state of mode Mi, the mode sequence in this case can be represented by SS ={(1,0), (0,0), (0,1)}.

The $\boldsymbol{A}_i$ and $\boldsymbol{B}_i$ matrices differ for each state and can be found using (8.22) to (8.29) and SS_i, as follows,

$$\begin{bmatrix} \dot{i}_{L\mathrm{in}} \\ \dot{i}_{Ls} \\ \dot{i}_{L\mathrm{m}} \\ \dot{v}_{C0} \\ \dot{v}_{C\mathrm{s}} \\ \dot{v}_{C\mathrm{m}} \end{bmatrix} = \begin{bmatrix} 0 & 0 & 0 & 0 & 0 & 0 \\ 0 & -\frac{R_{\mathrm{L}}}{L_{\mathrm{s}}} & 0 & 0 & -\frac{1}{L_{\mathrm{s}}} & 0 \\ 0 & 0 & -\frac{R_{\mathrm{m}}}{L_{\mathrm{m}}} & 0 & 0 & -\frac{1}{L_{\mathrm{m}}} \\ 0 & 0 & 0 & 0 & 0 & 0 \\ 0 & \frac{1}{C_{\mathrm{s}}} & 0 & 0 & 0 & 0 \\ 0 & 0 & \frac{1}{C_{\mathrm{m}}} & 0 & 0 & 0 \end{bmatrix} \begin{bmatrix} i_{L\mathrm{in}} \\ i_{Ls} \\ i_{L\mathrm{m}} \\ v_{C0} \\ v_{C\mathrm{s}} \\ v_{C\mathrm{m}} \end{bmatrix} + \begin{bmatrix} \frac{V_{\mathrm{DC}}}{L_{\mathrm{in}}} \\ 0 \\ 0 \\ 0 \\ 0 \\ 0 \end{bmatrix} = \boldsymbol{A}_1\boldsymbol{x} + \boldsymbol{B}_1 \tag{8.30}$$

$$\begin{bmatrix} \dot{i}_{L\mathrm{in}} \\ \dot{i}_{Ls} \\ \dot{i}_{L\mathrm{m}} \\ \dot{v}_{C0} \\ \dot{v}_{C\mathrm{s}} \\ \dot{v}_{C\mathrm{m}} \end{bmatrix} = \begin{bmatrix} 0 & 0 & 0 & -\frac{1}{L_{\mathrm{in}}} & 0 & 0 \\ 0 & -\frac{R_{\mathrm{L}}}{L_{\mathrm{s}}} & 0 & \frac{1}{L_{\mathrm{s}}} & -\frac{1}{L_{\mathrm{s}}} & 0 \\ 0 & 0 & -\frac{R_{\mathrm{m}}}{L_{\mathrm{m}}} & \frac{1}{L_{\mathrm{m}}} & 0 & -\frac{1}{L_{\mathrm{m}}} \\ \frac{1}{C_0} & -\frac{1}{C_0} & -\frac{1}{C_0} & 0 & 0 & 0 \\ 0 & \frac{1}{C_{\mathrm{s}}} & 0 & 0 & 0 & 0 \\ 0 & 0 & \frac{1}{C_{\mathrm{m}}} & 0 & 0 & 0 \end{bmatrix} \begin{bmatrix} i_{L\mathrm{in}} \\ i_{Ls} \\ i_{L\mathrm{m}} \\ v_{C0} \\ v_{C\mathrm{s}} \\ v_{C\mathrm{m}} \end{bmatrix} + \begin{bmatrix} \frac{V_{\mathrm{DC}}}{L_{\mathrm{in}}} \\ 0 \\ 0 \\ 0 \\ 0 \\ 0 \end{bmatrix} = \boldsymbol{A}_2\boldsymbol{x} + \boldsymbol{B}_2 \tag{8.31}$$

$$\begin{bmatrix} \dot{i}_{L\mathrm{in}} \\ \dot{i}_{Ls} \\ \dot{i}_{L\mathrm{m}} \\ \dot{v}_{C0} \\ \dot{v}_{C\mathrm{s}} \\ \dot{v}_{C\mathrm{m}} \end{bmatrix} = \begin{bmatrix} 0 & 0 & 0 & -\frac{1}{L_{in}} & 0 & 0 \\ 0 & -\frac{R_L}{L_s} & 0 & \frac{1}{L_s} & -\frac{1}{L_s} & 0 \\ 0 & 0 & -\frac{R_m}{L_m} & \frac{1}{L_m} & 0 & -\frac{1}{L_m} \\ 0 & 0 & 0 & 0 & 0 & 0 \\ 0 & \frac{1}{C_s} & 0 & 0 & 0 & 0 \\ 0 & 0 & \frac{1}{C_m} & 0 & 0 & 0 \end{bmatrix} \begin{bmatrix} i_{L\mathrm{in}} \\ i_{Ls} \\ i_{L\mathrm{m}} \\ v_{C0} \\ v_{C\mathrm{s}} \\ v_{C\mathrm{m}} \end{bmatrix} + \begin{bmatrix} \frac{V_{\mathrm{DC}}}{L_{\mathrm{in}}} \\ 0 \\ 0 \\ 0 \\ 0 \\ 0 \end{bmatrix} = \boldsymbol{A}_3\boldsymbol{x} + \boldsymbol{B}_3 \tag{8.32}$$

Below is a piecewise linear model for the operating sequence previously described. This model is derived by substituting the switch state sequence SS into the non-linear state-variable model equations (8.22) to (8.29).

$$\dot{\boldsymbol{x}}(t) = \begin{cases} \boldsymbol{A}_1\boldsymbol{x}(t_0) + \boldsymbol{B}_1 & t_0 \le t \le t_1 \\ \boldsymbol{A}_2\boldsymbol{x}(t_1) + \boldsymbol{B}_2 & t_1 \le t \le t_2 \\ \boldsymbol{A}_3\boldsymbol{x}(t_2) + \boldsymbol{B}_3 & t_2 \le t \le t_3 \end{cases} \tag{8.33}$$

Here

$$\boldsymbol{x} = [i_{Lin}\ i_{Ls}\ i_{Lm}\ v_{C1}\ v_{Cs}\ v_{Cm}]^{\mathrm{T}} = [x_1\ x_2\ x_3\ x_4\ x_5\ x_6]^{\mathrm{T}} \tag{8.34}$$

8.2.2 Cyclic-mode model for the class EF_2 inverter

In the cyclic-mode operation of the inverter, the final condition of state variables at the end of a cycle, $\boldsymbol{x}(t_3)$, should equal the initial condition of that cycle, $\boldsymbol{x}(t_0)$:

$$\boldsymbol{x}(t_0) = \boldsymbol{x}(t_3) = \boldsymbol{x}(t_0 + T_{sw}) \tag{8.35}$$

Given that the input is DC, starting from $t = t_0$, the state-vector at the end of Mode 1 is given by,

$$\boldsymbol{x}(t_1) = \boldsymbol{\Phi}_1\boldsymbol{x}(t_0) + \boldsymbol{\Gamma}_1 \tag{8.36}$$

where $\boldsymbol{\Phi}_1 = \exp(\boldsymbol{A}_1\delta_1 T_{\mathrm{sw}})$ and $\boldsymbol{\Gamma}_1 = \boldsymbol{A}_1^{-1}[\boldsymbol{\Phi}_1 - \boldsymbol{I}]\boldsymbol{B}_1$.

Similarly, the state-vector at the end of Mode 2 is given by,

$$\boldsymbol{x}(t_2) = \boldsymbol{\Phi}_2\boldsymbol{x}(t_1) + \boldsymbol{\Gamma}_2 \tag{8.37}$$

where $\boldsymbol{\Phi}_2 = \exp(\boldsymbol{A}_2\delta_2 T_{\mathrm{sw}})$ and $\boldsymbol{\Gamma}_2 = \boldsymbol{A}_2^{-1}[\boldsymbol{\Phi}_2 - \boldsymbol{I}]\boldsymbol{B}_2$.

During Mode 3, $t_2 \le t < t_3$, the switch voltage is discontinuous at the end of Mode 3. This requires forcing $v_{C0}(t_3) = 0$, defined as t_3^-, symbolizing the instant before t_3. The state vector at the end of Mode 3, prior to discontinuity, is:

$$\boldsymbol{x}(t_3^-) = \boldsymbol{\Phi}_3\boldsymbol{x}(t_2) + \boldsymbol{\Gamma}_3 \tag{8.38}$$

where $\boldsymbol{\Phi}_3 = \exp(\boldsymbol{A}_3\delta_3 T_{\mathrm{sw}}) = \exp(\boldsymbol{A}_3(1 - \delta_1 - \delta_2)T_{\mathrm{sw}})$ and $\boldsymbol{\Gamma}_3 = \boldsymbol{A}_3^{-1}[\boldsymbol{\Phi}_3 - \boldsymbol{I}]\boldsymbol{B}_3$.

To ensure that all state variables at time t_3, marking the end of the cycle, are equivalent to those at the start of the cycle, $v_{C0}(t_3)$ must be set to zero. $\boldsymbol{K}$ is defined as a unit matrix with the same dimensions as $\boldsymbol{A}_i$, except the fourth row is zero:

$$\boldsymbol{K} = \mathrm{diag}[1,1,1,0,1,1] \tag{8.39}$$

Therefore, at time t_3, the value of the state variable $\boldsymbol{x}(t)$ equals the value of $\boldsymbol{x}$ at time t_0:

$$\boldsymbol{x}(t_3) = \boldsymbol{K}\boldsymbol{x}(t_3^-) = \boldsymbol{x}(t_0) \tag{8.40}$$

The cyclic-mode initial condition $\boldsymbol{x}(t_0)$ can be determined by evaluating the final conditions of each mode:

$$\boldsymbol{x}(t_3) = \boldsymbol{K}\boldsymbol{\Phi}_{\text{tot}}\boldsymbol{x}(t_0) + \boldsymbol{K}\boldsymbol{\Gamma}_{\text{tot}} \tag{8.41}$$

where $\boldsymbol{\Phi}_{\text{tot}} = \boldsymbol{\Phi}_3\boldsymbol{\Phi}_2\boldsymbol{\Phi}_1$ and $\boldsymbol{\Gamma}_{\text{tot}} = \boldsymbol{\Phi}_3(\boldsymbol{\Phi}_2(\boldsymbol{\Gamma}_1) + \boldsymbol{\Gamma}_2) + \boldsymbol{\Gamma}_3$

If δ_1 and δ_2 values are known, then δ_3 be determined using $\delta_3 = 1 - \delta_1 - \delta_2$ from which the final condition $\boldsymbol{x}(t_3)$ can be found. Substituting (8.39) into (5.31) and rearranging gives the initial (final) condition,

$$\boldsymbol{x}(t_3) = (\boldsymbol{I} - \boldsymbol{K}\boldsymbol{\Phi}_{\text{tot}})^{-1}(\boldsymbol{K}\boldsymbol{\Gamma}_{\text{tot}}) = \boldsymbol{x}(t_0) \tag{8.42}$$

With $\boldsymbol{x}(t_0)$ obtained, the state variable value at every time can be determined by,

$$\boldsymbol{x}(t) = \begin{cases} \boldsymbol{\Phi}_1(t)\boldsymbol{x}(t_0) + \boldsymbol{\Gamma}_1(t) & t_0 \le t \le t_1 \\ \boldsymbol{\Phi}_2(t)\boldsymbol{x}(t_1) + \boldsymbol{\Gamma}_2(t) & t_1 \le t \le t_2 \\ \boldsymbol{\Phi}_3(t)\boldsymbol{x}(t_2) + \boldsymbol{\Gamma}_3(t) & t_2 \le t < t_3 \end{cases} \tag{8.43}$$

Here $\boldsymbol{\Phi}_i(t) = \exp(\boldsymbol{A}_i(t - t_i))$ and $\boldsymbol{\Gamma}_i(t) = \boldsymbol{A}_i^{-1}[\boldsymbol{\Phi}_i(t) - \boldsymbol{I}]\boldsymbol{B}_i$

8.2.3 Application of Newton's method to finding the cyclic condition

To determine the initial condition, $\boldsymbol{x}(t_0)$, each mode duty ratios are required. Since the duration of Mode 1 (δ_1) is the control input, its value is already known. However, the durations of modes 2 & 3 (δ_2 & δ_3=1-δ_1-δ_2) are a function of the operation condition and, so, are affected by the initial condition and therefore need to be determined simultaneously with $\boldsymbol{x}(t_0)$. Here, the shooting method technique is used where a new system model is formed by augmenting the initial condition model with models to determine the unknown mode durations. Subsequently, Newton's method is used to obtain the system solution.

The vector $\boldsymbol{X}$ in this case comprises the combination of the initial conditions $\boldsymbol{x}(t_0)$ of the cyclic-mode model and the duty cycle of mode two δ_2,

$$\boldsymbol{X} = [\boldsymbol{x}^{\mathrm{T}}(t_0) \quad \delta_2]^T \tag{8.44}$$

For $\boldsymbol{G}(\boldsymbol{X})$, since $\boldsymbol{X}$ comprises seven elements, $\boldsymbol{G}(\boldsymbol{X})$ needs to encompass seven equations,

$$\boldsymbol{G}(\boldsymbol{X}) = \begin{bmatrix} g_1(\boldsymbol{X}) \\ g_2(\boldsymbol{X}) \\ g_3(\boldsymbol{X}) \\ g_4(\boldsymbol{X}) \\ g_5(\boldsymbol{X}) \\ g_6(\boldsymbol{X}) \\ \hline g_7(\boldsymbol{X}) \end{bmatrix} \tag{8.45}$$

The initial condition model can be rewritten from (8.42) as a function of both the initial condition and duration of each mode,

$$\begin{aligned} &[g_1(\boldsymbol{x}(t_0), \delta_2) \quad \cdots \quad g_6(\boldsymbol{x}(t_0), \delta_2)]^T \\ &= (\boldsymbol{I} - \boldsymbol{K}\boldsymbol{\Phi}_{\mathrm{tot}})^{-1}(\boldsymbol{K}\boldsymbol{\Gamma}_{\mathrm{tot}}) - \boldsymbol{x}(t_0) \end{aligned} \tag{8.46}$$

where $\boldsymbol{K} = \mathrm{diag}[1,1,1,0,1,1]$.

At the end of Mode 2 the switch voltage should equal to antiparallel diode conducting voltage $-v_d$, which can be rewritten as,

$$v_{C0}(t_2^-) = -v_d \tag{8.47}$$

So, the expression for $g_7(\boldsymbol{X}) = v_{C0}(t_2^-) + v_d = 0$ is. In matrix form this is written as,

$$g_7(\boldsymbol{x}(t_0), \delta_2) = [0 \quad 0 \quad 0 \quad 1 \quad 0 \quad 0][\boldsymbol{\Phi}_2(\boldsymbol{\Phi}_1\boldsymbol{x}(t_0) + \boldsymbol{\Gamma}_1 + \boldsymbol{\Gamma}_2] + v_d \tag{8.48}$$

The expression for $\boldsymbol{G}(\boldsymbol{X})$ is derived by combining equations (8.46) and (8.48). When all the requisite conditions are met, $\boldsymbol{G}(\boldsymbol{X})$ is a 7× 1 column vector.

$$\boldsymbol{G}(\boldsymbol{X}) = [g_1(\boldsymbol{x}(t_0), \delta_2) \quad \cdots \quad g_7(\boldsymbol{x}(t_0), \delta_2)]^T \tag{8.49}$$

$$= \left[\frac{(\boldsymbol{I} - \boldsymbol{K}\boldsymbol{\Phi}_{\text{tot}})^{-1}(\boldsymbol{K}\boldsymbol{\Gamma}_{\text{tot}}) - \boldsymbol{x}(t_0)}{[0 \quad 0 \quad 0 \quad 1 \quad 0 \quad 0][\boldsymbol{\Phi}_2(\boldsymbol{\Phi}_1\boldsymbol{x}(t_0) + \boldsymbol{\Gamma}_1 + \boldsymbol{\Gamma}_2] + v_d}\right] = \begin{bmatrix} g_1(\boldsymbol{X}) \\ g_2(\boldsymbol{X}) \\ g_3(\boldsymbol{X}) \\ g_4(\boldsymbol{X}) \\ g_5(\boldsymbol{X}) \\ g_6(\boldsymbol{X}) \\ \hline g_7(\boldsymbol{X}) \end{bmatrix}$$

Newton's iterative method is then applied to estimate $\boldsymbol{X}$, beginning with the initial value $\boldsymbol{X}^0$ and proceeding through iteration,

$$\boldsymbol{X}^{k+1} = \boldsymbol{X}^k - \left[\boldsymbol{J}\left(\boldsymbol{X}^k\right)\right]^{-1}\boldsymbol{G}(\boldsymbol{X}^k) \tag{8.50}$$

Here, k denotes the index of the current iteration step, and $\boldsymbol{J}\left(\boldsymbol{X}^k\right)$ represents the Jacobian matrix of partial derivatives, evaluated at the current iteration k.

Subsequently, the Jacobian matrix for the Newton method is constructed as follows:

$$\boldsymbol{J}(\boldsymbol{X}) = \frac{\partial \boldsymbol{G}}{\partial X} = \begin{bmatrix} \frac{\partial g_1}{\partial X_1} & \cdots & \frac{\partial g_1}{\partial X_7} \\ \vdots & \ddots & \vdots \\ \frac{\partial g_7}{\partial X_1} & \cdots & \frac{\partial g_7}{\partial X_7} \end{bmatrix} = \begin{bmatrix} \frac{\partial g_1}{\partial i_{Lin}} & \cdots & \frac{\partial g_1}{\partial \delta_2} \\ \vdots & \ddots & \vdots \\ \frac{\partial g_7}{\partial i_{Lin}} & \cdots & \frac{\partial g_7}{\partial \delta_2} \end{bmatrix} \tag{8.51}$$

Utilize the method described in earlier Chapters to calculate the numerical Jacobian matrix, and then iterate. During each iteration, rederive the numerical Jacobian matrix.

The iteration halts when the L1-norm decreases below the threshold value λ.

$$\left|\boldsymbol{X}^{\text{final}} - \boldsymbol{X}^{\text{final}-1}\right| < \lambda \tag{8.52}$$

Utilizing the Newton-Raphson method alongside the numerical Jacobian matrix enables the determination of initial values and mode durations for the class EF_2 inverter's cyclic-mode model during three-mode operation.

8.2.4 RMS cyclic-mode modelling for the class EF_2 inverter

Having obtained the expression for the class EF_2 inverter's three-mode cyclic-mode model, The subsequent step involves deriving the expression for its RMS cyclic-mode model, following the methodology used for the class E inverter at previous section.

Initially, the Kronecker sum expressions for $\boldsymbol{A}_i \oplus \boldsymbol{A}_i$ and $\boldsymbol{B}_i \oplus \boldsymbol{B}_i$ are determined based on equations (8.30), (8.31), (8.32) . In this instance, $\boldsymbol{A}_i \oplus \boldsymbol{A}_i$ are 36×36 square matrices, while $\boldsymbol{B}_i \oplus \boldsymbol{B}_i$ are 36×6 matrices.

Once the expressions for $\boldsymbol{A}_i \oplus \boldsymbol{A}_i$ and $\boldsymbol{B}_i \oplus \boldsymbol{B}_i$ are acquired, the expression for $\overline{\boldsymbol{A}}_i$ and $\overline{\boldsymbol{B}}_i$ can be formulated. For the class EF_2 inverter, which includes six state variables, $\overline{\boldsymbol{A}}_i$ is a matrix of size 42×42. The expression for $\overline{\boldsymbol{B}}_i$ is a 42×1 column vector. $\overline{\boldsymbol{A}}_i$ and $\overline{\boldsymbol{B}}_i$ are derived by combining $\boldsymbol{A}_i$, $\boldsymbol{B}_i$, $\boldsymbol{A}_i \oplus \boldsymbol{A}_i$ and $\boldsymbol{B}_i \oplus \boldsymbol{B}_i$ according to (8.8). Having derived the expressions for $\overline{\boldsymbol{A}}_i$ and $\overline{\boldsymbol{B}}_i$, we can now establish the piecewise linear model for the class EF_2 inverter. This model's formula is identical to (8.9) and (8.10).

The expanded form of $\overline{\boldsymbol{x}}$ in this case is shown in the following formula

$$\overline{\boldsymbol{x}} = [x_1 \quad \ldots \quad \ldots \quad x_6 \quad x_1x_1 \quad \cdots \quad x_1x_6 \quad x_2x_1 \quad \cdots \quad x_2x_6 \quad x_3x_1 \quad \cdots \quad x_3x_6 \quad x_4x_1 \quad \cdots \quad x_4x_6 \quad x_5x_1 \quad \cdots \quad x_5x_6 \quad x_6x_1 \quad \cdots \quad x_6x_6]^{\mathrm{T}} \tag{8.53}$$

Equation (8.53) indicates that each element in the vector $\overline{\boldsymbol{x}}(t_0)$ is derived from a combination of one or two elements from $\boldsymbol{x}(t_0)$. Knowing the vector $\boldsymbol{x}(t_0)$ allows for the determination of $\overline{\boldsymbol{x}}(t_0)$'s elements, thus establishing $\overline{\boldsymbol{x}}(t_0)$'s values.

After obtaining the initial value of $\overline{\boldsymbol{x}}$ which is $\overline{\boldsymbol{x}}(t_0)$, the cyclic-mode model for $\overline{\boldsymbol{x}}$ can be written. Its structural expression is the same as (8.12). The subsequent step involves applying the cyclic averaging method to the class EF_2 inverter's square cyclic-mode model, beginning with the determination of $\overline{\overline{\boldsymbol{A}}}_i$ expression from (8.13) which sized 85×85 in this instance.

After obtaining the expressions for $\overline{\overline{\boldsymbol{A}}}_1$, $\overline{\overline{\boldsymbol{A}}}_2$ and $\overline{\overline{\boldsymbol{A}}}_3$, we define $\bar{\bar{\boldsymbol{z}}}(t)$ as the state variable vector that includes $\bar{\boldsymbol{x}}(t)$ and its cumulative proportional integral from the starting point t_0 to the endpoint t, denoted as $\bar{\boldsymbol{x}}_{\mathrm{acc}}(t)$. In this model with six state variables, $\bar{\bar{\boldsymbol{z}}}(t)$ is an 85×1 column vector. Due to the size constrain, the expression of them can not be given in this thesis.

Thus, the piecewise-linear state variable model for $\bar{\bar{\boldsymbol{z}}}(t)$ is formulated as follows:

$$\frac{\mathrm{d}}{\mathrm{d}t}\bar{\bar{\boldsymbol{z}}}(t)=\frac{\mathrm{d}}{\mathrm{dt}}\begin{bmatrix}\bar{\boldsymbol{x}}\\ \hline 1\\ \hline \bar{\boldsymbol{x}}_{\mathrm{acc}}\end{bmatrix}=\begin{cases}\overline{\overline{\boldsymbol{A}}}_i\,\bar{\bar{\boldsymbol{z}}}(t_{i-1}) & t_{i-1}\le t\le t_i\end{cases} \tag{8.54}$$

where i is the mode index $i=1,2,3$.

The initial value of $\bar{\bar{\boldsymbol{z}}}(t)$, denoted as $\bar{\bar{\boldsymbol{z}}}(t_0)$, is expressed as:

$$\bar{\bar{\boldsymbol{z}}}(t_0)=\begin{bmatrix}\bar{\boldsymbol{x}}(t_0)\\ \hline 1\\ \hline \mathbf{0}\end{bmatrix}=\begin{bmatrix}x_1(t_0)\\ \vdots\\ x_6(t_0)\\ x_1(t_0)x_1(t_0)\\ \vdots\\ x_6(t_0)x_6(t_0)\\ \hline 1\\ \hline 0\\ \vdots\\ 0\end{bmatrix} \tag{8.55}$$

where the zero-column vector $\mathbf{0}$ is of the same size as $\bar{\boldsymbol{x}}(t_0)$. The expression reveals that it consists of $\bar{\boldsymbol{x}}(t_0)$ and $\mathbf{0}$, which is already established, thus allowing for the determination of $\bar{\bar{\boldsymbol{z}}}(t_0)$'s value.

Utilizing (8.54) and (8.55) with each mode duration, we can obtain the final value of $\bar{\bar{\boldsymbol{z}}}(t)$, represented as $\bar{\bar{\boldsymbol{z}}}(t_0+T_{\mathrm{sw}})$, can be derived from equation (8.56),

$$\bar{\bar{\boldsymbol{z}}}(t_0+T_{\mathrm{sw}})=\overline{\overline{\boldsymbol{\Phi}}}_3\,\overline{\overline{\boldsymbol{\Phi}}}_2\,\overline{\overline{\boldsymbol{\Phi}}}_1\,\bar{\bar{\boldsymbol{z}}}(t_0)=\begin{bmatrix}\bar{\boldsymbol{x}}(t_0+T_{\mathrm{sw}}^-)\\ \hline 1\\ \hline \bar{\boldsymbol{x}}_{\mathrm{av}}\end{bmatrix} \tag{8.56}$$

$$=[\,\bar{\boldsymbol{x}}(t_0+T_{\mathrm{sw}}^-)^{\mathrm{T}}\mid 1\mid \boldsymbol{x}_{\mathrm{av}}{}^{\mathrm{T}}\quad (x_1{}^2)_{\mathrm{av}}\quad\cdots\quad (x_2{}^2)_{\mathrm{av}}\quad\cdots\quad (x_3{}^2)_{\mathrm{av}}\quad\cdots\quad (x_6{}^2)_{\mathrm{av}}\,]^{\mathrm{T}}$$

where $\overline{\overline{\boldsymbol{\Phi}}}_i=\exp\left(\overline{\overline{\boldsymbol{A}}}_i\delta_i T_{sw}\right)$

As per (8.56), the expanded form of $\bar{\bar{\mathbf{z}}}(t_0 + T_{\mathrm{sw}})$ is a column vector containing the periodic averages of $x_1^2,\ x_2^2,\ x_3^2,\ x_4^2,\ x_5^2$ and x_6^2. The RMS values of the original state variable $\boldsymbol{x}(t)$ can be derived from (8.19), using $h = 6$ and $n = 1, 2, 3, 4, 5, 6$. This corresponds to the RMS values of each inductor current and capacitor voltage.

$$
\begin{aligned}
i_{\mathrm{Lin(RMS)}} &= \sqrt{\langle \bar{\bar{\mathbf{z}}}(t_0 + T_{\mathrm{sw}})\rangle_{50}} = \sqrt{\langle \bar{\boldsymbol{x}}_{\mathrm{av}}\rangle_7} \\
i_{\mathrm{Ls(RMS)}} &= \sqrt{\langle \bar{\bar{\mathbf{z}}}(t_0 + T_{\mathrm{sw}})\rangle_{57}} = \sqrt{\langle \bar{\boldsymbol{x}}_{\mathrm{av}}\rangle_{14}} \\
i_{\mathrm{Lm(RMS)}} &= \sqrt{\langle \bar{\bar{\mathbf{z}}}(t_0 + T_{\mathrm{sw}})\rangle_{64}} = \sqrt{\langle \bar{\boldsymbol{x}}_{\mathrm{av}}\rangle_{21}} \\
v_{\mathrm{C0(RMS)}} &= \sqrt{\langle \bar{\bar{\mathbf{z}}}(t_0 + T_{\mathrm{sw}})\rangle_{71}} = \sqrt{\langle \bar{\boldsymbol{x}}_{\mathrm{av}}\rangle_{28}} \\
v_{\mathrm{Cs(RMS)}} &= \sqrt{\langle \bar{\bar{\mathbf{z}}}(t_0 + T_{\mathrm{sw}})\rangle_{78}} = \sqrt{\langle \bar{\boldsymbol{x}}_{\mathrm{av}}\rangle_{35}} \\
v_{\mathrm{Cm(RMS)}} &= \sqrt{\langle \bar{\bar{\mathbf{z}}}(t_0 + T_{\mathrm{sw}})\rangle_{85}} = \sqrt{\langle \bar{\boldsymbol{x}}_{\mathrm{av}}\rangle_{42}}
\end{aligned}
\tag{8.57}
$$

8.2.5 Model validation

To validate the accuracy of the RMS cyclic-mode model and the Newton method applied to the class EF_2 inverter. The inverter was designed to operate at an input voltage (V_{DC}) of 15 V and with a rated output of 1 W. An LT SPICE simulation model can be constructed. The auxiliary resonant branch of the simulation model was constructed with component values from a STEMiNC SMD25T85F234S piezoelectric resonator [8.1] Mason equivalent circuit. The shunt capacitor value is incorporating PT's input capacitance C_{in} value into the inverter's shunt capacitor C_0. The values for the main resonant branch and input inductor were obtained using techniques described by Aldhaher *et al.,*. [8.2]. The switching element is an ideal MOSFET. Component values for this design can be found in Table 8.4.

Table 8.4. The class EF_2 inverter components values for this design

Component's name	Component's value
R_m	4.27 Ω
L_m	8.25 mH
C_m	0.412 nF
C_0	22.5 nF
L_{in}	10 mH
L_s	0.8 mH
C_s	23 nF
R_L	40 Ω
V_{DC}	15 V

The SPICE model schematic diagram is shown in Fig. 8.6,

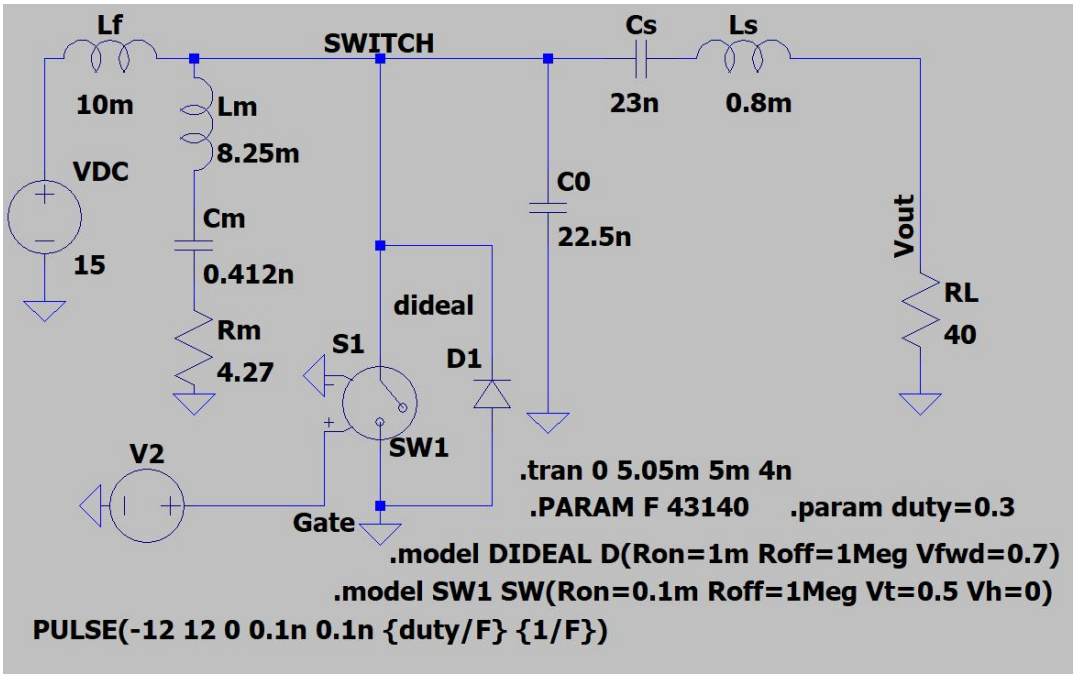

Fig. 8.6. SPICE model schematic diagram of the class EF_2 inverter

The duty cycle and frequency were set to $\delta_1 = 0.3$ and f_{sw}= 43.14 kHz, respectively. An initial estimate for δ_2 was set at 0.55. The rough estimation of $\boldsymbol{x}(t_0)$ from (8.42). Utilizing the Newton's method allowed for an accurate calculation of δ_2, yielding a value of 0.6295, which matches the LT SPICE model result.

Subsequently, the class EF_2 inverter cyclic-mode model can generate the waveforms for each inductor current and capacitor voltage. Fig. 8.7 and Fig. 8.8 compare the switch voltage and load voltage from the LT SPICE model with those from the cyclic-mode model.

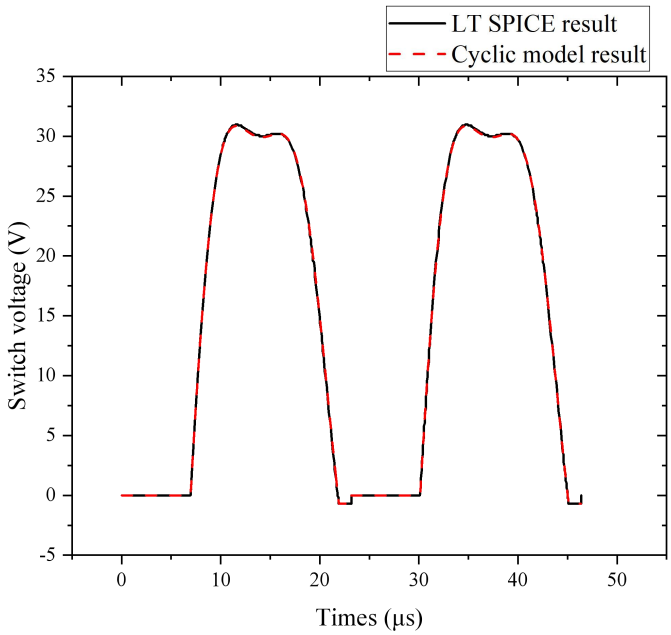

Fig. 8.7. The switch voltage v_{C0} waveform of the cyclic-mode model and SPICE simulation

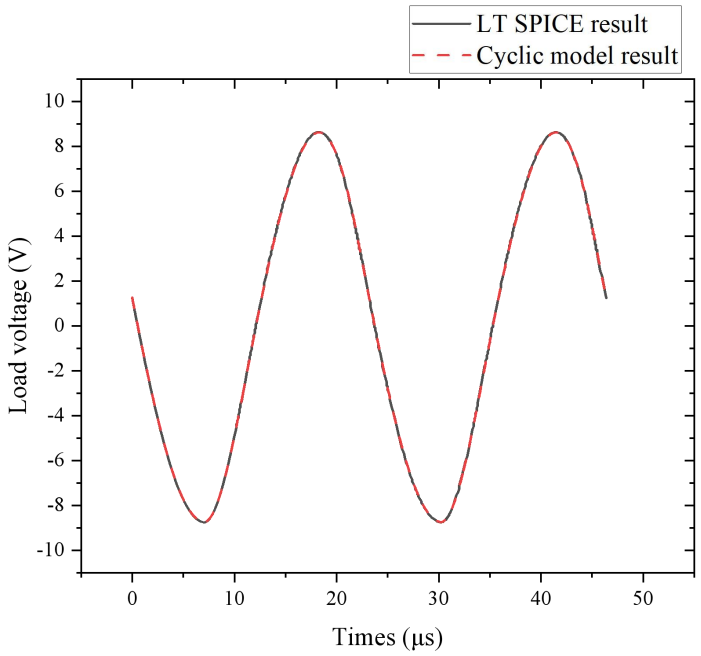

Fig. 8.8. The load voltage v_L waveform of cyclic-mode model and SPICE simulation

Table 8.5 presents a comparison of the RMS values from the cyclic-mode model with those from the LT SPICE model.

Table 8.5. Comparison of framework method RMS values with SPICE model RMS values in the class EF_2 inverter

RMS value	i_{Lin}	i_{Ls}	i_{Lm}	v_{C1}	v_{Cs}	v_{Cm}
LT SPICE model	0.10255 A	0.19275 A	0.10122 A	20.418 V	34.323 V	453.77 V
Framework method	0.1025 A	0.1929 A	0.1013 A	20.3945 V	34.3712 V	453.8637 V
Error	0.0488%	0.0778%	0.0791%	0.1151%	0.1405%	0.0207%

The RMS values calculated using the cyclic-mode model show good agreement with the SPICE results, with a maximum error of 0.14 %.

A similar approach with Table 8.3 is used to verify the performance difference between the two methods for switching power supply systems of different orders. The results of the two methods are compared for the same runtime by choosing a suitable time step for the waveform method so that the runtime required by both methods is similar. The cyclic RMS framework takes about two milliseconds to compute the RMS value. Meanwhile, the waveform method can generate six sets of periodic waveforms, each with an accuracy of seventy points per cycle, and calculate the RMS value of each state variable based on these waveforms within a runtime of two milliseconds. The relative errors of the waveform method compared to the framework method within the same running time are shown in Table 8.6.

Table 8.6. RMS values' error of the waveform method compared with the framework method

RMS values	i_{Lin} (A)	i_{Ls}(A)	i_{Lm}(A)	v_{C0} (V)	v_{Cs}(V)	v_{Cm}(V)
Waveform method	0.1025	0.1915	0.1012	20.2483	34.8353	453.7951
Framework method	0.1025	0.1929	0.1013	20.3945	34.3712	453.8637
Error	0.048%	0.71%	0.042%	0.72%	1.35%	0.016%

The table indicates that, within the same runtime, the waveform method still exhibits a certain degree of error. Since the accuracy of the RMS values from the waveform method depends on the precision of the plotted waveforms, as the simulation time increases, the precision of the waveforms generated by the waveform method can also be improved.

In order to further examine the differences between the frame and waveform methods, Fig. 8.9.was plotted using the plotting methodology of Fig. 7.5, which show the relative errors in the RMS values of the key parameters of the class EF_2 inverter as a direct function of the run time of the waveform method.

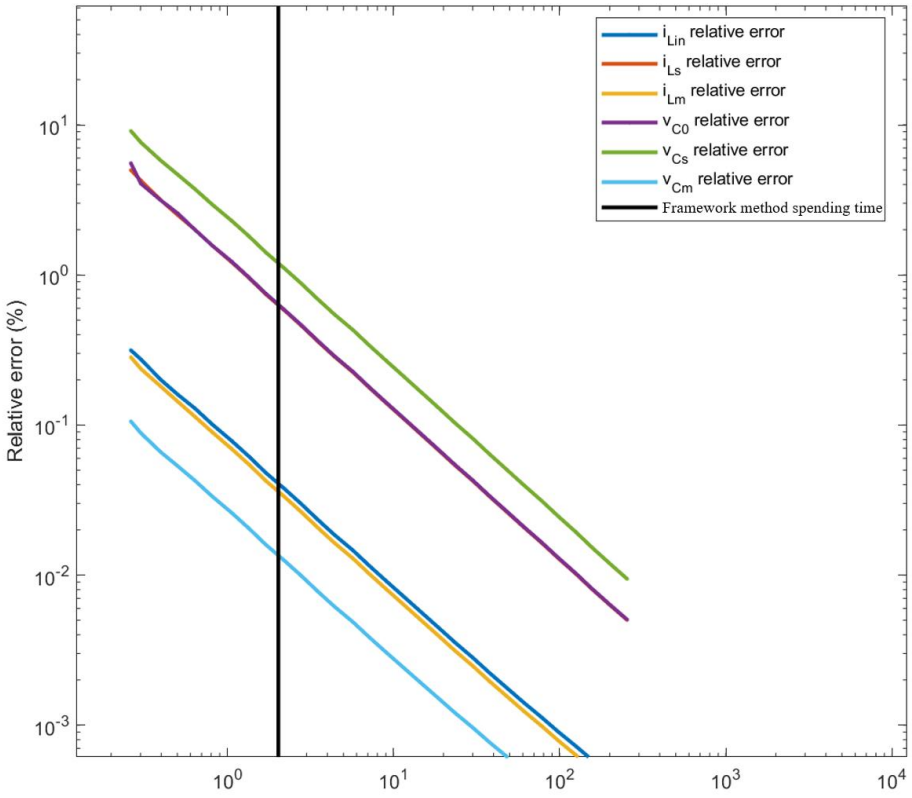

Fig. 8.9. The relative error of the waveform method varies with the waveform method operaing time

The vertical axis represents the relative error, while the horizontal axis denotes the time consumed per simulation run. The graph's vertical black solid line indicates that a single run of the framework method requires approximately two milliseconds. The six diagonal lines represent the error of the waveform method results relative to the framework method as the runtime of a single waveform method increases. This trend further substantiates the precision of the framework method.

8.3 RMS cyclic-mode modelling of the LLC converter

The LLC resonant converter is a popular DC-DC power supply topology owing to its low switching losses and good power density by virtue of being able to integrate three magnetic components into a single device. In this section the RMS cyclic-mode technique is applied to

an LLC resonant converter. The process begins with establishing a basic understanding of the LLC resonant converter. Next, a cyclic-mode model is developed by decomposing the state-variable model into piecewise linear equations representing each mode. Duty ratios associated with mode are estimated using a describing function and then refined using Newton's method. Finally, the RMS cyclic-model is described. Comparison with LT SPICE and experimental measure the model to provide good performance.

8.3.1 Derivation of RMS cyclic-mode model for the LLC converter

Fig. 8.10 shows the circuit diagram of an LLC resonant converter, highlighting the currents and voltages of the state variables in red. The half-bridge, composed of MOSFETs S_1 and S_2, chops the DC voltage (V_{DC}) to generate a variable frequency square wave (V_{in}). The voltage V_{in} is applied to the resonant tank circuit, which includes the inductors L_s, L_p, and the capacitor C_s. Through carefully design, the frequency of V_{in} is set to excite the resonant circuit, resulting in a sinusoidal current i_{Ls} that lags behind V_{in}, thus ensuring zero-voltage switching. A current, denoted as $N(i_{Ls} - i_{Lp})$, passes through the rectifier composed of D_1 and D_2 on the transformer's secondary side, which, after smoothing by capacitor C_f, produces the output voltage V_{out}.

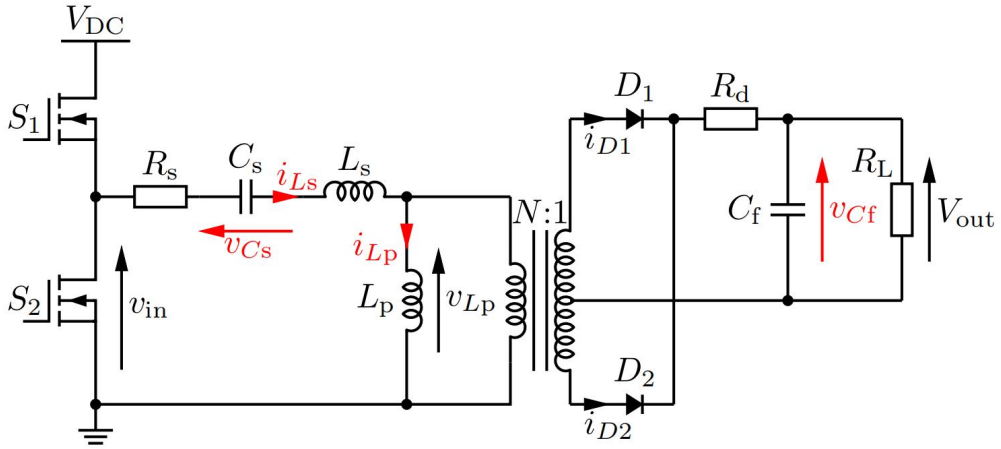

Fig. 8.10. Circuit diagram of the LLC converter

Equations (8.58) to (8.64) form a non-linear state-variable model for the LLC resonant converter. Here, $h_1(t)$ represents the state of the half-bridge, such that $V_{\text{in}}(t)$ equals $V_{\text{DC}}h_1(t)$, disregarding the essential deadtime between S1 and S2 needed to prevent shoot-through. Meanwhile, $h_2(t)$ signifies the rectifier's commutation.

$$\dot{i_{Ls}} = h_1(t)\frac{V_{DC}}{L_s} - \frac{v_{Lp}}{L_s} - \frac{v_{Cs}}{L_s} - \frac{i_{Ls}R_s}{L_s} \tag{8.58}$$

$$\dot{i_{Lp}} = \frac{v_{Lp}(t)}{L_p} \tag{8.59}$$

$$\dot{v_{Cs}} = \frac{i_{Ls}}{C_s} \tag{8.60}$$

$$\dot{v_{Cf}} = h_2(t)\frac{N(i_{Ls} - i_{Lp})}{C_f} - \frac{v_{Cf}}{C_f R_L} \tag{8.61}$$

$$h_1(t) = \begin{cases} 1 & t_0 \le t < T_{sw}/2 \\ 0 & T_{sw}/2 \le t < T_{sw} \end{cases} \tag{8.62}$$

$$h_2(t) = \begin{cases} 1 & D_1 \text{ on} \\ 0 & D_1 \,\&\, D_2 \text{ off} \\ -1 & D_2 \text{ on} \end{cases} \tag{8.63}$$

$$\begin{aligned} v_{Lp}(t) = {} & h_2(t)N\big(v_{Cf} + v_{\mathrm{d}} + N(i_{Ls} - i_{Lp})R_d\big) \\ & + (1 - |h_2(t)|)\frac{L_p}{L_s + L_p}(h_1(t)V_{DC} - v_{Cs}) \end{aligned} \tag{8.64}$$

Here, v_{d} refers to the diode's forward voltage drop, and R_d represents the diode's on-state resistance.

The operation of the LLC converter within a single switching cycle can be split into six modes, based on the conduction states of S_1, S_2, D_1 and D_2. These correspond to the six possible combinations of h_1 and h_2. An example of the operating waveforms is illustrated in Fig. 8.11.

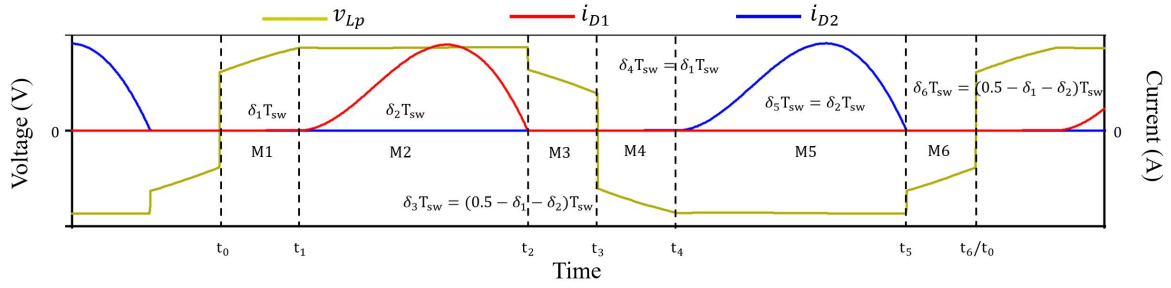

Fig. 8.11. Typical voltage and current waveforms for the LLC converter

The start of the cycle is defined as the instant S_1 turns-on ($t = t_0$). A single cycle runs from t_0 to $t_6 = t_0 + T_{sw}$ where t_i signifies the end time mode i. The modes of the converter are described as follows:

Mode M1 ($t_0 \le t < t_1$): At $t = t_0$, switch S_1 is activated for a duration of $t_1 - t_0 = \delta_1 T_{sw}$, setting V_{in} equal to V_{DC}. With diodes D_1 and D_2 not conducting, there is no

coupling between the primary and secondary sides of the transformer, allowing current i_{Ls} to circulate through the resonant circuit. The commutation functions for M1 are $h_1 = 1$ and $h_2 = 0$.

Mode M2 ($t_1 \leq t < t_2$): This mode begins when v_{Lp} at t_1 equals $N(v_{\mathrm{Cf}} + v_{\mathrm{d}})$, resulting in diode D_1 becoming forward biased. A current of $N(i_{\mathrm{Ls}} - i_{\mathrm{Lp}})$ exits the secondary. The commutation functions are set to $h_1 = 1$ and $h_2 = 1$.

Mode M3 ($t_2 \leq t < t_3 = T_{sw}/2$): Mode M3 initiates when D_1 turns off, which is when i_{Ls} at t_2 minus i_{Lp} at t_2 equals zero. This mode is similar to M1, with commutation functions $h_1 = 1$ and $h_2 = 0$.

Mode M4 ($t_3 \leq t < t_4$): At $t = t_3$, S_1 is turned-off and S_2 is engaged, resulting in V_{in} being 0 V. The commutation functions for this mode are both set to $h_1 = 0$ and $h_2 = 0$.

Mode M5 ($t_4 \leq t < t_5$): At $t = t_4$, $v_{Lp}(t_4) = -N(v_{Cf} + V_d)$, triggering D_2 to turn on and facilitate energy transfer from the primary to the secondary side of the transformer. The commutation functions are designated as $h_1 = 0$ and $h_2 = -1$.

Mode M6 ($t_5 \leq t < t_6$): D_2 turns off once $i_{Ls}(t_5) - i_{Lp}(t_5) = 0$. M6 is similar to M4 and concludes at $t = t_6 = t_0 + T_{sw}$, marking the point at which the cycle restarts. The commutation functions for M6 are $h_1 = 0$ and $h_2 = 0$.

To represent the switch state of mode Mi, we use SS_i=$(h_1(t_{i-1}), h_2(t_{i-1})$. Accordingly, the mode sequence shown in Fig. 8.11 is represented by SS= {(1,0), (1,1),(1,0),(0,0),(0,-1),(0,0)}. Note that the LLC resonant converter may operate in various mode sequences depending on the excitation and load conditions. For a more comprehensive description of the converter's behaviour, refer to the work of Martinelli & Lazar [8.3].

The following is a piecewise linear model for the operating sequence previously described. This model is derived similarly to references [8.4] and [8.5], beginning with the nonlinear state-variable model equations (8.58) to (8.64) and incorporating the switch state sequence SS. The model dictates identical behaviour for the circuit during modes M1 and M3 due to their

identical switch states (S_1 on, S_2 off, D_1 off, D_2 off), represented by $SS_{1,3}$=(1,0). Likewise, the behaviour for M4 and M6 is the same. The piecewise model is characterized as follows:

$$\dot{\boldsymbol{x}}(t) = \begin{cases} \boldsymbol{A}_1\boldsymbol{x}(t_0) + \boldsymbol{B}_1 & t_0 \le t < t_1 \\ \vdots & \vdots \\ \boldsymbol{A}_6\boldsymbol{x}(t_5) + \boldsymbol{B}_6 & t_5 \le t < t_6 \end{cases} \tag{8.65}$$

where

$$\boldsymbol{x} = \left[i_{Ls}\ i_{Lp}\ v_{Cs}\ v_{Cf}\right]^{\mathrm{T}} = [x_1\ x_2\ x_3\ x_4]^{\mathrm{T}} \tag{8.66}$$

and the $\boldsymbol{A}$ and $\boldsymbol{B}$ matrices differ for each state and can be found using (8.58) to (8.64) and SS as follows

$$\boldsymbol{A}_1 = \boldsymbol{A}_3 = \begin{bmatrix} -\dfrac{R_\mathrm{s}}{L_\mathrm{s}+L_\mathrm{p}} & 0 & -\dfrac{1}{L_\mathrm{s}+L_\mathrm{p}} & 0 \\ -\dfrac{R_\mathrm{s}}{L_\mathrm{s}+L_\mathrm{p}} & 0 & -\dfrac{1}{L_\mathrm{s}+L_\mathrm{p}} & 0 \\ \dfrac{1}{C_\mathrm{s}} & 0 & 0 & 0 \\ 0 & 0 & 0 & -\dfrac{1}{C_\mathrm{f}R_\mathrm{L}} \end{bmatrix} \tag{8.67}$$

$$\boldsymbol{A}_2 = \begin{bmatrix} -\dfrac{N^2R_\mathrm{d}+R_\mathrm{s}}{L_\mathrm{s}} & \dfrac{N^2R_\mathrm{d}}{L_\mathrm{s}} & -\dfrac{1}{L_\mathrm{s}} & -\dfrac{N}{L_\mathrm{s}} \\ \dfrac{N^2R_\mathrm{d}}{L_\mathrm{p}} & -\dfrac{N^2R_\mathrm{d}}{L_\mathrm{p}} & 0 & \dfrac{N}{L_\mathrm{p}} \\ \dfrac{1}{C_\mathrm{s}} & 0 & 0 & 0 \\ \dfrac{N}{C_\mathrm{f}} & -\dfrac{N}{C_\mathrm{f}} & 0 & -\dfrac{1}{C_\mathrm{f}R_\mathrm{L}} \end{bmatrix} \tag{8.68}$$

$$\boldsymbol{A}_4 = \boldsymbol{A}_6 = \begin{bmatrix} -\dfrac{R_\mathrm{s}}{L_\mathrm{s}+L_\mathrm{p}} & 0 & -\dfrac{1}{L_\mathrm{s}+L_\mathrm{p}} & 0 \\ -\dfrac{R_\mathrm{s}}{L_\mathrm{s}+L_\mathrm{p}} & 0 & -\dfrac{1}{L_\mathrm{s}+L_\mathrm{p}} & 0 \\ \dfrac{1}{C_\mathrm{s}} & 0 & 0 & 0 \\ 0 & 0 & 0 & -\dfrac{1}{C_\mathrm{f}R_\mathrm{L}} \end{bmatrix} \tag{8.69}$$

$$\boldsymbol{A}_5 = \begin{bmatrix} -\dfrac{N^2R_\mathrm{d}+R_\mathrm{s}}{L_\mathrm{s}} & \dfrac{N^2R_\mathrm{d}}{L_\mathrm{s}} & -\dfrac{1}{L_\mathrm{s}} & \dfrac{N}{L_\mathrm{s}} \\ \dfrac{N^2R_\mathrm{d}}{L_\mathrm{p}} & -\dfrac{N^2R_\mathrm{d}}{L_\mathrm{p}} & 0 & -\dfrac{N}{L_\mathrm{p}} \\ \dfrac{1}{C_\mathrm{s}} & 0 & 0 & 0 \\ -\dfrac{N}{C_\mathrm{f}} & \dfrac{N}{C_\mathrm{f}} & 0 & -\dfrac{1}{C_\mathrm{f}R_\mathrm{L}} \end{bmatrix} \tag{8.70}$$

$$\boldsymbol{B}_1 = \boldsymbol{B}_3 = \begin{bmatrix} \dfrac{V_\mathrm{DC}}{L_\mathrm{s}+L_\mathrm{p}} & \dfrac{V_\mathrm{DC}}{L_\mathrm{s}+L_\mathrm{p}} & 0 & 0 \end{bmatrix}^\mathrm{T} \tag{8.71}$$

$$\boldsymbol{B}_2 = \begin{bmatrix} \dfrac{V_\mathrm{DC}-Nv_\mathrm{d}}{L_\mathrm{s}} & \dfrac{Nv_\mathrm{d}}{L_\mathrm{p}} & 0 & 0 \end{bmatrix}^\mathrm{T} \tag{8.72}$$

$$\boldsymbol{B}_4 = \boldsymbol{B}_6 = \begin{bmatrix} \dfrac{V_\mathrm{DC}-Nv_\mathrm{d}}{L_\mathrm{s}} & \dfrac{Nv_\mathrm{d}}{L_\mathrm{p}} & 0 & 0 \end{bmatrix}^\mathrm{T} \tag{8.73}$$

$$\boldsymbol{B}_5 = \begin{bmatrix} \dfrac{Nv_\mathrm{d}}{L_\mathrm{s}} & -\dfrac{Nv_\mathrm{d}}{L_\mathrm{p}} & 0 & 0 \end{bmatrix}^\mathrm{T} \tag{8.74}$$

8.3.2 Cyclic-mode model for the LLC converter

Based on the definition of the cyclic-mode model, the following condition holds at the end of each mode:

$$\boldsymbol{x}(t_i) = \boldsymbol{\Phi}_i \boldsymbol{x}(t_{i-1}) + \boldsymbol{\Gamma}_i \tag{8.75}$$

where $\boldsymbol{\Phi_i} = \exp(\boldsymbol{A}_i \delta_i T_{\text{sw}})$ and $\boldsymbol{\Gamma}_i = \boldsymbol{A}_i^{-1}[\boldsymbol{\Phi}_i - \boldsymbol{I}]\boldsymbol{B}_i$

Therefore, the cyclic-mode model of the state variable $\boldsymbol{x}$ is presented in (8.76).

$$\boldsymbol{x}(t) = \begin{cases} \boldsymbol{\Phi}_1(t)\boldsymbol{x}(t_0) + \boldsymbol{\Gamma}_1(t) & t_0 \le t < t_1 \\ \vdots & \vdots \\ \boldsymbol{\Phi}_6(t)\boldsymbol{x}(t_5) + \boldsymbol{\Gamma}_6(t) & t_5 \le t < t_6 \end{cases} \tag{8.76}$$

where $\boldsymbol{\Phi_i}(t) = \exp(\boldsymbol{A}_i(t - t_i))$ and $\boldsymbol{\Gamma}_i(t) = \boldsymbol{A}_i^{-1}[\boldsymbol{\Phi}_i(t) - \boldsymbol{I}]\boldsymbol{B}_i$

To determine initial value of the cyclic-mode model $\boldsymbol{x}(t_0)$, using

$$\boldsymbol{x}(t_0) = [\boldsymbol{I} - \boldsymbol{\Phi}_{\text{tot}}]^{-1}\boldsymbol{\Gamma}_{\text{tot}} \tag{8.77}$$

where

$$\boldsymbol{\Phi}_{\text{tot}} = \prod_{i=m,m-1}^{1} \boldsymbol{\Phi}_i \,, \boldsymbol{\Gamma}_{\text{tot}} = \sum_{i=1}^{m-1} \left(\left(\prod_{j=m,m-1}^{i+1} \boldsymbol{\Phi}_{\text{j}} \right) \boldsymbol{\Gamma}_i \right) + \boldsymbol{\Gamma}_m \tag{8.78}$$

8.3.3 Refining the cyclic-mode condition using Newton's method

To evaluate the initial condition the mode duty ratios are required. Given the symmetry of the two half-cycles, we have $\delta_1 = \delta_4$, $\delta_2 = \delta_5$, $\delta_3 = \delta_6$ and the sum $\delta_1 + \delta_2 + \delta_3$ equals $1/2$. Therefore, determining δ_1 and δ_2 will yield the values for all other duty ratios. This study derives initial estimates for the duration times from phase information, utilizing an AC equivalent circuit model of the converter—a method akin to that outlined in [8.6]. Evaluating (8.77) and (8.78) with initial mode times furnishes an estimate for $\boldsymbol{x}(t_0)$. Subsequently, a refinement step is undertaken, employing the Newton's method [8.7] to enhance the estimates of $\boldsymbol{x}(t_0)$ and the duty ratios.

The operation of the converter over a single cycle, for a specific mode sequence, is determined by the initial conditions, $\boldsymbol{x}(t_0)$, and the duty cycles, δ_1 and δ_2. Let $\boldsymbol{X}$ represent a vector of these values:

$$\boldsymbol{X} = [\boldsymbol{x}^T(t_0) \quad \delta_1 \quad \delta_2]^T \tag{8.79}$$

In steady state operation, $\boldsymbol{x}(t_0)$ equals $\boldsymbol{x}(T_{\mathrm{sw}})$. The duty cycles, δ_1 and δ_2, are determined by diode conduction, as detailed in the converter operation section. These conditions are expressed as follows:

$$v_{L\mathrm{p}}(t_1^-) = N\left(v_{C\mathrm{f}}(t_1^+) + V_{\mathrm{d}}\right) \tag{8.80}$$

$$i_{L\mathrm{s}}(t_2^-) = i_{L\mathrm{p}}(t_2^+) \tag{8.81}$$

where, $t_1 = \delta_1 T_{\mathrm{sw}}$ and $t_2 = (\delta_1 + \delta_2)T_{\mathrm{sw}}$. While this model has no discontinuities, superscripts "+" and "−" are included for completeness. We introduce the cost vector $\boldsymbol{G}$, a function of $\boldsymbol{X}$ derived from the steady-state conditions outlined in (8.80) and (8.81). Once all these conditions are met, indicating steady state operation, $\boldsymbol{G}$ equals $\boldsymbol{0}$.

$$\boldsymbol{G}(\boldsymbol{X}) = \begin{bmatrix} \boldsymbol{x}(t_0 + T_{\mathrm{sw}}) - \boldsymbol{x}(t_0) \\ v_{L\mathrm{p}}(\delta_1 T_{\mathrm{sw}}^-) - N\left(v_{C\mathrm{f}}(\delta_1 T_{\mathrm{sw}}^+) + V_{\mathrm{d}}\right) \\ i_{L\mathrm{s}}((\delta_1+\delta_2)T_{\mathrm{sw}}^-) - i_{L\mathrm{p}}(((\delta_1+\delta_2)T_{\mathrm{sw}}^+) \end{bmatrix} = \begin{bmatrix} g_1 \\ \vdots \\ g_4 \\ g_5 \\ g_6 \end{bmatrix} \tag{8.82}$$

Newton's method is subsequently employed to estimate $\boldsymbol{X}$. The process begins with an initial estimate, $\boldsymbol{X}(0)$, using conjectures for δ_1 and δ_2, and estimates $\boldsymbol{x}(t_0)$ from (8.77). The application of Newton's method in matrix form to this problem is as follows:

$$\boldsymbol{X}^k = \boldsymbol{X}^{k-1} - \alpha\left[\boldsymbol{J}\left(\boldsymbol{X}^{k-1}\right)\right]^{-1}\boldsymbol{G}(\boldsymbol{X}^{k-1}) \tag{8.83}$$

The relaxation factor, $0 < \alpha \leq 1$, is used to enhance convergence. The current iteration step is indexed by k, and $\boldsymbol{J}(\boldsymbol{X}^k)$ represents the Jacobian matrix of partial derivatives computed at the current iteration. The Jacobian, $\boldsymbol{J}$, is defined as follows:

$$\boldsymbol{J}(\boldsymbol{X}) = \frac{\partial \boldsymbol{G}}{\partial \boldsymbol{X}} = \begin{bmatrix} \frac{\partial g_1}{\partial X_1} & \cdots & \frac{\partial g_1}{\partial X_6} \\ \vdots & \ddots & \vdots \\ \frac{\partial g_6}{\partial X_1} & \cdots & \frac{\partial g_6}{\partial X_6} \end{bmatrix} = \begin{bmatrix} \frac{\partial g_1}{\partial i_{Ls}} & \cdots & \frac{\partial g_1}{\partial \delta_2} \\ \vdots & \ddots & \vdots \\ \frac{\partial g_6}{\partial i_{Ls}} & \cdots & \frac{\partial g_6}{\partial \delta_2} \end{bmatrix} \tag{8.84}$$

Due to the complexity of expression (8.84), it is advantageous to utilize the numerical form of the Jacobian for evaluating the partial derivatives, which is using

$$\frac{\partial g_i(\boldsymbol{X})}{\partial X_j} \approx \frac{g_i\left(\boldsymbol{X} + \Delta \boldsymbol{X_j}\right) - g_i(\boldsymbol{X})}{\alpha_j} \tag{8.85}$$

Here, i represents the function index, j the variable index, and $\Delta \boldsymbol{X}_j$ is a 6×1 vector with a single non-zero element α_j in the j^{th} position, representing a small increment. Iteration stops when the L1-norm drops below a predefined acceptable threshold, λ.

$$\left|\boldsymbol{X}^{\text{final}} - \boldsymbol{X}^{\text{final}-1}\right| < \lambda \tag{8.86}$$

where $\boldsymbol{X}^{\text{final}}$ denotes the vector of true initial conditions for cyclic operation, encompassing $\boldsymbol{x}(t_0)$ and δ_1 and δ_2.

8.3.4 RMS cyclic-mode modelling of the LLC converter

After getting the state vector initial value $\boldsymbol{x}(t_0)$ and each mode duration. We can start to build the RMS cyclic-mode model for the LLC converter, similar to the process in previous sections on the class E and class EF_2 inverters. The detail process is as follows:

1. Derive the expression of $\boldsymbol{A}_i \oplus \boldsymbol{A}_i$ and $\boldsymbol{B}_i \oplus \boldsymbol{B}_i$ for each mode by (8.6) (8.7) and (8.67) -(8.74)
2. Derive the expression of $\overline{\boldsymbol{A}}_i$ and $\overline{\boldsymbol{B}}_i$ for each mode based on (8.8), the construct the piecewise linear model for $\overline{\boldsymbol{x}}$.
3. Derive the expression of $\overline{\overline{\boldsymbol{A}}}_i$ using (8.13) and subsequently construct the mean-square system using (8.16) (8.18).
4. Use $\boldsymbol{x}(t_0)$ to obtain the initial value expression for $\overline{\overline{\boldsymbol{z}}}(t_0)$.
5. Determine the RMS values of the original state variable $\boldsymbol{x}$ using (8.19).

8.3.5 Model validation

This section investigates the accuracy of the cyclic-mode model and the proposed root mean square (RMS) calculation. An LLC resonant converter was designed to deliver a regulated 5V output from an input voltage range of 45-55V, with a power rating of 25W. The converter was constructed, and its component values were precisely measured with an LCR meter, as presented in Table 8.7.

Table 8.7. Parameter values and operating range for the LLC converter

Parameter 's name	**Parameter 's value**
R_L (Ω)	$1.6 - 40$
L_s (mH)	4.8
C_s (nF)	66
L_p (uH)	20.34
C_{f} (uF)	10
V_{DC} (V)	$45 - 55$
f_{sw} (kHz)	$150 - 350$
N	5.5

The schematic diagram for the LLC converter board is shown in Fig. 8.12. As shown in Fig. 8.12, L1 and C1-C3 correspond to the LLC resonant circuit elements L_s and C_s, respectively. Transformer TR2 establishes the turns ratio N and the shunt inductance L_p of the converter, which is formed by inserting an air gap in the core. Transformer TR2 establishes the turns ratio N and the shunt inductance L_p of the converter, which is formed by inserting an air gap in the core. The secondary side of the transformer is rectified by D12. A TL431 shunt regulator is used to form a PI controller to adjust the frequency response of the converter. The error signal generated by the TL431 is transmitted across the isolation gate via an optocoupler U2. The error signal is forwarded to U1 (Texas Instruments UCC25600 controller IC), which regulates the output voltage by adjusting the frequency of the square-wave input voltage. Q1 and Q2 generate the input voltage to the resonant tank, whose gate signal is derived from the gate drive transformer of U1. The resistance and capacitance around U3 determine the compensation frequency response, and R9 and R14 set the bias level of the optocoupler. The converter protype is shown in Fig. 8.13.

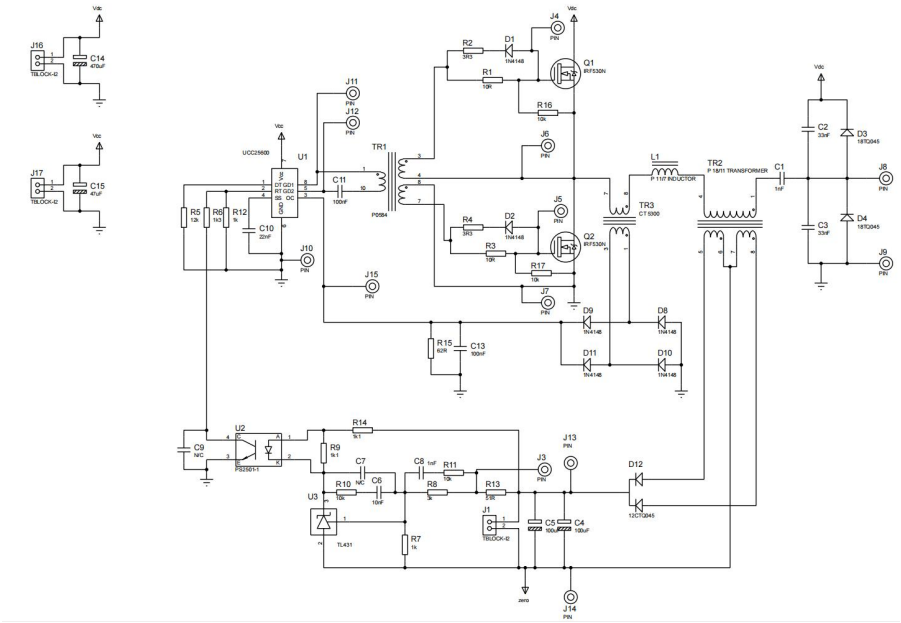

Fig. 8.12. Schematic diagram for the LLC converter board

(a)

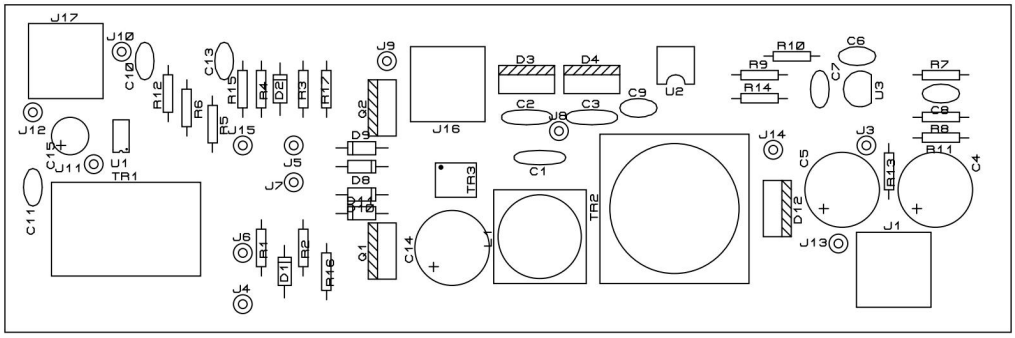

(b)

Fig. 8.13. (a) Photograph of Implemented LLC converter (b) The LLC converter PCB silk screen layout

Operating within its specified voltage range, the converter's series inductor current (i_{Ls}), series capacitor voltage (v_{Cs}), and operating frequency (f_{sw}) were measured. Additionally, an idealized SPICE model using identical parameters was created. Waveforms, along with periodic RMS and average values for i_{Ls} and v_{Cs}, were recorded for both the physical converter and the SPICE model. The SPICE model schematic diagram is shown in Fig. 8.14,

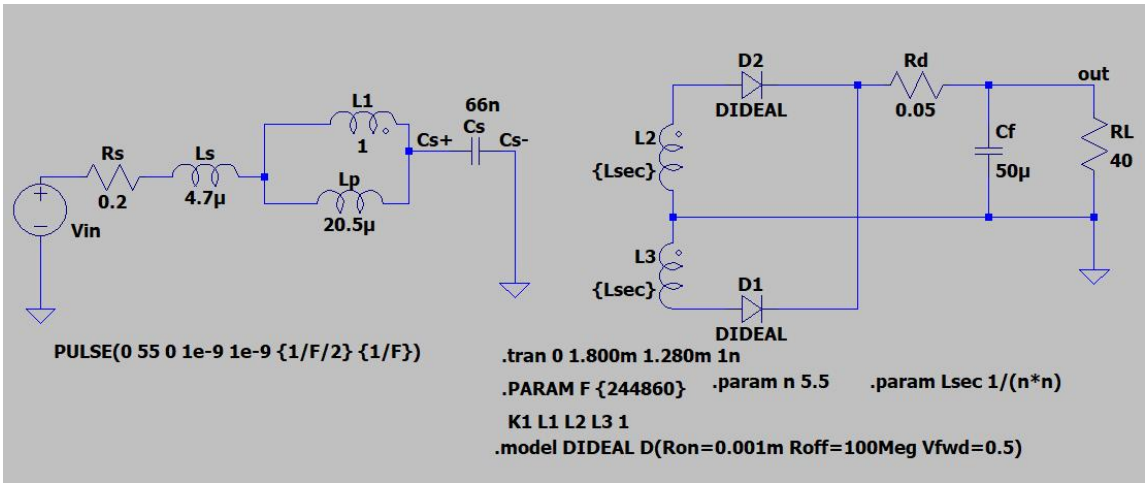

Fig. 8.14. Schematic diagram of the LLC converter SPICE model

The LLC converter model, defined by piecewise equations (4.18)-(8.64), along with its practical implementation, was analysed under three different loads, with the mode sequences detailed in Table 8.8.

Table 8.8. Converter operating sequences under different conditions

Load (Ω)	SS sequences	V_{DC} (V)	f_{sw} (kHz)
40	(1,0), (1,1), (1,0), (0,0), (0,-1), (0,0)	45	200
		50	219
		55	244
5.6	(1,0), (1,1), (1,0), (0,0), (0,-1), (0,0)	45	189
		50	206
		55	228
1.7	(1,1), (1,0) (0,-1), (0,0)	45	168
		50	182
		55	201

Mode sequences vary depending on the load. Table 8.8 lists the operating conditions for three distinct loads across three varying input voltages. For each scenario, the table provides the switching frequency (f_{sw}) needed to achieve a 5 V output.

During six-mode operation, both δ_1 and δ_2 were initially set at 0.2. In contrast, for four-mode operation, δ_1 was set to 0.25 with δ_2 being unused. The initial condition $\boldsymbol{x}(t_0)$ was estimated using equation (8.77), based on the initial duty cycle settings. These initial values were refined by applying Newton's method, as detailed in equations (8.79) to (8.86), with a relaxation factor α set to 0.1 for wider convergence, and a stopping criterion of λ set to 10^{-8}. The refined estimations are presented in Table 8.9.

Table 8.9. Steady-state initial conditions estimation results

$\boldsymbol{X}$	45 V, 40Ω		45 V, 5.6Ω		45 V, 1.7Ω	
	Initial	Refined	Initial	Refined	Initial	Refined
i_{Ls} (A)	−2.88	−1.63	−4.75	−1.84	−4.01	−1.94
i_{Lp} (A)	−1.96	−1.63	−2.86	−1.84	−1.96	−1.94
v_{Cs} (V)	21.48	21.75	23.90	16.59	−79.43	−10.73
v_{Cf} (V)	5.80	4.99	8.52	4.97	11.38	5.05
δ_1	0.20	0.17	0.20	0.10	0.25	0.30
δ_2	0.20	0.19	0.20	0.28	-	-

Fig. 8.15, Fig. 8.16, and Fig. 8.17 compare the resonant inductor current i_{Ls} and the series capacitor voltage v_{Cs} from both the cyclic-mode model and an idealized SPICE simulation, alongside experimental data collected with a PEM CWT015 Rogowski coil and a Keysight DSOX2002A oscilloscope, respectively. Both SPICE simulations and experimental waveform data were captured at steady state. Each data set corresponds to a different load level at a forty-five V_{DC} input, demonstrating the results for both mode sequences.

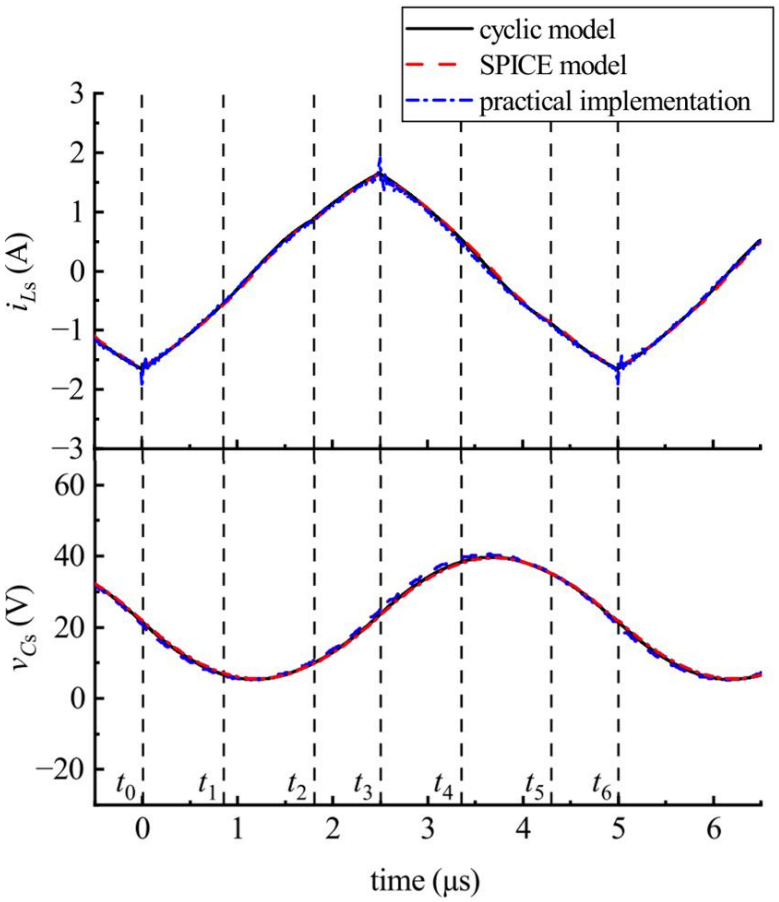

Fig. 8.15. Comparison of series inductor current i_{Ls} and series capacitor voltage, v_{Cs} at 200 kHz, 40 Ω and 45 V_{DC}. The cyclic-mode model, SPICE model and practical implementation are shown. t_0 to t_6 refer to the cyclic-model

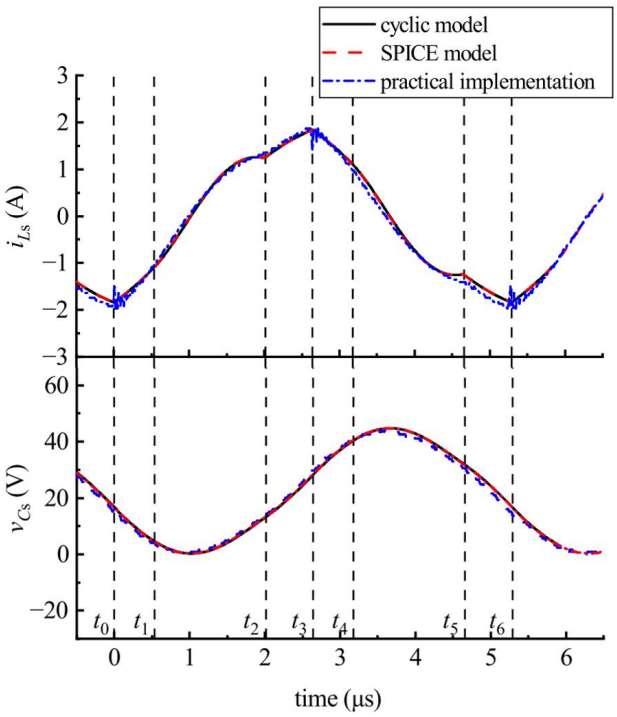

Fig. 8.16. Comparison of series inductor current i_{Ls} and series capacitor voltage, v_{Cs} at 189 kHz, 5.6 Ω and 45 V_{DC}. The cyclic-mode model, SPICE model and practical implementation are shown. t_0 to t_6 refer to the cyclic-model

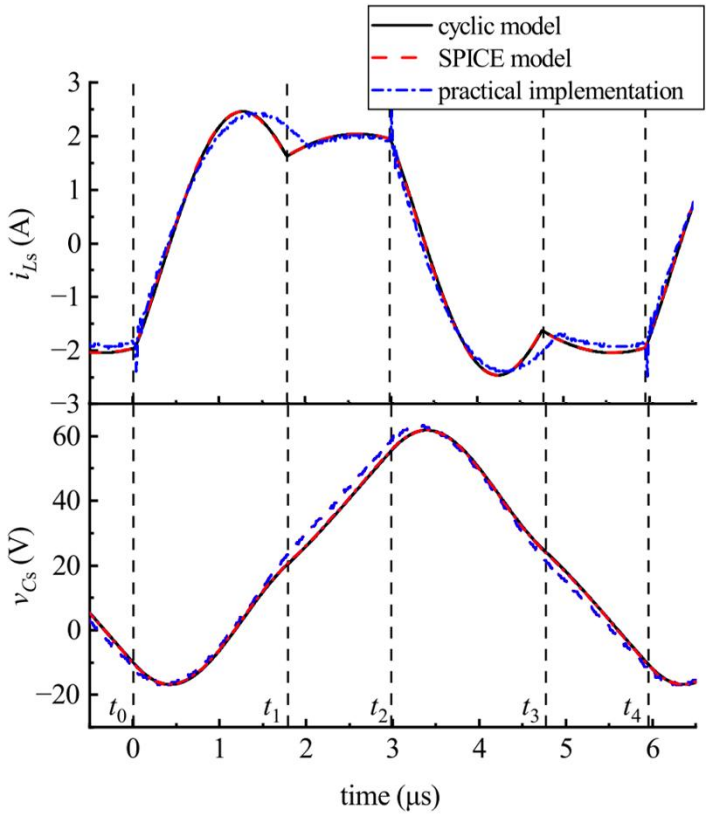

Fig. 8.17. Comparison of series inductor current i_{Ls} and series capacitor voltage, v_{Cs} at 168 kHz, 1.7 Ω and 45 V_{DC}. The cyclic-mode model, SPICE model and practical implementation are shown. t_0 to t_4 refer to the cyclic-model

The results indicate a negligible difference between the cyclic-mode and SPICE models, with the cyclic-mode model also closely matching practical outcomes. The root-mean-square errors (RMSE) for v_{Cs} in the experimental data are 0.8 V for 40 Ω, 0.8 V for 5.6 Ω, and 2.3 V for 1.7 Ω loads, relative to a 45 V_{DC} supply. Similarly, RMSE values for the resonant current are 0.04 A, 0.08 A, and 0.16 A for resonant currents in the range of 1-1.5 ARMS. The larger errors, particularly evident in Fig. 8.17, are attributed to the approximation inaccuracies of δ_1, where the diodes conduct for longer durations than anticipated. These discrepancies are likely due to unmodeled parasitic elements, like transformer losses, which have a more pronounced impact under higher loads.

Fig. 8.18 presents a comparison of RMS inductor currents across various loads and supply voltages. The cyclic-model's results align excellently with the nine practical outcomes displayed.

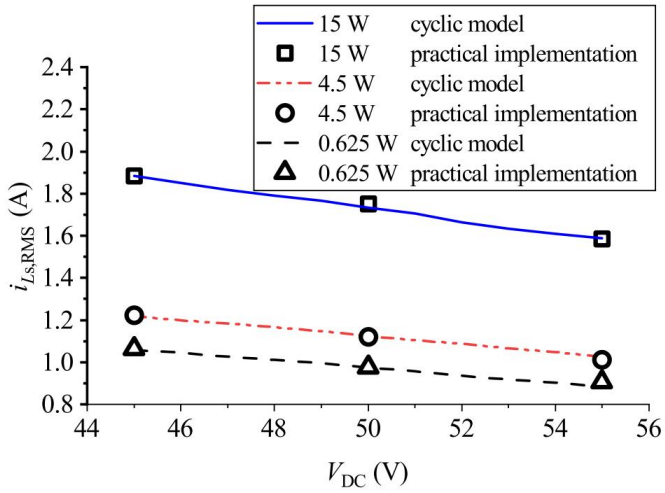

Fig. 8.18. Comparison of series inductor current i_{Ls} RMS value versus V_{DC} between cyclic-mode model result with experimental circuit result for three output power levels

Table 8.10 complements Fig. 8.18 by detailing specific average and RMS values of i_{Ls} for a particular operating condition. As expected, the average values of the signals are approximately zero. From both the figure and the table, it can be seen that the RMS values determined using the proposed cyclic-mode model are in strong agreement with the measurements with an error of less than 5%.

Table 8.10. Average and comparison at V_{DC}=45 V and R_L= 40 Ω

		i_{Ls} (A)	v_{Cs} (V)
Average	Cyclic-mode model	-0.009	22.5
	Practical implementation	0.005	22.2
RMS	Cyclic-mode model	1.02	25.8
	Practical implementation	1.01	25.6

8.4 Conclusion

This Chapter introduces a universal method for accurately computing the RMS values of a state vector in any DC input converter operating in cyclic steady-state, regardless of its order.

This technique necessitates only a piecewise state-variable model. It enables the direct derivation of precise RMS values for each state variable and accurate mode durations, thus circumventing complex algebraic computations.

The validity of this technique is demonstrated using three different systems: a sub-optional operation class E inverter, a sub-optional operation class EF2 inverter, and a discontinuous operation LLC converter. The accuracy of the waveform evaluation RMS method is critically assessed through SPICE models, which exhibit near-perfect concordance with the proposed approach. A practical implementation on an LLC converter indicates a root-mean-square error of less than 5%.

Overall, although the DC input assumption limits the technique's use, it has proven to be an effective method for analysing the steady-state behaviour of a wide range of DC-input switching power supplies, including resonant converters. This effectiveness is due to the significant reduction in computation time while maintaining accuracy. Future improvements could focus on enhancing Newton's method to consistently obtain accurate circuit operating condition.

8.5 References

[8.1] ‘STEMiNC Steiner & Martins. Piezoelectric disc information’. https://www.steminc.com/PZT/en/piezoelectric-disc-25x85mm-s-235-khz Accessed 05 November 2023

[8.2] Aldhaher, Samer, et al. “Modeling and Analysis of Class EF and Class E/F Inverters With Series-Tuned Resonant Networks.” *IEEE Transactions on Power Electronics*, vol. 31, no. 5, May 2016, pp. 3415–30. https://doi.org/10.1109/tpel.2015.2460997.

[8.3] Lazar, James F., and Robert Martinelli. "Steady-state analysis of the LLC series resonant converter." *Sixteenth Annual IEEE Applied Power Electronics Conference and Exposition* (APEC 2001). Vol. 2. 2001, https://doi.org/10.1109/apec.2001.912451.

[8.4] Visser, H. R., and P. P. J. Van den Bosch. "Modelling of periodically switching networks." *PESC'91 Record 22nd Annual IEEE Power Electronics Specialists Conference.* 1991, https://doi.org/10.1109/pesc.1991.162655.

[8.5] Gould, C., et al. “CLL resonant converters with output short-circuit protection.” *IEE Proceedings. Electric Power Applications*, vol. 152, no. 5, Jan. 2005, pp. 1296-1306. https://doi.org/10.1049/ip-epa:20045157.

[8.6] Foster, Martin P., et al. “Analysis of CLL Voltage-Output Resonant Converters Using Describing Functions.” IEEE Transactions on Power Electronics, vol. 23, no. 4, July 2008, pp. 1772–1781, https://doi.org/10.1109/tpel.2008.924835.

[8.7] Malyna, D., Duarte, J., Hendrix, M., & Van Horck, F. (2004). A comparison of methods for finding steady- state solution in power electronic circuits. *International Power Electronics and Motion Control Conference*, *3*, pp. 1700–1705. https://www.narcis.nl/publication/RecordID/oai%3Apure.tue.nl%3Apublications%2Fb41d8926-ee31-4229-bebb-237ffd33adaf.

Chapter 9. Conclusion and future work

9.1 Discussion

This thesis proposes techniques to improve the simulation of DC-input switch converters, focusing mainly on estimating mode durations, using models to predict circuit behaviour, and forecasting signal root mean square (RMS) values.

Chapter 1 discusses the motivation behind this work, emphasising that advances in power electronics aim to improve energy conversion efficiency. To achieve higher energy conversion efficiencies, enhancing the accuracy and efficiency of switching converter analyses has been identified as a key focus. This thesis, therefore, concentrates on and contributes to the improvement of switching power supply modelling techniques, as outlined below,

To familiarise the reader with the basics and state of the art in the field, Chapter 2 provides a literature review that introduces the main classifications of converters based on the switching principle, namely hard-switching converters, and soft-switching converters. It then describes various converter topologies, such as the boost converter and the class E inverter, highlighting the differences between hard-switching and soft-switching converters in terms of their operational behaviours. Subsequently, three mainstream switching converter modelling approaches are presented: fundamental mode analysis, state-space averaging, and cyclic-mode modelling. The principles and modelling processes of these approaches are described in detail, and their characteristics and applicable scenarios are analysed. Finally, the important role of RMS values in the analysis of switching circuits is illustrated, and some of the methods for calculating RMS are presented.

Although cyclic-mode modelling involves segmentation constant assumptions on the inputs and complex modelling, it remains a superior method for analysing a wide range of switching converters, including resonant converters. This is because it does not assume the operating

behaviour of the power supply, making it suitable for hard-switching converters with switching frequencies higher than the system's internal dynamic frequency, as well as for resonant converters with switching frequencies close to the system's internal dynamic frequency. By avoiding assumptions about the system's operation, cyclic-mode modelling minimises error, resulting in analysis that closely mirrors real operation. The final section points to RMS as a key parameter reflecting the circuit's effectiveness, and improvements to the modelling technique should make it easier to calculate the RMS values of the circuit's key variables. The main shortcomings of the cyclic-mode modelling approach are also identified, some of which have been addressed in this thesis.

Chapter 3 described the switch converter design techniques used in subsequent Chapters. The Chapter began with the design of boost converters, decomposing the circuit based on the conducting state of the switch components. This allowed for determining the value ranges of key components under various operating conditions. In designing class EF inverters, based on assumptions such as sufficiently large input inductance to consider the input current as DC, describing functions were used for modelling the converter and determining component values. For the design of LLC converters, the fundamental mode analysis method is employed to simplify the circuit structure, yielding gain curves under various parameter conditions to assist in the design process.

This chapter outlines the design process by analysing different switching converters, providing design guidelines for the creation of experimental circuits for the subsequent validation process. It is also observed that most analysis methods for switching power supplies make assumptions about the operational behaviour of the circuit to simplify the analysis process. However, these assumptions can lead to errors, making the analysis inaccurate. The analysis in this chapter represents the unique advantages of cyclic-mode modelling, an analytical approach that does not make assumptions about the operation of the circuit.

Chapter 4 employed cyclic-mode modelling to analyse the operation of class EF inverters. It was applied to class EF_2 inverters with a piezoelectric transformer (PT) as the auxiliary resonant branch, operating in an optimal state. Initially, a piecewise linear model is established for the optimal operating state, followed by the construction of its cyclic-mode model. The precision of the cyclic-mode model in simulating class EF_2 inverters is revealed through comparison with SPICE simulation models. Subsequently, the feasibility of replacing the auxiliary resonant branch of class EF_2 inverters with PT is demonstrated by comparing it with converter prototypes.

The analysis and validation in this chapter firstly demonstrates the accuracy of cyclic-mode modelling in analysing a resonant converter in steady state operation, and subsequently demonstrates the feasibility of using a PT to replace a conventional series resonant branch circuit, which provides ideas for a wider range of PT applications in the future. The analysis also revealed that the inputs to the cyclic-mode modelling are the operating conditions of the circuit, which include the number of modes, their order and the duty cycle of each mode. The accuracy of the cyclic-mode model depends on the accuracy of its inputs, and the model's requirement for accurate inputs points to the direction of improvement in modelling techniques.

Chapter 5 introduced a technique used in subsequent Chapters that combines the Newton-Raphson method with the cyclic-mode model to accurately determine the steady-state operating conditions of switch converters. This technique expands the application scope of the cyclic-mode model, enabling it to accurately simulate multi-mode converters. The efficacy of this technique has been confirmed through testing on class E inverters under suboptimal operating conditions.

This new application of Newton's method addresses the high accuracy requirement of inputs for cyclic-mode modelling. By simply inputting the order of the modes and a rough estimate of the duty cycle for each mode into Newton's method, the exact value of the duty cycle can be obtained, enabling accurate cyclic-mode models. The analysis acknowledges that although

the introduction of Newton's method increases the complexity of the modelling technique and necessitates an additional method to make a rough estimate of circuit operation, it significantly reduces the precision required for the inputs in cyclic-mode modelling. This reduction in input accuracy requirements simplifies the use of the technique and enhances the accuracy of the model. Consequently, the cyclic-mode modelling technique becomes more comprehensive, and its range of application expands.

Based on the request for improvements in modelling techniques in Chapter 2, Chapter 6 details the process of deriving the RMS cyclic-mode modelling framework. This framework can be applied to a cyclic-mode model to facilitate the prediction of cycle mean and RMS values of state variables without generating waveforms. Although the framework involves a complex derivation process, it integrates the squaring and averaging processes of RMS calculation into matrix integral process. This greatly simplifies the computation of RMS values for state variables using cyclic-mode models, extending the functionality of the cyclic-mode modelling technique to a wider range of applications.

Chapter 7 combined the Newton method and RMS cyclic-mode modelling technique, applying them to boost converters operating in discontinuous mode. The steady-state operating conditions obtained through the Newton method are input into the RMS cyclic-mode modelling process. This yielded an accurate RMS cyclic-mode model for the boost converter, capable of outputting precise signal waveforms, their periodic averages, and RMS values. Comparison with SPICE simulation models and converter prototypes validates not only the accuracy of these methods in simulating boost converters but also highlights the effectiveness of their combination.

The analyses in this chapter demonstrate the accuracy and speed of calculating the RMS of key circuit variables using the cyclic RMS framework. The analysis shows that the conventional method of calculating RMS values has a maximum error of more than 5% for the same runtime, whereas the cyclic RMS framework method has a maximum error of less than 1%. This chapter also illustrates both the feasibility and effectiveness of combining

Newton's method with the cyclic RMS framework, thereby defining the basic structure of the improved cyclic-mode modelling technique.

Chapter 8 introduced a simulation technique named 'cyclic RMS technique.' This technique is applied to different resonant converter topologies. Comparing its simulation results with those of SPICE models and practical implementations validates its accuracy in waveform prediction and speed in RMS calculations for multi-mode resonant converters.

The technique requires only the circuit structure, operating parameters, and component values as inputs. Cycle waveforms, cycle averages and RMS values can be obtained for each inductor current and capacitor voltage in the circuit. This is achieved by using FMA, describing function method, Newton's method, cyclic-mode modelling, and cyclic RMS framework and integrating them. Although the technique still has shortcomings in solving the boundary problem of circuits under different operating conditions, the presentation of this technique represents the fulfilment of the requirements for the improvement of the circuit analysis techniques mentioned in the literature review, which will make it possible to analyse switching power supplies with DC inputs more accurately and quickly.

9.2 Thesis conclusion

This thesis develops and improves modelling techniques to increase the efficiency and accuracy of analysing switching converters, achieved through the combined use of several techniques. It describes using the Newton-Raphson method to determine the steady-state operating conditions of a switching converter for given parametric conditions. By combining the Newtonian method, represented by the numerical Jacobi matrix, with the cyclic-mode model, it is possible to predict the steady-state operation of a multi-mode switching converter, thus extending the application of the cyclic-mode model. Both simulation and practical results demonstrate the effectiveness of these techniques.

In order to obtain RMS values more easily and accurately, we have developed the cyclic RMS framework. This framework, based on the concept of the cyclic-mode model, enables the calculation of RMS values without generating signal waveforms by integrating the squaring and averaging processes of RMS value computation into the matrix integration process. The accuracy and speed of the method have been verified through simulation and practical experiments. Finally, a modelling procedure called RMS cyclic-mode modelling is proposed, integrating existing circuit analysis techniques and the techniques studied in this thesis. This makes the analysis of switching power supplies with DC inputs easier and more efficient.

In summary, the techniques and modelling procedure presented in this thesis enable engineers to obtain accurate analysis results for DC-input switching power supplies more quickly. These advances have been achieved by improving the cyclic-mode model and using a combination of Newton's method in conjunction with established circuit analysis techniques. Some of the research in this work has been published in a conference paper.

9.3 Suggested future work

Although the techniques in this thesis represent advanced developments in the field, further improvements are possible. The following summarizes potential areas for further development.

9.3.1 Improvements to the Method of Calculating the Initial Values of the Model

After integrating the cyclic-mode model with the new application of Newton's method introduced in Chapter 5, the accuracy requirements for inputs in cyclic-mode modelling were reduced. However, Newton's method still necessitates a certain degree of accuracy in the model inputs. This requires additional computational methods to provide a rough estimate of

the converter's operating behaviour. Currently, the describing function method is used for estimation. While it works well in most cases, its assumption of sinusoidal waveform shapes can result in significant prediction deviations when the actual waveform deviates substantially from a sinusoidal shape. This prevents Newton's method from iterating correctly, leading to incorrect analyses.

The proposed improvement begins the power supply analysis with a sinusoidal waveform, allowing Newton's method to iterate successfully. Subsequently, the circuit parameters are finely tuned, and a reasonable prediction of the model's modes sequences for the next use of Newton's method is made based on the results of the previous successful iteration. This prediction is fed into Newton's method and re-iterated to obtain an accurate duty cycle for the modes. This improved analysis is then validated against simulation results, verifying the feasibility of the improvement.

9.3.2 Improved Analysis of Switching Behaviours in the Model

Although adding the switch on-resistance in the validation section of Chapter 8 makes the cyclic-mode model predictions more accurate, ideal assumptions about the switching behaviour in the model still limit the accuracy in applications requiring high precision.

To make cyclic-mode modelling more representative of real circuit operation and enhance its accuracy further, the proposed improvement involves a deep analysis of the operational principles of each type of switch components (including MOSFETs, transistors, diode etc.) during switching behaviour. The switching behaviour is added as a new mode to the original mode sequence. This improvement will be verified through comparisons with simulation and physical prototypes, demonstrating its feasibility.